

# Cosmic Ray Variability: Century of Its Observations

Guest Editors: Karel Kudela, Badruddin, and José F. Valdés-Galicia





---

# **Cosmic Ray Variability: Century of Its Observations**

Advances in Astronomy

---

## **Cosmic Ray Variability: Century of Its Observations**

Guest Editors: Karel Kudela, Badruddin,  
and José F. Valdés-Galicia



---

Copyright © 2013 Hindawi Publishing Corporation. All rights reserved.

This is a special issue published in “Advances in Astronomy.” All articles are open access articles distributed under the Creative Commons Attribution License, which permits unrestricted use, distribution, and reproduction in any medium, provided the original work is properly cited.

## Editorial Board

Cesare Barbieri, Italy  
Joshua S. Bloom, USA  
Michael Brotherton, USA  
Giovanni Carraro, Italy  
Alberto J. Castro-Tirado, Spain  
Michael Disney, UK  
Elmetwally Elabbasy, Egypt  
Nye Evans, UK  
Maurizio Falanga, Switzerland  
Duncan Forbes, Australia  
Andrew Fruchter, USA  
B. T. Gänsicke, UK  
Paul Goldsmith, USA  
Jonathan Grindlay, USA

Martin Hardcastle, UK  
Dean Hines, USA  
Dieter Horns, Germany  
Ivan Hubeny, USA  
John Hughes, USA  
Wing Huen Ip, Taiwan  
Valentina Klochkova, Russia  
Gregory Laughlin, USA  
Myung G. Lee, Republic of Korea  
Karen Leighly, USA  
Jeffrey Linsky, USA  
Mario Mateo, USA  
Ronald Mennickent, Chile  
Zdzislaw E. Musielak, USA

Valery Nakariakov, UK  
Jerome Orosz, USA  
George Pavlov, USA  
Juri Poutanen, Finland  
Somak Raychaudhury, UK  
William Reach, USA  
Peter Roming, USA  
Ata Sarajedini, USA  
Regina Schulte-Ladbeck, USA  
Ravi Sheth, USA  
Roberto Turolla, Italy  
Gary Wegner, USA  
Glenn J. White, UK  
Paul J. Wiita, USA

# Contents

**Cosmic Ray Variability: Century of Its Observations**, Karel Kudela, Badruddin, and José F. Valdés-Galicia  
Volume 2013, Article ID 680435, 2 pages

**Diffusion Coefficients, Short-Term Cosmic Ray Modulation, and Convected Magnetic Structures**,  
John J. Quenby, Tamitha Mulligan, J. Bernard Blake, and Diana N. A. Shaul  
Volume 2013, Article ID 429303, 10 pages

**On the Onset Time of Several SPE/GLE Events: Indications from High-Energy Gamma-Ray and Neutron Measurements by CORONAS-F**, Viktoria Kurt, Karel Kudela, Boris Yushkov, and Vladimir Galkin  
Volume 2013, Article ID 690921, 15 pages

**Cosmic Ray Investigation in the Stratosphere and Space: Results from Instruments on Russian Satellites and Balloons**, Yu. I. Logachev, L. L. Lazutin, and K. Kudela  
Volume 2013, Article ID 461717, 20 pages

**Latitudinal Dependence of Cosmic Rays Modulation at 1 AU and Interplanetary Magnetic Field Polar Correction**, P. Bobik, G. Boella, M. J. Boschini, C. Consolandi, S. Della Torre, M. Gervasi, D. Grandi, K. Kudela, S. Pensotti, P. G. Rancoita, D. Rozza, and M. Tacconi  
Volume 2013, Article ID 793072, 12 pages

**Thirty-Year Periodicity of Cosmic Rays**, Jorge Pérez-Peraza, Víctor Velasco, Igor Ya. Libin, and K. F. Yudakhin  
Volume 2012, Article ID 691408, 11 pages

**Long-Term Cosmic Ray Variability and the CME-Index**, Helen Mavromichalaki and Evangelos Paouris  
Volume 2012, Article ID 607172, 8 pages

**Measurement by FIB on the ISS: Two Emissions of Solar Neutrons Detected?**, Y. Muraki, K. Koga, T. Goka, H. Matsumoto, T. Obara, O. Okudaira, S. Shibata, and T. Yamamoto  
Volume 2012, Article ID 379304, 14 pages

**New Insights on Cosmic Ray Modulation through a Joint Use of Nonstationary Data-Processing Methods**, A. Vecchio, M. Laurenza, M. Storini, and V. Carbone  
Volume 2012, Article ID 834247, 9 pages

## Editorial

# Cosmic Ray Variability: Century of Its Observations

**Karel Kudela,<sup>1</sup> Badruddin,<sup>2</sup> and José F. Valdés-Galicia<sup>3</sup>**

<sup>1</sup> Department of Space Physics, Institute of Experimental Physics, Slovak Academy of Sciences, Watsonova 47, 04001 Košice, Slovakia

<sup>2</sup> Department of Physics, Aligarh Muslim University, Aligarh 202 002, India

<sup>3</sup> Instituto de Geofísica, Universidad Nacional Autónoma de México, Ciudad Universitaria, 04510 México, DF, Mexico

Correspondence should be addressed to Karel Kudela; [kkudela@kosice.upjs.sk](mailto:kkudela@kosice.upjs.sk)

Received 27 February 2013; Accepted 27 February 2013

Copyright © 2013 Karel Kudela et al. This is an open access article distributed under the Creative Commons Attribution License, which permits unrestricted use, distribution, and reproduction in any medium, provided the original work is properly cited.

Cosmic ray (CR) discovery in 1912 initiated the experimental and theoretical studies in various fields of physics. The issue call was targeted to variability of CR reflected in low energy CR measurements. To understand the propagation of CR in the heliosphere, the knowledge of the diffusion coefficients is important. A paper by J. J. Quenby et al. indicates the new possibilities of probing the fine structure of CR propagation when using the high count rate CR measurements on satellites (below the atmospheric cutoff) with the detector having a large geometrical factor. Implications for different descriptions of particle behavior studied in the three cases are reported. The method proposed, that is, using local particle conditions to check diffusion coefficients with locally derived plasma parameters, is a new way of validating the ability to model cosmic wave-particle interaction in a collisionless regime. Solar modulation is described using a 2D (radius and colatitude) Monte Carlo approach to solve the transport equation including diffusion, convection, drift, and adiabatic energy loss, in a paper by P. Bobík et al. In addition to earlier papers by the group, the IMF is here modified with latitudinal components and its effect is discussed.

Time variability and related modulation effects have been studied using the ground-based CR measurements in three papers. A. Vecchio et al. using Climax neutron monitor data proposed a new, combined application of the wavelet technique and an empirical mode decomposition. The authors were able to discern the CR variations induced by the solar activity and those possibly related to drift in large scale IMF of heliosphere. H. Mavromichalaki and E. Paouris used for the analysis data from another neutron monitor and CME SOHO catalogue for the period of 23rd

and a part of 24th solar cycle. The authors found that the best reproduction of CR intensity is obtained when using sunspot number, IMF, CME-index, and tilt angle of the heliospheric current sheet. For the temporal variability of CR, the paper by J. Pérez-Peraza et al. is using another source of information, namely, records of cosmogenic isotopes <sup>10</sup>Be and <sup>14</sup>C suitable to check CR variability on longer time scales. Using wavelet as well as ARMA technique, the authors revealed the persistence of ~30-year periodicity in CR flux that is of importance, for example, in a possible connection with climatic phenomena.

Two papers have been related to solar high energy particle emissions. V. Kurt et al. analyzed the high energy gamma and neutron emissions from solar flares as observed by low altitude polar satellite CORONAS-F in 2001–2005 (device SONG). The authors showed that SONG response was consistent with neutral pion-decay gamma ray and neutron emissions from a couple of flares and the onset times of GLEs were compared with the time of high energy photon emissions. The observations of solar neutrons on satellites are an important but not an easy task. One type of such measurements on ISS is described in a paper by Y. Muraki et al. Three years of observations are summarized by the authors. Their analysis shows that solar neutrons were possibly observed in connection with two solar flares, namely, March 7 and June 7 in 2011.

In addition to ground-based measurements, many of the results on CR variability were obtained on balloons and satellites. A review paper by Y. I. Logachev et al. summarizes selected results of CR research obtained over long time period by the Russian satellites and balloons.

We believe the papers collected in this issue constitute a good sample of relevant contemporary problems in the field of cosmic ray variability and could therefore give the readers a broad view of the topics under discussion in this important field of CR research.

*Karel Kudela*  
*Badruddin*  
*José F. Valdés-Galicia*

## Research Article

# Diffusion Coefficients, Short-Term Cosmic Ray Modulation, and Convected Magnetic Structures

John J. Quenby,<sup>1</sup> Tamitha Mulligan,<sup>2</sup> J. Bernard Blake,<sup>2</sup> and Diana N. A. Shaul<sup>1</sup>

<sup>1</sup> *Blackett Laboratory, Imperial College, London SW7 2BZ, UK*

<sup>2</sup> *Space Sciences Department, The Aerospace Corporation, Los Angeles, CA 90009, USA*

Correspondence should be addressed to Tamitha Mulligan; [tamitha.mulligan@aero.org](mailto:tamitha.mulligan@aero.org)

Received 2 August 2012; Revised 18 January 2013; Accepted 19 January 2013

Academic Editor: José F. Valdés-Galicia

Copyright © 2013 John J. Quenby et al. This is an open access article distributed under the Creative Commons Attribution License, which permits unrestricted use, distribution, and reproduction in any medium, provided the original work is properly cited.

Three cases of large-amplitude, small spatial-scale interplanetary particle gradients observed by the anticoincidence shield (ACS) aboard the INTEGRAL spacecraft in 2006 are investigated. The high data rates provided by the INTEGRAL ACS allow an unprecedented ability to probe the fine structure of GCR propagation in the inner Heliosphere. For two of the three cases, calculating perpendicular and parallel cosmic ray diffusion coefficients based on both field and particle data results in parallel diffusion appearing to satisfy a convection gradient current balance, provided that the magnetic scattering of the particles can be described by quasi-linear theory. In the third case, perpendicular diffusion seems to dominate. The likelihood of magnetic flux rope topologies within solar ejecta affecting the local modulation is considered, and its importance in understanding the field-particle interaction for the astrophysics of nonthermal particle phenomena is discussed.

## 1. Introduction

A Forbush Decrease (FD) is a global transient decrease in Galactic Cosmic-Ray (GCR) intensity followed by a substantially slower recovery. Since Scott Forbush's discovery and description of these phenomena in the late 1930s, FDs have been put into context with increasing developments within heliospheric physics. In particular, detailed observations of coronal mass ejections (CMEs) and in situ observations of the solar wind and energetic particles have greatly increased understanding of the underlying physics of FDs (see review articles by [1–3]).

This investigation focuses on small amplitude and high-frequency variability in the GCR corresponding to timescales less than a few hours, much shorter than that described by the classical FD. However, small-amplitude, mHz variability in the GCR is an experimental challenge in that very large instrumental geometric factors are required in order to make statistically significant measurements of the GCR in time periods of a few minutes or less. Therefore, only a few of these investigations can be found in the literature. Among these studies, [4] establishes the existence of short-spatial-scale GCR intensity gradients of a few percent amplitude

(at >200 MeV energies) convecting with the solar wind past the Earth, coincident with the observation of an FD. This study correlates magnetic substructures within interplanetary CMEs (ICMEs) with short-scale intensity variations in the GCR. The authors in [5] investigate four simple magnetic field models for explaining short-term reductions in the GCR intensity and associated energetic particle propagation concluding that only a magnetic flux rope topology similar to that found in magnetic cloud ICMEs provides the magnetic conditions most likely to explain the overall depth of an FD.

Exploring the detailed relationship between particle intensity and magnetic field variability within the substructure of solar wind transients exhibiting large, short-period GCR fluctuations may yield new insight into energetic particle propagation within the Heliosphere. The authors of [6] originally derived energetic particle diffusion coefficients described by resonant wave scattering and field line wandering under the quasi-linear approximation. However, discrepancies of up to a factor four have been found by [7] in a strong scattering regime. In an attempt to represent observed conditions, the authors of [7] use coefficients derived empirically from solar particle propagation studies and numerical trajectory investigations in model solar wind

fields. Computational models solve the transport equation describing three-dimensional long-term GCR modulation by employing empirically justified diffusion coefficients, based on the goodness of fit to the overall spatial, temporal, and energy dependence of the modulation (e.g., [8]). However, these approaches do not attempt to relate the coefficients to in situ field data. A preferred method is the more direct derivation of the radial coefficient by McDonald et al. [9], who relate the radial gradient of the long-term modulation to the convective term directly.

In Section 2 of this paper, we discuss the instrumentation and data used in the analysis. In Section 3, we discuss the observations, first focusing on the particle observations and then focusing on solar wind observations and the connection with solar wind transients. In Sections 4 and 5, we use a version of the approach in [9] to estimate the diffusion coefficients locally and then compare the result with the prediction of quasi-linear theory. In Section 6, we present our conclusions.

## 2. Particle and Field Data

Particle data for this investigation is obtained from the large-area ACS of the SPI spectrometer mounted on the ESA INTEGRAL gamma-ray satellite. With a  $24 R_E$  apogee, near continuous GCR monitoring is achieved. SPI consists of an array of 19 cooled Ge detectors, hexagonal in shape and of side 3.2 cm and height 7 cm [10]. The ACS is comprised of 91 bismuth germinate blocks. Several types of signals are available for GCR monitoring. The highest energy signals include the saturated counts of the ACS (ACSSAT) and the saturated counts of the Ge detector system (GEDSAT). Here “saturated” means that the amplitude from the energy deposited in the detector is sufficient to saturate the amplifier systems. The ACSSAT threshold is  $\sim 150$  MeV [11]. The GEDSAT signal has an energy threshold of 200 MeV (a consequence of the energy required to penetrate the spacecraft shielding to reach the Ge detectors and subsequently lose an additional 10 MeV to the Ge detectors) [12].

In addition to ACSSAT and GEDSAT, the system has an ACS channel that counts all triggers in the system above  $\sim 100$  keV. Much higher counting rates occur in this ACS channel because of the low-energy threshold. However, the lower-energy threshold also means that there are events in the run of the ACS data due to energetic magnetospheric electrons. Luckily, ACS counts due to magnetospheric electrons have a spikey nature and time periods when they occur are easily identified and removed or ignored. The three INTEGRAL SPI channels, GEDSAT, ACSSAT, and ACS, make omnidirectional measurements with a broad and poorly known energy response. Since the GCR energy spectra peak in the energy range of hundreds of MeV per nucleon, this is not a serious issue. The compelling reason to use these INTEGRAL data is the stunning statistics provided by the relatively huge count rates that permit unprecedented temporal resolution of temporal changes in the GCR [4]. Solar wind magnetic field and plasma data are obtained from the MAG and SWEPAM instruments aboard the ACE spacecraft.

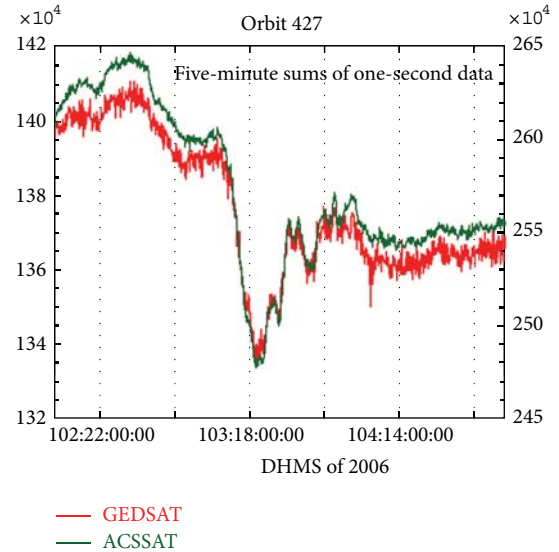


FIGURE 1: Five-minute sums of GEDSAT and ACSSAT count rates are plotted for Orbit 427.

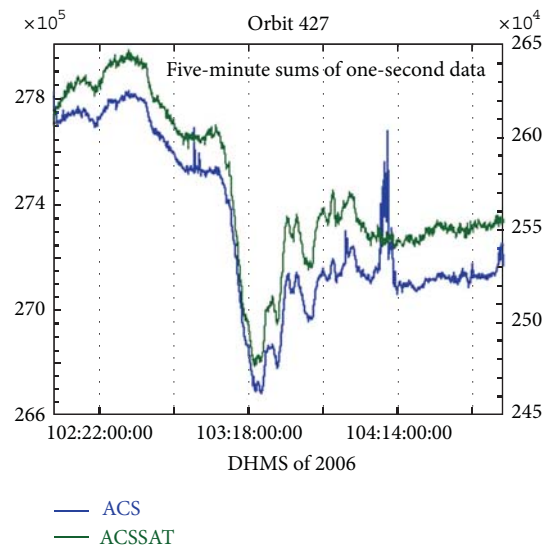


FIGURE 2: Five-minute sums of GEDSAT and ACSSAT count rates are plotted for Orbit 427.

## 3. Observations

**3.1. GCR Study Intervals.** Three periods of very rapid GCR intensity decrease were selected from 2006 INTEGRAL data, DOY 103 (orbit 427), DOY 117/118 (orbit 432), and DOY 1276/127 (orbit 435). Figure 1 compares the 5-minute sums of the GEDSAT and ACSSAT count rates for orbit 427 showing excellent agreement including the fine structure. The ACSSAT count rate is approximately twice that of the GEDSAT. Figure 2 similarly compares the ACS and ACSSAT rates. Excellent agreement is again found except for some spikes we ascribe to magnetospheric-related events. The orbits chosen for this analysis were selected based upon

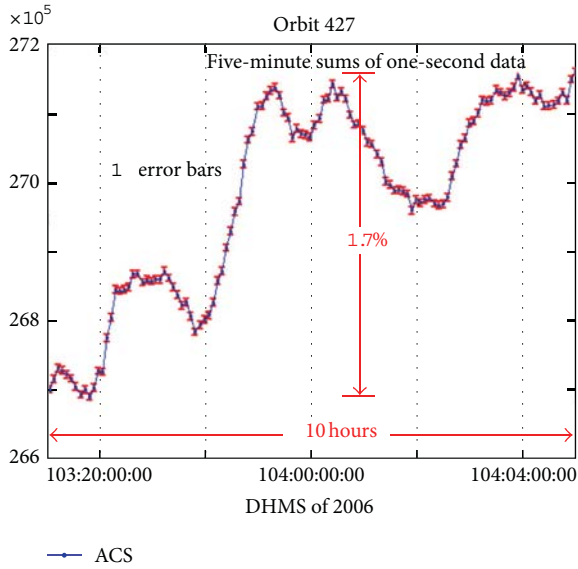


FIGURE 3: The data plotted in Figure 2 is replotted on expanded scales. The small size of the  $1\sigma$  standard error bars reveals the statistical significance of the GCR variations.

the striking short-term temporal changes in the GCR, and in the solar wind plasma and magnetic field. However the general tracking of the three channels lends confidence to the integrity of the measurement of the rapid flux variation.

The amplitude of the FD in which the sudden drop seen in both figures is encompassed is of magnitude  $\sim 3\%$ . The extraordinarily large number of counts in 5-minute sums of the ACS data provides a marvelous statistical accuracy to the measurement of the GCR time history. Clearly many of the wiggles and bumps are real. Figure 3 illustrates this last point in more detail where conventional  $1\sigma$  error bars are employed.

It has long been known that an FD has a similar time history to the evolution of Dst during the time period of the Forbush effect [13]. Sometimes they are nearly simultaneous while at other times there is a significant delay as was seen here (see Section 3.2 for more details on the Dst signature). To compensate for this effect, in Figure 4, we show the actual data for ACSSAT and Dst, while in Figure 5, Dst is shifted 14 hours earlier. The fact that such a time shift brings about a similarity in shape adds evidence for the convection model for the GCR-solar plasma structure over a time scale comparable to the duration of the rapid flux decrease studied.

Figure 6 plots the ACS data for orbit 427 along with the magnitude of the interplanetary field recorded by ACE. The field magnitude is seen to have increased abruptly at the time of the FD and remained high until the ACS recovered. This recovery did not return to pre-FD levels. (The spikes in the ACS count rate in this interval are due to leakage of magnetospheric electrons out of the radiation belts and can be safely ignored for this analysis.) To add to our confidence in the observed, rapid variability, we plot INTEGRAL in comparison with the lower statistical accuracy McMurdo neutron monitor data during the event in Figure 7.

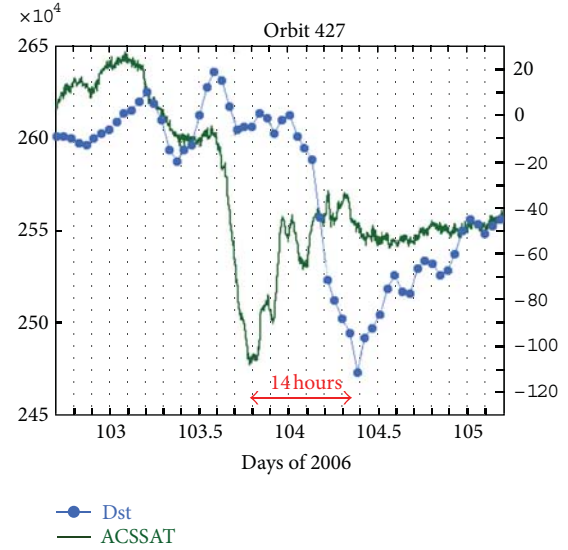


FIGURE 4: ACSSAT for Orbit 427 plotted with the time history of Dst.

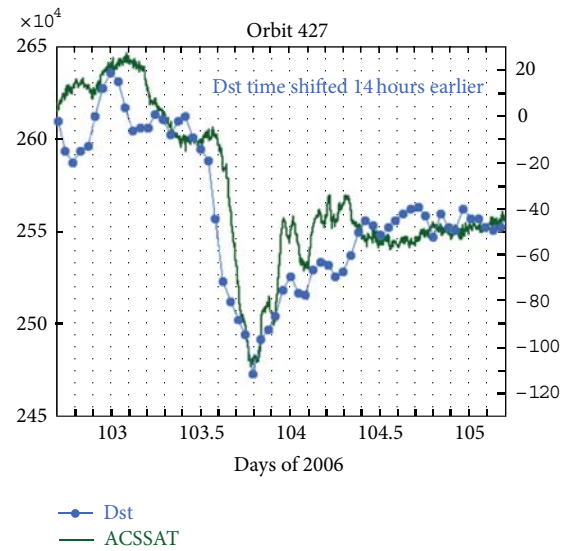


FIGURE 5: ACSSAT for Orbit 427 plotted with the time history of Dst shifted to earlier time by fourteen hours.

3.2. *Connection with Transient Solar Events.* Looking at the solar wind data during this time shows the existence of an ICME. The interplanetary magnetic field and plasma conditions during a four-day period bracketing the ICME are shown in Figure 8. The bottom panel of the figure shows the ACS data. The transient spikes in the ACS data (occurring around midday of DOY 104) occur at the trailing boundary of the ICME indicated by the vertical lines. Note that the ACS data has not been time shifted to correspond to the particle signature observed at by ACE at the L1 Lagrangian point several hundred Re sunward of the Earth. The region prior to the ICME contains slow, cold plasma. The proton speed increases near the leading edge of the ICME, which causes a compression region, but no shock exists. In passing, we comment that

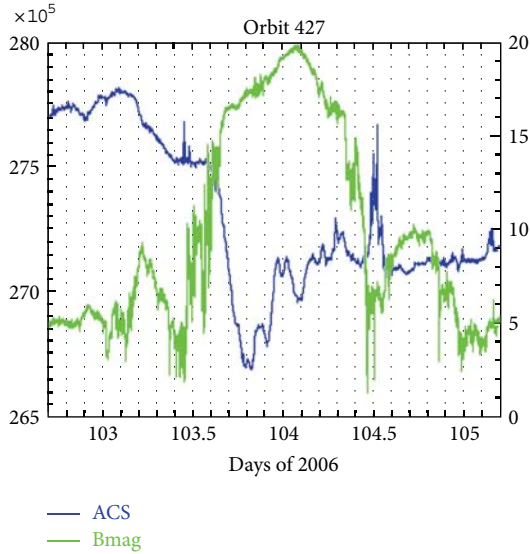


FIGURE 6: ACS is plotted for Orbit 427 along with the magnitude of the interplanetary field as seen by ACE.

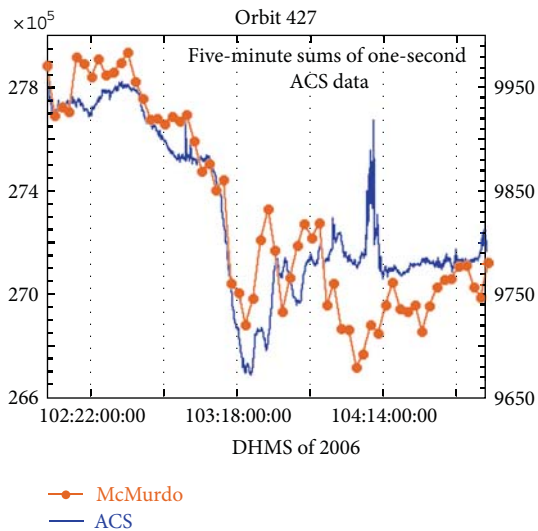


FIGURE 7: The ACS countrate is plotted with the countrate of the McMurdo neutron monitor for the time period of Orbit 427.

there is evidence that a shock front cannot be the basic cause of an FD. Close examination of the ICME reveals that the leading edge corresponds to the leading edge of the FD, but a simultaneous depression in Dst is not expected (see Figure 5) due to the presence of a strong northward component of the magnetic field (positive  $B_z$ ) during the first half of the ICME. The drop in Dst is expected to occur when the field turns southward (negative  $B_z$ ), which is some 12–15 hours after CME onset, consistent with the Dst drop shown in Figure 5.

A faster, warmer region is observed just downstream of the trailing ICME boundary. Taking a closer look at days 103 and 104 (04-13-06 and 04-14-06) shows some interesting details in the electron heat flux and ACS data during the period around the ICME. Inside the leading edge, sporadic

bidirectional electron heat flux persists through the end of day 103, as shown in Figure 8. During this period, the heat flux has intermittent regions of unidirectional and bidirectional streaming indicating that the spacecraft is passing through alternately open and closed magnetic field lines in rapid succession. This changing topology may correspond to the short-period oscillations in the ACS count rates. It is difficult to assess the exact correspondence without first determining the time delay from L1 (ACE) to the location of INTEGRAL.

At the beginning of day 104 (Figure 8), the electron heat flux is primarily unidirectional but then switches to counter-streaming near the trailing end of the ICME (marked with a vertical line). It is also during this time that the plasma temperature increases, although the proton speed remains nearly constant. At the ICME trailing boundary, the magnetic field reaches a minimum and the field turns northward.

Figure 9 plots the ACS count rate over the period encompassing the three events studied, together with field components and magnitude, solar wind speed, temperature and density, and low-energy electron heat flux. The two vertical bands in the figure mark periods when a simple flux rope model may be fitted. The first is in good coincidence with the day 103 event but there is no simple rope configuration fitting the day 117/118 (ICME 2) or day 126/127 (ICME 3) events. At this stage, we are only able to say that the latter two events coincide with complex transient magnetic structures likely to exist over significant regions of space.

#### 4. Derivation of the Quasi-Linear Diffusion Coefficients

The most basic derivation of the parallel diffusion coefficient can be found in [14]. We will first outline their approach because it both provides the most accessible expression to estimate this coefficient and illustrates the problems in any representation of the scattering in a realistic field model. The work of [14] assumes that particles follow helical trajectories along a nearly uniform field line, directed in the  $z$  direction, but suffer a series of small changes in pitch angle as they encounter transverse wave packets where the spatial wavelength of the wave along the field matches the projection of the cyclotron radius along the field. A perturbing force changes the parallel component of velocity and hence via conservation of the first adiabatic invariant, the pitch angle, depending on the spatial extent of the field perturbation. This extent of the wave-particle resonance is estimated as being within a spatial wave number range  $\pm k_{\parallel}/2$  where  $k_{\parallel} = \omega_B/v_{\parallel}$  for gyrofrequency  $\omega_B$  and particle velocity  $v_{\parallel}$  along field  $\mathbf{B}$ . Random pitch angle scatters summing to  $90^\circ$  to achieve “reflection” and evaluated for an average pitch angle lead to a parallel diffusion coefficient, which we call the Kennel-Petschek estimate  $K_{\parallel}^{K,P}$ :

$$K_{\parallel}^{K,P} = \frac{vVB^2}{12\pi P(f) f^2}, \quad (1)$$

where the resonant frequency  $f = k_{\parallel}V/2\pi$  for wind velocity  $V$  allows the particle gyration to match the spatial wavelength, and  $P(f)$  is the power in waves perpendicular to  $\mathbf{B}$

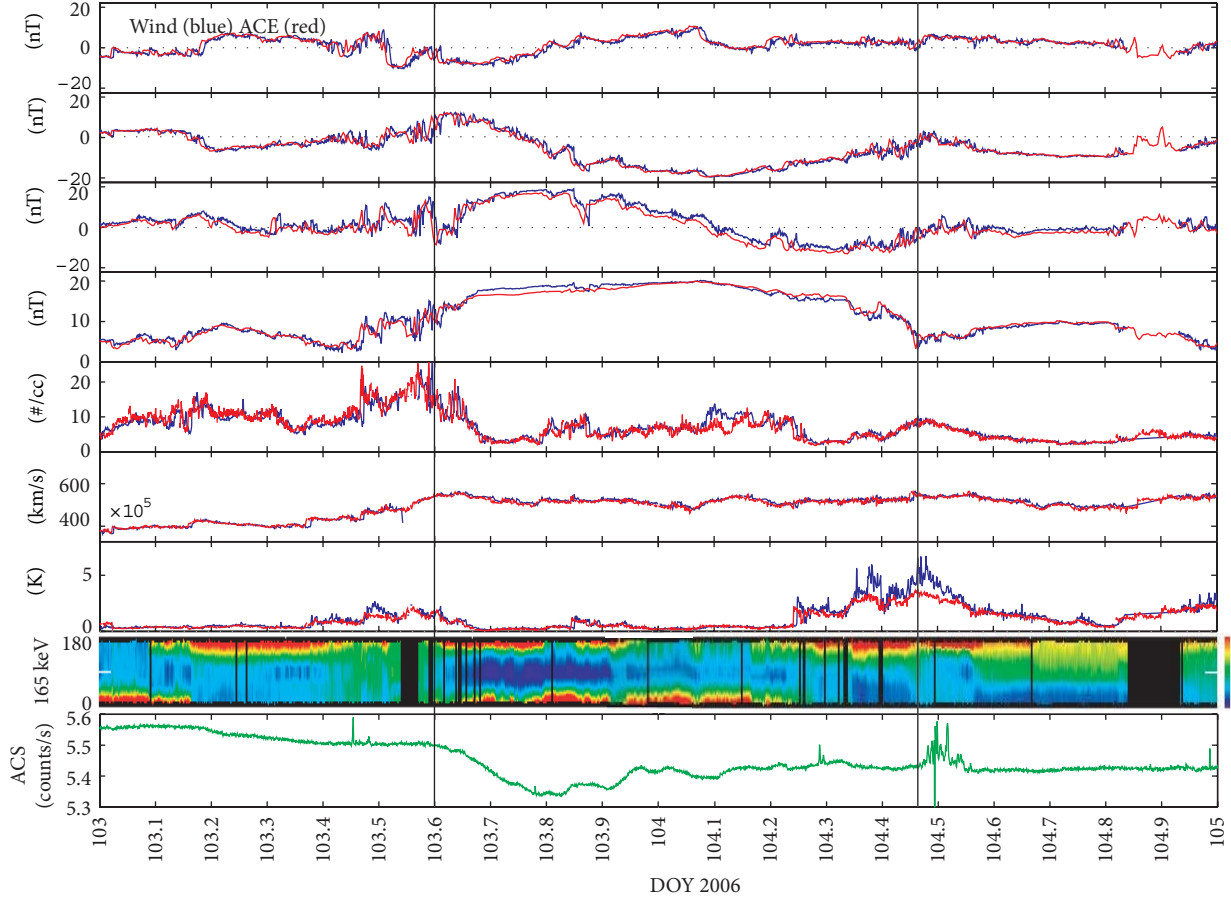


FIGURE 8: Wind and ACE IMF, plasma, and electron strahl (165 eV) data for 04-13 through 04-14 2006. INTEGRAL ACS data (unshifted) is shown in the bottom panel. The leading and trailing boundaries of the ICME are shown by vertical lines.

at  $f$ . The field model is known as a slab model where there is no dependence on  $x$  or  $y$ .

Even within the context of the assumption of transverse waves, the  $K_{\parallel}^{K,P}$  model fails to account in detail for the differing strength of scattering power at different pitch angles, and therefore the result must depend on spectral slope. Scattering at  $90^\circ$  is zero on the model because wave power falls to zero at very large  $k_{\parallel}$ . A more general approach to finding the parallel diffusion coefficient, allowing the effects of waves and turbulence in three dimensions, starts with the Hall-Sturrock relation usually employed in a weakly turbulent field for the pitch angle diffusion coefficient  $D_{\mu\mu}$  where  $\mu$  is cosine of pitch angle:

$$D_{\mu\mu}(\mu) = \text{Re} \int_0^{\infty} d\epsilon \left\langle \frac{d\mu(t)}{dt} \frac{d\mu^*(t+\epsilon)}{dt} \right\rangle. \quad (2)$$

Using the equation of motion for particles with unperturbed positions  $x$  and  $y$  with the mean field in  $z$ , the quasilinear approximation which picks out the dominant term perturbing the helical orbit leads to [15]

$$\frac{d\mu}{dt} = \frac{i\omega_B}{2^{0.5}B_0} \left( (1-\mu^2)^{0.5} \right) \times [\delta B_R(x(t)) e^{i\Phi} - \delta B_L(x(t)) e^{-i\Phi}], \quad (3)$$

where  $\Phi$  is phase angle. Left- and right-handed polarisation is allowed for the wavelike parts of the perturbed field components:

$$\begin{aligned} \delta B_L &= \frac{1}{2^{0.5}} (\delta B_x + i\delta B_y), \\ \delta B_R &= \frac{1}{2^{0.5}} (\delta B_x - i\delta B_y). \end{aligned} \quad (4)$$

Various models are then chosen which define the perturbed fields via Fourier transforms representing the wave motion or turbulent, convected field structure. The integral to be performed in (2) picks out the resonance of the stationary wave and convected structure patterns with the helical orbit. Here we concentrate on the simplest or slab model which attributes the perturbations to Alfvén waves propagating with  $k$  vectors parallel to the mean field which means that all change is in  $x$  or  $y$ . In [6], it was then found that

$$\frac{\langle (\Delta\mu)^2 \rangle}{\Delta t} = \frac{(1-\mu^2)}{|\mu|v} \frac{e^2 V}{m^2 c^2} P_{xx} \left( f = \frac{V\omega_0}{2\pi\mu v} \right), \quad (5)$$

where  $m = \gamma m_0$  and  $\omega_0 = eB/mc$ ,  $\gamma$  is the Lorentz factor, and  $P_{xx} = \delta/f^n$  is here the power in one perpendicular component with  $f$  running from  $-\infty$  to  $+\infty$ . A parallel diffusion

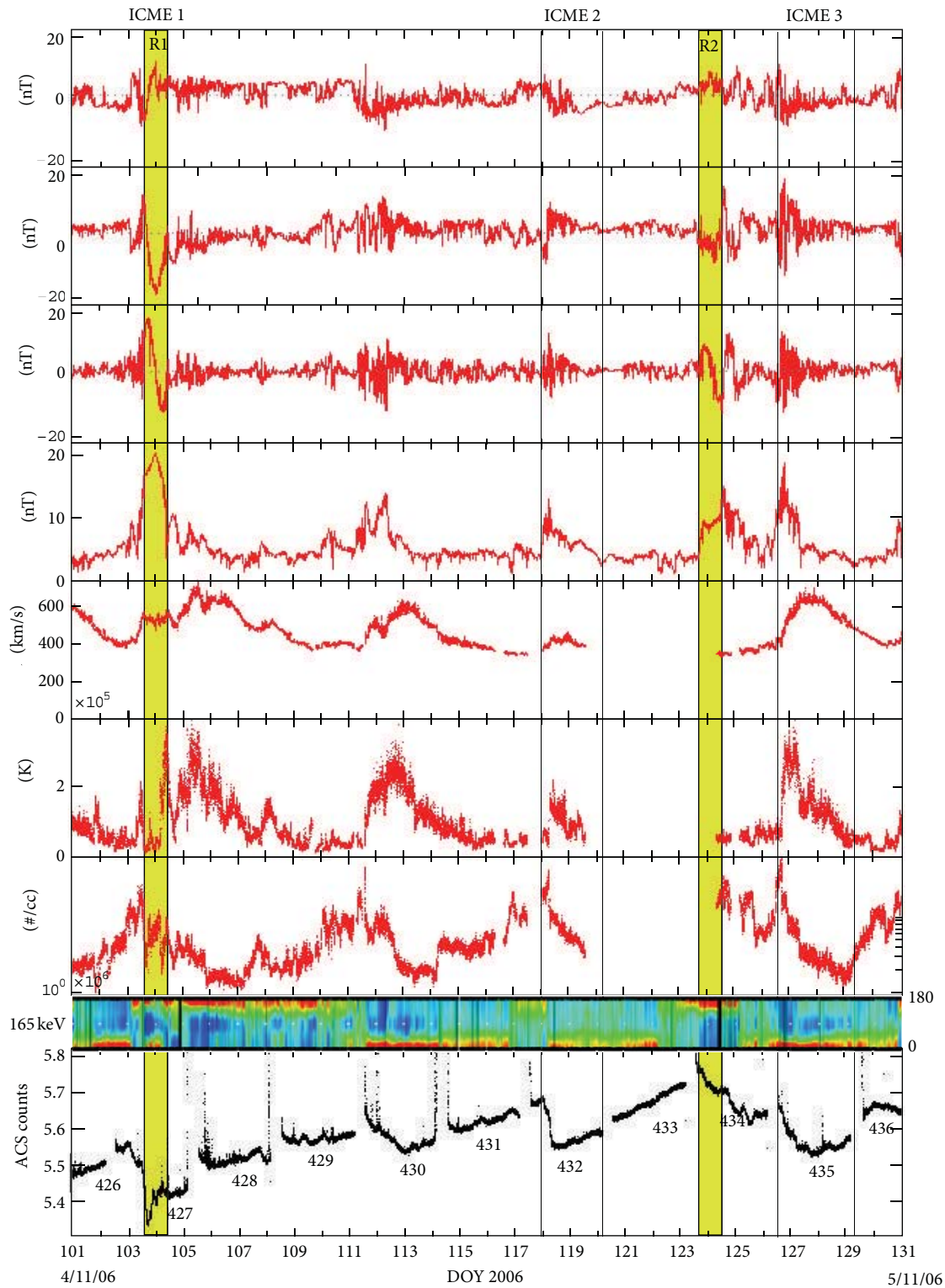


FIGURE 9: ACS count rate over entire period encompassing the three ICME events studied together with solar wind field and plasma components from ACE and electron strahl from Wind. Highlighted regions indicate presence of flux ropes.

coefficient is then obtained by studying the relaxation of a small anisotropy in pitch angle space and Hasselmann and Wibberenz [16] obtain

$$K_{\parallel} = \frac{v^2}{2} \int_{-1}^1 \left[ \int_0^{\mu'} \frac{1 - \mu^2}{\langle (\Delta\mu)^2 \rangle / \Delta t} d\mu \right] \mu' d\mu'. \quad (6)$$

Substituting (6) into (5) yields (e.g., [17])

$$K_{\parallel}^{HW} = v^{3-n} V^{n-1} \frac{B^2}{(2\pi)^n} \frac{\omega_s^{n-2}}{\delta} \frac{1}{(4-n)(2-n)}. \quad (7)$$

The symbol  $\delta$  is the coefficient arising from one of three field components obtained in a Fourier transform, and it is assumed that perpendicular power dominates power in the field magnitude. Note that axial symmetry has been assumed for the perturbation spectrum and also that the cyclotron radius of the scattered particles lies in a range of spatial wave frequencies which can be described by a single power law. This assumption is satisfied by the particle and magnetic data used subsequently in this work.

Under the approximation that the power spectrum of transverse fluctuations was proportional to  $f^{-1}$ , the author's result (6) leads to a  $K_{\parallel}$  value which is close to (1) and has been commonly used in the past. While values of  $n \approx 1.1$  have been found during disturbed periods, a Kolmogorov-like value of 5/3 is more usual.

Subsequent work, on  $K_{\parallel}$ , realised that the quasi-linear theory employed did not produce scattering through 90° pitch angles. However, Alfvénic waves propagating at a variety of angles to the mean field are found in the Solar Wind, and also compressional, longitudinal waves may provide 10% of the fluctuation power. Moreover, rotational discontinuities may occur several times in a CME. All these disturbances can provide “mirroring” to particle propagation where the pitch angle relative to the mean field is near 90°. Hence the scattering mechanism at large pitch angles may be the dominant influence on the rate of diffusion, and because such corrections to quasi-linear theory tend to decrease  $K_{\parallel}$  (e.g., [18]), (7) could be treated as an upper limit [18], unless most turbulence is purely Alfvénic with  $|\mathbf{B}|$  preserved so that scattering at large angle is only due to a small, compressive component of the field turbulence. However, the authors of [19] introduce a two-component field model, one describing the slab approximation and the second an axisymmetric power spectrum describing variations perpendicular to the mean field. Different correlation lengths are introduced for the two components. These workers compared the quasi-linear result (QLT) and their two component model, based on average solar wind conditions at 1 AU with the “Palmer Consensus” mean free paths, as determined by a compilation of determinations from particle propagation. They found that a model with 90% of power corresponding to the slab model gave  $\lambda_{\parallel}$  in the ~100 MV range at the bottom of the “Palmer” range while a model with 90% of the power concentrated in perpendicular direction fluctuations laid a factor three higher, at the top of the “Palmer” range. While the results of [19] might encourage us to believe that our use

of QLT may be only a factor two to three in error, previous numerical simulations by [7] appeared to confirm a series of investigations suggesting a larger underestimate (e.g., [17]). In [7], a field model was employed whereby each short segment of particle trajectory experienced a field obtained from actual  $B$  and  $V$  measurements as the wind flowed past a spacecraft. An equilibrium pitch angle distribution was then set up by numerically following particles within the field model after injection and until removal at boundaries. The slope of the distribution function in pitch angle space then gave  $D_{\mu\mu}$ . Solar particle propagation data used to deduce the spatial diffusion coefficient came from a contemporary solar particle event. The use of (7) gave an estimate a factor 8 less than that derived from the particle data and a factor 4 less than that obtained by the numerical model.

The approximation of (7) applies to an axisymmetric slab model of transverse fluctuations with no net polarisation and varying only parallel to the mean field, and we assume that corrections due to a finite Alfvén speed, as implied in the equations of motion of [15], can be neglected because the particles move close to  $c$ . Our subsequent use of (7), motivated by the complexity of the subsequent approaches which are beyond the scope of this paper, must be tempered by the knowledge that it is very likely to only represent a lower limit.

Concerning perpendicular diffusion, we again start by describing the well-known and easily accessible approximation, before mentioning analytical improvements to the theory and computational approaches which will allow an assessment of the error involved with the adopted equation. Since particles of small Larmor radii compared with the dominant scale of field fluctuations attempt to follow field lines, it is not surprising that deviation from a mean direction is thought of as a combination of motion of guiding centers following wandering field lines and diffusive scattering perpendicular to these lines. In [6], it was found that the dominant cause for perpendicular diffusion lays in the power at spatial frequencies of the turbulence approaching zero,  $P_{xx}(f = 0)$ , corresponding to the description of field line wandering. Resonance scattering similar to that described in the pitch angle case was found by Jokipii [6] to be relatively small. The result given for the perpendicular displacement  $\langle \delta x \rangle$  at cosine pitch angle  $\mu$  was

$$\frac{\langle \delta x^2 \rangle}{\delta t} = \frac{\mu v V P_{xx}(f = 0)}{B_s^2}. \quad (8)$$

Later, Foreman et al. [20] reevaluated this result and quote

$$K_{\perp} = 4 \times 10^{20} \left( \frac{v}{c} \right) \text{ cm}^2, \text{ sec}^{-1} \quad (9)$$

for  $P_{xx}(f = 0) = 4 \times 10^{-6} \text{ Gauss}^2/\text{Hz}$  longitudinal power,  $V = 4 \times 10^7 \text{ cm/sec}$ , and  $B = 4 \times 10^{-5} \text{ Gauss}$ . We shall use (9), scaled to fit the actual field and wind parameters, according to (8).

Subsequent analytical work, especially [21], finds that the interplay between parallel and perpendicular scattering can suppress the perpendicular motion, for example, if the reversal along the field allows the gyromotion to cause the particle

to sample field lines closely similar to those encountered before the scatter of parallel motion. Matthaeus et al. [21] define  $K_{\perp}$  according to the Taylor-Green-Kubo formulation which in their case they write as

$$K_{xx} = \frac{a^2}{B_0} \int_0^{\infty} dt' \langle v_z(0) v_z(t') \rangle \times \langle b_x[x(0), 0] b_x[x(t'), t] \rangle. \quad (10)$$

It has been assumed that the relation between the perpendicular velocity and the perpendicular field perturbation, assuming axial symmetry, is

$$v_x(t) = \frac{av_z(t) b_x[x_m(t)]}{B_0}, \quad (11)$$

where  $x_m$  is a mean of the gyromotion. This formula clearly describes motion following wandering field lines if  $a = 1$ , but in the work based on the approach outlined, a value  $a = 1/3$  is taken as fitting numerical simulations corresponding to the analytical model adopted, and no theoretical justification seems to be supplied as yet for the value of the constant.

The work of [22] is the most recent and general analytical approach to finding  $K_{\perp}$  in a medium of arbitrary turbulence, without the restrictions of, for example, the slab model or the two component model mentioned before. His nonlinear model leads to the following expression involving the power spectrum with arbitrary propagation vector  $P_{xx}(\mathbf{k})$ :

$$K_{\perp} = \frac{a^2 v^2}{3B_0^2} \int d^3k \frac{P_{xx}(\mathbf{k})}{A(\mathbf{k}) + (4/3) K_{\perp} k_{\perp}^2 + v/\lambda_{\parallel}}, \quad (12)$$

where

$$A(\mathbf{k}) = \frac{(vk_{\parallel})^2}{3K_{\perp} k_{\perp}^2}. \quad (13)$$

Suppressing the effects of parallel scattering allows this equation to tend to the field line wandering limit while restricting the power spectra to slab and axisymmetric perpendicular disturbance allows the results of [21] to be recovered. In a 3D turbulence model, the interplay of parallel and perpendicular effects is illustrated by considering the terms after the integral sign.

An alternative approach to incorporating 3D turbulence lies in computations similar to those described in [7]. The authors of [23] suppress variability in one of the three dimensions, so that  $\mathbf{B}(x, y)$  is constant in  $z$ . Diffusion in  $z$  due to field fluctuations in the  $x$ - $y$  plane was measured again by numerically tracking particles again in a steady-state experiment while drift in  $z$  was measured by following the time evolution of the distribution function. The numerical experiment had deliberately suppressed field line wandering in  $z$ . The result was a  $K_{\perp}$  of similar magnitude to the field line wandering estimate. Net drift was consistent with the combined effects of field gradient and curvature drifts due to the  $x$ - $y$  plane variability averaged over the one day sample used, calculated on guiding center theory. Our conclusion is

that employment of (9) could result in approximately a factor of two underestimate.

In applying the aforementioned expressions to field data, we employ ACE 4-minute component averages, using 0.71 of a day's data for convenience relating to the Matlab algorithm employed. We obtain the power in a typical perpendicular component by doing fast Fourier transforms to find the power in solar radial, tangential, and normal components as a function of frequency and then finding the sum of resolving each component in a direction perpendicular to the mean field. Power laws are used to fit these summed components. Field magnitudes are found from averages of the 4-minute total field magnitudes because the particles are actually attempting to follow the fluctuation field direction, rather than the mean field over 0.71 of a day. Solar wind data from ACE is used to determine the mean flow velocity of each selected period. Applying the aforementioned results to the field/plasma data of DOY 103, 2006 and the pairs of DOY 117, 118 and 126, 127 yields for 200 MeV protons the results of Table 1. Here  $\psi$  is the mean field-radial direction angle. It is noteworthy that the perpendicular power spectra with a negative slopes up to 1.7 are obtained, considerably steeper than for the  $n = 1$  assumed in (1). Hence the scattering at high pitch angles is less effective and  $K_{\parallel}^{K,P}$  is likely to be an underestimate.

## 5. Diffusion Coefficients, the GCR Gradient, and Short-Term Modulation

The maximum GCR drop in intensity during day 103 occurs between 103.6 and 103.8 Assuming that this is due to spatial convection of the feature, as is likely from previous studies of such events [4], the radial spatial gradient of the ACSSAT intensity is  $3.43 \times 10^{-14}$ /cm or 52 percent/AU, corresponding to 200 MeV GCR.

If we assume that a quasi-equilibrium is still maintained between convective outflow, adiabatic energy loss, and diffusive inflow,

$$CVU = -\left(K_{\parallel}^{\text{cr}} \cos^2 \chi + K_{\perp}^{\text{cr}} \sin^2 \chi\right) \frac{\partial U}{\partial r}, \quad (14)$$

where  $C$  is the Compton-Getting factor appropriate to the differential number density spectrum,  $U$ , at 200 MeV and  $\chi$  is the field-radial direction angle.  $C = 0.81$  close to the previous solar minimum, while  $\chi = 68^\circ$  on average during the interval of the rapid GCR decrease. We will now separately investigate whether parallel or perpendicular diffusion is the most important in maintaining the assumed quasi-equilibrium with small radial streaming by successively ignoring each term on the right-hand side of the above. Putting in values yields

$$\begin{aligned} K_{\parallel}^{\text{cr}} &= 8.4 \times 10^{21} \text{ cm}^2, \text{ sec}^{-1}, \\ K_{\perp}^{\text{cr}} &= 1.4 \times 10^{21} \text{ cm}^2, \text{ sec}^{-1}. \end{aligned} \quad (15)$$

Similar estimates are made for the other events, days 117/118 and 126/127. These cosmic-ray-derived diffusion coefficients,  $K_{\parallel}^{\text{cr}}$  and  $K_{\perp}^{\text{cr}}$ , are also entered in Table 1. For DOY 103,

TABLE 1: Diffusion coefficients obtained from power spectra and particle gradients in  $\text{cm}^2, \text{sec}^{-1}$ .

	DOY 103	DOY 117	DOY 118	DOY 126	DOY 127
$K_{\parallel}^{K,P}$	$6.3 \times 10^{20}$	$9.66 \times 10^{20}$	$2.41 \times 10^{20}$	$1.0 \times 10^{20}$	$3.40 \times 10^{20}$
$K_{\parallel}^{H,W}$	$5.5 \times 10^{21}$	$9.39 \times 10^{21}$	$2.8 \times 10^{21}$	$1.7 \times 10^{21}$	$1.99 \times 10^{21}$
$K_{\perp}$	$4.1 \times 10^{20}$	$1.38 \times 10^{20}$	$1.71 \times 10^{20}$	$1.54 \times 10^{21}$	$1.12 \times 10^{21}$
$\psi$	68	24.8	45.5	75.8	45.7
$K_{\parallel}^{\text{cr}}$	$8.4 \times 10^{21}$	$1.1 \times 10^{21}$	$2.19 \times 10^{21}$	$3.73 \times 10^{22}$	$7.13 \times 10^{21}$
$K_{\perp}^{\text{cr}}$	$1.4 \times 10^{21}$	$5.17 \times 10^{21}$	$2.15 \times 10^{21}$	$2.39 \times 10^{21}$	$6.79 \times 10^{21}$

and assuming the validity of the power spectral-based estimates, neither the perpendicular diffusion value nor the simple,  $K_{\parallel}^{K,P}$  parallel diffusion case can satisfy the quasi-equilibrium. However, because the field-based  $K_{\parallel}^{H,W}$  and gradient-based,  $K_{\parallel}^{\text{cr}}$  estimates are close, parallel diffusion seems to satisfy quasi-equilibrium. For the event of days 117/118 parallel diffusion again seems to give a better agreement between power spectrum calculated and gradient-derived diffusion coefficients, especially as the major part of the observed sharp decrease best corresponds to day 118 power spectral analysis. However for the event of days 126/127, perpendicular diffusion seems to give a little better accord, especially as the major drop lies around the day 126/127 boundary. Note the high  $\psi$  angle on day 126 which might indicate the reason for the dominance of perpendicular diffusion. On the other hand, previously noted, marked discrepancy between quasi-linear theory and diffusion computations based on actual field values may be in play here.

Inspection of Figure 8, Section 3.2, shows a rapid field rotation at the time of the rapid decrease with radial component going through zero and with the dominant field component normal to the ecliptic in the event of day 103. It is possible to imagine that nearer the sun the GCR intensity was significantly reduced by a field configuration unfavourable to radial diffusion. This allowed a new quasi-equilibrium to be set up with inflow from a large angle to the ecliptic plane and radial direction from some entry point at the boundary of the traveling large magnetic disturbance. What we see during the three events is the quasi-equilibrium expressed by (14) as it is convected past the Earth. The short-term modulation under consideration here is thus essentially due to a barrier mechanism, because true radial diffusion is largely inhibited during the events.

All three field components exhibit large changes but only one event clearly fits a flux rope model. A bidirectional heat flux persisting through to the end of day 103 has already been noted. We have already discussed the flux rope as a suitable GCR barrier [4, 5], although the detail of the proposed mechanism is different here.

## 6. Conclusions

We have set out to demonstrate the likely validity of a model for significant short-term reduction of the GCR intensity and the use of this model to obtain information on energetic particle diffusion. Approximate theoretical values of the parallel and perpendicular diffusion coefficients have been

obtained appropriate to the actual field turbulence present at the time of passage of three selected events. Reference to previous analytical and Monte Carlo numerical studies taking into account 2- or 3-dimensional field representations, not present in the slab approximation of the adopted calculation of the coefficients, allowed an assessment of errors in our procedure to be made. A sufficiently satisfactory explanation of the three events was provided by the idea of a quasi-equilibrium field/particle structure being convected past the Earth with a single, dominant mode of diffusive propagation, either parallel or perpendicular to the mean field of the event. Reasonable self-consistency between diffusion coefficients derived by particle gradient and analytic theory was achieved. Nevertheless, there is every reason to urge the application of more comprehensive modeling, for example, by the methods of [7, 19, 22], to better check the extent of this agreement.

Three-dimensional models of the overall heliospheric modulation assume diffusive scattering varying smoothly over large spatial scales with at most a dependence on angle with respect to the solar equatorial plane. The relative importance of this, near isotropic and homogeneous turbulence model, compared with barrier effects discussed in this work must depend on the abundance of flux rope magnetic topologies within the solar wind.

In terms of the wider, astrophysical significance, the method proposed here of using local particle conditions to check diffusion coefficients with locally derived plasma parameters seems unprecedented as a way of validating the ability to model cosmic wave-particle interaction in a collisionless regime. One only has to point to the extensive use made of quasi-linear theory for the interaction in nonthermal astrophysical shock modeling to appreciate the worth of the investigation.

## Acknowledgments

D. N. A. Shaul acknowledges Science & Technology Facilities Council (STFC) support. T. Mulligan and J. B. Blake acknowledge the support for this work under NASA Grant CG189307NGA. The authors would like to thank the INTEGRAL team for supplying the INTEGRAL data, the ACE MAG and SWEPAM teams for making their data available on the ACE Science Center website (<http://www.srl.caltech.edu/ACE/ASC/>), and the Wind 3DP team for making their data available on the WIND 3-D Plasma and Energetic Particle Investigation Web site (<http://sprg.ssl.berkeley.edu/wind3dp/esahome.html>).

## References

- [1] J. A. Lockwood, "Forbush decreases in the cosmic radiation," *Space Science Reviews*, vol. 12, no. 5, pp. 658–715, 1971.
- [2] H. V. Cane, "Coronal mass ejections and forbush decreases," *Space Science Reviews*, vol. 93, no. 1-2, pp. 55–77, 2000.
- [3] I. G. Richardson, "Energetic particles and corotating interaction regions in the solar wind," *Space Science Reviews*, vol. 111, no. 3-4, pp. 267–376, 2004.
- [4] T. Mulligan, J. B. Blake, D. Shaul et al., "Short-period variability in the galactic cosmic ray intensity: high statistical resolution observations and interpretation around the time of a Forbush decrease in August 2006," *Journal of Geophysical Research A*, vol. 114, no. 7, Article ID A07105, 2009.
- [5] J. J. Quenby, T. Mulligan, J. B. Blake, J. E. Mazur, and D. Shaul, "Local and nonlocal geometry of interplanetary coronal mass ejections: galactic cosmic ray (GCR) short-period variations and magnetic field modeling," *Journal of Geophysical Research*, vol. 113, no. A10, 2008.
- [6] J. R. Jokipii, "Cosmic-ray propagation. I. Charged particles in a random magnetic field," *The Astrophysical Journal*, vol. 146, p. 480, 1966.
- [7] J. F. Valdés-Galicia, G. Wibberenz, J. J. Quenby, X. Moussas, G. Green, and F. M. Neubauer, "Pitch angle scattering of solar particles: comparison of "particle" and "field" approach—I. Strong scattering," *Solar Physics*, vol. 117, no. 1, pp. 135–156, 1988.
- [8] U. D. Langer, M. S. Potgieter, and W. R. Webber, "Modelling of "barrier" modulation for cosmic ray protons in the outer heliosphere," *Advances in Space Research*, vol. 34, no. 1, pp. 138–143, 2004.
- [9] F. McDonald, Z. Fujii, P. Ferrando et al., "The cosmic ray radial and latitudinal intensity gradients in the inner and outer heliosphere 1996-2001.3," in *Proceedings of the 27th International Cosmic Ray Conference (ICRC'01)*, vol. 10, p. 3906, Hamburg, Germany, August 2001.
- [10] G. Vedrenne, J. P. Roques, V. Schönfelder et al., "SPI: the spectrometer aboard INTEGRAL," *Astronomy and Astrophysics*, vol. 411, no. 1, pp. L63–L70, 2003.
- [11] P. Jean, G. Vedrenne, J. P. Roques et al., "SPI instrumental background characteristics," *Astronomy and Astrophysics*, vol. 411, no. 1, pp. L107–L112, 2003.
- [12] B. J. Teegarden, J. Naya, H. Seifert et al., "SPI: a high resolution imaging spectrometer for INTEGRAL," in *Proceedings of the 4th Compton Symposium*, C. D. Dermer, M. S. Strickman, and J. D. Kurfess, Eds., vol. 410 of *AIP*, 1997.
- [13] K. Kudela and R. Brenkus, "Cosmic ray decreases and geomagnetic activity: list of events 1982–2002," *Journal of Atmospheric and Solar-Terrestrial Physics*, vol. 66, no. 13-14, pp. 1121–1126, 2004.
- [14] C. F. Kennel, H. Petscheck, and H. E., "Limit on stably trapped particle fluxes," *Journal of Geophysical Research*, vol. 71, no. 1, pp. 1–28, 1966.
- [15] A. Teufel and R. Schlickeiser, "Analytic calculation of the parallel mean free path of heliospheric cosmic rays: I. Dynamical magnetic slab turbulence and random sweeping slab turbulence," *Astronomy and Astrophysics*, vol. 393, no. 2, pp. 703–715, 2002.
- [16] K. Hasselmann and G. Wibberenz, "A note on the parallel diffusion coefficient," *The Astrophysical Journal*, vol. 162, p. 1049, 1970.
- [17] J. J. Quenby, G. E. Morfill, and A. C. Durney, "The solar proton diffusion mean free path and the anisotropic particle event of November 18, 1968," *Journal of Geophysical Research*, vol. 79, no. 1, pp. 9–16, 1974.
- [18] M. L. Goldstein, "The mean free path of low-rigidity cosmic rays," *Journal of Geophysical Research*, vol. 85, no. A6, pp. 3033–3036, 1980.
- [19] A. Shalchi, J. W. Bieber, W. H. Matthaeus, and R. Schlickeiser, "Parallel and perpendicular transport of heliospheric cosmic rays in an improved dynamical turbulence model," *Astrophysical Journal*, vol. 642, no. 1, pp. 230–243, 2006.
- [20] M. A. Foreman, J. R. Jokipii, and A. J. Owens, "Cosmic-ray streaming perpendicular to the mean magnetic field," *The Astrophysical Journal*, vol. 192, pp. 535–540, 1974.
- [21] W. H. Matthaeus, G. Qin, J. W. Bieber, and G. P. Zank, "Nonlinear collisionless perpendicular diffusion of charged particles," *Astrophysical Journal Letters*, vol. 590, no. 1, pp. L53–L56, 2003.
- [22] A. Shalchi, "A unified particle diffusion theory for cross-field scattering: subdiffusion, recovery of diffusion, and diffusion in three-dimensional turbulence," *Astrophysical Journal Letters*, vol. 720, no. 2, pp. L127–L130, 2010.
- [23] X. Moussas, J. J. Quenby, and J. H. Valdes-Galicia, "Drift motion and perpendicular diffusion of energetic particles in interplanetary space based on spacecraft data," *Astrophysics and Space Science*, vol. 86, no. 1, pp. 197–207, 1982.

## Research Article

# On the Onset Time of Several SPE/GLE Events: Indications from High-Energy Gamma-Ray and Neutron Measurements by CORONAS-F

Viktoria Kurt,<sup>1</sup> Karel Kudela,<sup>2</sup> Boris Yushkov,<sup>1</sup> and Vladimir Galkin<sup>1</sup>

<sup>1</sup> Skobeltsyn Institute of Nuclear Physics, Lomonosov Moscow State University, Moscow 119234, Russia

<sup>2</sup> Institute of Experimental Physics, Slovak Academy of Sciences, 04353 Kosice, Slovakia

Correspondence should be addressed to Boris Yushkov; [clef@srd.sinp.msu.ru](mailto:clef@srd.sinp.msu.ru)

Received 5 September 2012; Revised 17 December 2012; Accepted 24 December 2012

Academic Editor: José F. Valdés-Galicia

Copyright © 2013 Viktoria Kurt et al. This is an open access article distributed under the Creative Commons Attribution License, which permits unrestricted use, distribution, and reproduction in any medium, provided the original work is properly cited.

We analyzed the high-energy gamma and neutron emissions observed by the SONG instrument onboard the CORONAS-F satellite during August 25, 2001, October 28, 2003, November 4, 2003, and January 20, 2005 solar flares. These flares produced neutrons and/or protons recorded near Earth. The SONG response was consistent with detection of the pion-decay gamma emission and neutrons in these events. We supposed that a time profile of the soft X-ray derivative was a good proxy of time behavior of the flare energy release. Then we showed that time intervals of the maximum both of energy release and pion-decay-emission coincided well. We determined the onset time of GLEs 65, 69 on the basis of neutron monitor data using the superposed epoch method. The time of high-energy proton onset on November 4, 2003 was found from the GOES data. The time delay between the high-energy gamma ray observation and the high-energy protons onset time was <5 minutes. This time lag corresponds to the least possible proton propagation time. So, we conclude that in these events both protons interacted in the solar atmosphere and the first protons which arrived to Earth, belonged to one and the same population of the accelerated particles.

## 1. Introduction

Solar energetic protons, as Solar Proton Events (SPE) or Ground Level Enhancement (GLE), are observed directly over long time, most probably since the events on February 28 and March 7 in 1942 were identified by Forbush [1] and named later as GLE 1 and 2, respectively. Altogether during the systematic investigation of the GLEs 71 events were recorded. Lower energy of particles, detected by high-latitude neutrons monitors (NM), is ~450 MeV (this threshold is determined by atmospheric absorption), but the effective energy exceeds 1 GeV. The minimum energy for medium and low-latitude NM is even higher; it is determined by the geomagnetic cutoff. Satellite measurements allowed us to study accelerated particles below the atmospheric threshold (~400 MeV). A list of SPE events ( $N(>10 \text{ MeV}) > 10 \text{ protons cm}^{-2} \text{ s}^{-1} \text{ sr}^{-1}$ ) beginning from 1976 can be found, for example, at [2], <http://umbra.nascom.nasa.gov/SEP/>, and of GLE events at [http://neutronm.bartol.udel.edu/~pyle/GLE\\_List.txt](http://neutronm.bartol.udel.edu/~pyle/GLE_List.txt).

GLE connection with solar flares is not in doubt, but still debated question is whether the protons are accelerated up to subrelativistic energies directly during flare energy release or acceleration occurs later when the shock waves propagate in the upper corona. Direct study of the GLE dynamics does not answer this question, because particles' propagation in the interplanetary magnetic field (IMF) is a complex process controlled by a variety of factors. The onset time depends in particular on particle mean free path, angular separation between the site of observation and the Sun (e.g., [3]). In addition, the magnetospheric transmissivity has to be included to interpret the measurements correctly when observations are done within magnetosphere or on the ground.

However, there are two other channels which allow one to study the scenario of ion acceleration. During solar flares accelerated ions due to interaction with solar atmosphere are producing secondaries, among them neutrals (gamma-rays and neutrons); part of them can also be observed at the Earth's orbit. The advantage of these observations is that there

is no need of any assumptions on particle propagation in the interplanetary medium and the trajectory change in the magnetosphere. Protons are accelerated to  $>300$  MeV in the lower corona or they get there after being accelerated in the shock front. They interact with the matter and produce pions which in their turn decay and generate high-energy gamma-rays with specific spectrum [4, 5]. The cross-section of pion production increases rapidly to about 1 GeV and then continues to increase slowly. Thus, the high-energy gamma-rays are generated by protons with energies typical for GLE. Neutrons with energies accessible for detection with NMs can be only produced in the same inelastic interactions of high-energy protons.

The first solar neutron signal at the Earth's orbit was detected by Chupp et al. [6] using measurements with Gamma-Ray Spectrometer (GRS) on Solar Maximum Mission (SMM) during the solar flare on June 21, 1980. Second-time GRS recorded a solar neutron signal after the June 3, 1982, flare (X8.0/2B, E72S09) [7]. The solar neutron response was observed for the first time at the surface of Earth also in this event by neutron monitor (NM) measurements at Jungfraujoch with 1 min time resolution [8]. The air thickness along the line of sight to the Sun was  $745 \text{ g cm}^{-2}$  for the event at Jungfraujoch. Another high mountain NM located in central Europe, namely, Lomnický štít ( $883 \text{ g cm}^{-2}$ ), observed in 5 min records an  $\sim 3\%$  increase in 11:45–11:50 (all times hereinafter are UT). This increase was consistent with characteristic rigidity of accelerated particles  $\sim 200\text{--}250$  MV [9]. The energetic protons observed in interplanetary space from this eastern flare were interpreted as the decay products of neutrons. This event was discussed by Evenson et al. [10, 11] and the spectrum of neutrons was obtained in the range 10–100 MeV.

The June 3, 1982, flare motivated many neutron monitors to make measurements with higher statistical accuracy and better temporal resolution. It has also demanded the construction of new ground-based detectors (e.g., [12]) and new observation of gamma high-energy emission onboard the satellites. However, the neutron fluxes change significantly as a result of the velocity dispersion and decay of neutrons on the way from the Sun to the Earth (the half-life time of free neutrons is  $10^3$  s, which is comparable to the transit time of 1 AU for neutrons with energies 100–1000 MeV).

There are two “windows” in the electromagnetic emission spectrum which allow us to observe an appearance of accelerated protons in the solar atmosphere. Protons accelerated up to 10–50 MeV excite nuclei in the ambient solar atmosphere. These excited nuclei immediately emit narrow gamma-lines in the energy range of 2–7 MeV [4, 13]. The most intense lines are at 4.4 MeV ( $\text{C}^{12*}$ ) and 6.1 MeV ( $\text{O}^{16*}$ ) as well as the delayed neutron-capture line at 2.2 MeV. It seems that Hirasima et al. [14] were the first to observe solar gamma-ray lines accompanying the solar flares. Then these lines were also observed by Orbiting Solar Observatory (OSO-7) [15].

A second “spectral window” appears only when the energy of the accelerated protons reached 300 MeV. At such energies proton interactions with a matter of the solar atmosphere create neutral pions which decay immediately

and generate a broad gamma-ray line with a maximum near 70 MeV [4, 5]. Charged pions are also produced in the same interactions, and their decay produces electrons and positrons, which, in turn, generate high-energy bremsstrahlung with a broad energy spectrum extending up to the energies of the electrons and positrons themselves. The pion-decay gamma-ray spectrum could ride on top of the continuum deriving from primary electron bremsstrahlung.

Thus, observations of the pion-decay emission during a solar flare provide doubtless evidence of the proton acceleration up to high energies, and of the interaction with dense medium. *No other process can produce a spectral feature similar to the pion-decay emission.* When high-energy protons interact with a matter, pion-decay gamma-rays are emitted almost instantaneously. So the temporal behavior of the pion-decay emission follows the behavior of the acceleration mechanism intensity. Eliciting pion-decay component in the flare successive spectra allows us to determine with high accuracy the appearance of high-energy protons in the solar atmosphere.

Thus, in the hands of researchers, there are three tools to study processes of proton acceleration to relativistic energies—investigations of GLEs themselves, observations of high-energy gamma-rays, and observations of high-energy neutrons.

The first flare with convincing evidence of pion production was observed with GRS on June 3, 1982, as well as the neutron production [8, 16, 17]. More recently, the pion-decay emission was detected by SMM/GRS [18, 19], GRANAT/Phebus [20–22], Compton Gamma-Ray Observatory (CGRO) with Energetic Gamma-Ray Experiment Telescope (EGRET) [23, 24], and GAMMA/GAMMA1 [25, 26]. This emission was also detected during the declining phase of the solar cycle 23 with the Solar Neutrons and Gamma-rays (SONG) spectrometer [27] on the Complex Orbital Observations of the Active Sun (CORONAS-F) space mission from four solar flares [28, 29]. A brief review of these observations can be found in [30, 31]. The latest pion-decay emission observation in two flares during current solar cycle was performed onboard the *Fermi* mission with Large Area Telescope (LAT) [32]. The reviews of energetic ion properties in the solar atmosphere deduced from observations of neutrons and gamma-rays can be found in [33, 34].

The SONG spectrometer on CORONAS-F space mission was working from July 2001 until February 2005 and has increased considerably a poor statistic of the solar events with the data on the pion-decay gamma emission and neutrons. Our team highlighted the pion-decay component during the impulsive phase of August 25, 2001, October 28, 2003, November 4, 2003, and January 20, 2005, powerful flares as well as appearance of neutron fluxes after the first three events.

This work is to some extent a review of our results. Here, after short description of the SONG instrument we discuss the observations of gamma-rays and neutrons during above-mentioned events. These observations indicated the presence of protons accelerated up to high energy in solar atmosphere. The association of SPEs and GLEs with these flares is considered.

## 2. CORONAS-F/SONG Data: Analysis of Observations and Method of Spectra Restoration

A CsI crystal with a diameter of 20 cm and a height of 10 cm is the main detecting element of the SONG instrument [27]. The crystal was surrounded by an anticoincidence plastic scintillator shield to reject signals from charged particles. Neutrons with energies  $>20$  MeV produce recoil protons and other heavy nonrelativistic particles in a CsI(Tl) crystal, whereas gamma photons produce relativistic electrons. The intensity ratio of the fast and slow components of the scintillation pulses in the CsI(Tl) crystal depends on the particle ionising power, which in turn is different for relativistic electrons and slow heavy particles. This allows us to make discrimination between neutrons and gamma photons. Secondary particles produced by neutrons have a wide energy distribution below the energy of incident neutron. Therefore, the energy of a neutron cannot be determined from its energy deposition.

The time resolution of the SONG detector was 1 or 4 s depending on the observation mode. In-flight observation conditions and background subtracting procedure are presented in [35].

We studied the flare gamma-ray emission using the response function of the detector simulated with the help of the GEANT 3.21 program. To restore the incident gamma-ray spectrum, we used a two-component model:

- (i) a continuum component caused mainly by the primary electron bremsstrahlung;
- (ii) a pion-decay component in the form of a broad “line” due to neutral pion decay, peaking at 67 MeV [5], plus a continuum due to bremsstrahlung from electrons and positrons produced in charged pion decay (Murphy, 2009 private communication to VGK).

The continuum components were represented by a power law with gradual steepening at high energies. The latter function was applied in two forms: as a power law with an index gradually changing with energy or as an exponential high-energy cutoff (see more detailed description of the spectra restoration in [35, 36]). The fitting procedure allows us to obtain both a shape of the continuum spectrum and intensity of the pion-decay component.

We note that it is easier to elicit the pion-decay emission of the flare’s spectrum if maximum energy of primary accelerated electrons does not exceed 30–40 MeV. If a large number of electrons were accelerated to higher energies, it is sometimes difficult to select small fluxes created by pion-decay emission. In these cases, we can specify only an upper limit of the pion-decay component fluxes.

Let us consider four particular events in more detail. In all cases, the total time of flares’ observation in our experiment did not exceed 10–15 min. This limit is caused by the peculiarities of the satellite orbit with an altitude of  $\sim 500$  km and polar inclination. Observations of flare that generated gamma emission by SONG were restricted due to contamination of the detector count rate by high-energy particles during a passage of CORONAS-F through the radiation belts or due to arriving of solar high-energy particles.

To compare the time behavior of energy release manifested by hard X-ray emission and derivative of soft X-ray emission with time profile of the pion-decay emission, we used, in addition to SONG data, the Solar Spectropolarimeter (SPR-N) [37] data and GOES soft X-ray measurements. SPR-N is a monitor of hard X-ray emission. It had two energy bands of 15–40 and of 40–100 keV and operated also onboard the CORONAS-F. It has never been saturated during the events under consideration.

## 3. SONG Observations during the Solar Flares

*3.1. Solar Flare on August 25, 2001.* The impulsive phase of the August 25, 2001, solar flare (GOES X5.3/3B, S17E34) was characterized by a gradual increase in the total intensity and energy of accelerated particles (see [38–41]). It lasted in high-energy emission band not more than 4–5 min. Time profiles of soft X-rays, the soft X-ray derivative,  $dI_{\text{SXR}}/dt$ , hard X-ray, and gamma emissions observed during the flare are presented in Figure 1. The background in the CORONAS-F data has been subtracted. The time profile of  $dI_{\text{SXR}}/dt$  normalized hereinafter to its maximum value shows that maximum energy input into emitting volume took place near 16:31:30. This time moment corresponds to maximum intensity of hard X-ray (40–100 keV) and gamma-ray ( $>60$  MeV) emissions. Peak time of gamma emission with energies 0.3–2 MeV is slightly delayed. This time difference of hard X-rays with various energies is a consequence of the magnetic trapping of electrons near the loop top and the subsequent precipitation into the footprint. Unlike the no-diffusion case, electrons can escape from the magnetic trap via pitch-angle scattering which is strongly energy dependent. A detailed discussion of this issue is out of scope of this work.

The incident energy spectra of gamma-ray emission accumulated in three time intervals are shown in Figure 2. These spectra were calculated with fitted parameters of the incident spectra in the two-component model discussed above. Figure 2 demonstrates changing in the spectrum shape and intensity of the pion-decay emission which dominates at energies above 60 MeV. Maximum of pion-decay emission was at 16:31:38–16:31:46, that is, close to the peak time of  $dI_{\text{SXR}}/dt$  and hard X-rays with energy of 40–100 keV. The time interval of energy release maximum can be defined hereinafter as an interval when  $dI_{\text{SXR}}/dt$  value exceeds 0.9 of its maximum. Thus, time intervals of maximum energy release and of maximum pion-decay emission overlap.

We got an opportunity to build a combined spectrum using GOES soft X-ray, SPR-N, SONG, and Yohkoh (Hard X-ray Spectrometer (HXS) and Gamma-Ray Spectrometer (GRS) [42]) data. Figure 3 shows this spectrum, accumulated over 16:31:38–16:31:46. To restore SPR-N and SONG spectrum we used an algorithm described in [43]; spectra of Yohkoh/HXS and Yohkoh/GRS were restored by Kashapova (private communication). This spectrum demonstrates that the primary electron continuum with power law lasts up to 60–100 MeV. The narrow gamma-lines and the line of pion-decay were identified over it. The flare also provided clear signals of neutron production with sufficient intensity to be recorded by CORONAS-F/SONG [28] after 16:35 and by the

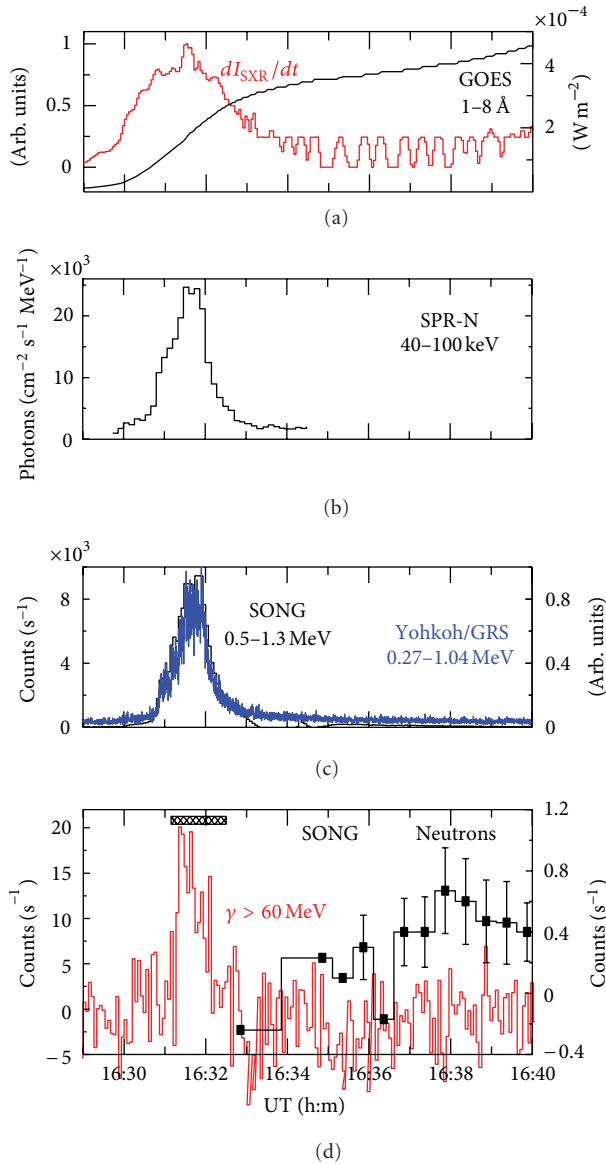


FIGURE 1: Time profiles of selected emissions from the August 25, 2001, flare: (a) soft X-ray flux (hereinafter black curve and right y-axis) and its derivative (hereinafter red curve and left y-axis); (b) hard X-ray 40–100 keV from CORONAS-F/SPR-N; (c) gamma-rays 0.5–1.3 MeV (CORONAS-F/SONG, black curve, left y-axis) and 0.27–1.04 MeV (Yohkoh/GRS, blue curve, right y-axis; <http://solar.physics.montana.edu/sxt/>); (d) gamma-rays >60 MeV (red, left y-axis) and neutrons (black, right y-axis) from CORONAS-F/SONG. Shaded rectangle in bottom panel denotes hereinafter the interval of undoubted observation of the pion-decay gamma-emission.

Chacaltaya NM in 16:35–16:36 [44]. This time lag relative to 16:31:30 corresponded to neutron energies >300 MeV. No GLE was observed after this eastern event.

3.2. *Solar Flare on October 28, 2003.* This prominent flare (X17.2/4B, S16E08) was observed in the soft X-ray and in

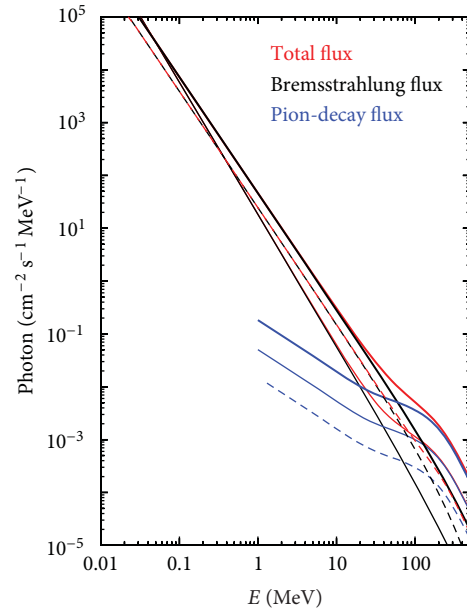


FIGURE 2: Restored energy spectra of gamma-rays for different time intervals. Thin lines correspond to 16:31:02–16:31:14, thick lines to 16:31:38–16:31:46, and dashed lines to 16:32:02–16:32:10. Red curves represent the total spectra, black curves electron bremsstrahlung, and blue curves the pion-decay component.

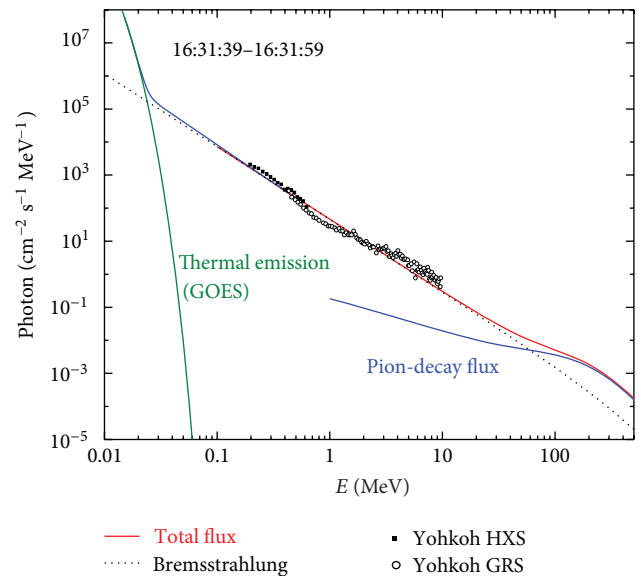


FIGURE 3: Combined spectrum of the August 25, 2001, flare. The total flux (blue curve) was restored from CORONAS-F data, the pion-decay flux—from SONG data.

$H\alpha$  ranging from 09:40 to 18:00 (<http://spidr.ngdc.noaa.gov/spidr/>). According to measurements within various ranges, the beginning of the impulsive phase (the beginning of the main energy release of this flare) was determined as 11:01–11:02 (see, e.g., [45–47]).

The increase in the hard X-ray emission over the background level caused by the solar flare was reliably detected

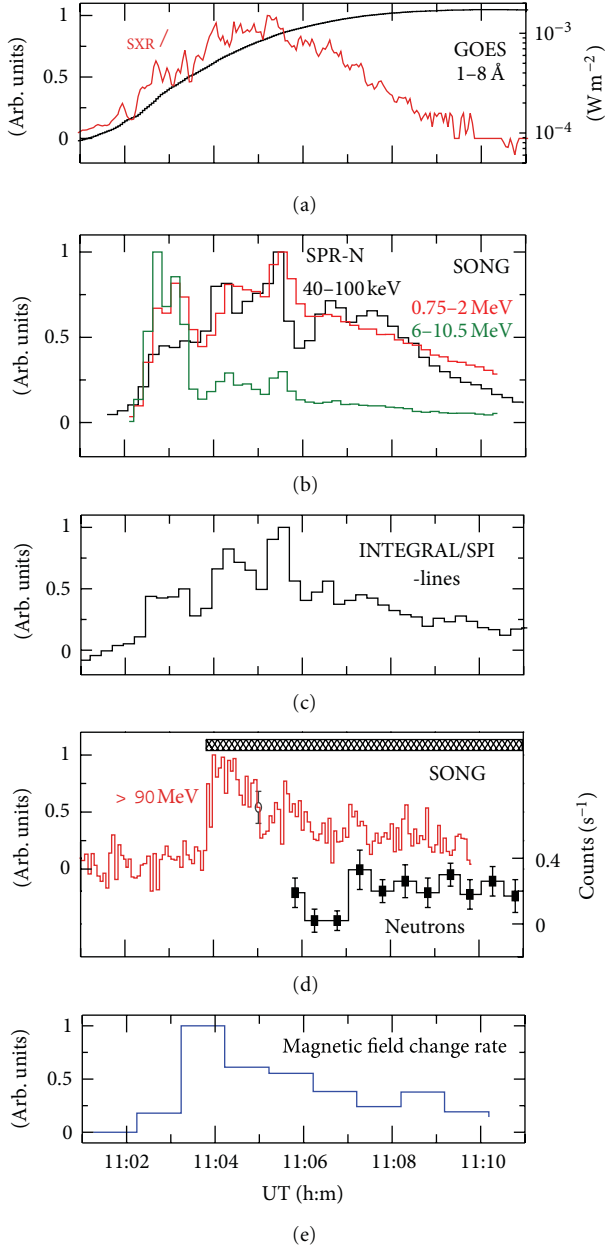


FIGURE 4: Normalized time profiles of selected emissions from October 28, 2003, flare: (a) soft X-ray flux and its derivative; (b) hard X-ray 40–100 keV from CORONAS-F/SPR-N (black curve); gamma-rays from CORONAS-F/SONG 0.75–2 MeV (red) and 6–10.5 MeV (green); (c) gamma-lines from INTEGRAL/SPI [46]; (d) gamma-rays  $> 90$  MeV (red, left y-axis) and neutrons (black, right y-axis) from CORONAS-F/SONG; (e) magnetic field change rate [48].

by the SONG instrument beginning from 11:02:11 to 11:12:30 (see Figure 4). This Figure presents also summarized intensity of the 4.4 + 6.1 MeV gamma-lines (INTEGRAL with the SPI spectrometer [46]) and the magnetic field change rate obtained with  $\sim 1$  min cadence [48].

The detailed study of SONG hard X-ray and gamma-ray emission measurement of this flare and neutrons can be

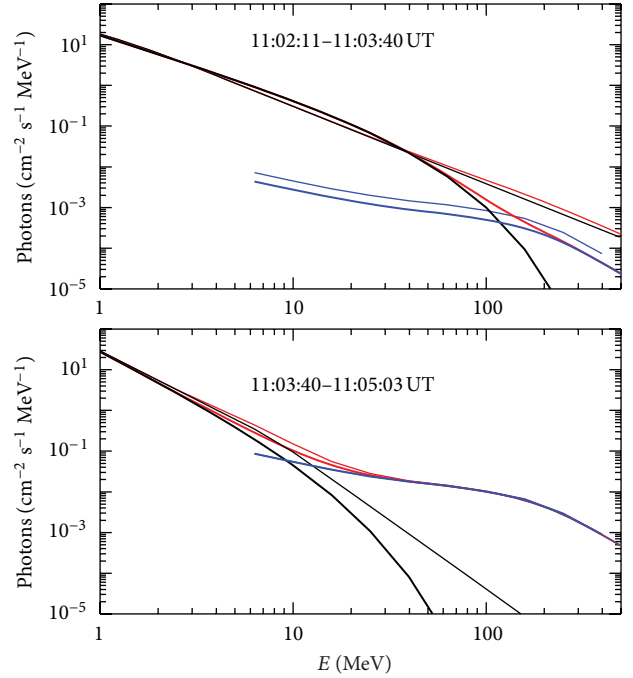


FIGURE 5: The restored incident gamma-ray spectra of the flare on October 28, 2003 (from [35]). Red curves represent the total spectra, black curves electron bremsstrahlung component, and blue curves the pion-decay gamma-ray spectrum. The thin curves correspond to a power law with varying index and the thick curves correspond to a power law with an exponential cutoff.

found in [35]. The important interval is 11:02:21–11:03:40, when power law spectrum caused by the electron bremsstrahlung extended up to very high energies of photons (100 MeV) was observed. We could not distinguish pion-decay contribution in this spectrum; consequently we could estimate the upper limits of pion-decay flux if any. At 11:03:51 a sharp increase of gamma-ray emission with energies above 40 MeV occurred. The shape of the spectrum changed substantially in this moment: a characteristic feature has appeared at energies above 30 MeV caused by the decay of neutral pions (see Figure 5). It was very surprising that the continuum created by primary electrons became more soft with a break around 40 MeV during this second energy release episode.

Comparing narrow gamma-line intensities [46] with the pion-decay flux at 100 MeV energy Kuznetsov et al. [35] has showed that the spectrum shape of the accelerated protons had also changed from exponential (11:02:21–11:03:40) to power law with spectral index equal to  $\sim 3$  after 11:03:51. This spectrum shape remained virtually unchanged, whereas the total intensity was decreasing gradually till 11:12, which was the end of our measurements. Regarding the time profile of hard X-rays and  $dI_{\text{SXR}}/dt$  it is evident that both curves reach their maximum values at 11:05–11:06 simultaneously with the time interval of maximum intensity of the pion-decay emission.

High-energy neutrons were measured by the SONG detector beginning at 11:06:20 [28, 35] and by the Tsumeb

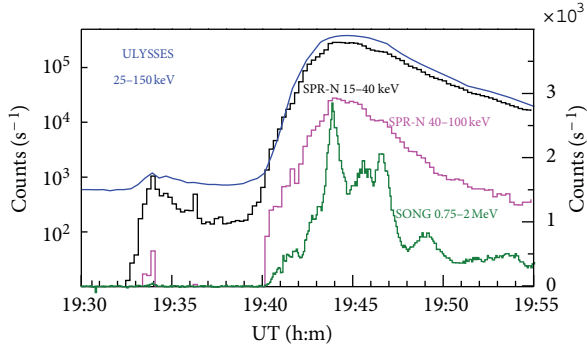


FIGURE 6: Time profiles of selected emissions from the November 4, 2003, flare measured by Ulysses and CORONAS-F. Left y-axis is suitable to Ulysses and SPR-N (15–40 keV) data; right y-axis to SPR-N (40–100 keV) and SONG data.

NM [49]. Bieber et al. [49] estimated the onset time of the neutron generation on the Sun to be  $10:56:30 \pm 1$  min, which corresponded to the time of the significant increase in the pion-decay emission (11:03:50–500 s) observed by the SONG detector.

**3.3. Solar Flare on November 4, 2003.** A new possibility to study the behavior of high-energy gamma-rays appeared during an unusually powerful flare on November 4, 2003 ( $X > 28/4B$ , S19W83), which occurred at the active region NOAA 10486 that approached the limb. The soft X-ray detectors onboard the GOES satellites were saturated within the 19:43–19:58 interval. However, soft X-ray importance  $> X28$  was later attributed to this flare. In addition to a very powerful soft X-ray burst, radio emission up to 405 GHz frequency was observed [50].

CORONAS-F satellite came out from the radiation belt region at 19:42:14 and was observing high-energy gamma-rays from this flare till the arrival of the intense flux of solar neutrons at 19:48:00–19:48:30. Beginning from this moment we could not reliably separate the detector signals with energies  $> 20$  MeV caused by photons from the signals caused by neutrons.

Since the flare was partly a behind-the-limb one, a question arises: do our measurements cover a time interval of the flare main energy release or they do not? We compared our data with the measurements of the 25–150 keV hard X-ray emission by the Ulysses spacecraft located at  $\sim 114^\circ$  westward from the Earth-Sun line at a distance of 5.28 AU from the Sun and measured X-ray emission from 19:33 [51]. The maximum of the Ulysses count rate was observed at approximately 19:44 (see Figure 6) taking into account the distance to Ulysses.

Figure 6 also shows the count rates of the hard X-ray emission measured by the SPR-N and SONG detectors onboard the CORONAS-F. One can see that a small intensity flare preceded the major flare (see also [52]). The main flare energy release onset was at 19:38:30. CORONAS-F started its observation at 19:42:14. This time by a lucky occasion is close to the beginning of the main energy release. Thus, 10 min of

our measurements covered practically the total time interval of the flare impulsive phase except the very beginning of the event between 19:38:30 and 19:42:14. Figure 7 shows in more detail the time behavior of various flare emissions.

Spectral analysis revealed a small contribution of the pion-decay component at the level  $> 1 \cdot 10^{-4}$  photons  $\text{cm}^{-2} \text{s}^{-1} \text{MeV}^{-1}$  within the time interval 19:42:14–19:42:40. The maximum of the gamma-rays from the pion decay is equal to  $1 \cdot 10^{-3}$  photons  $\text{cm}^{-2} \text{s}^{-1} \text{MeV}^{-1}$  (see Figure 8).

The high-altitude NMs at Mexico and Haleakala [53] and the SONG instrument [28] recorded intense fluxes of solar neutrons whose energy was estimated as 200 MeV on the basis of the time of flight method.

GLE associated with this flare was not observed, though the fluxes of solar protons with energy  $> 700$  MeV were recorded with High-Energy Proton and Alpha Particles Detector (HEPAD) on GOES (<http://umbra.nascom.nasa.gov/SEP/>).

**3.4. Solar Flare on January 20, 2005.** Throughout the history of flare studies the solar flare which occurred on January 20, 2005, (X7.1/3B, N14W61) is apparently the event with the best set of various experimental data (see, e.g., [36, 54, 55]). Radio data [54] and Ramaty High-Energy Solar Spectroscopic Imager (RHESSI) measurements indicated that intense acceleration of electrons up to energies 100 keV and protons up to energies 10–30 MeV began at approximately 06:42. Time profiles of selected emissions are presented in Figure 9. The increase of hard X-rays ( $> 40$  keV) and gamma-rays in the SPR-N and SONG data could be distinguished over the background count rates after 06:43:30.

Several distinguished episodes of energy release which led to the change in the emission spectrum shape are clearly seen in Figure 9. The maximum time of  $dI_{\text{SXR}}/dt$  coincides well with the maximum time of the energetic emission at 06:47:10 (see panels (c), (d), and (e)). At the same time the intensity of hard X-rays (40–100 and 100–300 keV) falls down. This decrease was probably caused by the reverse current, created by a very intense electron beam (see, e.g., [43, 56]). We merely note that accelerated protons can carry an additional input in the cumulative energy budget of the emitting plasma and we do not discuss this experimental fact in more detail, since it is beyond the scope of the present work.

Figure 10 presents four successive emission spectra calculated with various forms of continuum spectrum. Each of them was accumulated over 1 min. The figure demonstrates a gradual increase in the total intensity of gamma-rays. The plateau caused by pion-decay becomes distinctly pronounced over 06:44:40–06:48:40 time interval. This spectral peculiarity was distinguished even within the 06:44–06:45 interval at the very low level of  $(1-3) \cdot 10^{-4}$  photons  $\text{cm}^{-2} \text{s}^{-1} \text{MeV}^{-1}$  at the 100 MeV energy. Beginning from 06:45:40, a substantial increase of intensity of photon with energies  $> 10$  MeV is observed. The maximum of the high-energy gamma-ray emission was observed at 06:46–06:47 and was  $3.6 \cdot 10^{-3}$  photons  $\text{cm}^{-2} \text{s}^{-1} \text{MeV}^{-1}$  at the 100 MeV. Note that the

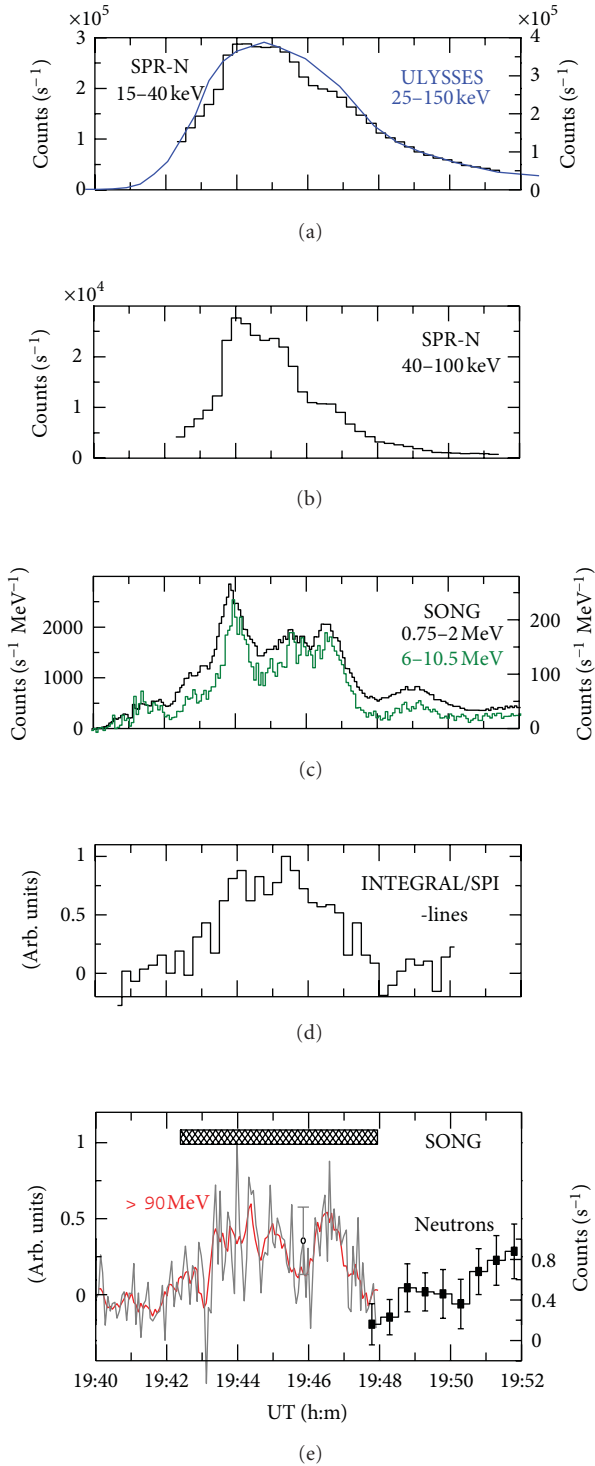


FIGURE 7: Time profiles of selected emissions from the November 4, 2003, flare: (a) hard X-ray measured by Ulysses (blue curve, right y-axis) and CORONAS-F/SPR-N (black curve, left y-axis); (b) hard X-rays (40–100 keV) from CORONAS-F/SPR-N; (c) gamma-rays 0.75–2 MeV (black, left y-axis) and 6–10.5 MeV (green, right y-axis) from CORONAS-F/SONG; (d) summarized normalized intensity of the 4.4 MeV + 6.1 MeV gamma-lines from INTEGRAL/SPI [53]; (e) gamma-rays >90 MeV (gray, left y-axis, data are normalized) and neutrons (black, right y-axis) from CORONAS-F/SONG. Red curve in the bottom panel presents smoothed data on gamma-rays.

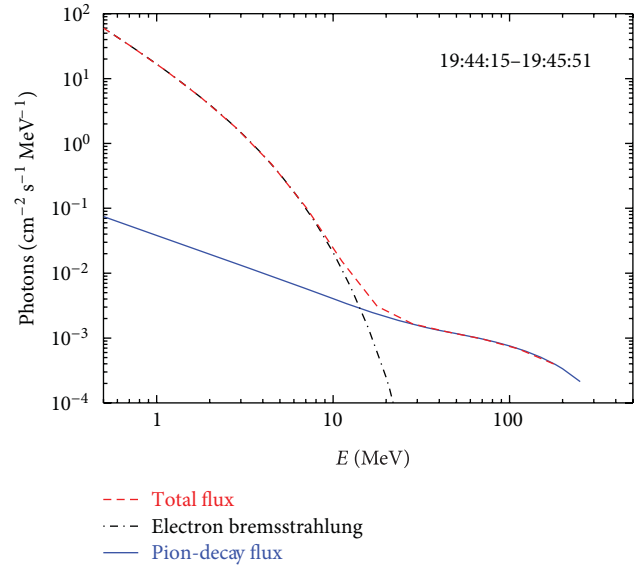


FIGURE 8: The restored incident gamma-ray spectrum of the flare on November 04, 2003. Red curve represents the total spectra, black curve electron bremsstrahlung component, and blue curve the pion-decay gamma-ray spectrum.

intensity of the pion-decay emission does not depend appreciably on a choice of continuum spectrum. Maximum pion-production coincided with time of maximum energy release.

The protons accelerated on the Sun were observed by the world NM network (GLE69) [2].

#### 4. GLEs and SPE Onset Associated with the Discussed Flares

The time profile of the pion-decay gamma emission corresponds to the time evolution of the population of the interacting protons and can be used to determine, at least, the onset time of proton acceleration. Further, the most important issue is to know the timing between the particle acceleration up to relativistic energies and time of release of protons, in some cases connected with GLE observations.

Suppose that a certain number of the accelerated protons escaped immediately into space after acceleration. So, if the onset or maximum time of the pion-decay emission was observed, we know the escaping time of the particles. In fact, this assumption means that protons interacting at the Sun (and generating pions) and protons responsible, at least for the initial phase of the GLE, should belong to the same population of accelerated particles.

Usually, when one analyzes the propagation of solar cosmic rays in the interplanetary space the ideal Parker model of the solar wind (SW) is used. It suggests that the IMF lines are in the form of Archimedean spirals. Their parameters (length and heliolongitude of magnetic field line connecting the Sun and Earth) are determined by averaged values over few days prior to the flare. The mean free path of individual particles may be less than the length of the nominal values of

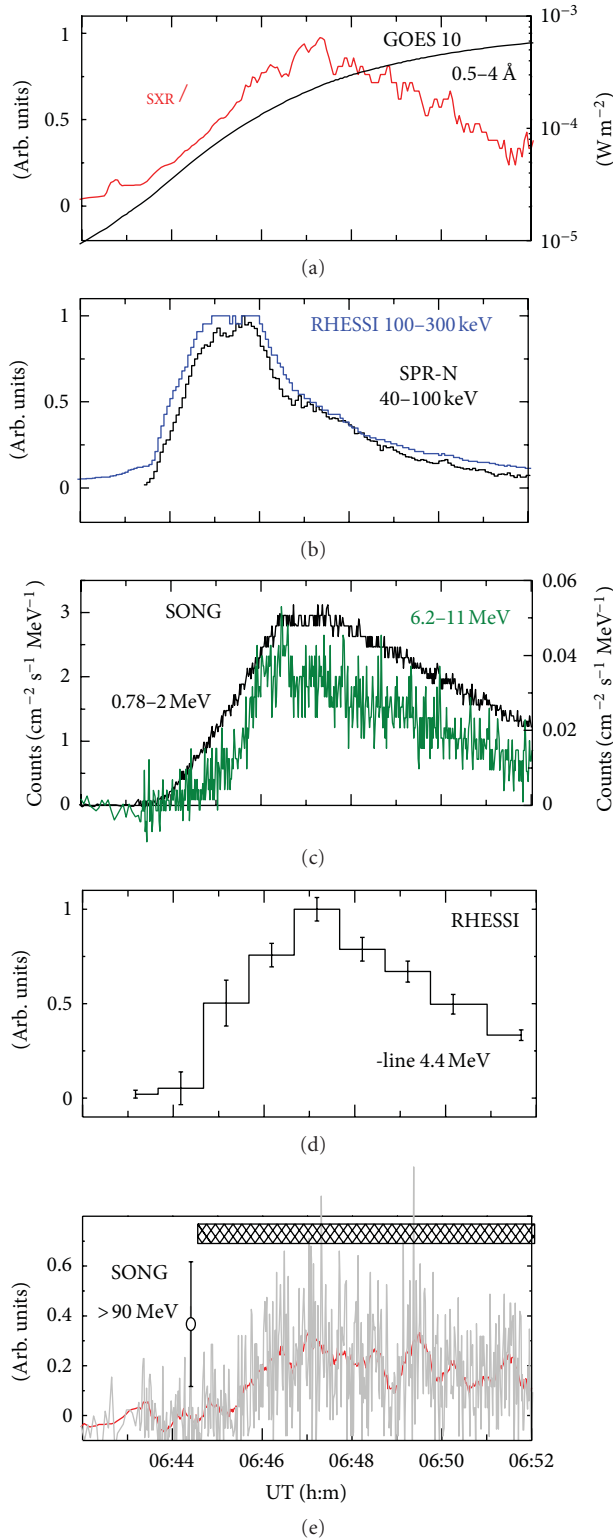


FIGURE 9: Time profiles of selected emissions from the January 20, 2005, flare: (a) soft X-ray flux (black curve) and its derivative (red curve); (b) hard X-rays (SPR-N and RHESSI, arbitrary units); (c) gamma-rays 0.78–2 MeV (black, left  $y$ -axis) and 6.2–11 MeV (green, right  $y$ -axis) from SONG; (d) the 4.4 MeV gamma line from RHESSI, courtesy G. Share; (e) high-energy gamma-rays (SONG). Red curve in the bottom panel presents smoothed data on gamma-rays.

IMF line, but not less than the distance from the Sun to Earth in this epoch (see, e.g., [57]).

It should be added that relativistic particle events are observed at times of high solar activity, when transient magnetic structures such as CMEs disrupt often the IMF structure as, for example, in the intervals August 1972, August 1989, June 1991, and October–November 2003. Therefore, in these cases it is unlikely to assume the regularity of the spiral structure of IMF. Sun–Earth magnetic connections can be rooted far from the nominal Parker spiral (see, e.g., [58, 59]).

The time lag between the onset of particles detected on Earth with respect to the particle release time from the Sun can be estimated from the following suggestions.

- (i) Let us assume that accelerated particles escaping from the Sun get on the shortest IMF lines with a small pitch angle.
- (ii) Particles are propagating with small or without scattering. Therefore, their trajectory lengths are close to the length of the IMF line.
- (iii) The threshold energy of the particles detected by high-latitude NM is  $\sim 450$  MeV due to an atmospheric absorption, but the effective energy of the particles detected by high-latitude neutron monitors exceeds 1 GeV (see, e.g., [60]). The latter energy corresponds to the particle velocity not less than the  $v = 0.875c$  ( $c$  is the speed of light). The energies of particles detected by the medium and low-latitude NMs are even higher, and these energies are determined by the geomagnetic cutoff.
- (iv) The propagation time of protons with energy of 1 GeV assuming the path length between 1 and 1.3 AU is equal to 581–755 s, respectively.
- (v) If this is true, we expect that a little short impulse or raising intensity springs out before the main event enhancement (i.e., a kind of precursor). It can be observed by one or several NMs with the lag, approximately  $670 \pm 80$  s relative to particle release time.

Let us compare the release time of these leader particles with the time of an efficient generation of protons in the flare (as determined by timing of the pion-decay emission). Remember that the propagation time of 1 AU for gamma photons is equal to  $\sim 500$  s. Thus, if we find that the precursor's particles were delayed with respect to gamma-rays at the  $\approx 3$ –5 min, we get the reason to believe that these protons were accelerated in the flare. Given the spread of path lengths and the uncertainty of data on the velocities of the first recorded particles, their delay relative to the *observation* time of the pion-decay gamma-rays should fall within the interval of 1–6 minutes.

Let us compare GLE 65 and 69 onset as well as SPE onset of November 4, 2003, with the time of pion-decay emission measurements during associated flares which occurred on October 28, 2003, January 20, 2005, and November 4, 2003.

First of all we determined the beginning of observation of GLEs 65, 69 [61]. We have carefully studied the excess above the background level in the analysis of all available NMs data.

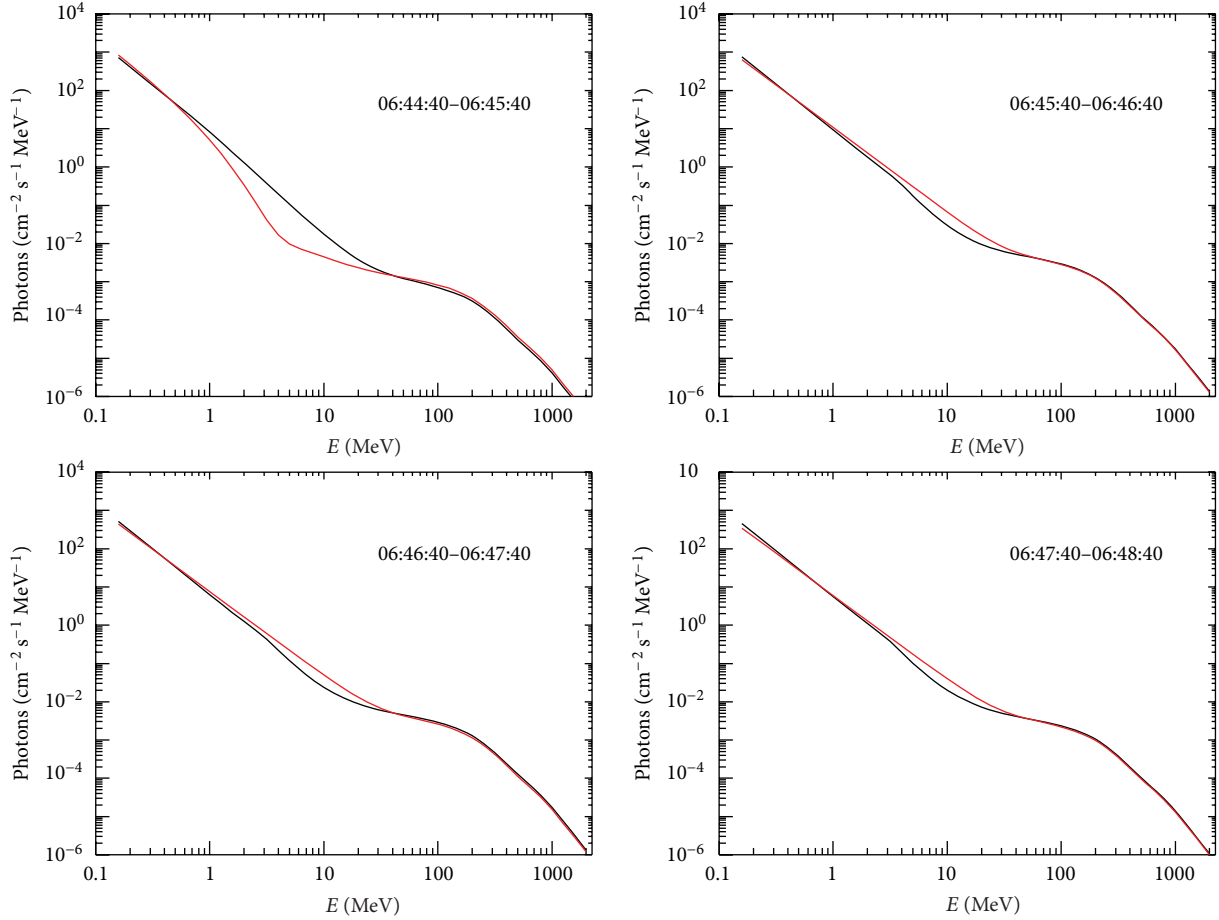


FIGURE 10: The total energy spectra of photons during the flare on January 20, 2005. The red curves correspond to a power law with varying index and the black curves correspond to a power law with an exponential cutoff.

If this excess is seen just in data of a single NM, it may be random, even if its value exceeds  $3\sigma$  level. To determine the interval of first particles arrival, we used the method of superposed epoch for the data from several stations hinting a notional excess.

Figures 11 and 12 illustrate our method and the results obtained in GLE65 and GLE69. For GLE65 data of Hermans, Irkutsk-2, McMurdo, Cape Shmidt, and Calgary NMs were used. The proton acceleration time and the maximum energy release were 11:04–11:06, and we determined the statistically significant time of the first particles' arrival as 11:06–11:08.

For GLE69 data of Oulu, Norilsk, Apatity NMs were used. In addition we show the NM South Pole data because these data are commonly used to demonstrate the onset of GLE 69 at 06:48–06:49. Our method determined the time of the first particle arrival as 06:47–06:48.

The proton acceleration time and the maximum energy release were 06:46–06:48.

To check the possibility of direct observation of solar neutrons by selected NMs we calculated an angle between the local vertical and the direction to the Sun at the time of the event under consideration [61]. Practically all cases of solar neutron observations were performed by high-altitude

NMs located near the subsolar point (e.g., the Tsumeb NM during the event on October 28, 2003 [49]). NMs whose data were used in this work had not a possibility to observe solar neutrons.

No GLE event associated with the November 4, 2003, flare was reported. We used data of the HEPAD detector onboard GOES-10 and -12 and found the high-energy ( $>700$  MeV) proton onset of the SPE between 19:45 and 19:55 (see Figure 13). The proton acceleration time and the maximum energy release were 19:44–19:48.

In Table 1 we summarize the timing of pion-decay emissions and high-energy particle onsets for events examined in this work.

## 5. Discussion

Before the launch of CORONAS-F data set of the flares with the pion-decay emission consisted only of 8 events. CORONAS-F measurements extended this set essentially. 120 flares with hard X-ray emission were observed with CORONAS-F, and high-energy electron bremsstrahlung with photon energy  $>5$  MeV was observed in 15 flares. We were lucky and have measured gamma-rays with energies up to

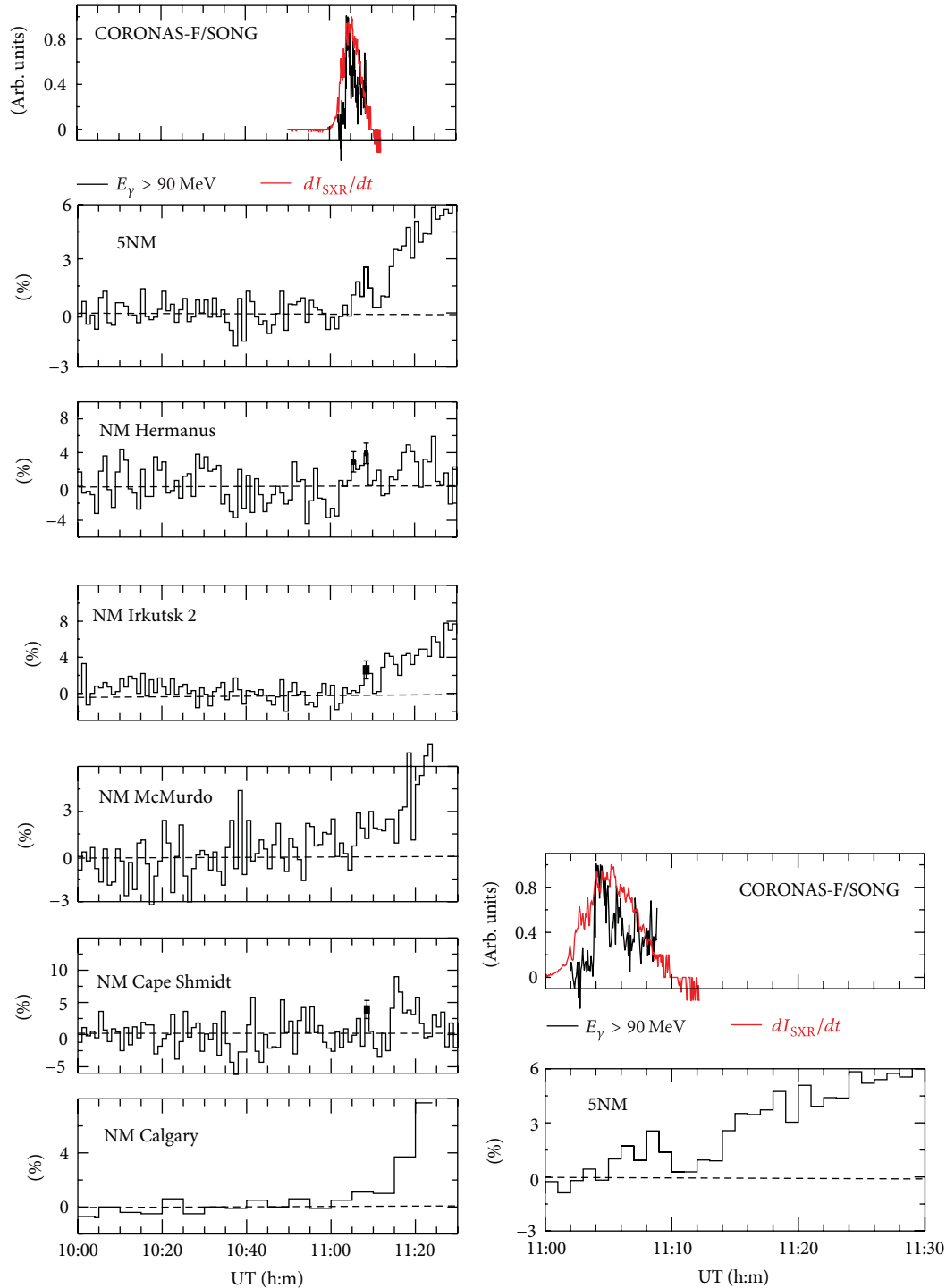


FIGURE 11: GLE 65, October 28, 2003. The left part, upper panel: SONG gamma-rays (black curve) and the soft X-ray derivative (red curve). The second panel: count rates of five NMs obtained by the method of superposed epoch. Five panels below: data of each NM separately. Right part: two upper panels from the left part displayed with better time resolution.

100–200 MeV when the impulsive phase of 4 powerful flares, namely, August 25, 2001, October 28, 2003, November 4, 2003, and January 20, 2005, was in progress. All these flares produced neutrons and/or protons, recorded near the Earth. We demonstrated that the SONG response was consistent

with detection of the pion-decay emission and high-energy neutron fluxes.

High-energy neutrons and pion-decay photons are produced in the same interactions of accelerated protons with ambient matter instantly. So it would be reasonable to expect

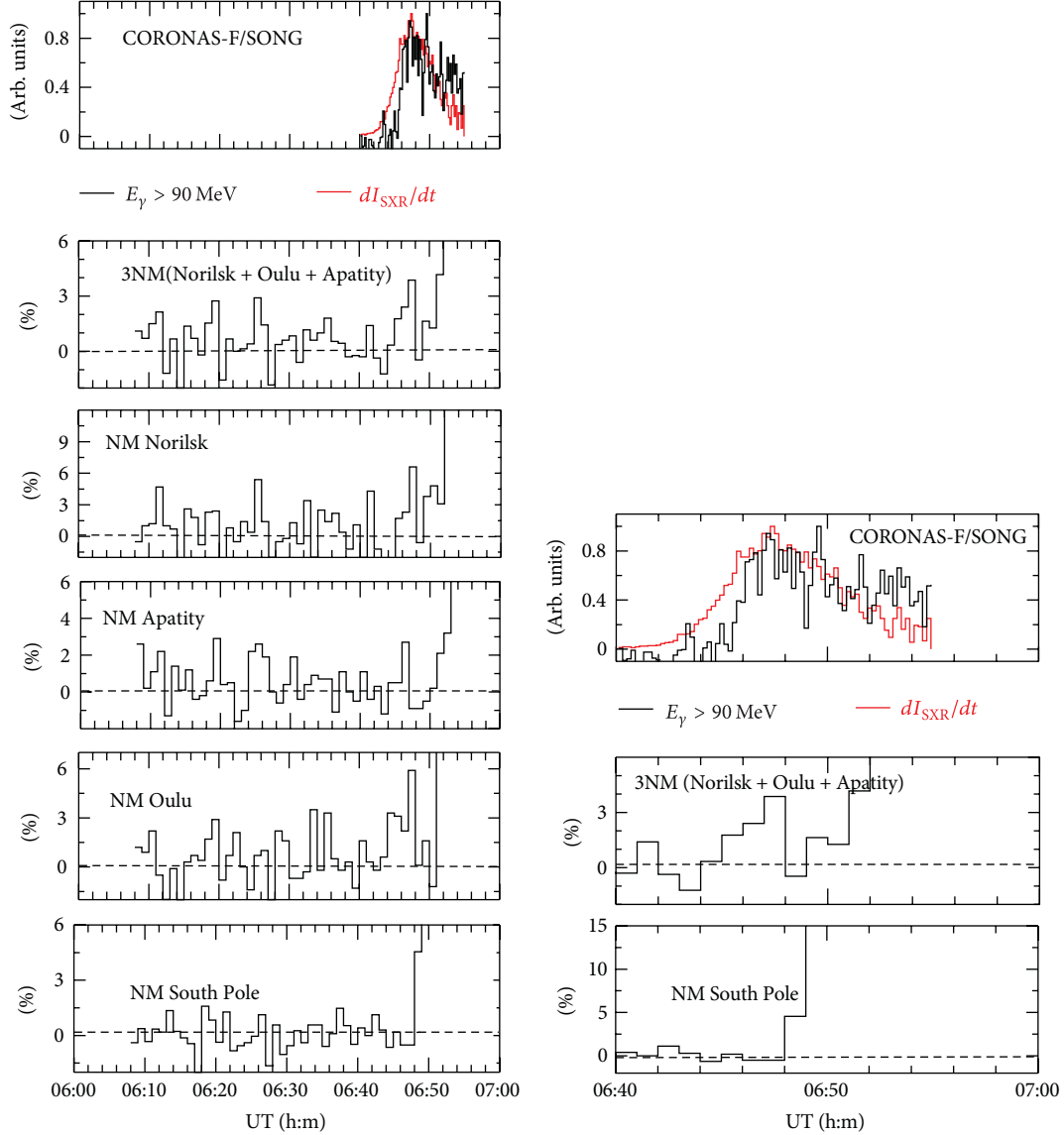


FIGURE 12: GLE 69, January 20, 2005. Left part, upper panel: SONG gamma-rays (black curve) and the soft X-ray derivative (red curve). The second panel: the count rates of three NMs obtained by the method of superposed epoch. Three panels below: Oulu, Apatity, and Norilsk NMs. The bottom panel: NM South Pole. Right: zoom of photon emissions and of count rates of 3NMs and NM South Pole.

TABLE 1: Timing of pion-decay gamma emission and high-energy particle onsets.

Date	August 25, 2001	October 28, 2003	November 4, 2003	January 20, 2005
Flare importance, location	X5.3/3B S17E34	X17.2/4B S16E08	X > 28/4B S19W83	X7.1/3B N14W61
Time of the pion-decay emission	16:31:10–16:32:30	From 11:04:50	19:42:30–19:48:00	From 06:44:40
Time of proton onset	No	11:06–11:08	19:45–19:55	06:47–06:48
Time of neutron onset	16:35–16:36	11:07:00–11:07:30	19:48:00–19:48:30	No

the observation of both in one and the same event. Indeed, neutrons were observed by SONG and NMs after three flares. On January 20, 2005, neither ground-level detectors nor CORONAS-F/SONG observed neutrons though the observation conditions were favorable for their detection by SONG. It

is difficult to understand the absence of neutrons, since GLE 69 accompanying this flare reached 5400%.

One can use any model of the incident photon spectrum to restore it from the detector pulse spectrum. In our simulation methods we performed the usual procedure of spectrum

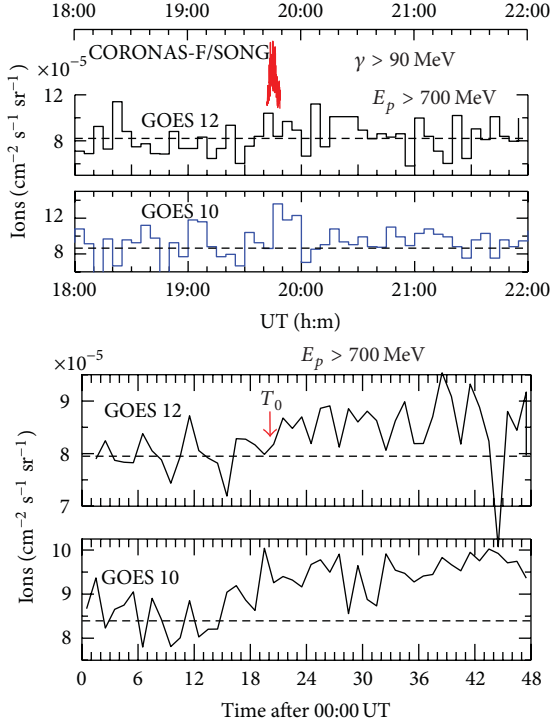


FIGURE 13: Time profiles of high-energy proton channels recorded by GOES-10 and -12 on November 4, 2003. Upper two panels: proton time profiles over 4 hours around the solar flare. Red curve in upper panel shows the increase observed in gamma-ray channel  $>90$  MeV. Two lower panels: proton time profiles measured by HEPAD during enlarged time period.  $T_0 = 19:42:30$ .

restoration, accepted by the scientific community studying high-energy gamma emission (see, e.g., [16, 22–24]). The fitting procedure including standard  $\chi^2$  permits to calculate the total incident spectrum and the pion-decay contribution. To elicit a pion-decay feature in the gamma-ray emission spectrum the intensity of the pion-decay emission must exceed the bremsstrahlung background. SONG spectrometer had the appropriate sensitivity and energy resolution for these purposes.

Exploring four flares we distinguished several acceleration episodes with substantially different characteristics during the time evolution of these flares which implies a substantial change in the spectrum shape of accelerated electrons as well as ions. We define maximum energy release as maximum  $dI_{\text{SXR}}/dt$  in this work. It is known that at the beginning of the flare impulsive phase the value of  $dI_{\text{SXR}}/dt$  does not exceed 20–30% of its peak value. Electrons are mainly accelerated during this time, which is manifested by bremsstrahlung hard X-ray and gamma-ray emission. The photon energy of such “pure electron spectrum” can reach 60–100 MeV. This was demonstrated earlier in June 21, 1980, May 24, 1990, and March 26, 1991, powerful flares [16, 21, 62].

The measurements of the narrow gamma-lines performed by SPI during October 28 and November 4, 2003, as well as RHESSI during January 20, 2005, events indicated the presence of protons accelerated up to 10–30 MeV near the

beginning of these events. We discovered that in the rise phase of August 25, 2001, and October 28, 2003, flares the energy of photons reached at least 80–100 MeV without any deposit from the pion-decay emission. At the beginning of November 4, 2003, and January 20, 2005, flares the spectral feature associated with the pion-decay process was very faint. It means that the number of ions accelerated up to the energy above the threshold of pion production ( $\sim 300$  MeV) was very small in these time intervals.

We emphasize that observation of the pion-decay gamma emission is the method of investigating proton acceleration up to hundreds of MeV and more because this spectral feature cannot be imitated by other processes.

We determined the time of the sharp increase of the pion-decay component intensity. Since pion-decay gamma-rays are emitted by accelerated ions almost instantaneously, the moment of the sharp rise of the pion-decay component indicates the time of the proton bulk appearance in the low corona. Neutron generation function (or more precisely the injection function) can be determined by solving the inverse problem (e.g., [49, 63]). The time of neutron production can be determined by this method with accuracy  $\geq 1$  min; the accuracy derived from the pion-decay emission data is higher.

We found that the time of the maximum efficiency of proton acceleration is close to the time interval when the  $dI_{\text{SXR}}/dt$  value exceeds 0.9 of its maximum. If our definition of flare energy release is correct, then this time closeness indicates that maximum efficiency of ion acceleration occurs in the time of flare energy release. The strong correlation between pion-decay flux time profile and magnetic-flux change rate was observed in October 28, 2003, flare (see Figure 5). Certainly it is only one case, but it implies that acceleration of high-energy protons may be an intrinsic property of the impulsive energy-release process, and it seems to be important for particle acceleration models.

We clearly saw that the increase in the electron energy (hardening of the spectral index) is not necessarily consistent with the episodes of the maximum efficiency of proton acceleration as it is clearly seen in October 28, 2003, flare.

Comparing the timing of pion-decay emission with the arrival time of the first energetic particles at 1 AU we found that these particles lagged  $\approx 3$ –5 min behind the gamma-rays emission. So we proved that these protons were accelerated in the flare simultaneously with the interacted protons (or they both belong to the same population of accelerated particles).

Our investigation of three events revealed that the maximum pion production indicating the maximum efficiency of proton acceleration was observed within the time interval of maximum energy release determined by  $dI_{\text{SXR}}/dt$ . This conclusion can be extended to the flare on November 4, 2003, if we assume that maximum energy release was determined from data on hard X-rays.

It is well known that for most of GLEs measurements of high-energy gamma emission from associated flares were absent. We showed in the present paper that the time of the most efficient proton acceleration coincided with the time interval of maximum energy release manifested by  $dI_{\text{SXR}}/dt$ . Taking this result as the “null” hypothesis, we have used it as a working tool for determining the time delay of the first

particles of GLE relative to the time of maximum efficiency of proton acceleration. We carried out a detailed study of the onset time of 43 GLEs and found that this delay did not exceed 10 minutes in 28 events [64]. This means that proton acceleration to relativistic energy starts typically within the time interval of maximum flare energy release.

The indirect methods of the initial moment determination and time duration of heavy particle acceleration up to relativistic energies (i.e., the analysis of radio emission, the determination of CME lift-off time, and the time of type II onset that are usually considered to be an indication of a shock wave in the corona, etc.) do not provide such a time accuracy.

## 6. Conclusions

We have analyzed high-energy gamma emission and neutron flux measurements of four solar flares: August 25, 2001, October 28, 2003, November 4, 2003, and January 20, 2005, obtained by CORONAS-F and combined with other observations of these flares. We showed that the SONG instrument response had been consistent with the detection of the pion-decay gamma emission and neutron fluxes in these events. We determined the onset time of GLEs 65 and 69 which accompanied October 28, 2003, and January 20, 2005, flares on the basis of the Neutron Monitor World Network data. For reliable determination of this time we used the superposed epoch method. We used data of HEPAD detectors onboard GOES 10 and 12 to determine the onset time of high-energy protons during SPE on November 4, 2003. We obtained the following results.

- (1) Observations of both pion-decay gamma-rays and high-energy neutrons in one and the same event prove undoubtedly that protons were accelerated up to relativistic energy, and then they interacted with solar matter. Detection of high-energy neutrons in the considered events proves that the observed feature in the gamma-ray spectrum was caused by the pion-decay process. Acceleration of protons responsible for GLE/SPE serves as an additional argument to ascribe this feature to the pion decay.
- (2) The pion-decay emission was observed within the time interval of the maximum flare energy release, which was manifested particularly by  $dI_{\text{SXR}}/dt$  time evolution. Hence, proton acceleration begins in the course of the flare but not later. However, we recognize that this conclusion is not the general rule. There are flares in which the pion-decay emission appeared only after the end of the main energy release.
- (3) GLEs/SPE onset was observed with a short  $<5$  min delay in respect to the time of the pion-decay gamma-rays' observations, which is the least possible value. So, we suggest that in the events which took place on October 28, 2003, November 4, 2003, and January 20, 2005, both protons interacted in the solar atmosphere, and the first protons which arrived to the Earth belonged to one and the same population of the accelerated particles.

Revealed relationship between high-energy gamma-rays and GLE may serve as an additional element for short-time forecasts of radiation hazard storms in addition to those based on ground-based devices (NMs) and lower energies emission measurements. Thus, it makes sense to continue to provide regular patrol of high-energy "neutral emissions" from the Sun on various satellites and spacecraft in order to investigate space weather.

## Acknowledgments

The authors are deeply indebted to G. Share and A.V. Belov for helpful discussions, R. Murphy for providing calculated pion-decay spectra, A. V. Belov for providing NM data set, V. V. Grechnev for providing Yohkoh data, and L. Kashapova for restoring the Yohkoh/HXS spectrum. This work was supported in part by the Russian Foundation for Basic Research (projects no. 05-02-17487 and 09-02-01145). K. Kudela wishes to acknowledge VEGA agency (project 2/0040/13) for support.

## References

- [1] S. E. Forbush, "Three unusual cosmic-ray increases possibly due to charged particles from the sun," *Physical Review*, vol. 70, no. 9-10, pp. 771-772, 1946.
- [2] A. V. Belov, E. A. Eroshenko, O. N. Kryakunova, V. G. Kurt, and V. G. Yanke, "Ground level enhancements of solar cosmic rays during the last three solar cycles," *Geomagnetism and Aeronomy*, vol. 50, no. 1, pp. 21-33, 2010.
- [3] M. B. Kallenrode and G. Wibberenz, "Influence of interplanetary propagation on particle onsets," in *Proceedings of the 21st International Cosmic Ray Conference*, vol. 5, pp. 229-232, Adelaide, Australia, 1990.
- [4] R. Ramaty and R. J. Murphy, "Nuclear processes and accelerated particles in solar flares," *Space Science Reviews*, vol. 45, no. 3-4, pp. 213-268, 1987.
- [5] R. J. Murphy, C. D. Dermer, and R. Ramaty, "High-energy processes in solar flares," *Astrophysical Journal Supplement Series*, vol. 63, pp. 721-748, 1987.
- [6] E. L. Chupp, D. J. Forrest, J. M. Ryan et al., "A direct observation of solar neutrons following the 01:18 UT flare on 1980 June 21," *Astrophysical Journal Letters*, vol. 263, pp. L95-L99, 1982.
- [7] H. Debrunner, E. O. Flückiger, E. L. Chupp, and D. J. Forrest, "The solar cosmic ray neutron event on June 3, 1982," in *Proceedings of the 18th International Cosmic Ray Conference*, vol. 4, pp. 75-78, Bangalore, India, 1983.
- [8] E. L. Chupp, H. Debrunner, E. O. Flückiger et al., "Solar neutron emissivity during the large flare on 1982 June 3," *Astrophysical Journal*, vol. 318, pp. 913-925, 1987.
- [9] Y. E. Efimov, G. E. Kocharov, and K. Kudela, "On the solar neutrons observation on high mountain neutron monitor," in *Proceedings of the 18th International Cosmic Ray Conference*, vol. 10, pp. 276-278, Bangalore, India, 1983.
- [10] P. Evenson, P. Meyer, and K. R. Pyle, "Protons from decay of solar flare neutrons," *Astrophysical Journal*, vol. 274, pp. 875-882, 1983.
- [11] P. Evenson, R. Kroeger, P. Meyer, and D. Muller, "Solar flare neutron fluxes derived from interplanetary charged particle measurements," in *Proceedings of the 18th International Cosmic Ray Conference*, vol. 4, pp. 97-100, Bangalore, India, 1983.

- [12] Y. Muraki, "Solar neutrons and particle acceleration at the sun: what we learnt from solar neutron telescope," in *Proceedings of the 30th International Cosmic Ray Conference*, vol. 6, pp. 181–194, Merida, Mexico, 2009.
- [13] R. J. Murphy, B. Kozlovsky, G. H. Share, X. M. Hua, and R. E. Lingenfelter, "Using gamma-ray and neutron emission to determine solar flare accelerated particle spectra and composition and the conditions within the flare magnetic loop," *Astrophysical Journal Supplement Series*, vol. 168, no. 1, pp. 167–194, 2007.
- [14] Y. Hirasima, K. Okudaira, and T. Yamagami, "Solar gamma ray burst observed on 27 Sept. 1968," in *Proceedings of the 11 International Cosmic Ray Conference*, vol. 2, pp. 683–686, Budapest, Hungary, 1970.
- [15] E. L. Chupp, D. J. Forrest, P. R. Higbie, A. N. Suri, C. Tsai, and P. P. Dunphy, "Solar gamma ray lines observed during the solar activity of August 2 to August 11, 1972," *Nature*, vol. 241, no. 5388, pp. 333–335, 1973.
- [16] D. J. Forrest, W. T. Vestrand, E. L. Chupp et al., "Neutral pion production in solar flares," in *Proceedings of the 19th International Cosmic Ray Conference*, vol. 4, pp. 146–149, 1985.
- [17] D. J. Forrest, W. T. Vestrand, E. L. Chupp, E. Rieger, J. Cooper, and G. H. Share, "Very energetic gamma-rays from the 3 June 1982 solar flare," *Advances in Space Research*, vol. 6, no. 6, pp. 115–118, 1986.
- [18] P. P. Dunphy, E. L. Chupp, and E. Rieger, "Analysis of SMM GRS high-energy ( $> 10$  MeV) data from the solar flare of 1988 December 16," in *Proceedings of the 21st International Cosmic Ray Conference*, vol. 5, pp. 75–78, Adelaide, Australia, 1990.
- [19] P. P. Dunphy and E. L. Chupp, "High-energy gamma-rays and neutrons from the solar flare of 1989 March 6," in *Proceedings of the 22nd International Cosmic Ray Conference*, vol. 3, pp. 65–68, Dublin, Ireland, 1991.
- [20] O. V. Terekhov, R. A. Sunyaev, A. Y. Tkachenko et al., "Deuterium synthesis during the solar flare of March 22, 1991 (Granat data)," *Astronomy Letters*, vol. 22, no. 2, pp. 143–147, 1996.
- [21] H. Debrunner, J. A. Lockwood, C. Barat et al., "Energetic neutrons, protons, and gamma rays during the 1990 May 24 solar cosmic-ray event," *Astrophysical Journal*, vol. 479, pp. 997–1011, 1997.
- [22] N. Vilmer, A. L. MacKinnon, G. Trottet, and C. Barat, "High energy particles accelerated during the large solar flare of 1990 May 24: X/ $\gamma$ -ray observations," *Astronomy and Astrophysics*, vol. 412, pp. 865–874, 2003.
- [23] E. J. Schneid, D. L. Bertsch, B. L. Dingus et al., "EGRET observations of X-class solar flares," *Astronomy and Astrophysics Supplement Series*, vol. 120, pp. 299–302, 1996.
- [24] P. P. Dunphy, E. L. Chupp, D. L. Bertsch, E. J. Schneid, S. R. Gottesman, and G. Kanbach, "Gamma-rays and neutrons as a probe of flare proton spectra: the solar flare of 11 June 1991," *Solar Physics*, vol. 187, no. 1, pp. 45–57, 1999.
- [25] V. V. Akimov, V. G. Afanassyev, A. S. Belousov et al., "Observation of high energy gamma-rays with the GAMMA-1 telescope ( $E > 30$  MeV)," in *Proceedings of the 22nd International Cosmic Ray Conference*, vol. 3, pp. 73–76, Dublin, Ireland, 1991.
- [26] V. V. Akimov, P. Ambrož, A. V. Belov et al., "Evidence for prolonged acceleration based on a detailed analysis of the long-duration solar gamma-ray flare of June 15, 1991," *Solar Physics*, vol. 166, no. 1, pp. 107–134, 1996.
- [27] S. N. Kuznetsov, K. Kudela, I. N. Myagkova, A. N. Podorolsky, S. P. Ryumin, and B. Y. Yushkov, "First experience with SONG-M measurements on board CORONAS-F satellite," *Indian Journal of Radio and Space Physics*, vol. 33, no. 6, pp. 353–357, 2004.
- [28] S. N. Kuznetsov, V. G. Kurt, I. N. Myagkova, B. Y. Yushkov, and K. Kudela, "Gamma-ray emission and neutrons from solar flares recorded by the SONG instrument in 2001–2004," *Solar System Research*, vol. 40, no. 2, pp. 104–110, 2006.
- [29] V. G. Kurt, B. Y. Yushkov, K. Kudela, and V. I. Galkin, "High-energy gamma radiation of solar flares as an indicator of acceleration of energetic protons," *Cosmic Research*, vol. 48, no. 1, pp. 70–79, 2010.
- [30] E. L. Chupp, G. Trottet, P. P. Dunphy, and E. Rieger, "What we know and what we do not know about high energy neutral emissions from solar flares (a challenge for future missions)," in *Proceedings of the 28th International Cosmic Ray Conference*, pp. 3171–3174, Tsukuba, Japan, 2003.
- [31] E. L. Chupp and J. M. Ryan, "High energy neutron and pion-decay gamma-ray emissions from solar flares," *Research in Astronomy and Astrophysics*, vol. 9, no. 1, pp. 11–40, 2009.
- [32] M. Ackermann, M. Ajello, A. Allafort et al., "FERMI detection of  $\gamma$ -ray emission from the M2 soft X-ray flare on 2010 June 12," *Astrophysical Journal*, vol. 745, pp. 144–154, 2012.
- [33] N. Vilmer, A. L. MacKinnon, and G. J. Hurford, "Properties of energetic ions in the solar atmosphere from gamma-ray and neutron observations," *Space Science Review*, vol. 159, pp. 167–224, 2011.
- [34] L. I. Miroshnichenko and W. Q. Gan, "Particle acceleration and gamma rays in solar flares: recent observations and new modeling," *Advances in Space Research*, vol. 50, pp. 736–756, 2012.
- [35] S. N. Kuznetsov, V. G. Kurt, B. Y. Yushkov, K. Kudela, and V. I. Galkin, "Gamma-ray and high-energy-neutron measurements on CORONAS-F during the solar flare of 28 October 2003," *Solar Physics*, vol. 268, no. 1, pp. 175–193, 2011.
- [36] S. Masson, K. L. Klein, R. Bütikofer et al., "Acceleration of relativistic protons during the 20 January 2005 flare and CME," *Solar Physics*, vol. 257, pp. 305–322, 2009.
- [37] I. A. Zhitnik, Y. I. Logachev, A. V. Bogomolov et al., "Polarization, temporal, and spectral parameters of solar flare hard X-rays as measured by the SPR-N instrument onboard the CORONAS-F satellite," *Solar System Research*, vol. 40, no. 2, pp. 93–103, 2006.
- [38] T. R. Metcalf, D. Alexander, H. S. Hudson, and D. W. Longcope, "Trace and Yohkoh observations of a white-light flare," *Astrophysical Journal*, vol. 595, pp. 483–492, 2003.
- [39] M. Siarkowski and R. Falewicz, "Variations of the hard X-ray footpoint asymmetry in a solar flare," *Astronomy and Astrophysics*, vol. 428, no. 1, pp. 219–226, 2004.
- [40] J. P. Raulin, V. S. Makhmutov, P. Kaufmann et al., "Analysis of the impulsive phase of a solar flare at submillimeter wavelengths," *Solar Physics*, vol. 223, no. 1–2, pp. 181–199, 2004.
- [41] V. S. Makhmutov, V. G. Kurt, B. Yu. Yushkov et al., "Spectral peculiarities of high energy X-ray radiation, gamma radiation, and submillimeter radio emission in the impulsive phase of a solar flare," *Bulletin of the Russian Academy of Sciences, Physics*, vol. 75, pp. 747–750, 2011.
- [42] J. Sato, Y. Matsumoto, K. Yoshimura et al., "Yohkoh/WBS recalibration and a comprehensive catalogue of solar flares observed by Yohkoh SXT, HXT and WBS instruments," *Solar Physics*, vol. 236, no. 2, pp. 351–368, 2006.
- [43] V. G. Kurt, S. I. Svertilov, B. Y. Yushkov et al., "Dynamics and energetics of the thermal and nonthermal components in the solar flare of January 20, 2005, based on data from hard electromagnetic radiation detectors onboard the CORONAS-F satellite," *Astronomy Letters*, vol. 36, no. 4, pp. 280–291, 2010.

- [44] K. Watanabe, Y. Muraki, Y. Matsubara et al., “Solar neutron event in association with a large solar flare on August 25, 2001,” in *Proceedings of the 28th International Cosmic Ray Conference*, pp. 3179–3182, Tsukuba, Japan, 2003.
- [45] S. N. Kuznetsov, V. G. Kurt, B. Y. Yushkov et al., “28 October 2003 flare: high-energy gamma emission, type II radio emission and solar particle observations,” *International Journal of Modern Physics A*, vol. 20, no. 29, pp. 6705–6707, 2005.
- [46] J. Kiener, M. Gros, V. Tatischeff, and G. Weidenspointner, “Properties of the energetic particle distributions during the October 28, 2003 solar flare from INTEGRAL/SPI observations,” *Astronomy and Astrophysics*, vol. 445, pp. 725–733, 2006.
- [47] G. Trottet, S. Krucker, T. Lüthi, and A. Magun, “Radio submillimeter and  $\gamma$ -ray observations of the 2003 October 28 solar flare,” *Astrophysical Journal*, vol. 678, pp. 509–514, 2008.
- [48] C. H. Miklenic, A. M. Veronig, and B. Vršnak, “Temporal comparison of nonthermal flare emission and magnetic-flux change rates,” *Astronomy and Astrophysics*, vol. 499, pp. 893–904, 2009.
- [49] J. W. Bieber, J. Clem, P. Evenson, R. Pyle, D. Ruffolo, and A. Sáiz, “Relativistic solar neutrons and protons on 28 October 2003,” *Geophysical Research Letters*, vol. 32, no. 3, article L03S02, 5 pages, 2005.
- [50] P. Kaufmann, J. P. Raulin, C. G. Giménez de Castro et al., “A new solar burst spectral component emitting only in the terahertz range,” *Astrophysical Journal Letters*, vol. 603, pp. L121–L124, 2004.
- [51] S. R. Kane, J. M. McTiernan, and K. Hurley, “Multispacecraft observations of the hard X-ray emission from the giant solar flare on 2003 November 4,” *Astronomy and Astrophysics*, vol. 433, no. 3, pp. 1133–1138, 2005.
- [52] P. Kaufmann, G. D. Holman, Y. Su et al., “Unusual emissions at various energies prior to the impulsive phase of the large solar flare and coronal mass ejection of 4 November 2003,” *Solar Physics*, vol. 279, pp. 465–475, 2012.
- [53] K. Watanabe, M. Gros, P. H. Stoker et al., “Solar neutron events of 2003 October–November,” *Astrophysical Journal*, vol. 636, pp. 1135–1144, 2006.
- [54] V. V. Grechnev, V. G. Kurt, I. M. Chertok et al., “An extreme solar event of 20 January 2005: properties of the flare and the origin of energetic particles,” *Solar Physics*, vol. 252, no. 1, pp. 149–177, 2008.
- [55] C. Bouratzis, P. Preka-Papadema, A. Hillaris et al., “Radio observations of the 20 January 2005 X-class Flare,” *Solar Physics*, vol. 267, no. 2, pp. 343–359, 2010.
- [56] V. V. Zharkova, N. S. Meshalkina, L. K. Kashapova, A. T. Altyntsev, and A. A. Kuznetsov, “Effect of a self-induced electric field on the electron beam kinetics and resulting hard X-ray and microwave emissions in flares,” *Geomagnetism and Aeronomy*, vol. 51, pp. 1029–1040, 2011.
- [57] C. Pei, J. R. Jokipii, and J. Giacalone, “Effect of a random magnetic field on the onset times of solar particle events,” *Astrophysical Journal*, vol. 641, pp. 1222–1226, 2006.
- [58] K. L. Klein, S. Masson, R. Miteva, S. Samwel, O. Malandraki, and G. Trottet, “The Sun–Earth connection of energetic particles,” *EAS Publications Series*, vol. 55, pp. 321–326, 2012.
- [59] S. Masson, P. Démoulin, S. Dasso, and K. L. Klein, “The interplanetary magnetic structure that guides solar relativistic particles,” *Astronomy and Astrophysics*, vol. 538, article A32, 14 pages, 2012.
- [60] C. Plainaki, A. Belov, E. Eroshenko, H. Mavromichalaki, and V. Yanke, “Modeling ground level enhancements: event of 20 January 2005,” *Journal of Geophysical Research A*, vol. 112, no. 4, article A04102, 16 pages, 2007.
- [61] V. G. Kurt, B. Y. Yushkov, and A. V. Belov, “On the ground level enhancement beginning,” *Astronomy Letters*, vol. 36, no. 7, pp. 520–530, 2010.
- [62] V. V. Akimov, N. G. Leikov, V. G. Kurt, and I. M. Chertok, “The GAMMA-1 data on the March 26, 1991 solar flare,” in *Proceedings of AIP Conference. High-energy solar phenomena—a new era of spacecraft*, vol. 294, pp. 106–111, 1994.
- [63] A. V. Belov and M. A. Livshits, “Neutron burst on May 24, 1990,” *Astronomy Letters*, vol. 21, pp. 37–40, 1995.
- [64] V. Kurt, B. Yushkov, A. Belov, I. Chertok, and V. Grechnev, “Determination of acceleration time of protons responsible for the GLE onset,” *Journal of Physics: Conference Series*, <http://conferenceseries.iop.org/content/home>. In press.

## Review Article

# Cosmic Ray Investigation in the Stratosphere and Space: Results from Instruments on Russian Satellites and Balloons

Yu. I. Logachev,<sup>1</sup> L. L. Lazutin,<sup>1</sup> and K. Kudela<sup>2</sup>

<sup>1</sup> Skobeltsyn Institute of Nuclear Physics, Lomonosov Moscow State University, 119991 Moscow, Russia

<sup>2</sup> Institute of Experimental Physics, Slovak Academy of Sciences, Watsonova 47, 04001 Kosice, Slovakia

Correspondence should be addressed to L. L. Lazutin; [lll@srd.sinp.msu.ru](mailto:lll@srd.sinp.msu.ru)

Received 31 August 2012; Accepted 26 November 2012

Academic Editor: Badruddin

Copyright © 2013 Yu. I. Logachev et al. This is an open access article distributed under the Creative Commons Attribution License, which permits unrestricted use, distribution, and reproduction in any medium, provided the original work is properly cited.

Selected activities aimed to investigate cosmic ray fluxes and to contribute to the understanding of the mechanisms behind, over a long-time period using space research tools in the former USSR/Russia and Slovakia, are reviewed, and some of the results obtained are presented. As the selection is connected with the institutes where the authors are working, it represents only a partial review of this wide topic.

## 1. Some Milestones until the Middle of the Last Century

The investigation of cosmic rays began in 1900-1901, more than 100 years ago. During the first ten years the researchers were not aware that what they were studying were cosmic rays. All began at the time of measurements of the conductivity of various gases including the air, when some “residual” ionization, that is, a weak “dark current,” was observed even without ionizing sources. First publications of those experiments relate to the period of 1900-1901 [1-3]. One of the first researchers of the “dark current” was Charles Wilson, well known as the inventor of Wilson chamber (1911), which was widely used for studying various types of radiation, including cosmic rays. Later, in 1927, Wilson received the Nobel Prize in physics for this finding. Thanks to those experiments it became clear that at sea level some not intense but strongly penetrating radiation is always present (which was also observed in strongly shielded chambers). At the beginning it was thought that the radiation is emanating from the soil, similarly to Earth’s radioactivity, and that is why it must be declining above the Earth’s surface. However, the radiation was decreasing just up to the altitude about one km, while above this level its intensity was increasing. The fact that radiation intensity increases with altitude was discovered in 1912 after by the experiments of the Austrian physicist Hess [4], who measured radiation by ionization chamber up

to more than 5 km. Hess called it “altitude radiation.” This name was used until 1925. The nature of that radiation was not clarified for a long time. Several hypotheses of its origin have been proposed (e.g., it originated in the upper layers of the atmosphere due to atmospheric electricity). Finally, the extraterrestrial origin of “altitude radiation” was proved by Millikan et al. (USA) in 1923-1924, who introduced the term “cosmic rays” [5, 6]. At that time Millikan was already awarded the Nobel Prize (in 1923 for the measurement of the charge of electron). Cosmic rays remained the “mystery effect” for a rather long time. This is argued by the fact that Nobel Prize for his discovery was awarded to Victor Hess in 1936 only, that is, 24 years after his experiments were performed.

In this short review a few selected milestones in the cosmic ray research are discussed, to which the authors of the present paper among many other scientists of the former USSR and Czechoslovakia contributed.

In 1926, physicists in Leningrad Myssowsky and Tuwim found that the intensity of cosmic rays was changing with the pressure of air. They discovered barometric effect of cosmic rays which is well known at present [7]. Skobelzyn in 1927 when working with a Wilson chamber put it into a magnetic field and found that cosmic rays at the sea level are composed of electrically charged particles of very high energy [8].

Starting from the 1920s, scientists in the former USSR began to deal with cosmic ray research intensively. Let us

mention the works of several groups in Leningrad, Kharkov, and Moscow. The basic successes of the groups are results of Myssowsky and his colleagues, Skobelzyn, and of the group of Vernov. The work in the former USSR was conducted along the same scientific directions as in other countries of the world, however, with some delay due to the tense international and domestic situation as well as to the complicated exchange of information during that time. Until the works of Myssowsky the dominant opinion was that the altitude radiation is close to the radiation of radioactive nuclei. Myssowsky and Tuwim in 1926 accomplished measurements of the absorption coefficient of the altitude radiation in the water at Lake Onega [9], which appeared to be by one order lower than that for gamma rays of Ra, indicating that the altitude radiation possesses much higher penetration ability as compared to gamma rays emitted by radioactive nuclei. These works, along with the experiments by Millikan and Cameron [10, 11] on the absorption of altitude radiation in water at various levels above the sea level led to the conclusion that the altitude radiation is coming to the ground from above and that it has a very high penetration ability.

In 1927, Skobelzyn found in a Wilson chamber inserted in magnetic field that a couple of tracks of relativistic particles were not bent by the magnetic field. He determined the energy of particles and came to the conclusion that these are particles of altitude radiation [8], which, according to Millikan, obtained the name “cosmic rays” [12].

In 1929, Skobelzyn published a paper where he showed that cosmic rays (CR) may create several particles, forming showers of cosmic rays [13]. After several years with the help of a Wilson chamber, controlled by the system of coincidence of detectors surrounding the chamber, various researchers obtained photographs of cosmic ray showers with high number of particles (see, e.g., [14]). The importance of the discovery of cosmic ray showers lies in the awareness of the fact of the processes in cosmic rays which do not exist in particle interactions at lower energies. Cosmic rays allowed to get in deeper into the structure of elementary particles and initiated the development of acceleration technique.

The third group of cosmic ray researchers was established and led by Vernov. It was especially that group which in the following period carried out the most exhaustive and numerous cosmic ray research in the USSR: on the ground, at mountain altitudes, in the stratosphere, and subsequently on satellites and other space vehicles. These investigations are shortly described below.

We should like to say few words about the leader of the works of the group—Sergey Nikolaevich Vernov (SNV, 1916–1982), who started his cosmic ray studies at the age just above 20. SNV was a student at Skobelzyn. He was familiar with the works and results of physicists in Leningrad, and he has seen how distinguished scientists deal with cosmic ray physics, and thus his choice proved quite appropriate. In the first half of 1930s only hypotheses about the primary cosmic rays existed, that is, particles accessing the Earth’s atmosphere from outer space. Thus, for understanding the nature of cosmic rays, experiments had to be performed closer to its source, near the boundary of the atmosphere. That is, why SNV decided to carry out measurements in the upper stratosphere. However,

on this way there was a serious difficulty because at that time the experimenters had no chance to raise instruments to high altitudes. That is, why experimental devices with automatic recording system have been developed which could provide measurements without human assistance.

The research of stratosphere was started also by other researchers and flights of stratostats began. Near Moscow on September 30, 1933, a stratostat named “SSSR-1” was launched and reached an altitude of 19 km. Astronauts helped by the electrometers of Hess and Kohlhoester measured cosmic ray intensity and confirmed the data about cosmic (extraterrestrial) origin of the rays and about the role of atmosphere in their attenuation. One of the flights of stratostats ended with tragedy—three astronauts died. Vernov found a solution for this problem—to transmit the results of measurements by radio waves. He utilized the experience of Leningrad’s professor P. A. Molchanov, who, in 1930, for the first time in the world constructed a radiosonde transmitting meteorological information by radio. SNV developed an instrument jointly with Molchanov and Mysovsky in 1934 and, for the first time, cosmic ray measurements in the atmosphere were transmitted to Earth by radio. The report of the Academy of Sciences of USSR for the year 1934 wrote that “experience with detection of cosmic rays was provided by the PhD student of Radio Institute Vernov.” The first automatic-adjusting flight of a radiosonde took place on April 1, 1935 [15, 16]. In the same year Vernov defended his PhD thesis on the subject “Investigation of cosmic rays in the stratosphere by means of radiosondes.” Academician S. I. Vavilov liked the thesis by Vernov and invited him for a doctoral study to FIAN (Physical Institute of Academy of Sciences) to continue his research of cosmic rays. This was the end of the research by Vernov in Leningrad. In 1935, he moved to Moscow where he continued working until his death.

By improving the method of measurement of cosmic rays on the stratospheric balloons, Vernov and Mironov conducted a successful study of the latitudinal effect of cosmic rays in the stratosphere in 1936–1938 at several sites: Leningrad, Yerevan, and in the region of the Equator [17]. For that purpose Vernov organized and led a nautical expedition. A tanker named “Sergo Ordzhonikidze” sailed from Odessa to Vladivostok and back and in the Indian ocean stratospheric balloons were flown from the board. Experiments made in the stratosphere have shown that the flux of cosmic rays near the Equator is by ~4 times lower than at high latitudes. This suggested that the magnetic field of the Earth reduces the intensity of cosmic rays and consequently, cosmic rays should consist of charged particles. Similar experiments were done somewhat earlier by Bowen et al. [18], which definitely proved that cosmic rays are not neutral particles as, for example, gamma quanta. First balloon observations showing the protons to be the main component of primary cosmic rays were by Schein et al. [19].

In that period Vernov’s group was concerned with the research of cosmic rays in the upper layers of atmosphere by means of instruments flown on radiosondes. In Figure 1 the moment of launch of the instrument on the garland of balloons is seen which required quiet conditions of the atmosphere and the known expertness to get rid of

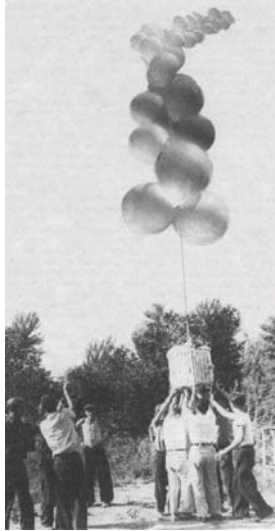


FIGURE 1: The moment of launch of the instrument for cosmic ray research on the garland of balloons.

the pendulum effect and avoid impact with neighboring structures.

The way in cosmic ray research by SNV was not easy. There were only a few experimental facts and they were frequently contradictory, so that his viewpoints were changing in accordance with the emerging new facts. First he supposed that cosmic ray particles have small mass so they are light particles like electrons. Later it appeared that the particles passing through materials are not behaving as electrons, as their “multiplication” is not described by quantum theory assuming even relativistic effects. SNV was moving towards the idea that primary cosmic rays are heavier, that is, protons, and proving it requires determining the charge of particles. This was done by using the geomagnetic field as a giant magnetic analyzer sensitive to the charge of analyzed particles. For that purpose an instrument was elevated into the stratosphere, where the effect is more pronounced, from the board of the research vessel “Vityaz.” The first flight confirmed the assumption about positive electric charge of primary particles, which, by augmentation during passage of atmosphere, produce secondary particles, that is, electrons [20].

At present the knowledge about the composition of primary cosmic rays is almost complete. We know that primaries consist of nuclei of all elements of the Mendeleev table, predominantly protons and alpha particles; however, oxygen and nuclei up to iron are also present, and very rarely, even uranium nuclei. We now know that cosmic rays arrive to the vicinity of Earth from distant space and that they bring negligible flux of energy ( $10^8$  times lower than that of solar light). We also know that individual particles can carry enormous energies (more than  $10^3$  times higher than those in the collider at CERN). We also know that these particles with enormous energy collide with the nuclei of the atmosphere producing extensive air showers, but no black holes. Cosmic

rays have been interacting with the Earth for millions of years and did not crash anybody.

Regular registration of cosmic rays in the stratosphere started in the former USSR in 1957 and is still running regularly till today. This allowed obtaining continuous long-time records of cosmic ray data, studying the mechanisms of primary cosmic ray interactions with the nuclei of atmosphere, finding that the Sun is also generating cosmic rays with somewhat lower energies than the primary galactic CRs. The year 1957 marked the start of the space era. SNV immediately used the new technical tool for cosmic ray studies. The takeoff of those investigations was amazing; the scientific group led by SNV accomplished more than 300 experiments onboard various spacecrafts. The weight of the developed scientific devices carrying out measurements in space, depending on the tasks and possibilities, ranged from 500 g to 10 tons. Some of these experiments have not been repeated, and in this paper they are mentioned shortly.

For the investigation of very high-energy particles SNV created a—for that time—huge equipment at the Lomonosov Moscow State University, consisting of hundreds of units placed over the territory of university campus, each of them with a complex device detecting each secondary particle produced in the Earth’s atmosphere by a primary particle. Such equipments have been installed later on in Yakutsk (in Moscow there was no sufficient area available) and in Samarkand (for better atmospheric conditions). In this manner SNV’s scientific activity splitted into three competitive directions: cosmic ray research in the atmosphere of Earth, in space, and on the ground. Due to his brilliant experience and large effort all three directions were successfully developed. More details about his papers and scientific results can be found in [20].

The experiments performed in the stratosphere and in space are shortly described below. The research of extensive atmospheric showers is not touched since the authors of the paper did not participate in that scientific direction.

## 2. Cosmic Ray Research on Artificial Satellites of Earth, on Other Spacecrafts, and in the Upper Atmosphere

*2.1. Galactic Cosmic Rays.* The preparation of experiments for satellites began in USSR in 1956. At a meeting of the Academy of Sciences of USSR a task was formulated for the leading specialists on upper atmosphere physics, magnetic field, ionosphere, and cosmic rays to give suggestions, that is, to create projects for experiments on artificial satellites of Earth. Academician Skobeltsyn, who participated in the meeting, authorized Vernov to conduct these activities. Along with one of the authors of the paper (Yu. I. Logachev), SNV stepped up to design and develop a device to detect cosmic ray particles. The trajectories of the first satellites were at altitudes of 300–1500 km. At these altitudes, beyond cosmic ray particles, particles trapped in geomagnetic field are present and form the radiation belts of Earth. However, during the development of the measuring device for the first artificial satellites of Earth, this was yet unknown and

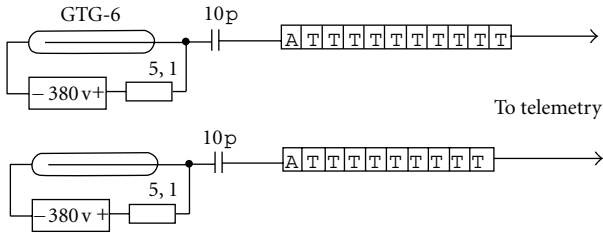


FIGURE 2: Block diagram of detectors and electronics placed onboard the second Soviet satellite. A: amplifier of the signal from counter, T: trigger of the reducer of count rate.

the apparatus was targeted only to cosmic ray research. Figure 2 shows the block diagram of the detectors and of the electronics for the instruments installed aboard the second Soviet satellite flown into orbit on November 3, 1957. The deadlines were tight, the technology was new, and naturally, the suggestions of the authors on the construction of the instrument were limited by very simple understanding: to utilize gas discharge counters and semiconductor electronics as detectors. Vernov fully supported these suggestions. Let us remark that presently rather sophisticated complex detector systems are working in space, utilizing practically all recent methods of particle detection: scintillation and semiconductor counters, magnetic spectrometers, track detectors, and their combinations. The orbital elements of orbit of the second Soviet artificial satellite were the following: altitude at perigee 225 km, at apogee 1670 km, and the apogee was located in the southern hemisphere at latitude  $\sim 45^\circ$ . The telemetry system was switched on 2 to 3 times per day along the parts of orbits passing over the territory of the USSR. The points of acceptance of telemetry information were deployed also above the territory of USSR. There were no memory elements onboard the satellite and thus the information about the cosmic rays encompassed only the latitudes and longitudes of the USSR and the altitudes in the range of 225 to 600 km.

The flight of the second satellite confirmed the existing pieces of knowledge about cosmic rays: the observed latitudinal and altitude dependence of cosmic ray intensity did not contradict data obtained earlier, and already on a single orbit an anomalously high counting rate of detectors was registered (Figure 3), which was interpreted to be due to the penetration of solar particles into the polar regions of the magnetosphere of the Earth. Later it became clear that on November 7, 1957, the satellite observed the precipitation of radiation belt particles into the upper layers of the atmosphere due to moderate geomagnetic activity [21, 22].

The discovery of the radiation belts of the Earth (RB) substantially changed the plans for future research works, pushing cosmic ray investigations aside. Nevertheless, in all possibilities, during the flights of various space vehicles, cosmic ray measurements were carried out as well. Space flights, where detectors of primary (galactic) as well as of solar cosmic rays were used, are as follows:

- (i) flights to the Moon;

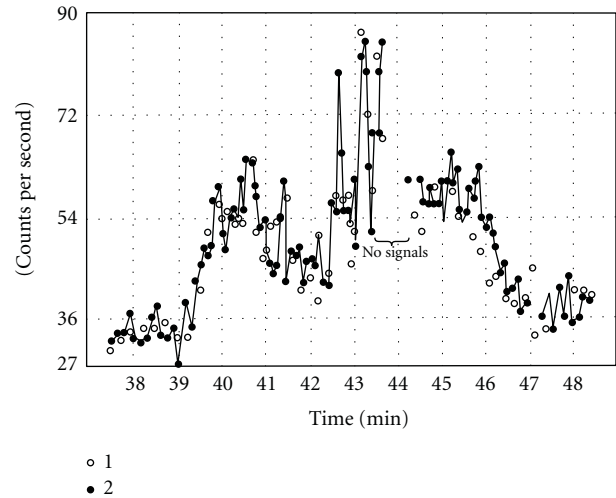


FIGURE 3: Variations of cosmic ray intensity along one of the orbits of the second satellite over the northern regions of the USSR. Nowadays it is clear that they were due to the precipitation of the particles from the outer radiation belt during geomagnetic activity. Numbers 1 and 2 correspond to the read-outs of the two detectors.

- (ii) interplanetary flights: to Venus, Mars, and interplanetary probes;
- (iii) heavy Proton satellites;
- (iv) selected satellites of the Cosmos series.

**2.1.1. Lunar Programme.** By the launch of three satellites and thus demonstrating the possibilities of cosmic technology of USSR, which was important during the nonquiet time period, it became necessary to provide new steps in the space programme, since the launch of just a few satellites would not induce large resonance. And the task number one became the Moon. It was necessary to send out a rocket to the Moon to demonstrate that Moon was reached. Also discussed were versions to explode an atomic bomb on the lunar surface. Fortunately, such suggestions did not find support. The first successful launch took place on January 2, 1959. The second one happened on September 12, 1959, and the third on October 4, 1959, exactly two years after the launch of the first artificial satellite of Earth. The task of the first two flights was to reach the surface of the Moon; the third was aimed to take photos of the reverse side of the Moon. Although the first space vehicle did not reach the Moon, it approached relatively close to its surface (5000 km). The second device reached the lunar surface, and before it crashed and destroyed by hitting the ground, it succeeded to measure the magnetic field and radiation in the vicinity of the Moon. The flight of that device was observed by the Jodrell Bank Observatory in UK. In Europe this was the only observatory which had a sufficiently large antenna capable to receive weak radiosignals. The Observatory confirmed the hit of the apparatus on lunar surface just in the computed time. The flight of lunar station and its “meeting” with the Moon on September 14, 1959, were absolutely important events in the history of space research and they became the triumph of

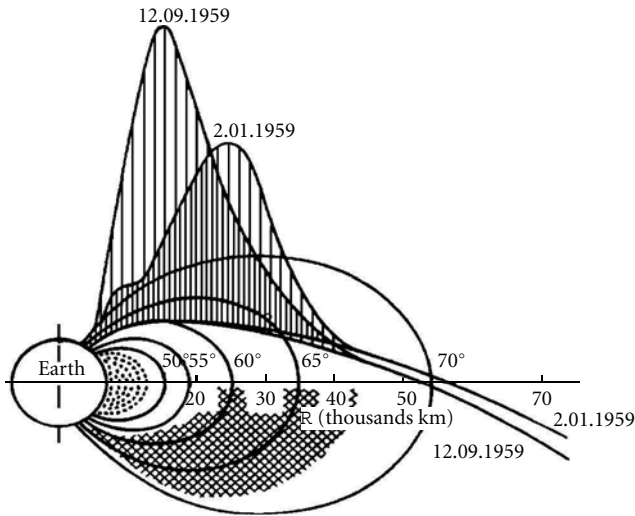


FIGURE 4: Ionization in NaI(Tl) crystal during the flights of the space Luna-1 (02/01/1959) and Luna-2 stations (12/09/1959) through the radiation belts of Earth.

the Soviet rocket and electronic technology. More details about the lunar flights can be found in [23].

The third device made snapshots of the lunar surface, and although not very bright, they were the first ever pictures of the reverse side of the Moon. It became clear that the reverse side of Moon is similar to the visible one; there were craters, seas, and other peculiarities as well. In the Atlas of the reverse side of the Moon issued, the peculiarities were assigned the names of important persons, who contributed to the discussions on origin of the Moon, to the new hypotheses, and so forth.

Aboard all the three of the Soviet lunar devices, named subsequently as Luna-1, Luna-2, and Luna-3, our scientific instruments were placed to measure cosmic ray particles and particles of radiation belts of Earth.

A particularly large complex of the instruments was put onboard the Luna-1 and -2 spacecrafts. Among the instruments there were scintillation and gas-discharged counters with various shieldings. The complex of devices of the first lunar missions is described in [24]. The main task of the flight of the station Luna-3 was to take photographs of the Moon and that is why the place and weight for other devices were very limited.

Aboard all the three lunar missions our device was working very well and interesting results were obtained. Along with the US probes Pioneer-1 and -3, the Soviet spacecrafts flew through the whole thickness of radiation belts and they determined the spatial distribution of the radiation at large distances from Earth and at slightly higher latitudes. In Figure 4 the dependence of ionization in the NaI(Tl) crystal is shown along the trajectory from the distance and latitudinal projections of geomagnetic field lines for Luna-1 and Luna-2 stations.

It is obvious that the two different flights at close trajectories have shown different structures of outer radiation belt, indicating the instability of the outer belt—temporal

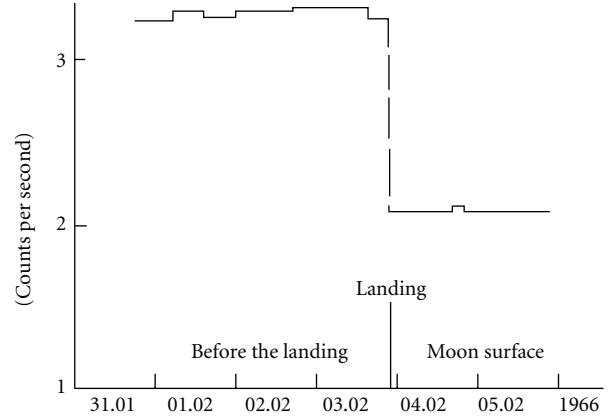


FIGURE 5: Radiation flux in the interplanetary space and on the lunar surface according to data of the gas-discharge counter onboard the station Luna-9.

variations of the particle fluxes within the trapping region. Measurements aboard Luna-1 for the first time allowed determining the altitude profile of the intensity of trapped particles along the geomagnetic field line. Luna-1 crossed the same geomagnetic field line three times, namely, at altitudes 8700, 11000, and 18250 km, respectively. At those altitudes the scintillation detectors observed the energy deposited in the crystal corresponding to 30, 65, and 145 GeV. Such values of energy deposition show that the altitude profile at larger distances from the Earth is weaker than that observed at low altitudes on the same field line; possibly the Earth's atmosphere plays a more important role in the losses of trapped particles.

This part of the lunar mission programme laid the foundations of the beginning of systematic research of the radiation belts of Earth, which was subsequently continued intensively using other space vehicles (Electron, Molnija, geostationary satellites, etc.). Onboard these satellites studies not only of radiation belts were carried out, but also the magnetosphere was explored in its complexity, including its structure, variations, relation to the solar activity processes, and other effects.

Later on the research of radiation belts of Earth was not conducted in the frame of lunar programmes which were targeted exclusively for studies of the lunar environment. The studies of the Moon, however, included also that of the fluxes of galactic and solar cosmic rays, the radioactivity of the lunar surface, and fluxes of lunar albedo particles, that is, secondary particles emitted from the surface due to the interaction of galactic and solar cosmic rays with nuclei of the materials of the surface. Such measurements were performed aboard all stations from Luna-4 through Luna-16 as well as during the flight of automatic interplanetary station Zond-3 (July–December 1965) which provided pictures of the reverse side of the Moon once again. Among the Luna missions a specific place belongs to the Luna-9 station which landed softly on the lunar surface on February 3, 1966. The results of our experiment operated there are depicted in Figure 5. The flux of cosmic rays in the interplanetary space should be two times

higher than on the lunar surface where the field of view of the instrument was lower by factor of 2 due to screening by the body of Moon. It appears that the surface flux was lower only by a factor of 1.6 instead of 2 as expected due to the radioactivity of the surface and the albedo cosmic ray particles. Based on these factors it was possible to estimate the radioactivity emission of the surface of Moon, which was found to be close to the radioactivity of the Earth's ground [25]. This result proved that there was no dangerous radiation on the lunar surface, and that a man can stay there for a long time without specific problems.

Speaking about the investigations of the Moon from a more general point of view, not only in the context of cosmic rays, it is necessary to recall the phenomenal success of US scientists accomplishing the first landing on the Moon and the safe recovery of all astronauts visiting the Moon to the Earth. For the first time man came to Moon in 1969 and after that the expeditions were repeated five times. There is an extended literature describing these activities. These flights have shown the theoretical possibility to establish scientific stations on the Moon for long-term operations, including cosmic ray observations as well. Cosmic ray research on the Moon would possess a number of substantial advantages in comparison with Earth-based research, since the Moon stays more than 80% of the time in the interplanetary space, and only 20% of the total time within the distant magnetospheric tail, where the shielding by the magnetic field is not significant. This means that measurements of cosmic rays by lunar satellites on the Moon or in its vicinity are not affected by the influence of Earth's magnetosphere, which is not the case of inner-magnetospheric satellites of the Earth flying even within the magnetospheric boundaries into near interplanetary space (Soviet Prognoz satellites, US IMP satellites, etc.). Because of that onboard all lunar space stations that landed on the Moon, on lunokhods, and on the artificial satellites of the Moon, instruments were installed for investigations of solar and galactic cosmic rays.

*2.1.2. "Proton" Satellites and Other Spacecrafts Studying Very High-Energy Cosmic Rays.* In the former USSR on the initiative of Vernov studies of cosmic rays were performed aboard heavy artificial satellites for the first time. It started with the 4 heavy satellites of the Proton series, which provided the first direct measurements of the energy spectra of all particles of cosmic rays up to energy  $10^{14}$  eV and measured the dependence of proton-proton interaction cross section in the range of  $10^{11}$ – $10^{12}$  eV.

In the sixties an intensive development and testing of new rockets took place both in the USSR and in the US. In the USSR, along with the rocket which launched into the space the first satellites of Earth and sondes towards Moon, in 1962, the rocket of the type Kosmos was constructed, and in 1965 the tests of a new rocket started which was at that time the most powerful one and was later used to launch heavy satellites not only of Russian production but also many satellites of other countries—rocket Proton. Its name was originated from the name of satellites of the type Proton launched by that rocket in 1965. The history of those launches

is the following: when the time for the tests of the new rocket capable to launch into the Earth's orbit approached several tons, two possible loads were discussed: several tons of sand or scientific instruments. Of course sand was the simpler load having no risk if the launch proved unsuccessful. Nobody at that time has constructed any scientific instrument of such weight so to launch a unique scientific instrument for the first testing flight was risky. What would happen if the launch fails? And the deadline of the flight was approaching; only less than a year remained. However, the Institute of Nuclear Physics of the Lomonosov Moscow State University suggested a scientific task, requiring to build the heavy device, and committed oneself to construct such apparatus by the required deadline (it was already hoped that people dealing with the construction of rockets would also be delayed). The scientific task consisted in the research of the energy spectra and composition of galactic cosmic rays in the energy range  $10^{11}$ – $10^{14}$  eV. The measurement of the energy of such particles requires its stopping within the volume of the detector system itself. Stopping the particles in the device allows determining their energy; however, the range of protons and production of secondary particles inside the system at such high energies is equivalent to the thickness more than a meter of iron; that is, the absorption requires a device of very large volume filled with heavy material (lead, iron, etc.). To accelerate charged particles to such high energies was impossible by means of accelerators in laboratories, and the planned experiments, aside the astrophysical tasks as measurements of energy spectra and of chemical composition of cosmic rays, were promising in the sense of nuclear physics aspects, as understanding the behavior of cross section of proton and/or nucleus-nucleus interactions of heavier elements at high energies.

At that time for the measurement of the energy of cosmic rays in ground-based experimental equipments ionization calorimeters developed earlier in USSR laboratories were widely used [26]. The same methodology was also applied on Proton satellites as well as on a couple of others, launched later on with the purpose of similar-type studies. The method of measurement was proposed by Grigorov et al. who led the research oriented on the construction of this type of devices and the analysis of data obtained [27]. Aboard Proton-1 satellite the device SEZ-14 was placed (an acronym of Russian words spectra, energy, and charge, up to  $10^{14}$  eV) weighing about 7 tons. The complex device SEZ-14, along with the calorimeter, included also charged particle detectors-ionization chambers and the target composed of graphite and iron, where the interactions with the material took place. The construction of SEZ-14 is schematically shown in Figure 6. Even for the Institute of Nuclear Physics of Lomonosov Moscow State University (Institute in what follows), the design and construction of such a complex device within the short time interval required an enormous effort. According to the instruction of headquarters (Vernov) to construct that apparatus all the resources of the Institute have been thrown up including financial ones. Almost the whole potential of mechanical workshops (and in 1960s it was by far not negligible) as well as the large group of electronic engineers

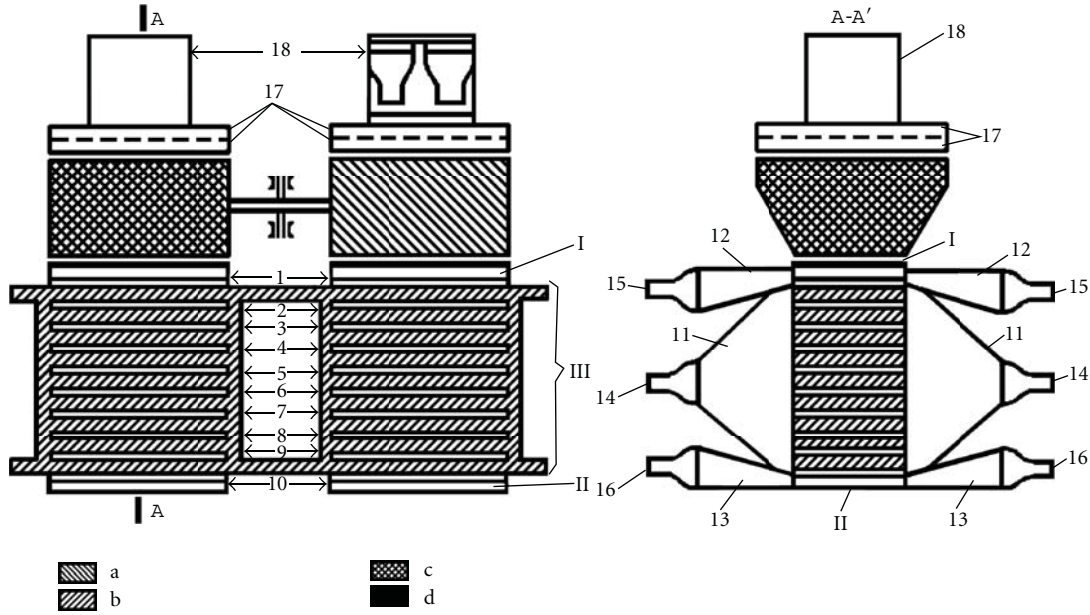


FIGURE 6: Schematic view of the device SEZ-14. I: detector of interactions; II: lower scintillation detector; III: ionization calorimeter; 1-10: scintillators of the detector of energy; 11: diffuser of the detector of energy; 12: diffuser of detector of interactions; 13: diffuser of lower scintillation detector; 14-16: photomultipliers; 17: charge detector (doubled proportional counter); 18: detector of the direction; a: absorber; b: iron; c: carbon; d: lead.

was involved in the work manufacturing the apparatus for Proton-type satellites. The authority of Vernov and Grigorov made it possible to prepare a prototype of the device SEZ-14 and of its basic elements (construction elements, fixation of the iron absorber) by utilizing the power of the construction department, where the rocket-carrier and the satellite itself were manufactured. This was a significant component of the successful “production” of the device; however, all the main questions of the equipment design were discussed and decided within the institute: the device was equipped by extensive electronics: for example, it involved several hundreds of pulse amplifiers. Never before the Proton satellites had such extensive and complicated devices been constructed and launched. The team of the institute accomplished a scientific record by constructing the device within a very short time—9 months. That device was operating for around 3 months in space without failure.

During the flights of Proton-1, -2, and -3 satellites a unique result about the change of the slope of the energy spectra of protons around  $2 \times 10^{12}$  eV was obtained. Until now this result has not been either confirmed or declined. At the same time the slope of the energy spectra of the sum of all cosmic ray primaries (protons, He, heavier elements) remained without that break, in agreement with the results of other indirect measurements. If the spectra of protons were really bent with significant change of the slope, that would mean that in the high energy part of the spectra of primary cosmic rays a significant change of chemical composition of primaries with enrichment of heavy elements had to take place, since the fraction of protons at high energies is negligibly small. This means that corrections in the mechanisms of acceleration in the source must be included,

requiring predominant acceleration of nuclei with  $Z > 2$ . The importance of those conclusions is evident; however, it is desirable to have higher confidence in this respect.

To confirm that result and to shift towards the measurements at higher energies, a new device with a 10 times larger geometric factor named IK-15 (ionization calorimeter up to  $10^{15}$  eV) was constructed for Proton-4. However, the results from Proton-4 did not give unambiguous result about the spectral break of the proton spectra. A couple of more flights with the device (Table 1) could provide no clear reply to that question either.

The methodological reasons of the change of slope of energy spectra may lie in the nature of the energetic particles themselves, namely, in the so-called reverse flux in the detector of charge—“converting” the event of detection of proton into an event of particle with higher charge which may reduce the count rate of protons. The importance of this effect increases with energy. The analysis of tracks in photo emulsions exposed to cosmic rays aboard Intercosmos-6 was done in collaboration with other laboratories; one of them was IEP SAS Kosice.

To cope with the reverse flux, in the device named SOKOL (acronym from the Russian words of the main target of the experiment—composition of cosmic rays) directional Cherenkov detectors with small dimensions were used to measure protons and alpha particles. Such devices were working on Cosmos-1543 and Cosmos-1713 satellites launched 10 years after the Proton satellites (Table 1). This allowed eliminating the effect of reverse flux when determining the charge. Furthermore, the passage of the particle through the device was visualized, so that it was possible to set off the particles as well as the electromagnetic cascades produced by

TABLE 1: Earth orbiting satellites with measurements of high-energy cosmic rays.

Satellite	Year	Device	Weight of device (in tons)	Time of active work in space	Comment
Proton-1	1965	SEZ-14	7	3 months	
Proton-2	1965	SEZ-14	7	3 months	
Proton-3	1966	SEZ-14	7	3 months	
Proton-4	1968	IK-15	12,5	8 months	
Intercosmos-6	1972	Photoemulsions	2,4	4 days	Device returned to the Earth
Cosmos-1543	1984	SOKOL	2,4	27 days	
Cosmos-1713	1986	SOKOL	2,4	25 days	

them in the alignment of the device. This approach allowed determining the energy of particle with better confidence.

The experiments aboard Cosmos-1543 and Cosmos-1713 with the SOKOL device confirmed that this device reduced the effect of reverse flux effectively. However, no unambiguous reply to the main question about the shape of primary proton spectra was achieved because the operational time of the satellites was less than one month and the statistics of protons obtained were insufficient to draw substantiated conclusions. In order to obtain a conclusive settlement about that important question the launch of a similar experiment with longer time measurement in space is required. Up to now no such experiment has been carried out yet. As an alternative the experiment ATIC that runs in the frame of international collaboration on balloons detecting cosmic rays at high altitudes over Antarctica may be considered [28, 29]. Figure 7 exhibits the energy spectra of C, O, and the Fe group. By fitting the spectra with power law the index is  $\gamma = 2.5$ . Nearly the same slope is obtained for the energy spectra of He nuclei. The ratios of cosmic ray fluxes at different energies characterizing the composition of particles at a particular energy are practically the same as those at low energies. This means that in the frame of that approximation, the cosmic ray composition remains practically the same throughout the energy range of 1 GeV/nucleon to 1000 GeV/nucleon. At higher energies there are indications for the enrichment of heavy nuclei in galactic cosmic rays.

Let us mention that these experiments allowed increasing the observed energies of cosmic rays up to about 2 TeV/nucleon for C and O nuclei. The statistical errors in this energy range are still large. Such type of measurements has to be continued to accumulate better statistics, especially at high energies. Using the SOKOL equipment for this aim is an adequate approach for this task: it is necessary to enhance the duration of the measurements by factor of 10–20, which is fully possible with using the existing tools of space technology. Along with that, the institute prepared proposals for a couple of new experiments qualified to move to even higher energies of cosmic rays aboard satellites [30, 31]. The experiments described in the aforementioned publications are now under discussion and they are planned to be accomplished in nearest years. On satellites Cosmos-1543 and Cosmos-1713 He, C, O, and Fe nuclei were also observed in the energy range of 50–1000 GeV/nucleon [32].

Important data on primary cosmic rays have been obtained recently from the experiment Pamela installed on

the Resurs-DK1 satellite launched onto a low altitude nearly polar orbit in June 2006. More details about that mission, international collaboration, and publications can be found at <http://pamela.roma2.infn.it/index.php/>. The description of the experiment can be found, for example, in [33]. The recent results of the ATIC and PAMELA experiments prove that the spectra of protons and He are different and have peculiarities at energies of several hundred GeV/n (e.g., [34]). The new results do not seem to confirm the Proton findings. Nevertheless, the Proton results stimulated investigations enormously.

In the Pamela mission the increase of the fraction of positrons in electron-positron component of cosmic rays with increase of energy, ratio  $J_+/J_+ + J_-$ , was discovered [34]. This might be a signature for the existence of dark matter. Or, alternatively, another additional source of positrons may exist producing them with efficiency increasing with the energy. The data on the positron component are reliable thanks to the high statistical accuracy of the measurements. The spectrometer has a permanent magnet and separation of electrons and positrons is reliable. The energy of particles is measured sufficiently accurately with the help of the calorimeter. The excess of positron fraction and its increase with energy has been confirmed recently in the Fermi mission [35].

*2.2. Solar and Galactic Cosmic Rays at Lower Energies.* One of the admirable properties of galactic cosmic rays is the relative stability of their intensity in time. Above this “background” sudden strong increases of cosmic ray intensity related to powerful processes on the Sun were observed. It became clear that from time to time the Sun generates strong fluxes of energetic particles; they received the name solar cosmic rays (SCR). Powerful solar energetic particle (SEP) events appear relatively rarely, while less powerful ones are observed more frequently, as it is usual for nature.

The first observations of SCRs have been carried out with the help of instruments on the ground sensitive only to higher primary energies (>1 GeV). Experiments on balloons in the stratosphere could observe particles with a lower energy threshold (>100 MeV). Measurements at high altitudes utilizing satellites and other space vehicles allowed to observe less powerful effects, and until now more than 1000 SEP events with energetic particle emissions connected to solar flares have been registered. While the first observed events of energetic particles have been related to effects of very high power and still those could only be detected with

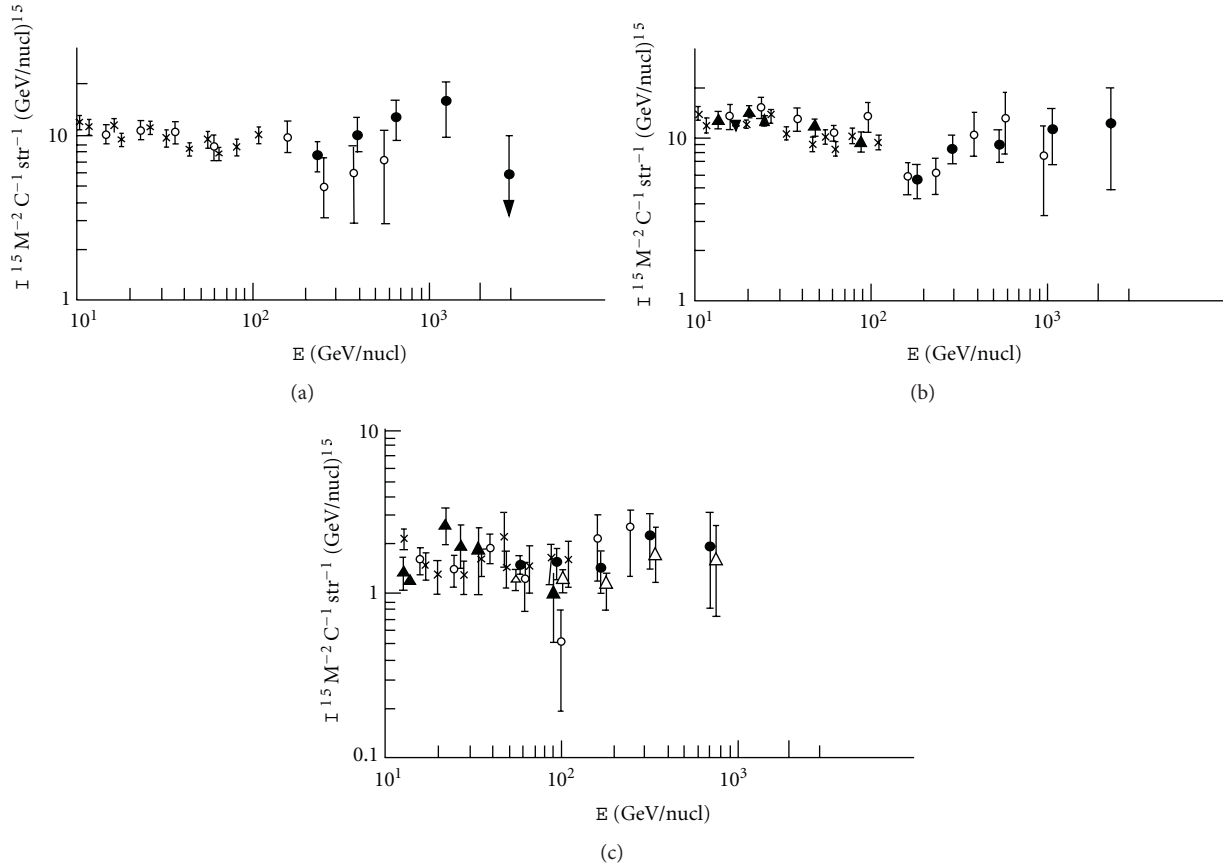


FIGURE 7: Energy spectra of carbon C (a), oxygen O (b), and iron Fe (c) nuclei at high energies according to the results of flights equipped with the complex device SOKOL.

ground-based devices, nowadays instruments on satellites and space probes allow observing practically all increases of SCR flux reaching the vicinity of Earth. At present they remain unnoticed only in a few cases of small SEP events on the reverse hemisphere of Sun, from which energetic charged particles cannot reach the Earth's orbit or an interplanetary probe. To exclude these gaps it is proposed to "patrol" the space around the Sun at various heliolongitudes including the reverse hemisphere of the Sun. The solar mission STEREO is already fulfilling this programme.

Usually, the energy of accelerated solar particles does not exceed 10 MeV/nucl (1 MeV for electrons). Such SEP events during the solar activity maximum occur about once per week. The associated particles are observed beyond the magnetospheric boundaries, within its peripheral regions or in the polar cap. Less frequently, typically once a month flares accelerating particles up to energies  $\sim 100$  MeV/nucl and higher are observed. Such particles penetrate into the atmosphere of Earth in the polar latitudes and can be observed during the flights of high-altitude balloons. In even more rare events, observed typically once per year, particles are accelerated to 1 GeV. Extremely powerful SEP events, occurring 2-3 times per 11-year cycle of solar activity, are characterized by very high fluxes of accelerated particles with a maximum energy 10 GeV or even more. Most frequently

they are observed by neutron monitors distributed all over the world.

### 2.2.1. Ground-Based Observations of CR Variability and SCR.

The interplanetary magnetic field (IMF) is partly screening the flux of galactic cosmic rays. This shielding effect, especially at lower energies, is varying in time and thus the cosmic ray intensity observed near the Earth is temporary variable. Both regular and quasiperiodic (e.g., diurnal,  $\sim 27$  day,  $\sim 11$  year) variations are connected with solar activity and provide information about the structure of interplanetary magnetic field and on the solar wind in the heliosphere. More detailed reviews on cosmic ray variations can be found in [36, 37] and in monographs [38, 39]. The research of cosmic ray variations requires long-time series of homogeneous measurements. The first instrument devoted to this task was the ionization chamber developed and constructed by A. Compton in 1934. In USSR the measurements of cosmic ray flux with purpose to study its variations started in 1936 by Yu. G. Shafer in the Yakutsk Pedagogical Institute with an independently constructed ionization chamber—electrometer. These works have been broken by the World War, in which Shafer went through the fighting course from Stalingrad to Berlin, and he recovered the measurement of cosmic rays in 1947 in the Yakutsk Institute of Space Physics and Aeronomy by building



FIGURE 8: Neutron monitor in Yakutsk.

the ionization chamber named ASK. By this instrument the network of stations over the whole territory of USSR was equipped.

Before and during the International Geophysical Year (1957) the whole world network of cosmic ray stations was equipped by neutron monitors (NMs) developed by J. Simpson in 1948. Such equipments were installed also in USSR, for example, in IZMIRAN (Troitsk, near Moscow), at Apatity (Polar Geophysical Institute), where the measurement is continuous until present. One of NMs operating in Russia until now is seen in Figure 8.

A neutron monitor consists of the group of proportional counters. Two types of counters are used, namely, those filled with gas having a high concentration of the isotope  $^{10}\text{B}$  or  $^3\text{He}$ . The counters are surrounded by the moderator serving to slow down the neutrons before entering the counter and also to reflect low-energy neutrons. The moderator is inserted into the lead producer surrounded by the outer moderator-reflector. This rejects unwanted low-energy external evaporation neutrons produced in the local environment. During the years the neutron monitor design has been changed. First the IGY monitors were used and in some places they are still in use. For that the moderator and reflector material is paraffin. In 1964, the network of neutron monitors with larger counting rate, named supermonitors (NM64), replaced the original IGY NMs in many places.

The network of NM64 in the USSR was created under the leadership of Vernov while the main role in the construction work was done by I. N. Kapustin, the engineer in Polar Geophysical Institute. The NM64 monitor has a low-density polyethylene moderator and reflector. The differences are also in geometry and tubes. More information about neutron monitors can be found, for example, in [39].

High mountain NMs having higher statistics play an important role. One of them was constructed at Lomnický štít (2634 m above sea level, High Tatra mountains, run by IEP SAS, one of the authors—K. Kudela—is the PI of it since 1982) during IGY as a contribution of Czechoslovak physicists to IGY activity. It is operating until now (data are available at <http://neutronmonitor.ta3.sk/>). Let us mention just one result: since 1950s it was assumed that solar protons accelerated to high energies and interacting with residual solar atmosphere can produce neutrons which can

be detected even at the Earth's orbit. After 30 years, during the solar flare on June 3, 1982, the increase corresponding to solar neutrons at two high altitude NMs in central Europe, namely, at Jungfraujoch and at Lomnický štít, been observed in coincidence with satellite measurements of increased flux of high-energy gamma rays reported by E. L. Chupp. The high statistical accuracy of the measurements (5 min resolution at that time) at Lomnický štít contributed to that finding [40, 41]. Selected results obtained with use of that NM are presented in [42].

**2.2.2. SCRs Observed on Balloons.** The measurements of SCRs on balloons are filling the energy gap of 100–1000 MeV between those observed by ground-based devices and on satellites and space probes. The first SCRs in the stratosphere were registered independently in the US, Minneapolis, Fort Churchill, and in USSR, Murmansk, in 1958. Regular measurements in the stratosphere in USSR started in 1957 by the group of A. N. Charakhchyan in Moscow (Dolgoprudnyj), in the vicinity of Murmansk and episodically in Yakutsk and Tixie (Yu. G. Shafer, V. D. Sokolov, and A. N. Novikov) as well as in Simeiz, Crimea (Stepanyan). Later on, from 1962, regular flights of radiosondes began in Apatity (L. L. Lazutin, one of the authors). The measurements have been conducted during short-time flights on rubber balloons by radiosondes with the use of two Geiger counters; a short pulse was transmitted to the Earth in the case of single detector count; longer pulse meant the coincidence of two counters. A metallic shield was placed between the counters to register charged particles in two energy channels. The needle of the barograph interrupted the transmission on seven contacts—serving for the measurement of residual pressure of air above the balloon. Figure 9 shows the scheme of radiosonde RK-2 by A. N. Charakhchyan using valves, which were replaced later by semiconductors in all devices of regular measurements in Moscow, Mirnyj, and Apatity. Figure 10 shows the results of measurement—the altitude profile in the coincidence channel during four solar flares with SCR emission. Figure 11 shows the moment before the launch of radiosonde of cosmic rays in Apatity observatory.

Along with the measurements of SCRs described shortly above, regular stratospheric measurements of cosmic rays are running with the purpose to check cosmic ray variations at different depths in the atmosphere by the group at the Lebedev Physical Institute of Russian Academy of Sciences, Moscow (G. V. Bazilevskaya and Yu. I. Stozhkov). Figure 12 exhibits such registrations [44, 45].

**2.2.3. SCR Observed on Satellites and Space Probes.** In the USSR, Vernov established the service of continuous monitoring of cosmic rays in the upper layers of the atmosphere—daily launches of the same type of device in Moscow, Apatity, and sometimes also in the southern part of the country (region of Alma-Ata). Along with that, during each flight of the satellites where it was possible to put the scientific device measuring cosmic rays, such device was installed on board. By this way the detection of solar and galactic cosmic rays

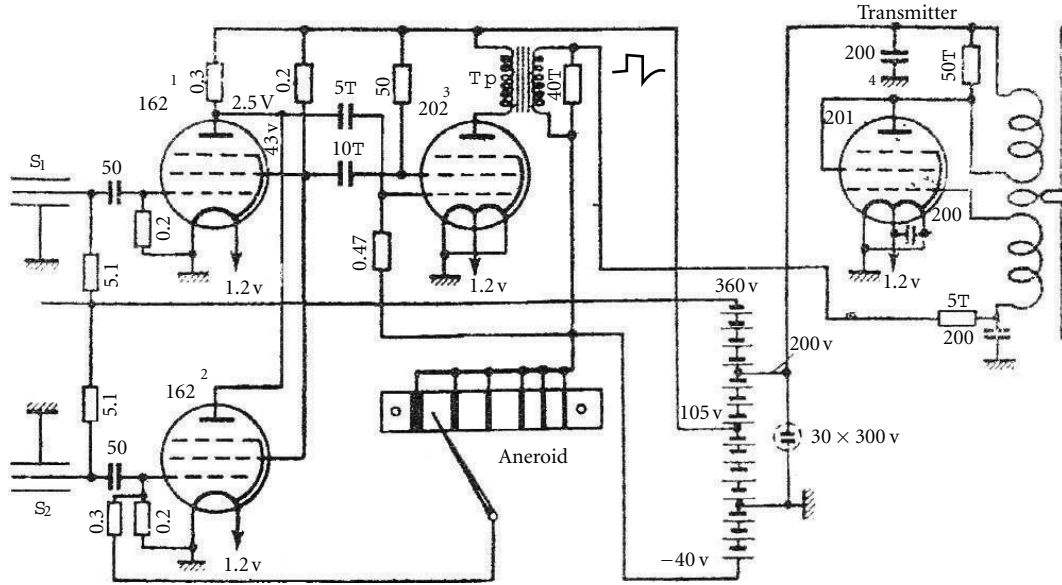


FIGURE 9: Electronic block diagram of the experiment measuring cosmic rays on a radiosonde.

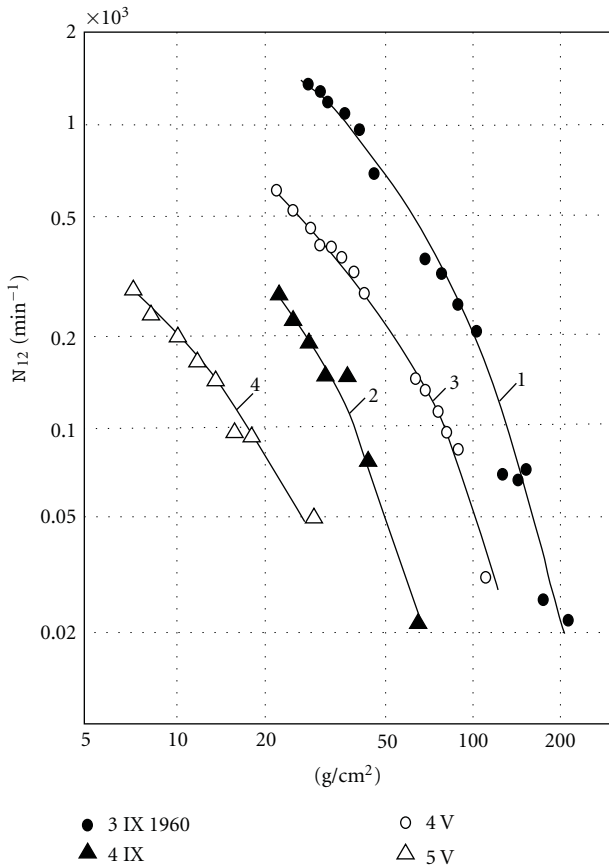


FIGURE 10: The counting rates (per min) of coincidence pulses versus altitude (in atmosphere pressure) of two GM tubes on radiosondes during four different SEP events [43].

was conducted during all flights to Venus and Mars as well as during the flights of several Zond interplanetary stations.



FIGURE 11: Academician B. M. Pontecorvo visiting the launch site of radiosondes in Apatity before one of the launches.

Particularly successful was the flight of Venera-4, where the measurement of cosmic rays was performed over the whole route. This was a period of enhanced solar activity (1967) and the devices observed a large number of solar energetic particle events. During the subsequent flights to Venus many measurements were carried out; however, the flight of Venera-4 was the most impressive because it was the first really successful and interesting information that was obtained over a long-time period including the landing on Venus.

In the majority of events the particle increases at relatively low energies were not intense. Thus, they were observable only outside the magnetosphere. In particular, low inclination satellites could not see them because of geomagnetic field filtering. Aboard Venera-4 protons and heavier nuclei were detected using two identical semiconductor detectors that looked into opposite directions and thus allowed to observe partial spatial anisotropy. If the particles are emitted by

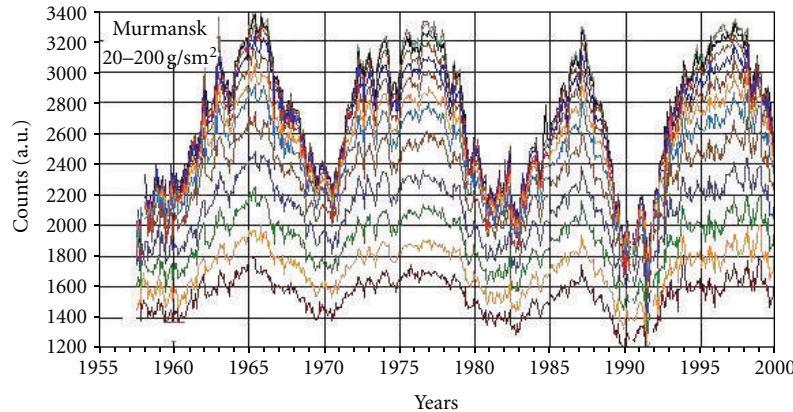


FIGURE 12: Temporal profile of cosmic ray intensity measured over Murmansk since 1957 at different depths of the atmosphere [44, 45].

Sun, their motion is directed by the field lines of IMF approximated by an Archimedean spiral (with an angle of about  $45^\circ$  to the sunward direction at 1AU). These field lines are not smooth—irregularities of various dimensions are superimposed on them, and charged particles are scattering on the irregularities, sometimes changing direction of velocity to the opposite. Due to such scattering during their lengthy stay in the IMF, particles “forget” their initial direction of motion, and their angular distribution becomes nearly isotropic. Thus, in such cases the anisotropy is equal to zero. The flight of the space probe Venera-4 has shown that such situation is found relatively frequently; however, at the same time the devices looking toward the Sun observed much higher particle fluxes over several hours in comparison with those looking in the opposite direction (Figure 13). This means that in the given events the Sun emitted rather large fluxes of particles over an extended time period, sometimes up one day, and the lines of IMF controlling their motion were sufficiently smooth. This way these particles propagated without scattering, so that there was low number of particles flowing from the opposite direction. Such picture corresponds to a high positive anisotropy of particle fluxes from solar flares. Such type of events was later observed quite often; they obtained the name of SEP events without scattering; however, Venera-4 was the first space probe which observed these phenomena. Now it has become clear that the anisotropy of solar flare particles in the interplanetary space is developing in general quite regularly. First the anisotropy is sufficiently high and it is directed from the Sun along the interplanetary field lines, later it is decreasing and becomes radial, and finally, the angular distribution takes a form with maximum flux perpendicular to the field lines, which is connected with the drift of charged particles in the crossed electric and magnetic field (the electric field arises due to motion of the magnetic field line together with the solar wind plasma).

The previous flights around Venus did not give a reply to the question about existence of the trapped radiation in its vicinity. Venera-4 has shown that near Venus there is no trapped radiation even at the smallest distances to its surface: when the device was approaching the surface the radiation

was not increasing but even decreasing in accordance with geometry (because of the screening by the solid body of Venus). This important result is in agreement with the lack of noticeable magnetic field of Venus measured by the team of IZMIRAN during the same mission.

Data from Venera-4 have shown that while the Sun produces charged particles with large diversity, it also creates conditions in the interplanetary space that control the motion of the particles in the heliosphere. Those particle fluxes which are observed along the Earth’s orbit or in another point of space are determined by both the conditions of the source (solar flares) as well as by the properties of interplanetary medium, which they pass through on their way from the Sun to the periphery of heliosphere. The propagation of particles brings significant “corrections” into their fluxes: at the Earth’s orbit we do not observe identical temporal profiles of the fluxes of accelerated particles, the energy spectra formed at the site of their generation changes, part of the accelerated particles is not escaping from the Sun, and so forth. Let us treat, for example, the instant generation and outflow of particles from the solar surface. In the simplest case of diffusive propagation of particles, an extended time profile will be observed on the Earth’s orbit (so-called diffusional wave, Figure 14): high-energy (high velocity) particles arrive first, later followed by lower energy particles, and so forth. The comparison of observed temporal profiles of particle fluxes with computed ones assuming diffusion indicates that sometimes particles are released really instantaneously on the Sun and propagate further diffusively, as it is, for example, in the flare on November 22, 1977, and in the couple of other cases.

The Prognoz satellites started to be launched in 1972, constructed to study SCRs and in particular to develop a method for forecasting powerful solar flares, representing estimates of radiation hazard during space flights. Table 2 gives basic information about the satellites Prognoz launched in USSR.

We must admit that the primary task of the Prognoz project—to obtain reply on the question about the causes of solar flares and to elaborate the method of the prediction of solar flares with potential of radiation hazards—was not

TABLE 2: Dates of launch and orbits of the satellites Prognoz—measurements out of the magnetosphere.

Satellite	Date of launch	Initial apogee altitude ( $10^3$ km)	Orbital period (days)	Time of active operation (months)
Prognoz-1	14.04.1972	$\approx 200$	$\approx 4$	4,4
Prognoz-2	29.06.1972	$\approx 200$	$\approx 4$	5,5
Prognoz-3	15.02.1973	$\approx 200$	$\approx 4$	12,5
Prognoz-4	22.12.1975	$\approx 200$	$\approx 4$	2,5
Prognoz-5	25.11.1976	$\approx 200$	$\approx 4$	7,8
Prognoz-6	22.09.1977	$\approx 200$	$\approx 4$	5,3
Prognoz-7	30.10.1978	$\approx 200$	$\approx 4$	6,8
Prognoz-8	25.12.1980	$\approx 200$	$\approx 4$	8,8
Prognoz-9	01.07.1983	$\approx 720$	$\approx 27$	8,0
Prognoz-10	26.04.1985	$\approx 200$	$\approx 4$	9,3

achieved. However, it gave an opportunity to step forward in the understanding of some acceleration processes and especially of propagation of accelerated particles in the interplanetary medium, in the research of recurrent particle fluxes, and other phenomena. A summary of the results of the experiments can be found in proceedings [46, 47]. Below we list some important results obtained with the help of satellites Prognoz.

*Protons Are Accelerated in All Flares.* It was shown that in all solar flares both accelerated electrons of relatively low energy ( $>40$  keV) and protons appear (on satellites Prognoz protons with  $>1$  MeV were measured). This fact enabled to exclude the term “electron flares” from the terminology which supposed that flares accelerate electrons exclusively. Until the flight of the Prognoz satellites this opinion was widely accepted and it was assumed that particle acceleration in such flares is due to betatron mechanism which has a low efficiency for the acceleration of heavy particles. It was shown that for all flares detected on Prognoz satellites, including the weakest events, electrons were accompanied by protons [48]. Further research showed that the energy spectra of electrons and protons are similar if represented as dependence on kinetic energy of particles and this requires a mechanism completely different from betatron acceleration.

*Coherent Propagation of Particles.* An unusual mode of fast propagation of particles was discovered: in a narrow angular interval near the magnetic field line connected to the region of flare, electrons are propagating practically without scattering, that is, conserving their angular distribution along most of their path from the Sun to the Earth. This assures high velocity of their motion through space. During propagation such a “bubble” of particles generates radiowave emission of type III, for which the frequency depends on the density of medium where the propagation takes place. This mode of propagation was named coherent. On Prognoz satellites the coherent propagation was observed also for protons [49, 50].

Detecting the coherent propagation of particles is difficult, since to cross a narrow beam of the particles has low probability. Such an event on the Earth’s surface takes place just for 10–20 min, and subsequently, the beam flowing over the space vehicle is stretched along the field line only at 0.5–1 AU. Near the Sun the beam has even smaller dimensions,

because due to propagation in space it is broadening. Furthermore, for the existence of energetic particle “huddles” there are necessary specific conditions in space, sufficient smoothness of the magnetic field and its focusing in the ecliptic plane.

*Energy Spectra of Protons in the Interplanetary Space during Quiet Sun.* In the absence of intensive particle fluxes accelerated at the Sun, that is, in periods of quiet Sun, there are low fluxes of energetic particles in interplanetary space still exist. The origin of such particle fluxes has not been identified for a long time. Before the launch of Prognoz satellites the energy spectra of protons and other particles was known only above 500 keV/nucleon. If one artificially extrapolates energy spectra of protons from 500 keV towards lower energies (Figure 15), such spectra will coincide with the solar wind one. Thus, it was natural to assume that the observed spectra of protons and heavier particles are just the continuation—a tail—of the solar wind particles. The nonthermal character of this tail was assumed because with using the Gaussian distribution of solar wind protons with measured temperature ( $10^4$  K) the proton flux would decrease so sharply with energy that it is impossible to speak about any agreement with the observed proton flux at energies 0.5–1 MeV—the difference would be several orders of magnitude. In this case the energy spectra of particles during quiet time another minimum should appear in the energy range about 30–100 keV. It would be interesting to find such a minimum its existence would have principal implication because it would separate populations of different nature, that is, having different origin.

*The Interplanetary Medium during Periods of Quiet Sun.* Studies of variations of solar particle flux suggested that the interplanetary space in each given period of time is in a certain dominant (characteristic) state, to which it tends to recover after various disturbances. Such a dominant state is controlled by the magnetic field of the Sun and by solar wind, which in general are not changing very frequently. On the average one can assume that during low solar activity the structure of the interplanetary medium remains stable for 1–2 or more solar rotations. The structure of interplanetary medium is closely associated with various active regions on the Sun, thus affecting the properties of the interplanetary medium in the solid angle formed by the magnetic field lines flowing out from active regions. The structure near the Sun

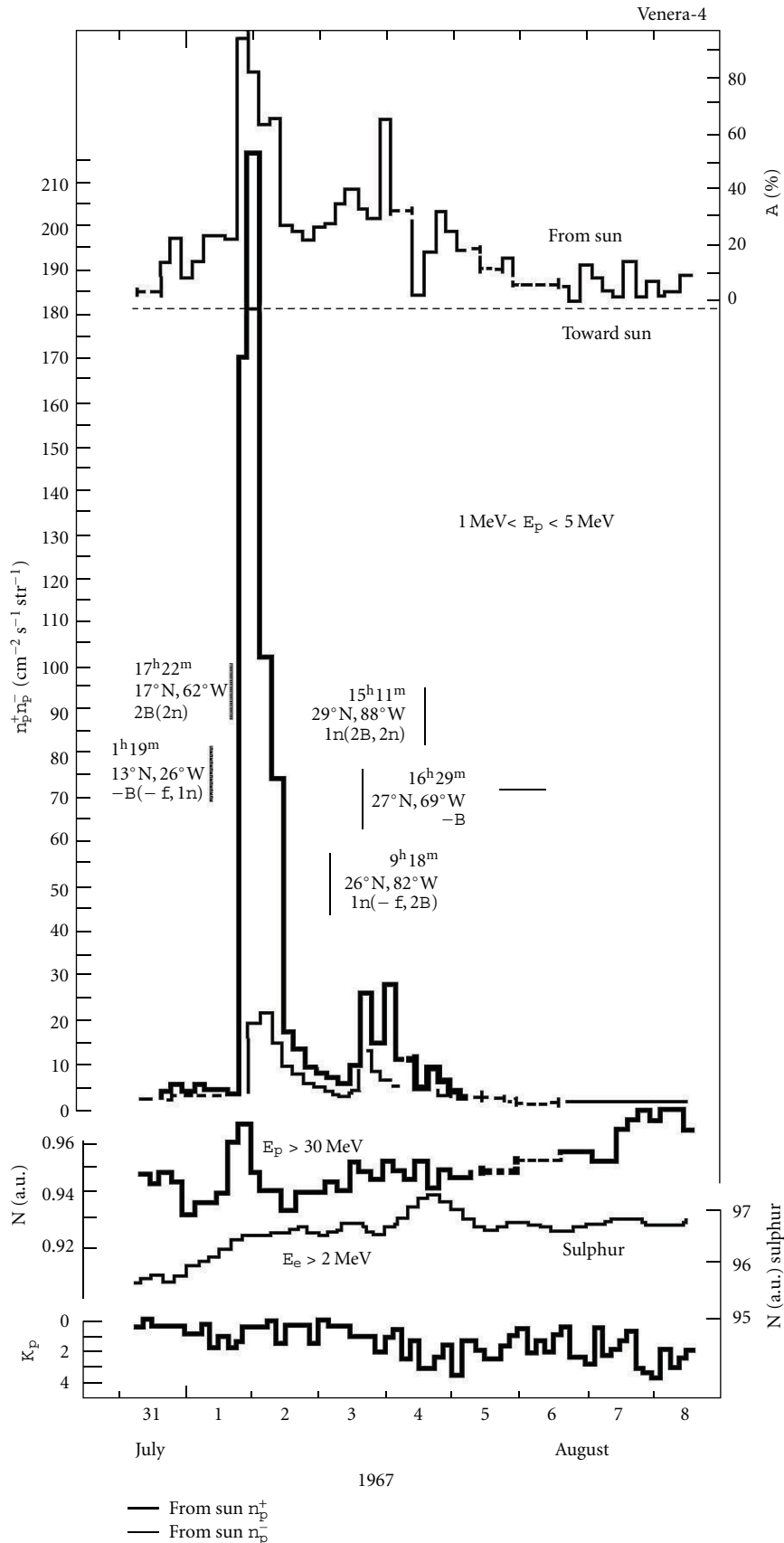


FIGURE 13: Fluxes of particles from a couple of solar flares during July-August 1967, according to the measurement of instrument AMS aboard Venera-4. Upper curves indicate the anisotropy of protons with  $E_p > 1 \text{ MeV}$ . The thick line represents the proton flux from the Sun; the thin one is toward the Sun.

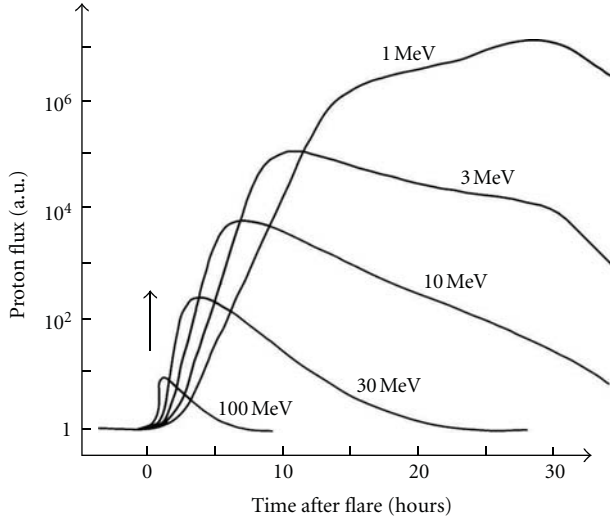


FIGURE 14: Sketch of the diffusional wave of solar protons—temporal profiles of various energy proton fluxes at 1 AU for impulsive acceleration at the Sun at 1 AU.

is bound to its surface and is rotating together with that. This is clearly observed in the solar particle fluxes at various time scales. In the Prognoz 1 and 2 data the fine structure of interplanetary medium was clearly demonstrated. The Prognoz satellites registered the long-lasting quasi-stationary structure of interplanetary medium as well. This emerges from the rate of decay of solar particle fluxes in events associated with flares after reaching the diffusive maximum. The decay rate is an independent feature of the extent of disturbance of the IMF and solar wind velocity. It was found out that for the majority of solar particle increases ( $>1$  MeV) during the year 1972 the decay followed the exponential law with the same characteristic time of about 16 hours [51]. Even after the largest solar flares in 1972 when the interplanetary space was disturbed due to passage of strong shock waves, just after a few days all characteristics recovered to their original state and the characteristic time of decay rate was again about 16 hours (Figure 16).

The decay phase of the SEP event after the maximum contains information about solar wind velocity, turbulence of the IMF, and other parameters of the interplanetary medium. The level of disturbance of IMF is one of the main factors of the state of interplanetary medium characterized by the diffusion coefficient of particles in the medium, and the solar wind velocity determines the form of temporal profile of particle flux, the rate of its increase, and decay after maximum.

Various models of particle propagation predicted various shapes of the decay profile during the late stage of the event. The temporal profile of particle flux in solar events usually has a characteristic form. At 1 AU for a SEP event connected with a single flare, the particle flux has a rather fast onset, reaching the maximum and subsequently decreasing to the level before the event. Events with a picture adequately described by diffusion approximation are frequently observed. In such cases, assuming an impulsive injection of particles (the time of

generation is much shorter than the transit time to the site of observation), the temporal profile  $J(t)$  in the decay phase has a power-law profile and the flux is proportional to  $t^{-3/2}$ . For prolonged injection, one has to assume an injection function of particle source leading thus to the prolongation of the event; however, it is negligibly reflected on the late stage of the event.

If the influence of the solar wind is essential, the convective outflow of particles and their adiabatic cooling may be important. Then the decay form can be approximated by  $J(t) \sim e^{-t/\tau}$  [52–55]. Power law works sufficiently well for high-energy particles ( $>100$  MeV). For lower energy particles ( $<10$  MeV), however, the convective outflow process begins to play much more important role, and the decay becomes exponential. It turns out that in the majority of solar energetic particle events, lower energy ( $<10$  MeV) proton fluxes decay exponentially, while at 30–60 MeV the convective outflow, although less pronounced, is observed too. Often the particle propagation is accompanied by various processes of additional acceleration which leads to the modification of the “smooth” temporal profile so that decay cannot be described by any single functional form. Apart from sufficiently frequent observations of events with exponential decays, in many studies until now no adequate attention has been paid to that form of intensity decrease.

If in the decay phase of the SEP event convective outflow of particles and adiabatic cooling dominate over the diffusion, for the characteristic time of decay the following relation was found [52]:

$$\tau = \frac{3r}{2V(2 + \alpha\gamma)}, \quad (1)$$

where  $V$  is solar wind speed,  $\gamma$  is the index of energy spectra of particles,  $r$  stands for the distance of the site of observation to the Sun, and  $\alpha \approx 2$  for nonrelativistic particles. The analysis performed indicates that in a considerable fraction of events (up to 50%), when  $V$  remained constant during the whole decay phase,  $\tau$  is satisfactorily well described by the above expression.

Due to rotation of the Sun, real measurements carried out near the Earth take place in different flux tubes, where the magnetic conditions are usually different. In some cases the stability of particle fluxes along the longitudes is observed only over a short-time period. In such cases two devices located within a small angular distance (sometimes  $\leq 10^\circ$ ) observe entirely different fluxes. At the same time, relatively frequently, same conditions for particle propagation appear over a wide latitudinal extent, what is confirmed by simultaneous measurements of different space devices. In such cases the particle fluxes are constant over the large angular extents (even up to  $>100^\circ$ ) [56].

Long-term studies, including almost three full solar activity cycles, have shown that for a remarkable fraction (almost half of the solar energetic particles events), the value  $\tau$  for energies 1–10 MeV is 16–20 hours, in agreement with the above formula for the typical values of the parameters involved. This means that the interplanetary medium remains in the state corresponding to the same value of  $\tau$  during these

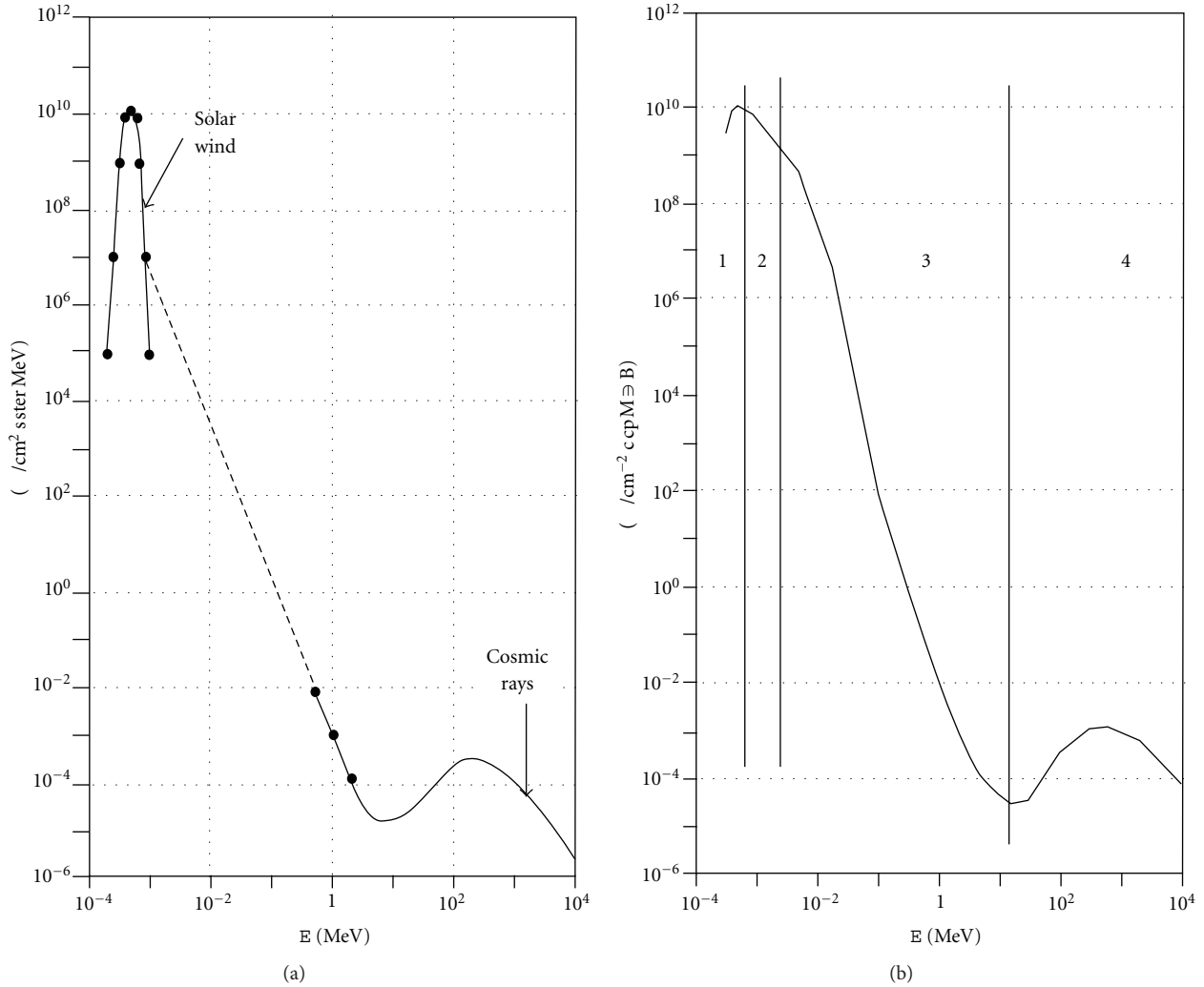


FIGURE 15: Energy spectra of protons at 1 AU during quiet Sun according to understanding in 1970s (a) and at present (b). 1: solar wind, 2: suprathermal particles, 3: energetic particles of solar origin, 4: galactic cosmic rays. One of the tasks of the Prognoz-3 satellite consisted of measurements of particle flux at energies as close as possible to the energies of solar wind particles. The experiment conducted allowed to measure spectra during the quietest periods within the active interval of Prognoz-3. Energy spectra were measured down to 30 keV and the minimum of the proton flux was found. Presently it is clearly confirmed that there are no peculiarities in the energy spectra of particles in the energy range between energetic particles ( $<1 \text{ MeV}$ ) and solar wind. The energy spectra of protons measured in quiet time period of the Sun according to recent observations are shown in (b).

time periods. Around 20% of events have larger values of  $\tau$  reaching sometimes 50 hours or more [57].

*Recurrent Solar Particle Fluxes.* The flights of the first two Prognoz satellites took place in the period of decreasing solar activity, and the devices on board often observed recurrent fluxes of particles in the interplanetary space, that is, fluxes persisting over long-time periods, which were rotating together with the Sun. Several different series of such type of fluxes were observed, their characteristics obtained, and it was shown that a part of them was connected with the Sun. The most interesting was the conclusion that if an active region emits recurrent fluxes of particles, the energy is not accumulated within the region, and consequently there is no need to release superfluous energy by an explosive manner. This means that no solar flares are taking place there [58].

A further study of recurrent fluxes has shown that they are most frequently connected with the so-called coronal holes—regions with lower level of emission in soft X rays, which are also the sites of origin of high-speed solar wind.

Long intervals of stationary conditions in the interplanetary space can be found during the periods of low solar activity due to recurrent fluxes of low-energy particles having the spatial structure saved over the extended period of time. Recurrent fluxes sometimes exist over several rotations of the Sun, which was observed several times on Prognoz satellites as well [59]. The longest one comprised 26 solar rotations in the declining phase of the solar cycle 21 [60].

In addition, it turns out that not only recurrent increases of fluxes are observed, but recurrent minima corotating along with the Sun as well. We named these deep decreases of

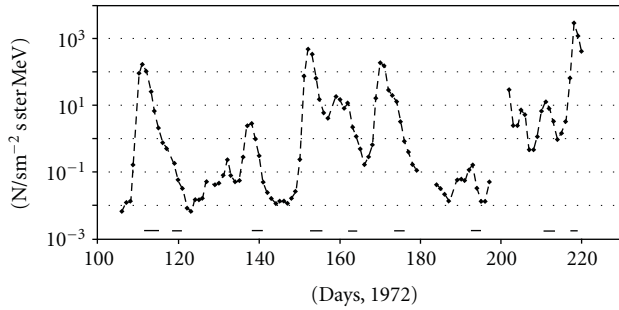


FIGURE 16: Fluxes of solar protons observed on Prognoz-1. Within 70 days eight increases of SCRs were observed with exponential decay profiles (energy  $E_p \approx 1$  MeV) of nearly identical characteristic times  $\tau = 16.5$  hours. This provides an evidence of long-term (more than two solar rotations) stationary state of the interplanetary medium in the inner heliosphere.

particle intensity as “canyons” (due to the similarity of the spatial structure of fluxes with those in the ground canyons). Figure 17, constructed using IMP-8, Pioneer-11, and Voyager-1 and -2 space probe data, is illustrating that [61].

Such regions of minimum fluxes corotating with the Sun arise due to the existence of constant background fluxes of particles at some minimum level in the heliosphere. During periods of high solar activity the background fluxes are overlapped and they can only be observed during quiet Sun periods, but even that is limited to the observations in some of the sectors of space surrounding the Sun.

*Radiation Dose from Solar Flares.* For two powerful solar flares, namely, August 4 and 7, 1972, the radiation dose was determined in the interplanetary space from Prognoz satellite measurements [62]. The dose obtained outside of the Earth’s magnetosphere was significantly higher than that observed on Earth’s orbiting satellites. This is important for the interplanetary missions as well as missions towards the Moon.

*High-Energy Gamma Rays and Neutrons from Solar Flares.* IEP SAS, Kosice, started satellite measurements of cosmic rays and energetic particles in the cooperation with SINP Moscow and with other institutes in the frame of the Interkosmos programme in 1977. Before that period IEP SAS participated in magnetospheric energetic particle studies by data analysis since the flight of low-altitude satellite IK-3 in 1971, with the instrument constructed at Charles University in Prague. This scientific direction later continued also experimentally and included measurements aboard Prognoz-type satellites too (Intershock, Interball). It has contributed to the understanding of mechanisms important for the identification of sources, transport, and losses of particles within the magnetosphere as well as in the vicinity of its boundary regions like the magnetopause and bow shock as well as in the geomagnetic tail. These scientific tasks are out of scope of this paper. A short summary before 2003 can be found, for example, in [63], and a later review is in [64].

Around 1975, a small experimental group was established at IEP SAS developing electronics and later also completing devices for the measurement of energetic particles in the

interval of energies well above those of solar wind but below the typical energies of cosmic rays. Important works in electronics were done by J. Rojko († 2011). One of the authors (K. Kudela), along with organizing measurements on satellites, was dealing with data analysis and its physical interpretation, together with other colleagues (L. Just † 2008, M. Slivka, and others), in cooperation with colleagues in the institutes of the former USSR/Russia and in other countries. This cooperation, based on data obtained from Russian satellites, was significantly enhanced after 1989, by the possibility to collaborate also with colleagues in the US, west Europe, Japan, and so forth.

The first device for measurement in space with participation of IEP SAS was the SK-1 developed jointly with Ioffe Physico-Technical Institute in Leningrad and launched in 1977 aboard the IK-17 satellite. The task was to detect neutrons of solar origin in the vicinity of Earth. Although solar neutrons were not detected, this experiment measured the flux of cosmic ray albedo neutrons and gamma rays at different latitudes in detail [65]. In collaboration with SINP MSU the devices SONGs were constructed (IEP SAS was responsible for the electronic box) for the detection of high-energy neutrons and gamma rays [66]. These devices were in operation onboard the low-altitude polar orbiting CORONAS-I (1994) and CORONAS-F (2001–2005) satellites. CORONAS-F mission: was Especially productive several solar flares with high-energy gamma ray emissions were detected with energy spectra up to  $>100$  MeV as well as with solar neutrons (e.g., [66, 67]), indicating the acceleration of protons in these flares up to very high energies. They also provided information about the interaction of accelerated protons with the residual solar atmosphere (the production of neutral pions with their subsequent decay into two gamma quanta of high energies) as well as showing the timing of acceleration which is in some cases seen as a precursor before the onset of GLE (ground level events) observed by neutron monitors [68, 69].

### 3. Conclusion

In the conclusion we emphasize that the past 100 years of cosmic ray research allowed to move substantially in understanding the nature of cosmic rays, in clarifying the crucial moments of its generation and propagation in the heliosphere and in Galaxy as well as in understanding the role of the Sun and of the planets in the formation of radiation conditions in the vicinity of the Sun. Apart from the fact that substantial progress in space physics and cosmic ray physics was achieved, there are a number of questions which are not clarified yet. Some of the main open problems are as follows:

- (i) the form of the energy spectrum of cosmic rays at very high energies ( $>10^{20}$  eV/nuc);
- (ii) the change of composition with energy above  $10^{17}$  eV/nuc;
- (iii) the determination of the composition of nonmodulated cosmic rays at relatively low energies ( $<10$  GeV),

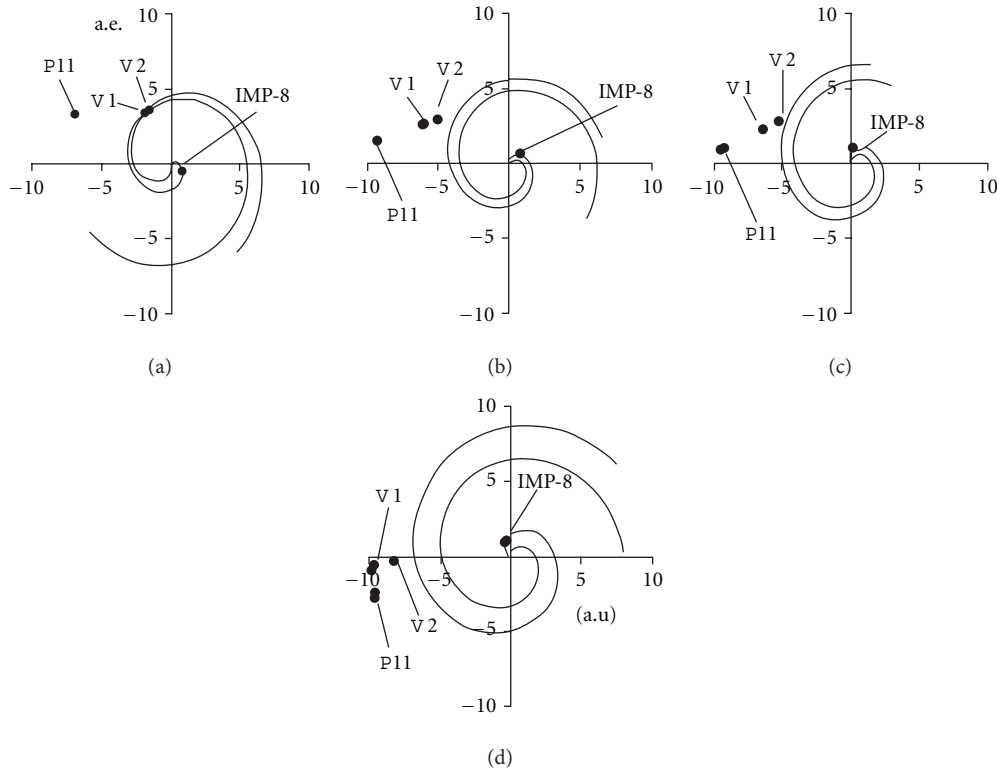


FIGURE 17: Spatial structures, bordered by spirals of IMF and comprising decreased fluxes of low-energy protons ( $E_p \sim 1$  MeV), projected onto the ecliptic plane. Time periods from left to right: August 22–September 04, 1978; October 29–November 09, 1979; December 06–23, 1979; January 05–23, 1981. The spirals were calculated from solar wind velocities measured on IMP-8 at the beginning and at the end of intervals with “caverns”—intervals with low fluxes of protons.

that is, in the interstellar medium beyond the heliospheric border;

- (iv) the influence of cosmic rays on the weather and climate on Earth;
- (v) Forecasting radiation hazardous flares with high flux of SCRs putting obstacles for interplanetary propagation of space technology and living organisms.

## Acknowledgments

The authors thank Professor G. V. Bazilevskaya and Dr. K. Kecskemety for the valuable advices. K. Kudela wishes to acknowledge VEGA grant agency Project 2/0081/10 for support.

## References

- [1] J. Elster and H. Geitel, “Weitere Versuche über die Elektrizitätszerstreuung in abgeschlossenen Luftmengen,” *Zeitschrift für Physik*, vol. 2, p. 560, 1900.
- [2] C. T. R. Wilson, “On the leakage of electricity in the dust-free air,” *Proceedings of the Cambridge Philosophical Society*, vol. 11, p. 32, 1900.
- [3] C. T. R. Wilson, “On the ionization of atmospheric air,” *Proceedings of the Royal Society of London*, vol. 68, pp. 151–161, 1901.
- [4] V. F. Hess, “Über beobachtungen der durchdringenden Strahlung bei sieben Freiballonfahrten,” *Zeitschrift für Physik*, vol. 13, pp. 1084–1091, 1912.
- [5] R. A. Millikan and I. S. Bowen, “Penetrating radiation at high altitudes,” *Proceedings of the American Physical Society*, p. 198, 1923.
- [6] R. A. Millikan and R. M. Otis, “High frequency rays of cosmic origin II. Mountain peak and airplane observations,” *Physical Review*, vol. 27, no. 6, pp. 645–658, 1926.
- [7] L. Myssowsky and L. Tuwim, “Unregelmässige Intensitätsschwankungen der Höhenstrahlung in geringer Seehöhe,” *Zeitschrift für Physik*, vol. 39, no. 2-3, pp. 146–150, 1926.
- [8] D. Skobelzyn, “Die Intensitätsverteilung in dem Spektrum der  $\gamma$ -Strahlen von Ra C,” *Zeitschrift für Physik*, vol. 43, no. 5-6, pp. 354–378, 1927.
- [9] L. Myssowsky and L. Tuwim, “Versuche über die Absorption der Höhenstrahlung im Wasser,” *Zeitschrift für Physik*, vol. 35, no. 4, pp. 299–303, 1926.
- [10] R. A. Millikan and G. H. Cameron, “High altitude tests on the geographical, directional, and spectral distribution of cosmic rays,” *Physical Review*, vol. 31, no. 2, pp. 163–173, 1928.
- [11] R. A. Millikan and G. H. Cameron, “High frequency rays of cosmic origin III. Measurements in snow-fed lakes at high altitudes,” *Physical Review*, vol. 28, no. 5, pp. 851–868, 1926.
- [12] B. B. Rossi, *Cosmic Rays*, McGraw-Hill, New York, NY, USA, 1964.
- [13] D. Skobelzyn, “Über eine neue Art sehr schneller  $\beta$ -Strahlen,” *Zeitschrift für Physik*, vol. 54, no. 9-10, pp. 686–702, 1929.

- [14] P. M. S. Blackett and G. Occhialini, "Some photographs of the tracks of penetrating radiation," *Proceedings of the Royal Society*, vol. 139, pp. 699–726, 1933.
- [15] S. Veibnoff, "Radio-transmission of cosmic ray data from the stratosphere," *Nature*, vol. 135, no. 3426, pp. 1072–1073, 1935.
- [16] S. N. Vernov, "On the study of cosmic rays at the great altitudes," *Physical Review*, vol. 46, p. 822, 1934.
- [17] S. N. Vernov and A. V. Mironov, "Investigation of cosmic rays in stratosphere near the magnetic equator," *DAN (Reports of the Academy of Sciences)*, vol. 23, pp. 138–140, 1939.
- [18] I. S. Bowen, R. A. Millikan, and H. V. Neher, "New light on the nature and origin of the incoming cosmic rays," *Physical Review*, vol. 53, pp. 217–223, 1938.
- [19] M. Schein, W. P. Jesse, and E. O. Wollan, "The nature of the primary cosmic radiation and the origin of the mesotron," *Physical Review*, vol. 59, no. 7, p. 615, 1941.
- [20] S. N. Vernov, N. L. Grigorov, N. A. Dobrotin et al., "Estimation of primary cosmic ray particle charge by measurements of the azimuthal asymmetry in stratosphere near the equator," *DAN (Reports of the Academy of Sciences)*, vol. 68, pp. 235–255, 1949.
- [21] S. N. Vernov, I. Yu. Logachev, N. L. Grigorov, and A. E. Chudakov, "Study of cosmic radiation on board 2 AES," *DAN (Reports of the Academy of Sciences)*, vol. 120, pp. 1231–1233, 1958.
- [22] S. N. Vernov, "Chudakov A.E Study of cosmic rays by rockets and satellites in USSR," in *Proceedings of the 2nd International Conference on Peaceful Exploration of Nuclear Energy*, vol. 1, pp. 267–271, Atomizdat, 1957.
- [23] B. E. Chertok, *Rockets and Peoples*, vol. 4, Lunar Race PTCoft, Moscow, Russia, 2007.
- [24] P. V. Vakulov, E. V. Gorchakov, and Yu. I. Logachev, "Earth radiation belts, study by soviet artificial satellites and space rockets in 1957–1959," *Kosmicheskie Luchi*, no. 6, pp. 1–115, 1965.
- [25] S. N. Vernov, P. V. Vakulov, E. V. Gorchakov et al., "Measurements of the penetrating radiation on the Moon surface," *DAN (Reports of the Academy of Sciences)*, vol. 169, no. 5, pp. 1044–1047, 1966.
- [26] N. L. Grigorov, V. S. Murzin, and I. D. Rapoport, "Method of the measurements of particles with energy higher than 1011eV," *Journal of Experimental and Theoretical Physics*, vol. 34, no. 2, p. 506, 1958.
- [27] N. L. Grigorov, V. E. Nesterov, and I. D. Rapoport, "Study of the energetic spectra and composition of primary cosmic rays of high and extrahigh energy range by ISZ Proton 1 and 2," *Cosmic Research*, vol. 5, no. 3, p. 395, 1967.
- [28] V. I. Zatsepin, J. H. Adams, H. S. Ahn et al., "Rigidity spectra of protons and helium as measured in the first flight of the ATIC experiment," in *Proceedings of the 28th International Cosmic Ray Conference (ICRC '03)*, vol. 4, p. 1829, 2003.
- [29] T. G. Guzik, J. H. Adams, H. S. Ahn et al., "The energy spectra of protons and helium measured with the ATIC experiment," *Advances in Space Research*, vol. 33, no. 10, pp. 1763–1770, 2004.
- [30] G. K. Garipov, B. A. Khrenov, M. I. Panasyuk et al., "UV radiation from the atmosphere: results of the MSU "tatiana" satellite measurements," *Astroparticle Physics*, vol. 24, no. 4–5, pp. 400–408, 2005.
- [31] I. P. Ivanenko, V. Y. Shestoporov, L. O. Chikova et al., "Energy spectrum of cosmic ray different components with energies higher than 2 TeV measured by SOKOL device," *Izvestiya Rossiiskoi Akademii Nauk, Seriya Fizicheskaya*, vol. 57, no. 7, pp. 76–79, 1993.
- [32] N. L. Grigorov and E. V. Tolstaya, "On the direct cosmic ray measurements up to  $10^{16}$  eV on low weight satellite," *Vestnik of MSU*, vol. 3, no. 6, pp. 27–30, 1997.
- [33] V. Bonvicini, G. Barbiellini, M. Boezio et al., "The PAMELA experiment in space," *Nuclear Instruments and Methods in Physics Research A*, vol. 461, pp. 262–268, 2001.
- [34] O. Adriani, G. C. Barbarino, G. A. Bazilevskaya et al., "PAMELA measurements of cosmic-ray proton and helium spectra," *Science*, vol. 332, no. 6025, pp. 69–72, 2011.
- [35] M. Ackermann, M. Ajello, A. Allafort et al., "Measurement of separate cosmic-ray electron and positron spectra with the Fermi Large Area Telescope," *Physical Review Letters*, vol. 108, Article ID 011103, 2012.
- [36] K. Kudela, "On energetic particles in space," *Acta Physica Slovaca*, vol. 59, no. 5, pp. 537–652, 2009.
- [37] K. Kudela, "Variability of low energy cosmic rays near earth," in *Exploring the Solar Wind*, M. Lazar, Ed., InTech, 2012.
- [38] L. I. Dorman, *Cosmic Ray Variations*, Moscow Neutron Monitor, Moscow, Russia, 1957.
- [39] J. W. Bieber, E. Eroshenko, P. Evenson, E. O. Flückiger, and R. Kallenbach, "Cosmic rays and earth," *Space Science Reviews*, vol. 93, no. 1–2, pp. 1–409, 2000.
- [40] E. Yu. Efimov, G. E. Kocharov, and K. Kudela, "On the solar neutrons observation on high mountain neutron monitor," in *Proceedings of the 18th International Cosmic Ray Conference (ICRC '83)*, vol. 10, pp. 276–278, Bangalore, India, 1983.
- [41] H. Debrunner, E. O. Flückiger, E. L. Chupp, and D. J. Forrest, "The solar cosmic ray neutron event on June 3, 1982," in *Proceedings of the 18th International Cosmic Ray Conference (ICRC '83)*, vol. 4, pp. 75–78, Bangalore, India, 1983.
- [42] K. Kudela and R. Langer, "Cosmic ray measurements in High Tatra mountains: 1957–2007," *Advances in Space Research*, vol. 44, no. 10, pp. 1166–1172, 2009.
- [43] G. A. Bazilevskaya, V. S. Makhmutov, Y. I. Stozhkov, A. K. Svirzhetskaya, and N. S. Svirzhovsky, "Solar proton events recorded in the stratosphere during cosmic ray balloon observations in 1957–2008," *Advances in Space Research*, vol. 45, no. 5, pp. 603–613, 2010.
- [44] Y. I. Stozhkov, N. S. Svirzhovsky, G. A. Bazilevskaya et al., "Cosmic rays in the stratosphere in 2008–2010," *Astrophysics and Space Sciences Transactions*, vol. 7, pp. 379–382, 2011.
- [45] G. A. Bazilevskaya, M. B. Krainev, V. S. Makhmutov et al., "Solar Proton Events registered at stratosphere experiment of FIAN," *Geomagnetism and Aeronomie*, vol. 43, pp. 442–452, 2003.
- [46] *Problems of Solar Activity and PROGNOZ Space System*, Nauka, Moscow, Russia, 1977.
- [47] *Problems of Solar Activity and PROGNOZ Space System*, Nauka, Moscow, Russia, 1984.
- [48] M. Zeldovich, V. G. Kurt, I. Yu. Logachev et al., "Discovery at 1 a.u. of proton fluxes  $E_p > 1$  MeV associated with small solar flares," *Cosmic Research*, vol. 15, no. 3, pp. 485–488, 1977.
- [49] V. G. Kurt, Y. I. Logachev, and N. F. Pissarenko, "Coherent propagation of non-relativistic solar electrons," *Solar Physics*, vol. 53, no. 1, pp. 157–178, 1977.
- [50] N. N. Volodichev, G. Y. Kolesov, A. N. Podorolsky, I. A. Savenko, and A. A. Suslov, "Collimated propagation of low energy protons from solar flares," in *Proceedings of the 9th Leningrad Seminar on Space Physics*, pp. 324–329, Leningrad, Russia, 1978.
- [51] S. N. Vernov, N. L. Grigorov, O. B. Likin et al., "Cosmic ray study by PROGNOZ Satellite," *Izvestiya Akademii Nauk, Seriya Fizicheskaya*, vol. 37, no. 6, pp. 1138–1143, 1973.

- [52] M. A. Forman, "Convection- dominated transport of solar cosmic rays," *Journal of Geophysical Research*, vol. 76, no. 4, pp. 759–767, 1971.
- [53] J. R. Jokipii, "Propagation of solar cosmic rays in the solar wind," in *Solar Activity Observations and Predictions*, P. S. McIntosh and M. Dryer, Eds., MIT press, 1972.
- [54] K. G. McCracken, U. R. Rao, R. P. Bukata, and E. P. Keath, "The decay phase of solar flare events," *Solar Physics*, vol. 18, no. 1, pp. 100–132, 1971.
- [55] A. J. Owens, "Interplanetary diffusion of cosmic rays: a new approximate analytic solution," *Journal of Geophysical Research*, vol. 84, no. 8, pp. 4451–4456, 1979.
- [56] E. I. Daibog, V. G. Stolpovskii, G. Erdos et al., "Decay phases in gradual and impulsive solar energetic particle events," in *Proceedings of the 27th International Cosmic Ray Conference (ICRC '01)*, vol. 3631, 2001.
- [57] E. I. Daibog, Y. I. Logachev, S. Kahler, and K. Kecskeméty, "Statistical properties of SEP event flux declines," *Advances in Space Research*, vol. 32, no. 12, pp. 2655–2660, 2003.
- [58] M. A. Zeldovich, B. M. Kuzhevsky, and Yu. I. Logachev, "Low energy proton fluxes from non- flare solar active regions," in *Problems of Solar Activity and PROGNOZ Space System*, pp. 110–124, Nauka, Moscow, Russia, 1977.
- [59] M. A. Zeldovich and I. Yu. Logachev, "Recurrent increases of low-energy particle flux measured on ISZ Prognoz-3," *Cosmic Research*, vol. 19, no. 1, pp. 53–65, 1981.
- [60] Yu. I. Logachev, M. A. Zeldovich, V. Stolpovsky et al., "Recurrent increases of energetic particle flux on decrease phase of 21st solar cycle," *Cosmic Research*, vol. 30, no. 3, pp. 368–377, 1992.
- [61] Yu. I. Logachev, M. A. Zeldovich, and K. Kecskeméty, "Spatial regions with low level 1–10 Mev proton fluxes during quiet time in the inner heliosphere down to 10 a.u.," *Izvestiya Akademii, Seriya Fizicheskaya*, vol. 65, no. 3, pp. 364–366, 2001.
- [62] A. I. Sladkova, "Investigation of the radiation environment on PROGNOZ stations," in *Problems of Solar Activity and PROGNOZ Space System*, pp. 149–155, Nauka, Moscow, Russia, 1977.
- [63] K. Kudela, J. Baláž, and I. Strhářský, "Energetic particle monitoring in space: three-decades of experience at IEP SAS," in *Proceedings of the International Conference on Recent Advances in Space Technologies (RAST '03)*, pp. 182–187, 2003.
- [64] K. Kudela and M. Slivka, "Space physics in Košice: history, present status, and benefit of EU funds for the future," *Contributions of the Astronomical Observatory Skalnaté Pleso*, vol. 40, pp. 142–150, 2010.
- [65] Y. E. Efimov, A. A. Gusev, K. Kudela, L. Just, and G. I. Pugacheva, "Spatial distribution of albedo particles on altitudes ~500 km," *Czechoslovak Journal of Physics*, vol. 35, no. 12, pp. 1371–1381, 1985.
- [66] S. N. Kuznetsov, K. Kudela, I. N. Myagkova, A. N. Podorolsky, S. P. Ryumin, and B. Y. Yushkov, "First experience with SONG-M measurements on board CORONAS-F satellite," *Indian Journal of Radio and Space Physics*, vol. 33, no. 6, pp. 353–357, 2004.
- [67] S. N. Kuznetsov, V. G. Kurt, B. Y. Yushkov, K. Kudela, and V. I. Galkin, "Gamma-ray and high-energy-neutron measurements on CORONAS-F during the Solar Flare of 28 October 2003," *Solar Physics*, vol. 268, no. 1, pp. 175–193, 2011.
- [68] I. N. Myagkova, S. N. Kuznetsov, V. G. Kurt et al., "X-ray,  $\gamma$ -emission and energetic particles in near-Earth space as measured by CORONAS-F satellite: from maximum to minimum of the last solar cycle," *Advances in Space Research*, vol. 40, no. 12, pp. 1929–1934, 2007.
- [69] V. G. Kurt, B. Yu. Yushkov, and A. V. Belov, "On the ground level enhancement beginning," *Astronomy Letters*, vol. 36, no. 7, pp. 520–530, 2010.

## Research Article

# Latitudinal Dependence of Cosmic Rays Modulation at 1 AU and Interplanetary Magnetic Field Polar Correction

**P. Bobik,<sup>1</sup> G. Boella,<sup>2</sup> M. J. Boschini,<sup>2,3</sup> C. Consolandi,<sup>2,4</sup> S. Della Torre,<sup>2,5</sup> M. Gervasi,<sup>2,4</sup> D. Grandi,<sup>2</sup> K. Kudela,<sup>1</sup> S. Pensotti,<sup>2,4</sup> P. G. Rancoita,<sup>2</sup> D. Rozza,<sup>2,5</sup> and M. Tacconi<sup>2,4</sup>**

<sup>1</sup> *Institute of Experimental Physics, Watsonova 47, 040 01 Kosice, Slovakia*

<sup>2</sup> *INFN Sez. of Milano-Bicocca, Piazza della Scienza 3, 20126 Milano, Italy*

<sup>3</sup> *CINECA, via R. Sanzio 4, Segrate (MI), Italy*

<sup>4</sup> *Department of Physics, University of Milano-Bicocca, Piazza della Scienza 3, 20126 Milano, Italy*

<sup>5</sup> *Department of Science and High Technology, University of Insubria, Via Valleggio 11, 22100 Como, Italy*

Correspondence should be addressed to P. G. Rancoita; [piergiorgio.rancoita@mib.infn.it](mailto:piergiorgio.rancoita@mib.infn.it)

Received 11 October 2012; Accepted 6 December 2012

Academic Editor: José F. Valdés-Galicia

Copyright © 2013 P. Bobik et al. This is an open access article distributed under the Creative Commons Attribution License, which permits unrestricted use, distribution, and reproduction in any medium, provided the original work is properly cited.

The cosmic rays differential intensity inside the heliosphere, for energy below 30 GeV/nuc, depends on solar activity and interplanetary magnetic field polarity. This variation, termed solar modulation, is described using a 2D (radius and colatitude) Monte Carlo approach for solving the Parker transport equation that includes diffusion, convection, magnetic drift, and adiabatic energy loss. Since the whole transport is strongly related to the interplanetary magnetic field (IMF) structure, a better understanding of his description is needed in order to reproduce the cosmic rays intensity at the Earth, as well as outside the ecliptic plane. In this work an interplanetary magnetic field model including the standard description on ecliptic region and a polar correction is presented. This treatment of the IMF, implemented in the HelMod Monte Carlo code (version 2.0), was used to determine the effects on the differential intensity of Proton at 1 AU and allowed one to investigate how latitudinal gradients of proton intensities, observed in the inner heliosphere with the Ulysses spacecraft during 1995, can be affected by the modification of the IMF in the polar regions.

## 1. Introduction

The Solar Modulation, due to the solar activity, affects the Local Interstellar Spectrum (LIS) of Galactic Cosmic Rays (GCR) typically at energies lower than 30 GeV/nucl. This process, described by means of the Parker equation (e.g., see [1, 2] and Chapter 4 of [3]), is originated from the interaction of GCRs with the interplanetary magnetic field (IMF) and its irregularities. The IMF is the magnetic field that is carried outwards during the solar wind expansion. The interplanetary conditions vary as a function of the solar cycle which approximately lasts eleven years. In a solar cycle, when the maximum activity occurs, the IMF reverse his polarity. Thus, similar solar polarity conditions are found almost every 22 years [4]. In the HelMod Monte Carlo code

version 1.5 (e.g., see [2]), the “classical” description of IMF, as proposed by Parker [5], was implemented together with the polar corrections of the solar magnetic field suggested subsequently in [6, 7]. This IMF was used inside the HelMod [2] code to investigate the solar modulation observed at Earth and to partially account for GCR latitudinal gradients, that is, those observed with the Ulysses spacecraft [8, 9]. In order to fully account for both the latitudinal gradients and latitudinal position of the proton-intensity minimum observed during the Ulysses fast scan in 1995, the HelMod Code was updated to the version 2.0 to include a new treatment of the parallel and diffusion coefficients following that one described in [10]. In the present formulation, the parallel component of the diffusion tensor depends only on the radial distance from the Sun, while it is independent of solar latitude.

## 2. The Interplanetary Magnetic Field

Nowadays, we know that there is a Solar Wind plasma (SW) that permeates the interplanetary space and constitutes the interplanetary medium. In IMF models the magnetic-field lines are supposed to be embedded in the nonrelativistic streaming particles of the SW, which carries the field with them into interplanetary space, producing the large scale structure of the IMF and the heliosphere. The “classical” description of the IMF was proposed originally by Parker (e.g., see [2, 5, 11–14] and Chapter 4 of [3]). He assumed (i) a constant solar rotation with angular velocity ( $\omega$ ), (ii) a simple spherically symmetric emission of the SW, and (iii) a constant (or approaching an almost constant) SW speed ( $V_{sw}$ ) at larger radial distances ( $r$ ), for example, for  $r > r_b \approx 10R_\odot$  (where  $R_\odot$  is the Solar radius), since beyond  $r_b$  the wind speed varies slowly with the distance. The “classical” IMF can be analytically expressed as [15]

$$\mathbf{B}_{\text{Par}} = \frac{A}{r^2} (\mathbf{e}_r - \Gamma \mathbf{e}_\varphi) \left[ 1 - 2H(\theta - \theta') \right], \quad (1)$$

where  $A$  is a coefficient that determines the IMF polarity and allows  $|\mathbf{B}_{\text{Par}}|$  to be equal to  $B_\oplus$ , that is, the value of the IMF at Earth’s orbit as extracted from NASA/GSFC’s OMNI data set through OMNIWeb [16, 17];  $\mathbf{e}_r$  and  $\mathbf{e}_\varphi$  are unit vector components in the radial and azimuthal directions, respectively,  $\theta$  is the colatitude (polar angle);  $\theta'$  is the polar angle determining the position of the Heliospheric Current Sheet (HCS) [18];  $H$  is the Heaviside function: thus,  $[1 - 2H(\theta - \theta')]$  allows  $\mathbf{B}_{\text{Par}}$  to change sign in the two regions above and below the HCS [18] of the heliosphere; finally,

$$\Gamma = \tan \Psi = \frac{\omega (r - r_b) \sin \theta}{V_{sw}}, \quad (2)$$

with  $\Psi$  the spiral angle. In the present model  $\omega$  is assumed to be independent of the heliographic latitude and equal to the sidereal rotation at the Sun’s equator. The magnitude of Parker field is thus

$$B_{\text{Par}} = \frac{A}{r^2} \sqrt{1 + \Gamma^2}. \quad (3)$$

In 1989 [6], Jokipii and Kota have argued that the solar surface, where the *feet* of the field lines lie, is not a smooth surface, but a granular turbulent surface that keeps changing with time, especially in the polar regions. This turbulence may cause the *footpoints* of the polar field lines to wander randomly, creating transverse components in the field, thus causing temporal deviations from the smooth Parker geometry. The net effect of this is a highly irregular and compressed field line. In other words, the magnitude of the mean magnetic field at the poles is greater than in the case of the smooth magnetic field of a pure Parker spiral. Jokipii and Kota [6] have therefore suggested that the Parker spiral field may be generalized by the introduction of a perturbation parameter  $[\delta(\theta)]$  which amplifies the field strength at large

radial distances. With this modification the magnitude of IMF, (3), becomes [6]

$$B_{\text{Pol}} = \frac{A}{r^2} \sqrt{1 + \Gamma^2 + \left(\frac{r}{r_b}\right)^2 \delta(\theta)^2}. \quad (4)$$

The difference of the IMF obtained from (3) and (4) is less than  $\sim 1\%$  for colatitudes  $20^\circ \leq \theta \leq 160^\circ$  (e.g., see Figure 1(a)) and increases for colatitudes approaching the polar regions (e.g., see Figure 2 of [2]).

In the present treatment, the heliosphere is divided into *polar* regions and a *equatorial* region where different description of IMF are applied. In the *equatorial* region the Parker’s IMF, Equation (3) is used, while in the *polar* regions we used a modified IMF that allows a magnitude as in (4)

$$\begin{aligned} \mathbf{B}_{\text{Pol}} &= \frac{A}{r^2} \left[ \mathbf{e}_r + \frac{r}{r_b} \delta(\theta) \mathbf{e}_\theta - \frac{\omega (r - r_b) \sin \theta}{V_{sw}} \mathbf{e}_\varphi \right] \\ &\quad \times \left[ 1 - 2H(\theta - \theta') \right] \quad \text{Polar regions,} \\ \mathbf{B}_{\text{Par}} &= \frac{A}{r^2} \left[ \mathbf{e}_r - \frac{\omega (r - r_b) \sin \theta}{V_{sw}} \mathbf{e}_\varphi \right] \\ &\quad \times \left[ 1 - 2H(\theta - \theta') \right] \quad \text{Equatorial region,} \end{aligned} \quad (5)$$

where equatorial regions are those with colatitude  $X^\circ \leq \theta \leq (180^\circ - X^\circ)$ . The symbol  $\theta_{X^\circ}$  indicates the corresponding polar regions.

In order to have a divergence-free magnetic-field we require that the perturbation factor  $[\delta(\theta)]$  has to be

$$\delta(\theta) = \frac{\delta_m}{\left[ 1 - 2H(\theta - \theta') \right] \sin \theta}, \quad (6)$$

where  $\delta_m$  is the minimum perturbation factor of the field. The perturbation parameter is left to grow with decreasing of the colatitude. However, in their original work, Jokipii and Kota [6] estimated the value of the parameter  $\delta$  between  $10^{-3}$  and  $3 \times 10^{-3}$ .

Since the polar field is only a perturbation of the Parker field, it is a reasonable assumption that stream lines of the magnetic field do not cross the equatorial plane, thus, remaining completely contained in the solar hemisphere of injection. This allows one to estimate an upper limit on the possible values of  $\delta_m$  (see, Figure 1(b)). Currently, we use  $\delta_m = 1 \times 10^{-5}$  by comparing simulations with observations at Earth orbit during Solar Cycle 23 (see, Section 5).

## 3. The Propagation Model

Parker in 1965 [1] (see also, [2], Chapter 4 of [3] and references therein) treated the propagation of GCRs through the interplanetary space. He accounted for the so-called adiabatic energy losses, outward convection due to the SW and drift

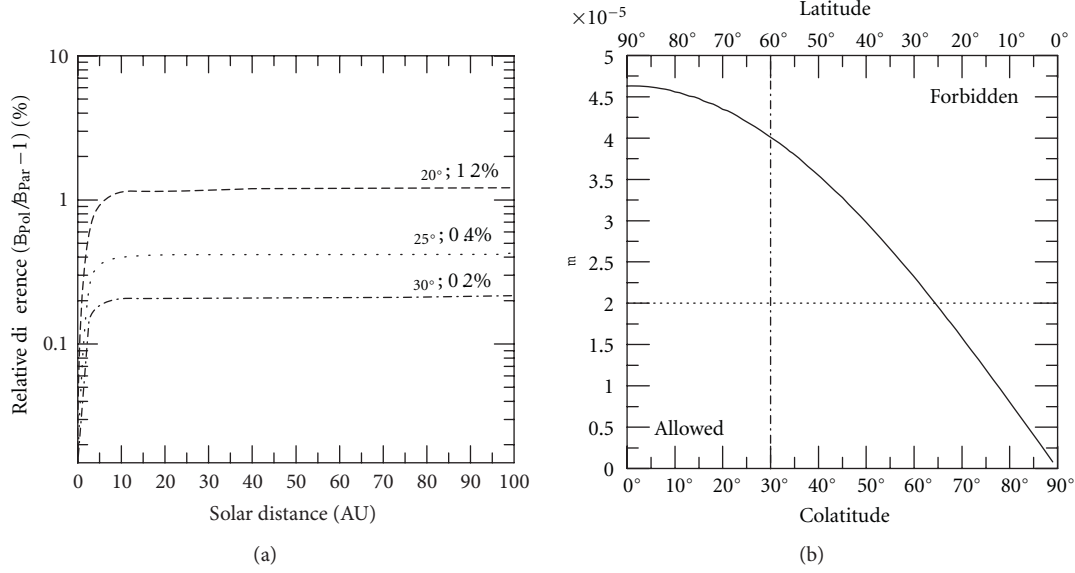


FIGURE 1: (a) Maximum percentage difference between  $\mathbf{B}_{\text{Pol}}$  and  $\mathbf{B}_{\text{Par}}$  as a function of the solar distance inside the colatitude regions  $20^\circ \leq \theta \leq 160^\circ$  ( $\theta_{20^\circ}$ ),  $25^\circ \leq \theta \leq 155^\circ$  ( $\theta_{25^\circ}$ ), and  $30^\circ \leq \theta \leq 150^\circ$  ( $\theta_{30^\circ}$ ). (b) Maximum value allowed of  $\delta_m$  as a function of colatitude: values in the “allowed” region guarantee that the stream line originated from the polar magnetic field do not cross the equatorial plane. Since (5) is symmetric with respect to the solar equatorial plane, values greater than  $90^\circ$  of colatitude lead to same results of those presented.

effects. In the heliocentric system the Parker equation is then expressed (e.g., see [2, 19]):

$$\begin{aligned} \frac{\partial U}{\partial t} = & \frac{\partial}{\partial x_i} \left( K_{ij}^S \frac{\partial U}{\partial x_j} \right) - \frac{\partial}{\partial x_i} [(V_{sw,i} + v_{d,i}) U] \\ & + \frac{1}{3} \frac{\partial V_{sw,i}}{\partial x_i} \frac{\partial}{\partial T} (\alpha_{\text{rel}} T U), \end{aligned} \quad (7)$$

where  $U$  is the number density of particles per unit of particle kinetic energy  $T$ , at the time  $t$ .  $V_{sw,i}$  is the solar wind velocity along the axis  $x_i$  [20],  $K_{ij}^S$  is the symmetric part of diffusion tensor [1],  $v_d$  is the drift velocity that takes into account the drift of the particles due to the large scale structure of the magnetic field [21–23], and, finally,

$$\alpha_{\text{rel}} = \frac{T + 2m_r c^2}{T + m_r c^2}, \quad (8)$$

where  $m_r$  is the rest mass of the GCR particle. The last term of (7) accounts for adiabatic energy losses [1, 24]. The number density  $U$  is related to the differential intensity  $J$  as ([2, 25], Chapter 4 of [3] and references therein):

$$J = \frac{vU}{4\pi}, \quad (9)$$

where  $v$  is the speed of the GCR particle.

Equation (7) was solved using the HelMod code (see the discussion in [2]). This treatment (i) follows that introduced in [10, 26–30] and (ii) determines the differential intensity of GCRs using a set of approximated stochastic differential equations (SDEs) which provides a solution equivalent to that from (7). The equivalence between the Parker equation,

that is a Fokker-Planck type equation, and the SDEs is demonstrated in [28, 31]. In the present work, we use a 2D (radius and colatitude) approximation for the particle transport. The model includes the effects of solar activity during the propagation from the effective boundary of the heliosphere down to Earth’s position.

The set of SDEs for the 2D approximation of (7) in heliocentric spherical coordinates is

$$\begin{aligned} \Delta r = & \frac{1}{r^2} \frac{\partial}{\partial r} (r^2 K_{rr}^S) \Delta t - \frac{\partial}{\partial \mu(\theta)} \left[ \frac{K_{r\mu}^S \sqrt{1 - \mu^2(\theta)}}{r} \right] \Delta t \\ & + (V_{sw} + v_{d,r}) \Delta t + (2K_{rr}^S)^{1/2} \omega_r \sqrt{\Delta t}, \end{aligned} \quad (10a)$$

$$\begin{aligned} \Delta \mu(\theta) = & - \frac{1}{r^2} \frac{\partial}{\partial r} [r K_{\mu r}^S \sqrt{1 - \mu^2(\theta)}] \Delta t \\ & + \frac{\partial}{\partial \mu(\theta)} \left[ K_{\mu\mu}^S \frac{1 - \mu^2(\theta)}{r^2} \right] \Delta t \\ & - \frac{1}{r} v_{d,\mu} \sqrt{1 - \mu^2(\theta)} \Delta t \\ & - \frac{2K_{r\mu}^S}{r} \left[ \frac{1 - \mu^2(\theta)}{2K_{rr}^S} \right]^{1/2} \omega_r \sqrt{\Delta t} \\ & + \frac{1}{r} \left\{ [1 - \mu^2(\theta)] \frac{K_{\mu\mu}^S K_{rr}^S - (K_{r\mu}^S)^2}{0.5K_{rr}^S} \right\}^{1/2} \omega_\mu \sqrt{\Delta t}, \end{aligned} \quad (10b)$$

$$\Delta T = - \frac{\alpha_{\text{rel}} T}{3r^2} \frac{\partial V_{sw,r}^2}{\partial r} \Delta t, \quad (10c)$$

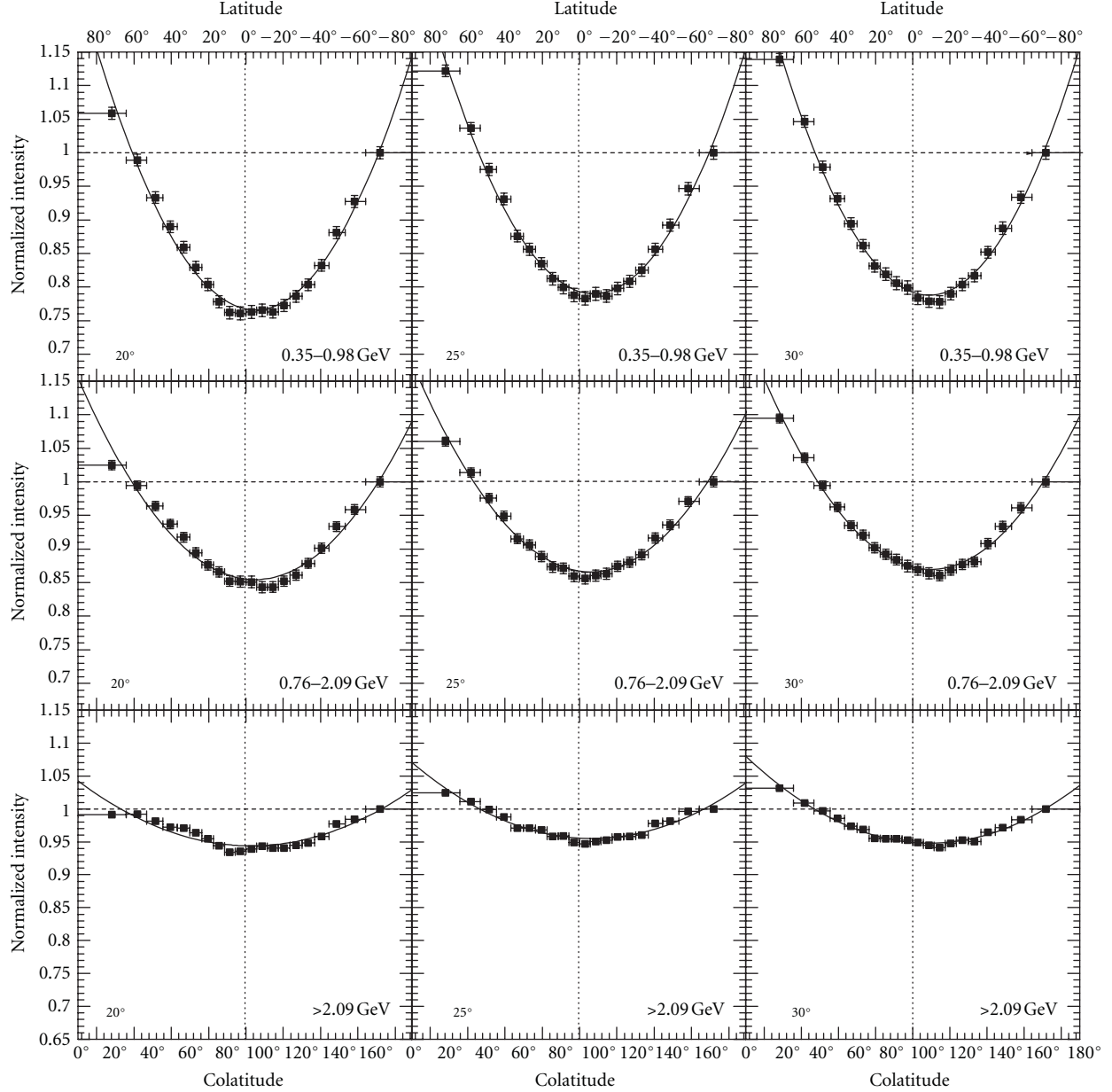


FIGURE 2: Latitudinal relative intensity at  $r = 1$  AU, obtained at different solar colatitudes for protons in the energy range defined in the Table 2 and using three definitions of *polar regions*:  $\theta_{20^\circ}$ ,  $\theta_{25^\circ}$ , and  $\theta_{30^\circ}$ .

where  $\mu(\theta) = \cos\theta$  and  $\omega_i$  is a random number following a Gaussian distribution with a mean of zero and a standard deviation of one. The procedure for determining the SDEs can be found in [2].

In a coordinate system with one axis parallel to the average magnetic field and the other two perpendicular to this the symmetric part of the diffusion tensor  $K_{ij}^S$  is (see e.g., [32]):

$$K_{ij}^S = \begin{bmatrix} K_{\parallel} & 0 & 0 \\ 0 & K_{\perp,r} & 0 \\ 0 & 0 & K_{\perp,\theta} \end{bmatrix}, \quad (11)$$

with  $K_{\parallel}$  the diffusion coefficient describing the diffusion parallel to the average magnetic field and  $K_{\perp,r}$  and  $K_{\perp,\theta}$  are the diffusion coefficients describing the diffusion perpendicular to the average magnetic field in the radial and polar directions, respectively. In this work  $K_{\parallel}$  is that one proposed by Strauss and collaborators in [10] (see also [33–35]):

$$K_{\parallel} = \frac{\beta}{3} K_0 \frac{P}{1 \text{ GV}} \left( 1 + \frac{r}{1 \text{ AU}} \right), \quad (12)$$

where  $K_0$  is the diffusion parameter—described in Section 2.1 of [2]—which depends on solar activity and polarity,  $\beta$  is the particle speed in unit of speed of light,  $P = pc/|Ze|$

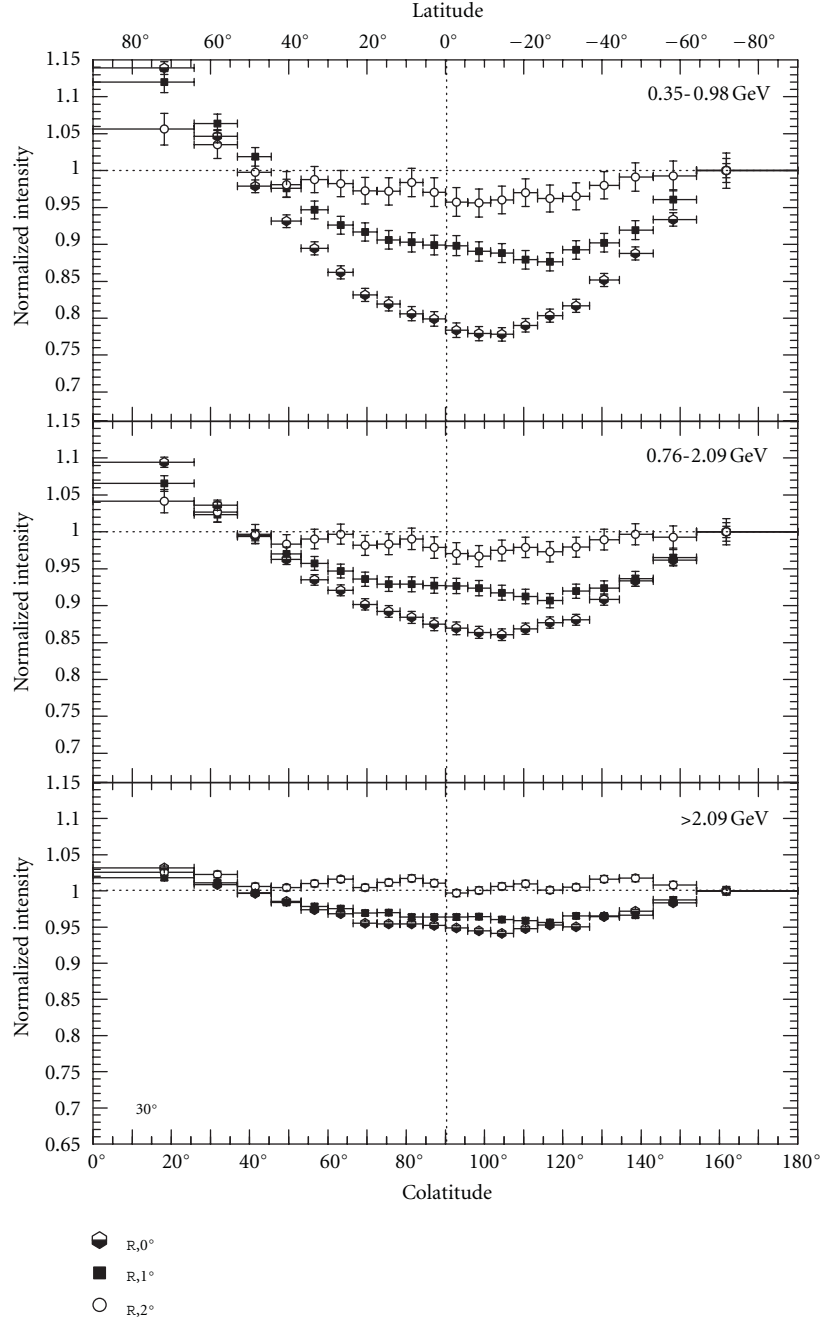


FIGURE 3: For the *polar regions*  $\theta < 30^{\circ}$  and  $\theta > 150^{\circ}$ , latitudinal relative intensity at  $r = 1$  AU, accounting for GCR particles with  $0^{\circ} < \theta < 180^{\circ}$  ( $\theta_{R,0}$ ),  $1^{\circ} < \theta < 179^{\circ}$  ( $\theta_{R,1}$ ), and  $2^{\circ} < \theta < 178^{\circ}$  ( $\theta_{R,2}$ ), respectively, are shown as a function of the proton kinetic energy and solar colatitude. Results with  $10^{\circ} < \theta < 170^{\circ}$  ( $\theta_{R,10}$ ) are comparable with those obtained with  $\theta_{R,2}$ .

is the particle rigidity expressed in GV, and, finally,  $r$  is the heliocentric distance from the Sun in AU.

In the current treatment,  $K_{\parallel}$  has a radial dependence proportional to  $r$ , but no latitudinal dependence. Mc Donald and collaborators (see, [36]) remarked that (i) a spatial dependence of  $K_{\parallel}$ —like the one proposed here—can affect the latitudinal gradients at high latitude and (ii) it is consistent with that originally suggested in [6]. Furthermore,

the perpendicular diffusion coefficient is taken to be proportional to  $K_{\parallel}$  with a ratio  $K_{\perp,i}/K_{\parallel} = 0.13$  for both  $r$  and  $\theta$   $i$ -coordinates. The latter value is discussed in Section 5.

In addition, the practical relationship between  $K_0$  and monthly Smoothed Sunspot Numbers (SSN) [37] values—discussed in Section 2.1 of [2]—is currently updated using the most recent data from [38]. As in [2], the  $K_0$  data are subdivided into four sets, that is, ascending and descending

TABLE 1: Definition of ascending and descending periods.

	Period	Years
(I)	$A < 0$ ascending	1964.79–1968.87, 1986.70–1989.54, 2008.95–2009.95
(II)	$A < 0$ descending	1964.53–1964.79, 1979.95–1986.70, 2000.28–2008.95
(III)	$A > 0$ ascending	1976.20–1979.95, 1996.37–2000.28
(IV)	$A > 0$ descending	1968.87–1976.20, 1989.54–1996.37

phases for both negative and positive solar magnetic-field polarities (Table 1). It has to be remarked that after each maximum the sign of the magnetic field (i.e., the  $A$  parameter in (5)) is reversed. The updated practical relationships between  $K_0$  in  $\text{AU}^2\text{GV}^{-1}\text{s}^{-1}$  and SSN values for  $1.4 \leq \text{SSN} \leq 165$  for the four periods (from I up to IV, listed in Table 1) are

$$(I) K_0 = 0.000297 - 2.9 \cdot 10^{-6}\text{SSN} + 8.1 \cdot 10^{-9}\text{SSN}^2 + 1.46 \cdot 10^{-10}\text{SSN}^3 - 8.4 \cdot 10^{-13}\text{SSN}^4, \quad (13a)$$

$$(II) K_0 = \begin{cases} 0.000304846 \\ -5.8 \cdot 10^{-6}\text{SSN}, & \text{if } \text{SSN} \leq 20, \\ \frac{0.00195}{\text{SSN}} \\ -2.3 \cdot 10^{-10}\text{SSN}^2 + 9.1 \cdot 10^{-5}, & \text{if } \text{SSN} > 20, \end{cases} \quad (13b)$$

$$(III) K_0 = 0.0002391 - 8.453 \cdot 10^{-7}\text{SSN} \quad (13c)$$

$$(IV) K_0 = 0.000247 - 1.175 \cdot 10^{-6}\text{SSN}. \quad (13d)$$

The rms (root mean square) values of the percentage difference between values obtained with (13a), (13b), (13c), and (13d) from those determined using the procedure discussed in Section 2.1 of [2] applied to the data from [38] were found to be 6.0%, 10.1%, 7.0%, and 13.2% for the period I (ascending phase with  $A < 0$ ), II (descending phase with  $A < 0$ ), III (ascending phase with  $A > 0$ ), and IV (descending phase with  $A > 0$ ), respectively.

#### 4. The Magnetic Field in the Polar Regions

Section 2 describes an IMF following the Parker Field with a small region around the poles in which such a field is modified. As already mentioned (see e.g., [6, 39–43]), the correction is needed to better reproduce the complexity of the magnetic field in those regions.

Moreover, Ulysses spacecraft (see e.g., [44–46]) explored the heliosphere outside the ecliptic plane up to  $\pm 80^\circ$  of solar latitude at a solar distance from  $\sim 1$  up to  $\sim 5$  AU. Using these observations, the presence of latitudinal gradient in the proton intensity could be determined (e.g., see Figure 2 of [9] and Figure 5 of [8]). The data collected during the *latitudinal fast scan* (from September 1994 up to August

TABLE 2: Kinetic energy bins (in GeV) selected with HelMod Code and the corresponding proton energy channel for KET instruments on board the Ulysses spacecraft [8].

HelMod Energy bin	KET channel
(0.35–0.98) GeV	(0.4–1.0) GeV
(0.76–2.09) GeV	(0.8–2.0) GeV
(2.09–200) GeV	>2 GeV

1995) show (a) a nearly symmetric latitudinal gradient with the minimum near ecliptic plane, (b) a southward shift of the minimum, and (c) an intensity in the North polar region at  $80^\circ$  exceeding the South polar intensity. In [9] a latitudinal gradient of  $\sim 0.3\%$ /degree for proton with kinetic energy  $> 0.1$  GeV was estimated. While in [8] the analysis to higher energy was extended estimating a gradient of  $\sim 0.22\%$ /degree for proton with kinetic energy  $> 2$  GeV. The minimum in the charged particle intensity separating the two hemispheres of the heliosphere occurs  $\sim 10^\circ$  South of the heliographic equator [9]. In addition, an independent analysis that takes into account the latitudinal motion of the Earth and IMP8 confirms a significant ( $\sim 8^\circ \pm 2^\circ$ ) southward offset of the intensity minimum [9] for  $T > 100$  MeV proton. Furthermore in [8], a southward offset of about  $\approx 7^\circ$  is evaluated; this offset of the intensity minimum results to be independent of the particle energy up to 2 GeV. Finally, in [9], the intensity in the North polar region at  $80^\circ$  is observed to exceed the South polar intensity of  $\sim 6\%$  for protons with  $T > 100$  MeV.

Using the present HelMod code (version 2.0), we could investigate (i) the latitudinal gradient of GCR intensities resulting from solar modulation and (ii) how the magnetic-field structure of the polar regions, as defined in Section 2, is able to influence the GCR spectra on the ecliptic plane. As previously defined, we denote with  $\theta_{X^\circ}$  a polar region of amplitude  $X^\circ$  from polar axis, that is,  $\theta < X^\circ$  and  $\theta > 180^\circ - X^\circ$ . Three regions with  $X^\circ = 20^\circ, 25^\circ,$  and  $30^\circ$  were investigated. Outside any of these regions, the ratio between  $\mathbf{B}_{\text{Pol}}$  and  $\mathbf{B}_{\text{Par}}$  in (5) is less than  $\sim 1\%$  (see Figure 1) and, thus, it ensures a smooth transition between polar and equatorial regions. For the purpose of this study we consider an energy binning closer to those presented in [8]. The KET instrument [47] collects proton data in three “channels” one with energies ranging from 0.038 GeV up to 2.0 GeV and two for particle with kinetic energy  $T > 0.1$  GeV and  $T > 2$  GeV, respectively. A successive reanalysis of the collected data allowed the authors to subdivide the 0.25–2 GeV “channel” in three “subchannels” of intermediate energies. Since the Present Model is optimized—as discussed in [2]—for particles with rigidity greater than 1 GV (i.e.,  $\approx 0.444$  GeV), the present results are compared only with the corresponding “channel” or “subchannels” suited for the corresponding energy range (see Table 2).

At 1 AU and as a function of the solar colatitude, the GCR intensities for protons are shown in Figure 2. For a comparison with Ulysses observations, the modulated intensities of protons—resulting from HelMod code—were investigated from  $80^\circ$  (North) and down to  $-80^\circ$  (South). They were

obtained using the HelMod code and selected using the energy bins reported in Table 2. In Figure 2, the latitudinal intensity distribution is normalized to the corresponding South Pole intensity. The quoted errors include statistical and systematic errors. The distributions were interpolated using a parabolic function expressed as

$$I(\theta_{\text{lat}}) = a + c(\theta_{\text{lat}} + d)^2, \quad (14)$$

where  $I(\theta_{\text{lat}})$  is the normalized intensity,  $\theta_{\text{lat}}$  is the latitudinal angle (the latitudinal angle is  $\theta_{\text{lat}} = 90^\circ - \theta$ ), and  $a$ ,  $b$ , and  $c$  are parameters determined from the fitting procedure. The so obtained fitted curves are shown as continuous lines in Figure 2. Furthermore, the latitudinal positions of minimum intensity ( $\theta_{\text{lat,min}}$ ), percentages of North-South asymmetry of intensities ( $\Delta_{\text{N-S}}$ ), and differences in percentage between the maximum and minimum intensities ( $\Delta_{\text{max}}$ ) were also determined from the fitting procedure and are listed in Tables 3, 4, and 5, respectively. The quoted errors—following a procedure discussed in [2]—are derived varying the fitted parameters in order to obtain a value of the parameter  $\eta_{\text{rms,lat}}$  two times larger than the one resulting from the best fit ( $I_{\text{best}}$ ).  $\eta_{\text{rms,lat}}$  is defined as

$$\eta_{\text{rms,lat}} = \sqrt{\frac{\sum_i (\eta_{i,\text{lat}}/\sigma_{\eta_{i,\text{lat}}})^2}{\sum_i 1/\sigma_{\eta_{i,\text{lat}}}^2}} \quad (15)$$

with

$$\eta_{i,\text{lat}} = \frac{I(\theta_i) - I_{\text{best}}(\theta_i)}{I_{\text{best}}(\theta_i)}, \quad (16)$$

where  $\theta_i$  is the central value of the  $i$ th latitudinal bin of the differential intensity distribution and  $\sigma_{\eta_{i,\text{lat}}}$  are the errors including the experimental and Monte Carlo uncertainties. For  $\theta_{30^\circ}$ , that is, assuming a modified polar magnetic-field for  $\theta < 30^\circ$  and  $\theta > 150^\circ$ , we found a general agreement with Ulysses observations. The position of  $\theta_{\text{lat,min}}$  is compatible within the errors with one observed in [8], as well as the values of  $\Delta_{\text{N-S}}$  and  $\Delta_{\text{max}}$ .

The HelMod code allows one to investigate the relevance of the treatment of the polar region magnetic-field with respect to the resulting modulation of GCR. Thus, the latitudinal normalized intensities were obtained excluding a few (small) regions nearby the poles. This was determined from reducing the latitudinal spatial phase-space admissible for *pseudo-particles* (see [2]), that is, the latitudinal extension of GCR particles taken into account—to  $1^\circ < \theta < 179^\circ$  ( $\theta_{R,1}$ ),  $2^\circ < \theta < 178^\circ$  ( $\theta_{R,2}$ ) and  $10^\circ < \theta < 170^\circ$  ( $\theta_{R,10}$ ). The so obtained latitudinal gradients are compared with the full latitudinal extension,  $\theta_{R,0}$  ( $0^\circ < \theta < 180^\circ$ ), in Figure 3. By an inspection of Figure 3, one may lead to the conclusion that the GCR diffusion nearby the polar axis has a large impact on the latitudinal gradients in the inner heliosphere. As a consequence, the IMF description in the polar regions is relevant in order to reproduce the observed modulated GCR spectra.

TABLE 3: Latitudinal positions of minimum proton intensity ( $\theta_{\text{lat,min}}$ ) (in degrees) as a function of the kinetic energy, using three values for the extension of the polar regions.

Energy range	$\theta_{\text{lat,min}}$ (in degrees)		
	$\theta_{20^\circ}$	$\theta_{25^\circ}$	$\theta_{30^\circ}$
0.35–0.98 GeV	$-5_{-5}^{+4}$	$-8_{-4}^{+4}$	$-9_{-3}^{+3}$
0.76–2.09 GeV	$-5_{-7}^{+6}$	$-6_{-6}^{+5}$	$-10_{-4}^{+4}$
2.09–200 GeV	$-3_{-7}^{+7}$	$-7_{-7}^{+7}$	$-9_{-6}^{+5}$

TABLE 4: Percentages of North-South asymmetry of proton intensities ( $\Delta_{\text{N-S}}$ ) as a function of the kinetic energy, using three values for the extension of the polar regions.

Energy range	$\Delta_{\text{N-S}}$ (%)		
	$\theta_{20^\circ}$	$\theta_{25^\circ}$	$\theta_{30^\circ}$
0.35–0.98 GeV	$-8_{-6}^{+6}$	$-11_{-4}^{+5}$	$-13_{-4}^{+4}$
0.76–2.09 GeV	$-5_{-6}^{+5}$	$-6_{-5}^{+5}$	$-6_{-3}^{+3}$
2.09–200 GeV	$-1_{-1}^{+3}$	$-3_{-3}^{+3}$	$-4_{-2}^{+2}$

TABLE 5: Differences in percentage between the maximum and minimum proton intensities ( $\Delta_{\text{max}}$ ) as a function of the kinetic energy, using three values for the extension of the polar regions.

Energy range	$\Delta_{\text{max}}$ (%)		
	$\theta_{20^\circ}$	$\theta_{25^\circ}$	$\theta_{30^\circ}$
0.35–0.98 GeV	$-34_{-5}^{+5}$	$-35_{-4}^{+4}$	$-36_{-3}^{+4}$
0.76–2.09 GeV	$-22_{-7}^{+6}$	$-23_{-4}^{+5}$	$-25_{-3}^{+3}$
2.09–200 GeV	$-8_{-3}^{+4}$	$-9_{-3}^{+3}$	$-10_{-2}^{+2}$

## 5. Comparison with Observations during Solar Cycle 23

The agreement of HelMod simulated spectra with observations during solar cycle 23 is investigated via quantitative comparisons using (17) and (18). However, since the structure of the heliosphere is different in high and low solar activity the two periods are separately analyzed.

The HelMod Code [2] (version 2.0) allowed us to investigate how the modulated (simulated) differential intensities are affected by the (1) particle drift effect, (2) polar enhancement of the diffusion tensor along the polar direction ( $K_{\perp,\theta}$ , e.g., see [48]), and, finally, (3) values of the tilt angle ( $\alpha_t$ ) calculated following the approach of the “R” and “L” models [49]. This analysis also allows us to estimate the values of IMF parameters that better describe the modulation along the entire solar cycle. The effects related to particle drift were investigated via the suppression of the drift velocity (*No Drift* approximation), this accounts for the hypothesis that magnetic drift convection is almost completely suppressed during solar maxima. The differential intensities were calculated for  $K_{\perp,\mu} = \rho_E K_{\perp,r}$  with values of  $\rho_E$  of 1, 8, and 10, that is, no enhancement, that suggested in [50] and that suggested in [2, 48] (and reference there in), respectively. Furthermore, the modulated proton spectra were derived from a LIS whose normalization constant depends on the experimental set of data and were already discussed in [2]). In addition, the differential intensities were calculated accounting for

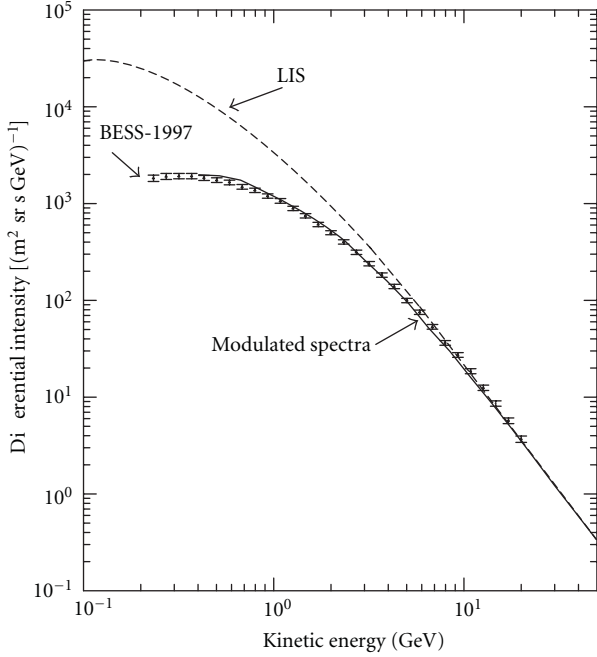


FIGURE 4: Proton differential intensity determined with the HelMod code (continuous line) compared to the experimental data of BESS-1997; the dashed line is the LIS (see the text).

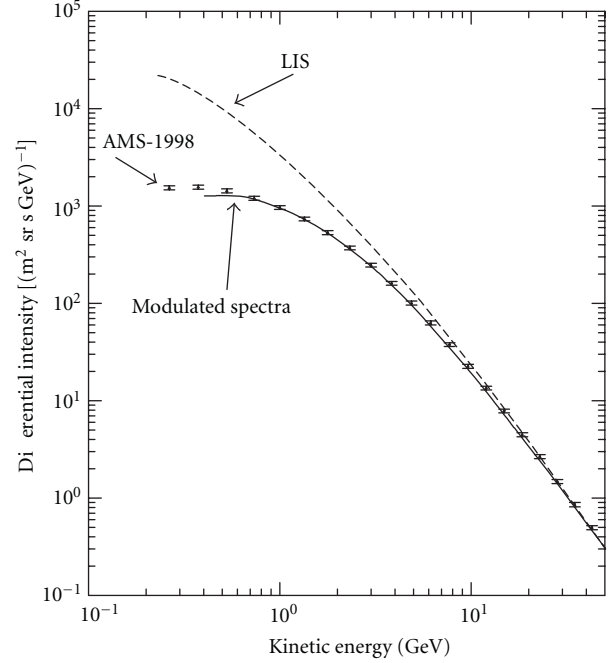


FIGURE 5: Proton differential intensity determined with the HelMod code (continuous line) compared to the experimental data of AMS-1998; the dashed line is the LIS (see the text).

particles inside heliospheric regions where solar latitudes are lower than  $[5.7^\circ]$ .

During the period of high solar activity for the solar cycle 23, the BESS collaboration took data in the years 1999, 2000, and 2002 (see sets of data in [51]). For period not dominated by high solar activity in solar cycle 23, BESS, AMS, and PAMELA collaborations took data, that is, BESS-1997 [51], AMS-1998 [52], and PAMELA-2006/08 [53].

Following the procedure described in [2], the observation data were compared with those obtained from HelMod code using the error-weighted root mean square ( $\eta_{\text{rms}}$ ) of the relative difference ( $\eta$ ) between experimental data ( $f_{\text{exp}}$ ) and those resulting from simulated differential intensities ( $f_{\text{sim}}$ ). For each set of experimental data and with the approximations and/or models described above, we determined the quantity

$$\eta_{\text{rms}} = \sqrt{\frac{\sum_i (\eta_i / \sigma_{\eta_i})^2}{\sum_i 1 / \sigma_{\eta_i}^2}}, \quad (17)$$

with

$$\eta_i = \frac{f_{\text{sim}}(T_i) - f_{\text{exp}}(T_i)}{f_{\text{ref}}(T_i)}, \quad (18)$$

where  $T_i$  is the average energy of the  $i$ th energy bin of the differential intensity distribution and  $\sigma_{\eta_i}$  are the errors including the experimental and Monte Carlo uncertainties; the latter account for the Poisson error of each energy bin. The simulated differential intensities are interpolated with a cubic spline function. The modulation results are studied varying

the parameters  $\delta_m$ —from 0, that is, the nonmodified Parker IMF, up to  $3 \times 10^{-5}$ , see Figure 1(b)—,  $K_{\perp,r}/K_{\parallel} = \rho_k$  (from 0.10 up to 0.14) and  $K_{\perp,\theta}/K_{\perp,r} = \rho_E$  (from 1 up to 10) seeking a set of parameters set that minimize  $\eta_{\text{rms}}$ . In Table 6, the average values of  $\eta_{\text{rms}}$  (in percentage, %) for low solar activity periods are listed. They were obtained in the energy range (Above 30 GeV, the differential intensity is marginally (if at all) affected by modulation.) from 444 MeV up to 30 GeV using the “L” and “R” models for the tilt angle  $\alpha_t$  and for the No Drift approximation and without any enhancement of the diffusion tensor along the polar direction ( $K_{\perp,\mu}$ ). The results derived with the enhancement of the diffusion tensor along the polar direction indicate that for  $\rho_E = 8$  and 10 one obtains a value of  $\eta_{\text{rms}}$  that is from 1.5 up to 3 times larger with respect the case without enhancement (For a comparison, the *scalar* approximation presented in [2], that is, assuming that the diffusion propagation is independent of magnetic structure, leads to an average  $\eta_{\text{rms}}$  of  $\sim 15\%$ ). From inspection of Table 6, one can remark that the drift mechanism leads to a better agreement with experimental data. Furthermore the “R” and “L” models for tilt angles are comparable within the precision of the method (discussed in [2]). The minimum difference with respect to the experimental data occurs when  $\rho_k = 0.11\text{--}0.13$  and  $\delta_m = 1.0 \times 10^{-5}$  for both “R” and “L” models, with the “L” model slightly preferred to “R”.

In Figures 4, 5, and 6, the differential intensities determined with the HelMod code are shown and compared to the experimental data of BESS-1997, AMS-1998, and PAMELA-2006/08, respectively; in these figures, the dashed lines are the LIS as discussed in [2]. These modulated intensities are the ones calculated for a heliospheric region where solar latitudes

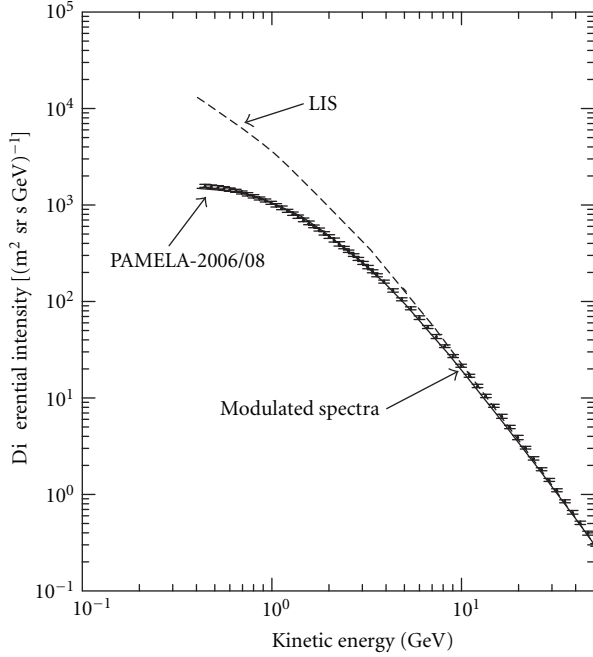


FIGURE 6: Proton differential intensity determined with the HelMod code (continuous line) compared to the experimental data of PAMELA 2006/08; the dashed line is the LIS (see the text).

are lower than  $|\delta_m|$ , using  $\rho_k = 0.13$ ,  $\delta_m = 1.0 \times 10^{-5}$  and  $\rho_E = 1$  with the “L” model. Finally, one can remark that the present code, combining diffusion and drift mechanisms, is also suited to describe the modulation effect in periods when the solar activity is no longer at the maximum.

In Table 7 we present the averages  $\eta_{rms}$  (in percentage, %) during the periods dominated by high solar activity. The simulated differential intensities were obtained for a heliospheric region where solar latitudes are lower than  $|\delta_m|$  without any enhancement of the diffusion tensor along the polar direction ( $K_{\perp,\mu}$ ). The simulations with  $\rho_E = 8$  and 10 lead to  $\eta_{rms}$  comparable with those presented in Table 7. However, using  $\rho_E = 1$  provides a better agreement to experimental data at lower energy. From inspection of Table 7, one can note that “R” and “L” models for tilt angles yield comparable results within the precision of the method. Furthermore the minimum difference with the experimental data occurs when  $\rho_k = 0.10$  and  $\delta_m = (2.0 - 3.0) \times 10^{-5}$  with the “L” model slightly preferred to “R”. The HelMod parameter configuration, which minimizes the difference to the experimental data, are reported in Table 8: one may remark that the No Drift approximation is (almost) comparable to a drift treatment for both BESS-2000 and BESS-2002 with data collected during and after the maximum of the solar activity. Apparently, the drift treatment is needed in order to describe BESS-1999 with data taken during a period approaching the solar maximum.

In Figures 7, 8, and 9, the differential intensities determined with the HelMod code are shown and compared with the experimental data of BESS-1999, BESS-2000, and BESS-2002, respectively; in these figures, the dashed lines are the

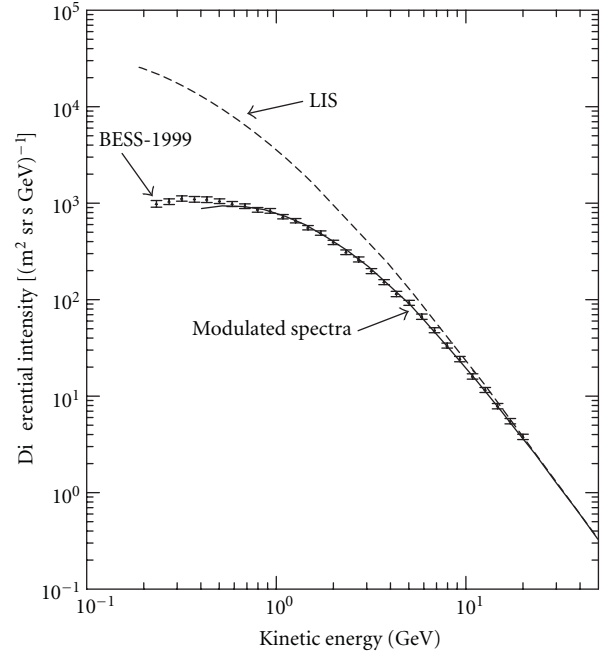


FIGURE 7: Proton differential intensity determined with the HelMod code (continuous line) compared to the experimental data of BESS-1999; the dashed line is the LIS (see the text).

TABLE 6: Average values (last three columns) of  $\eta_{rms}$  (in percentage, %) as a function of  $\delta_m$  ( $\times 10^{-5}$ ) and  $\rho_k$ , for BESS-1997, AMS-1998, PAMELA-2006/08, obtained from (17) without enhancement of the diffusion tensor along the polar direction ( $\rho_E = 1$ ), using “R” and “L” models for the tilt angle and No Drift approximation. The differential intensities were calculated accounting for particles inside the heliospheric regions for which solar latitudes are lower than  $|\delta_m|$ .

$\delta_m(\times 10^{-5})$	$\rho_k$	“R” model	“L” model	No drift
0.0	0.10	14.1	11.0	33.4
1.0	0.10	11.7	8.7	33.2
2.0	0.10	11.6	8.3	33.7
3.0	0.10	11.6	8.3	33.7
1.0	0.11	6.4	9.0	27.7
2.0	0.11	7.8	9.0	28.3
3.0	0.11	7.5	8.8	29.2
1.0	0.12	6.3	7.1	23.5
2.0	0.12	6.3	7.3	24.7
3.0	0.12	7.1	6.9	24.4
1.0	0.13	6.3	6.4	20.1
2.0	0.13	6.6	7.6	20.4
3.0	0.13	6.7	7.7	20.5
1.0	0.14	7.3	7.0	15.9
2.0	0.14	7.3	7.2	16.4
3.0	0.14	7.2	6.5	16.8

LIS as discussed in [2]. These modulated intensities are the ones calculated for a heliospheric region where solar latitudes are lower than  $|\delta_m|$ , using  $K_{\perp,\mu} = K_{\perp,r}$  independently of the

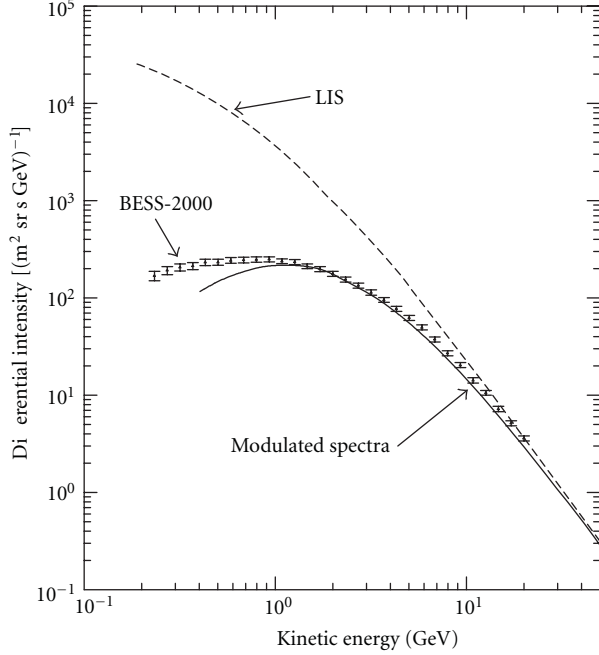


FIGURE 8: Proton differential intensity determined with the HelMod code (continuous line) compared to the experimental data of BESS-2000; the dashed line is the LIS (see the text).

TABLE 7: Average values (last three columns) of  $\eta_{rms}$  (in percentage, %) as a function of  $\delta_m (\times 10^{-5})$  and  $\rho_k$ , for BESS-1999, BESS-2000, BESS-2002 obtained from (17) without enhancement of the diffusion tensor along the polar direction ( $\rho_E = 1$ ), using “R” and “L” models for the tilt angle and No Drift approximation. The differential intensities were calculated accounting for particles inside the heliospheric regions for which solar latitudes are lower than  $|5.7^\circ|$ .

$\delta_m (\times 10^{-5})$	$\rho_k$	“R” model	“L” model	No drift
0.0	0.10	11.2	10.8	15.4
1.0	0.10	11.0	10.1	15.8
2.0	0.10	9.6	10.0	16.7
3.0	0.10	9.6	10.0	16.7
1.0	0.11	13.4	13.1	16.0
2.0	0.11	12.7	12.9	15.4
3.0	0.11	12.7	12.5	16.2
1.0	0.12	18.7	17.7	13.4
2.0	0.12	18.3	16.9	12.8
3.0	0.12	18.1	17.3	12.8
1.0	0.13	23.3	23.5	14.3
2.0	0.13	25.0	24.7	13.3
3.0	0.13	24.3	24.2	13.1
1.0	0.14	32.3	30.7	18.0
2.0	0.14	32.8	30.8	17.1
3.0	0.14	31.5	30.7	17.9

latitude and including particle drift effects with the values of the tilt angle from the “L” model. Finally, it is concluded that the present code combining diffusion and drift mechanisms

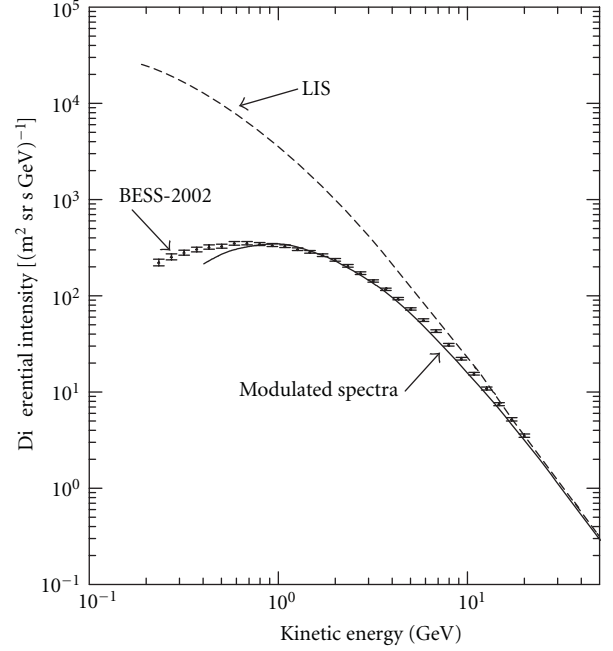


FIGURE 9: Proton differential intensity determined with the HelMod code (continuous line) compared to the experimental data of BESS-2002; the dashed line is the LIS (see the text).

TABLE 8: Average  $\eta_{rms}$  (in percentage, %), for BESS-1999, BESS-2000, and BESS-2002 obtained from (17) without enhancement of the diffusion tensor along the polar direction ( $\rho_E = 1$ ),  $\delta_m = 2.0 \times 10^{-5}$ ,  $\rho_k = 0.10$ , and using “R” and “L” models for the tilt angle and No Drift approximation. The differential intensities were calculated accounting for particles inside the heliospheric regions for which solar latitudes are lower than  $|5.7^\circ|$ .

Observations	“R” model	“L” model	No drift
BESS-1999	9.3	10.6	25.7
BESS-2000	12.5	12.6	16.7
BESS-2002	6.9	6.7	7.7

is suited to describe the modulation effect in periods with high solar activity [2, 50, 54].

## 6. Conclusion

In this work an IMF, which combines the Parker Field and its polar modification, is presented. In the polar regions, the Parker IMF was modified with an additional latitudinal components according to those proposed by Jokipii and Kota in [6]. We found the maximum perturbed value with this component yielding, as a physical result, streaming lines completely confined in the solar hemisphere of injection.

The proposed IMF is, then, used within the HelMod Monte Carlo code to determine the effects on the differential intensity of protons at 1 AU as a function of the extension of *polar region*, in which the modified magnetic-field is employed. We found that a *polar region* contained within  $30^\circ$  of colatitude is that one ensuring a very smooth transition to the equatorial region and allows to reproduce qualitatively

and quantitatively the latitudinal profile of the GCR intensity, and the latitudinal dip shift with respect to the ecliptic plane. Finally we determined how the *polar region* diffusion is mostly responsible of the proton intensity latitudinal gradient observed in the inner heliosphere with the Ulysses spacecraft during 1995.

## Acknowledgments

K. Kudela wishes to acknowledge VEGA Grant agency project 2/0081/10 for support. Finally, the authors acknowledge the use of NASA/GSFC's Space Physics Data Facility's OMNI-Web service and OMNI data.

## References

- [1] E. N. Parker, "The passage of energetic charged particles through interplanetary space," *Planetary and Space Science*, vol. 13, no. 1, pp. 9–49, 1965.
- [2] P. Bobik, G. Boella, M. J. Boschini et al., "Systematic investigation of solar modulation of galactic protons for solar cycle 23 using a monte carlo approach with particle drift effects and latitudinal dependence," *The Astrophysical Journal*, vol. 745, p. 132, 2012.
- [3] C. Leroy and P. G. Rancoita, *Principles of Radiation Interaction in Matter and Detection*, World Scientific Publishing, River Edge, NJ, USA, 3rd edition, 2011.
- [4] R. D. Strauss, M. S. Potgieter, and S. E. S. Ferreira, "Modeling ground and space based cosmic ray observations," *Advances in Space Research*, vol. 49, pp. 392–407, 2012.
- [5] E. N. Parker, "Dynamics of the interplanetary gas and magnetic fields," *The Astrophysical Journal*, vol. 128, p. 664, 1958.
- [6] J. R. Jokipii and J. Kota, "The polar heliospheric magnetic field," *Geophysical Research Letters*, vol. 16, pp. 1–4, 1989.
- [7] U. W. Langner, *Effect of termination shock acceleration on cosmic ray in the heliosphere [Ph.D. thesis]*, Potchestroom University, Potchestroom, South Africa, 2004.
- [8] B. Heber, W. Dröge, P. Ferrando et al., "Spatial variation of >40 MeV/n nuclei fluxes observed during the Ulysses rapid latitude scan," *Astronomy and Astrophysics*, vol. 316, no. 2, pp. 538–546, 1996.
- [9] J. A. Simpson, "Ulysses cosmic-ray investigations extending from the south to the north polar regions of the Sun and heliosphere," *Nuovo Cimento della Societa Italiana di Fisica C*, vol. 19, no. 6, pp. 935–943, 1996.
- [10] R. D. Strauss, M. S. Potgieter, I. Büsching, and A. Kopp, "Modeling the modulation of galactic and jovian electrons by stochastic processes," *The Astrophysical Journal Letters*, vol. 735, no. 2, article 83, 2011.
- [11] E. N. Parker, "Newtonian development of the dynamical properties of ionized gases of low density," *Physical Review*, vol. 107, pp. 924–933, 1957.
- [12] E. N. Parker, "The hydrodynamic theory of solar corpuscular radiation and stellar winds," *The Astrophysical Journal*, vol. 132, p. 821, 1960.
- [13] E. N. Parker, "Sudden expansion of the corona following a large solar flare and the attendant magnetic field and cosmic-ray effects," *The Astrophysical Journal*, vol. 133, p. 1014, 1961.
- [14] E. N. Parker, *Interplanetary Dynamical Processes*, Wiley-Interscience, New York, NY, USA, 1963.
- [15] M. Hattingh and R. A. Burger, "A new simulated wavy neutral sheet drift model," *Advances in Space Research*, vol. 16, no. 9, pp. 213–216, 1995.
- [16] J. H. King and N. E. Papitashvili, "Solar wind spatial scales in and comparisons of hourly Wind and ACE plasma and magnetic field data," *Journal of Geophysical Research A*, vol. 110, no. 2, Article ID A02104, 2005.
- [17] NASA-OMNIweb, online database, 2012, <http://omniweb.gsfc.nasa.gov/form/dx1.html>.
- [18] J. R. Jokipii and B. Thomas, "Effects of drift on the transport of cosmic rays. IV—modulation by a wavy interplanetary current sheet," *The Astrophysical Journal*, vol. 243, pp. 1115–1122, 1981.
- [19] J. R. Jokipii, E. H. Levy, and W. B. Hubbard, "Effect of particle drift on cosmic-ray transport. I. general properties, application to solar modulation," *The Astrophysical Journal Letters*, vol. 213, pp. L85–L88, 1977.
- [20] E. Marsch, W. I. Axford, and J. F. McKenzie, "Solar wind," in *Dynamic Sun*, B. N. Dwivedi, Ed., pp. 374–402, 2003.
- [21] J. R. Jokipii and E. H. Levy, "Effects of particle drifts on the solar modulation of galactic cosmic rays," *The Astrophysical Journal Letters*, vol. 213, pp. L85–L88, 1977.
- [22] M. S. Potgieter and H. Moraal, "A drift model for the modulation of galactic cosmic rays," *The Astrophysical Journal*, vol. 294, part 1, pp. 425–440, 1985.
- [23] R. A. Burger and M. Hattingh, "Steady-state drift-dominated modulation models for galactic cosmic rays," *Astrophysics and Space Science*, vol. 230, no. 1-2, pp. 375–382, 1995.
- [24] J. R. Jokipii and E. N. Parker, "On the convection, diffusion, and adiabatic deceleration of cosmic rays in the solar wind," *The Astrophysical Journal*, vol. 160, p. 735, 1970.
- [25] L. J. Gleeson and W. I. Axford, "Solar modulation of galactic cosmic rays," *The Astrophysical Journal*, vol. 154, p. 1011, 1968.
- [26] Y. Yamada, S. Yanagita, and T. Yoshida, "A stochastic view of the solar modulation phenomena of cosmic rays," *Geophysical Research Letters*, vol. 25, pp. 2353–2356, 1998.
- [27] M. Gervasi, P. G. Rancoita, I. G. Usoskin, and G. A. Kovaltsov, "Monte-Carlo approach to Galactic cosmic ray propagation in the heliosphere," *Nuclear Physics B*, vol. 78, no. 1–3, pp. 26–31, 1999.
- [28] M. Zhang, "A Markov stochastic process theory of cosmic-ray modulation," *The Astrophysical Journal*, vol. 513, pp. 409–420, 1999.
- [29] K. Alanko-Huotari, I. G. Usoskin, K. Mursula, and G. A. Kovaltsov, "Stochastic simulation of cosmic ray modulation including a wavy heliospheric current sheet," *Journal of Geophysical Research A*, vol. 112, no. 8, Article ID A08101, 2007.
- [30] C. Pei, J. W. Bieber, R. A. Burger, and J. Clem, "A general time-dependent stochastic method for solving Parker's transport equation in spherical coordinates," *Journal of Geophysical Research A*, vol. 115, no. 12, Article ID A12107, 2010.
- [31] C. W. Gardiner, *Handbook of Stochastic Methods: For Physics, Chemistry and Natural Sciences*, Springer, New York, NY, USA, 1985.
- [32] J. R. Jokipii, "Propagation of cosmic rays in the solar wind," *Reviews of Geophysics and Space Physics*, vol. 9, pp. 27–87, 1971.
- [33] I. D. Palmer, "Transport coefficients of low-energy cosmic rays in interplanetary," *Reviews of Geophysics and Space Physics*, vol. 20, pp. 335–351, 1982.
- [34] M. S. Potgieter and S. E. S. Ferreira, "Effects of the solar wind termination shock on the modulation of Jovian and galactic

- electrons in the heliosphere,” *Journal of Geophysical Research A*, vol. 107, article 1089, 9 pages, 2002.
- [35] W. Dröge, “Probing heliospheric diffusion coefficients with solar energetic particles,” *Advances in Space Research*, vol. 35, no. 4, pp. 532–542, 2005.
- [36] F. B. McDonald, P. Ferrando, B. Heber et al., “A comparative study of cosmic ray radial and latitudinal gradients in the inner and outer heliosphere,” *Journal of Geophysical Research A*, vol. 102, no. 3, pp. 4643–4651, 1997.
- [37] SIDC-team, “The International Sunspot Number,” Monthly Report on the International Sunspot Number, online catalogue, 1964–2010.
- [38] I. G. Usoskin, G. A. Bazilevskaya, and G. A. Kovaltsov, “Solar modulation parameter for cosmic rays since 1936 reconstructed from ground-based neutron monitors and ionization chambers,” *Journal of Geophysical Research A*, vol. 116, no. 2, Article ID A02104, 2011.
- [39] A. Balogh, E. J. Smith, B. T. Tsurutani, D. J. Southwood, R. J. Forsyth, and T. S. Horbury, “The heliospheric magnetic field over the south polar region of the sun,” *Science*, vol. 268, no. 5213, pp. 1007–1010, 1995.
- [40] H. Moraal, “Proton modulation near solar minimum periods in consecutive solar cycles,” in *Proceedings of the International Cosmic Ray Conference*, vol. 6, p. 140, 1990.
- [41] C. W. Smith and J. W. Bieber, “Solar cycle variation of the interplanetary magnetic field spiral,” *The Astrophysical Journal Letters*, vol. 370, no. 1, pp. 435–441, 1991.
- [42] L. A. Fisk, “Motion of the footpoints of heliospheric magnetic field lines at the sun: implications for recurrent energetic particle events at high heliographic latitudes,” *Journal of Geophysical Research*, vol. 101, pp. 15547–15554, 1996.
- [43] M. Hitge and R. A. Burger, “Cosmic ray modulation with a Fisk-type heliospheric magnetic field and a latitude-dependent solar wind speed,” *Advances in Space Research*, vol. 45, no. 1, pp. 18–27, 2010.
- [44] T. R. Sanderson, R. G. Marsden, K. P. Wenzel, A. Balogh, R. J. Forsyth, and B. E. Goldstein, “High-latitude observations of energetic ions during the first Ulysses polar pass,” *Space Science Reviews*, vol. 72, no. 1-2, pp. 291–296, 1995.
- [45] R. G. Marsden, “The 3-D heliosphere at solar maximum,” *The Publications of the Astronomical Society of the Pacific*, vol. 113, pp. 129–130, 2001.
- [46] A. Balogh, R. G. Marsden, and E. J. Smith, *The Heliosphere Near Solar Minimum. The Ulysses Perspective*, Springer, New York, NY, USA, 2001.
- [47] B. Heber, M. S. Potgieter, and P. Ferrando, “Solar modulation of galactic cosmic rays: the 3D heliosphere,” *Advances in Space Research*, vol. 19, no. 5, pp. 795–804, 1997.
- [48] M. S. Potgieter, “Heliospheric modulation of cosmic ray protons: role of enhanced perpendicular diffusion during periods of minimum solar modulation,” *Journal of Geophysical Research A*, vol. 105, no. 8, pp. 18295–18303, 2000.
- [49] J. T. Hoeksema, “The large-scale structure of the heliospheric current sheet during the Ulysses epoch,” *Space Science Reviews*, vol. 72, no. 1-2, pp. 137–148, 1995.
- [50] S. E. S. Ferreira and M. S. Potgieter, “Long-term cosmic-ray modulation in the heliosphere,” *The Astrophysical Journal*, vol. 603, pp. 744–752, 2004.
- [51] Y. Shikaze, S. Orito, S. Haino et al., “Measurements of 0.2–20 GeV/n cosmic-ray proton and helium spectra from 1997 through 2002 with the BESS spectrometer,” *Astroparticle Physics*, vol. 28, no. 1, pp. 154–167, 2007.
- [52] M. Aguilar, J. Alcaraz, and J. Allaby, “The Alpha Magnetic Spectrometer (AMS) on the International Space Station: part I—results from the test flight on the space shuttle,” *Physics Reports*, vol. 366, pp. 331–405, 2002.
- [53] O. Adriani, G. C. Barbarino, G. A. Bazilevskaya et al., “PAMELA measurements of cosmic-ray proton and helium spectra,” *Science*, vol. 332, no. 6025, pp. 69–72, 2011.
- [54] D. C. Ndiitwani, S. E. S. Ferreira, M. S. Potgieter, and B. Heber, “Modelling cosmic ray intensities along the Ulysses trajectory,” *Annales Geophysicae*, vol. 23, no. 3, pp. 1061–1070, 2005.

## Research Article

# Thirty-Year Periodicity of Cosmic Rays

Jorge Pérez-Peraza,<sup>1</sup> Víctor Velasco,<sup>1</sup> Igor Ya. Libin,<sup>2</sup> and K. F. Yudakhin<sup>3</sup>

<sup>1</sup>*Instituto de Geofísica, Universidad Nacional Autónoma de México, C.U., 04510 Coyoacán, DF, Mexico*

<sup>2</sup>*International Academy for Appraisal and Consulting (MAOK), Moscow, Russia*

<sup>3</sup>*IZMIRAN, Academy of Sciences of Russia, Troitsk, Moscow 142092, Russia*

Correspondence should be addressed to Jorge Pérez-Peraza, perperaz@yahoo.com.mx

Received 6 September 2012; Accepted 27 October 2012

Academic Editor: Karel Kudela

Copyright © 2012 Jorge Pérez-Peraza et al. This is an open access article distributed under the Creative Commons Attribution License, which permits unrestricted use, distribution, and reproduction in any medium, provided the original work is properly cited.

Cosmogenic isotopes have frequently been employed as proxies of ancient cosmic ray fluxes. On the basis of periodicities of the <sup>10</sup>Be time series (using data from both the South and North Poles) and the <sup>14</sup>C time series (with data from Intercal-98), we offer evidence of the existence of cosmic ray fluctuations with a periodicity of around 30 years. Results were obtained by using the wavelet transformation spectral technique, signal reconstruction by autoregressive spectral analysis (ARMA), and the Lomb-Scargle periodogram method. This 30-year periodicity seems to be significant in nature because several solar and climatic indexes exhibit the same modulation, which may indicate that the 30-year frequency of cosmic rays is probably a modulator agent for terrestrial phenomena, reflecting the control source, namely, solar activity.

## 1. Introduction

The importance of cosmic ray variations was pointed out long ago in a vast compendium of relevant research [1]. Here we encounter a periodicity that has not been studied within the framework of cosmic ray variations. Let us begin by emphasizing that 30-years cycles are quite common in nature: the so-called Markowitz wave (Markowitz wobble-MW) is a quasi-harmonic variation of the middle pole of the Earth with a period of 30 year and an amplitude of 0.02'' - 0.03'' [2]. Similar results were obtained in different years by many researchers who were trying to measure the Earth's magnetic field [3–5], by evaluating the conductivity of the lower mantle and who established 60- and 30-year variations of the geomagnetic field of the lower mantle. The authors in [6], through studies of high-growth anomalies of the secular variation with foci located in South Asia and in the middle of the Indian Ocean, revealed that the increase in the current focus is the initial stage of the 30-year and 60-year variations.

Authors in [4] by evaluating the conductivity of the lower mantle have found evidence of 60 - and 30-year variations in the geomagnetic field. By conducting a qualitative analysis of timelines with data from planetary indices Ap/aa, interplanetary magnetic field intensity and sunspot numbers, as

well as cosmic rays data strings taken from 1937 to 2010 [7, 8] have shown quasi-periodic three-cycle trends, which are particularly very well correlated with solar wind, polar coronal holes and the size of solar activity cycle 23 [9, 10].

Authors in [11] have found 32-year variations in temperature by analyzing the spectrum of periodical air-surface temperature fluctuations for 1423 years in Greenland ice cores, and for 1400 and 800 years in the California Arctic pine tree rings. A 30-year variation in storminess data was found by applying the “Caterpillar” method in [12]. In fact, the authors identified frequencies at 90 to 100 years, 28 to 32 years, 20 to 22 years, 9 to 13 years, and some others; it is shown that even if the accuracy of this method for determining periods is not high, the fundamental frequency obtained by the “Caterpillar” is real.

The application of wavelet analysis to the paleoclimatic proxy data [13] to large-scale atmospheric phenomena (the Atlantic Multidecadal Oscillation and Southern Oscillation Indexes), and hurricane phenomena, led to the discovery of a high coherence with periods of  $30 \pm 2$  years, between climatic oscillations and cosmic rays (<sup>10</sup>Be at the North Pole). Furthermore, some properties of hurricanes, such as their total cyclonal energy and the tropical storms appearance along the Atlantic coast of México, together with other

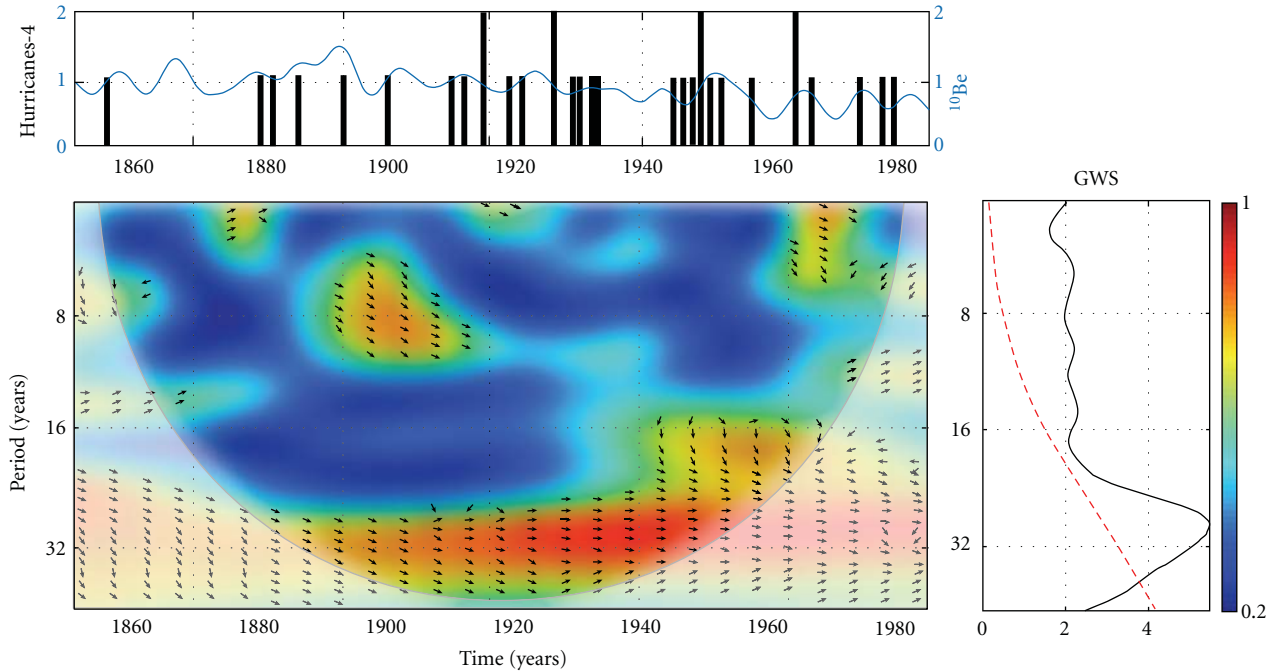


FIGURE 1: The upper panel shows time series of category-4 hurricane versus  $^{10}\text{Be}$ . The coherence between both series appears in the middle panel, and the global wavelet spectrum (GWS) appears in the right-hand part of the figure, where the red dashed line indicates the border, also with the reliability of 95%. The scale color bar at the right indicates the level of coherence.

properties linked to hurricanes show such a 30-year cycle [14]. Figure 1 illustrates the particular case of category-4 hurricanes

Curiously, not only in nature but in several areas of contemporary human activity, such as business and commerce, 30-year cycle indexes are also found. (e.g., <http://www.search.yahoo.com/search?p=30+years+cycle&ei=UTF-8&fr=mz35/>). Incidentally, they are often associated with solar activity.

In the present work, we present evidence of the existence of a thirty-year periodicity for the cosmic rays: preliminary results were presented at the 2008COSPAR meeting in Montreal.

## 2. Data and the Spectral Wavelet Analysis

The spectral analysis of cosmic ray data from neutron monitors has been widely studied through several different methods, for instance [1, 15–18] and references included. Though most of these studies are out of the scope of this work, since they rather concern short-term periodicities, they are, however, very helpful for solar-terrestrial physics.

One of the main problems in determining significant long-term periodicities in the flux of cosmic rays is that the time series of data are relatively very short, as they have been available only for the last five to six decades, when data on cosmic rays (CR) from different stations throughout the world began to be organized and homologated. Because of this restriction, a proxy for cosmic rays has often been employed, one of which in our case allows us in a

deterministic way to provide evidence of a 30-year cycle for cosmic rays.

The cosmogenic isotopes Beryllium-10 ( $^{10}\text{Be}$ ) and Carbon-14 ( $^{14}\text{C}$ ) are conventionally considered to be proxies for cosmic rays, in such a way that an adequate spectral analysis may reveal important periodicities. These cosmogenic isotopes are mainly produced by galactic cosmic ray flux modulated by changes in interplanetary and geomagnetic magnetic fields. The analysis of cosmogenic isotopes stored in natural archives, such as  $^{10}\text{Be}$  in polar ice cores and  $^{14}\text{C}$  in tree rings, provides a means of extending our knowledge of solar variability over much longer periods (e.g., [19, 20]). In addition, the nature of climatic response to solar variability can be assessed over several time scales. It should be remembered that the analysis of the cosmogenic isotopes record is more difficult than the analysis of sunspot numbers. This is due to the fact the  $^{14}\text{C}$  and  $^{10}\text{Be}$  concentrations reflect the production rate, which is modulated by not only solar activity but also by atmospheric transport and deposition processes [21, 22]

Data on  $^{10}\text{Be}$  and  $^{14}\text{C}$  can be obtained for periods of thousands of years: we use the INTCAL 98 (<http://www.depts.washington.edu/qil/>) for the  $^{14}\text{C}$  time series and the  $^{10}\text{Be}$  time series from [21], which give the concentration found in the Dye-3 ice core (62.5 N, 43.8 W). For the South Pole we used data from [23].

The spectral techniques for analyzing periodicities of cosmophysical phenomena are very varied. The simplest technique for investigating periodicities is the Fourier Transform (FT). Although useful for stationary time series, this method is not appropriate for time series that do not fulfill

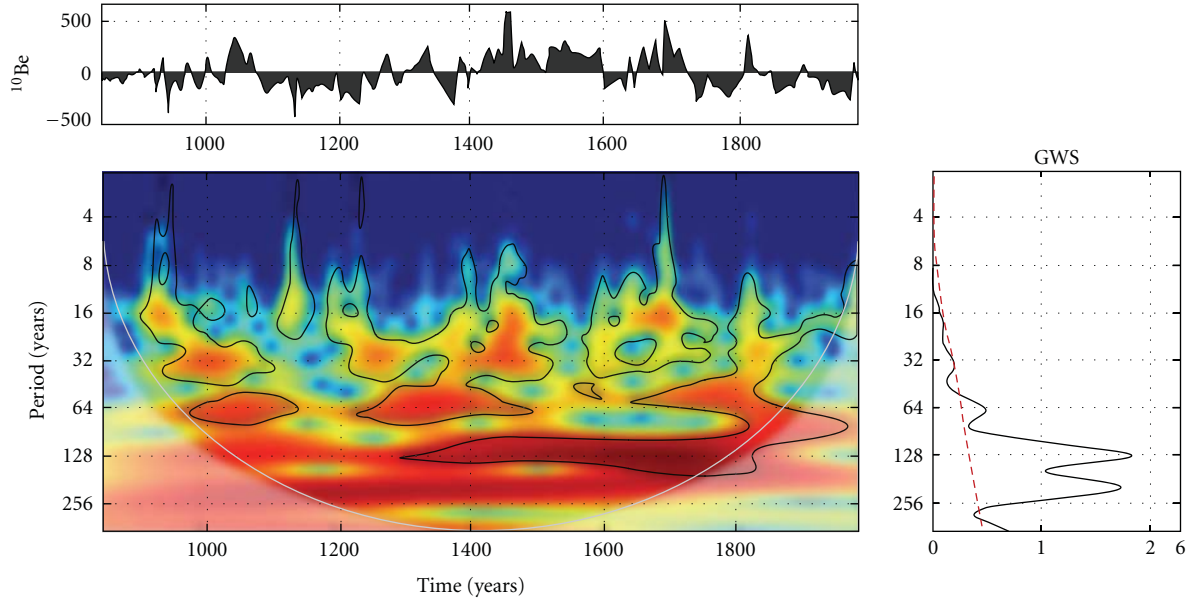


FIGURE 2: The upper panel shows the time series of the  $\text{Be}^{10}$  from the South Pole. The wavelet spectrum appears in the middle panel, and the global wavelet spectra appear in the right-most part of the figure, where the red dashed line indicates the border of 95% reliability.

the steady state condition, as is the case with cosmogenic isotopes.

In order to find the time evolution of the main frequencies of the time series, we apply the wavelet method using the Morlet mother wavelet ([24–26]. Wavelet analysis can be used for analyzing localized variations of power within a given time series at many different frequencies. However, even using this powerful tool, the reconstruction (filtering) of a signal is one of the main problems in the field, as is well known in Signals Theory and signal processing; this follows from the fact that the use of indiscriminate algorithms may lead to findings of spurious nonexistent periodicities in the time series. Furthermore, some real existing frequencies may be masked by more prominent frequencies. To avoid these problems, the Daubechies algorithm [27] has been used. This has proven to be highly efficient for the decomposition of signals in low and high frequencies, with the advantage that it does not create fictitious periodicities in the time series and, in some cases, may be more powerful than the multianalysis wavelet procedure (see Appendix A).

In Figures 2 to 7 we present the results of the wavelet analysis for the time series: the time series studied; the time series themselves are shown in the upper panel. The wavelet Morlet spectrum for the series appears in the mid panel of every figure, and the global wavelet spectrum appears in the right-hand part of the figures, where the dashed line indicates a border of 95% reliability.

It can be seen in Figure 2 that the 30-year periodicity has a confidence of 95%; however, it looks less prominent relative to the 60, 120, and 240 years frequencies, which show confidences far above 95%.

Figure 3 shows the Wavelet of  $^{14}\text{C}$ ; it can be seen that precisely at the 30-yr. frequency there appears a small hump relative to the importance of the other periodicities. It would

then be natural to ask how to know if such periodicity really does exist with a good reliability.

This turns out to be a very complex problem, to give relevance to the periodicity of 30 years; on the other hand, it is necessary for one side to filter that signal and, on the other hand, to eliminate masking frequencies higher or lower than 30 years. It is precisely in such a situation that the *Daubechies* algorithm [27] turns out to be a very powerful tool, as shown in Figures 4 and 5 where, after the filtering process, the 30-year frequency for  $^{10}\text{Be}$  and  $^{14}\text{C}$  at the North Pole appears very clearly, both with high reliability, far above 95%.

The way to discern whether the periodicity of 30 years found in the  $^{10}\text{Be}$  time series really reflects a cosmic ray fluctuation or is merely a local phenomenon of the cosmogenic isotope at earth level is to compare the behavior of  $^{10}\text{Be}$  at both the North and South Poles. Since concentrations are quite different from one pole to another, it should be expected that their behavior would also be quite different if the existence of such periodicity is a local phenomenon. However, an examination of Figure 6 indicates that the wavelet coherence between the  $^{10}\text{Be}$  at both the North and South Poles is very high,  $>0.9$  (red color in the color bar of Figure 1)) at their common frequencies. This is an alternative way to confirm other arguments published in the literature, that this particular cosmogenic isotope is a proxy of cosmic rays.

Cosmic ray variations are mostly caused by time variations in the interplanetary magnetic field (IMF), so periodicities in cosmic ray data must be reflected in IMF data. Unfortunately, confident data from the IMF only date from the beginning of the spacecraft era, not even two 30-year cycles. However, since presumably the main source of such modulation is found in solar activity (SA); to confirm such an hypothesis we carried out a wavelet analysis of SA by

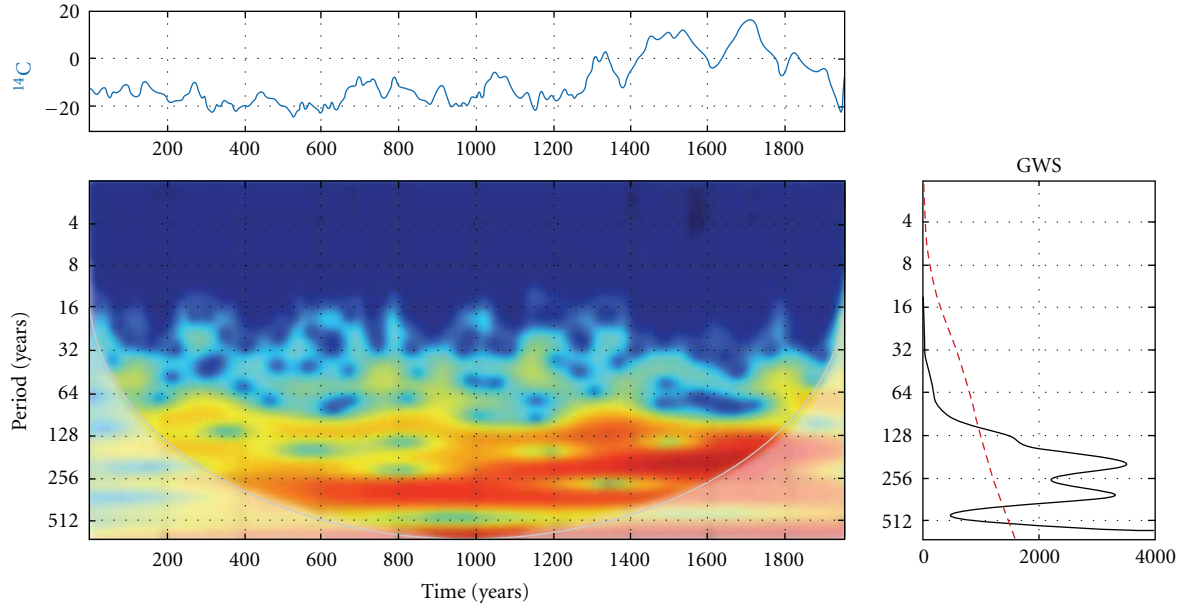


FIGURE 3: The upper panel shows the time series for the  $^{14}\text{C}$  from the South Pole. The wavelet spectrum appears in the middle panel, and the global wavelet Spectrum appears in the right-hand part of the figure, where the red dashed line indicates a border of reliability of 95%.

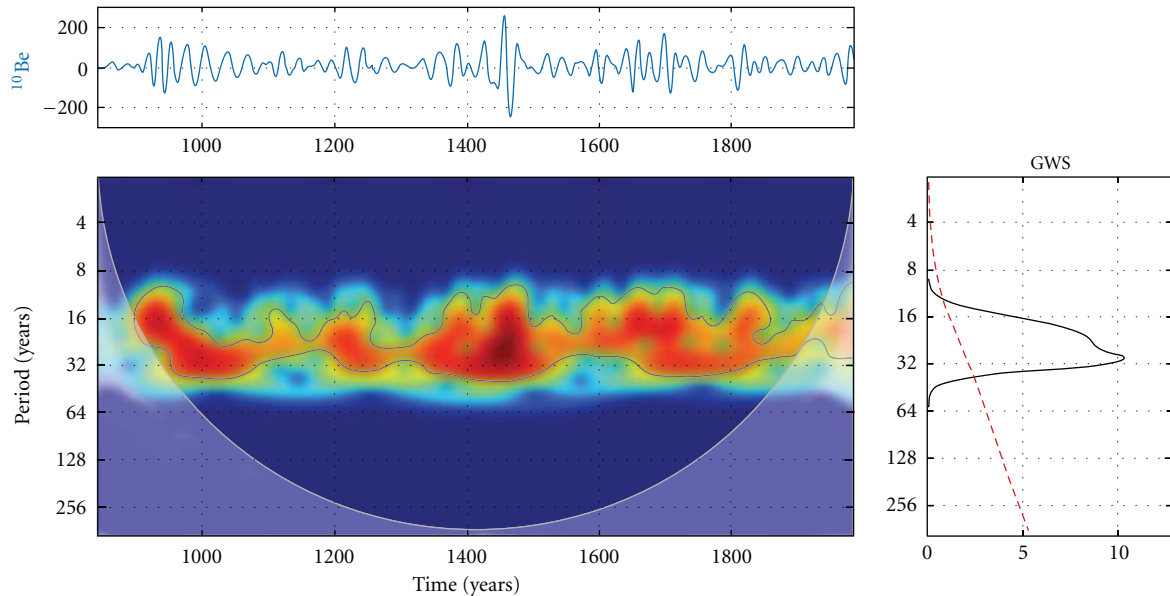


FIGURE 4: The upper panel shows the ( $^{10}\text{Be}$ ) time series in the North Pole. The wavelet spectrum is a continuous one throughout all the entire time scale. The global spectrum at the right-hand panel shows that the 30-year periodicity has an extremely high confidence level.

using a time series of sunspot data ([ftp://ftp.ngdc.noaa.gov/STP/SOLAR\\_DATA/SUNSPOT\\_NUMBERS/](ftp://ftp.ngdc.noaa.gov/STP/SOLAR_DATA/SUNSPOT_NUMBERS/) and also <http://sidc.oma.be/sunspot-data/>). This analysis allows us once again to find the existence of such a 30-year frequency (Figure 7), where the results are presented without filters.

Since the 30-year periodicity appears as a small peak, (though one with higher than 95% confidence), instead of applying the Daubechies filter [27], to confirm that its existence is real, we have applied collateral methods that confirm such a periodicity for cosmic rays. In the next section the periodicity of 30 years of solar activity is clearly shown,

which in the unfiltered spectrum of Figure 7 is just barely perceptible.

### 3. Autoregressive Spectral Analysis ARMA

To verify the results obtained, Libin and Yudakin have calculated the mutual power spectra and coherence spectra for solar activity and temperature (Figure 8), solar activity and storminess (Figure 9), solar activity and the level of Lake Baykal (Figure 10) and, finally, solar activity and cosmic ray intensity from neutron monitor data and measurements

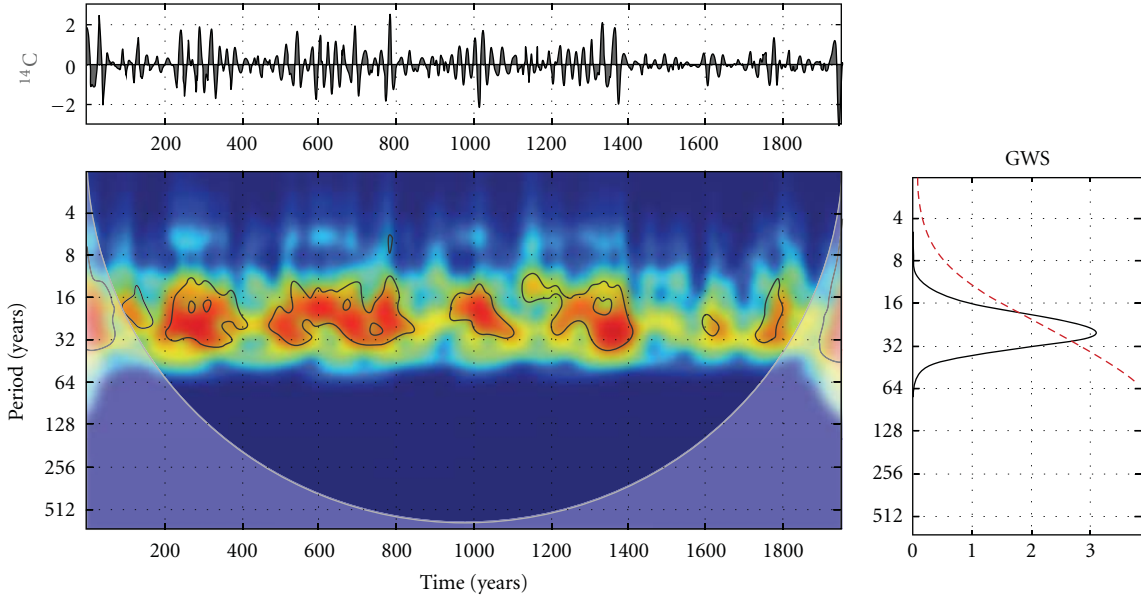


FIGURE 5: The upper panel shows the ( $^{14}\text{C}$ ) time series. The wavelet spectrum is a continuous one throughout the entire time scale. The global spectrum at the right panel shows that the 30-years periodicity has a confidence level higher than 95%.

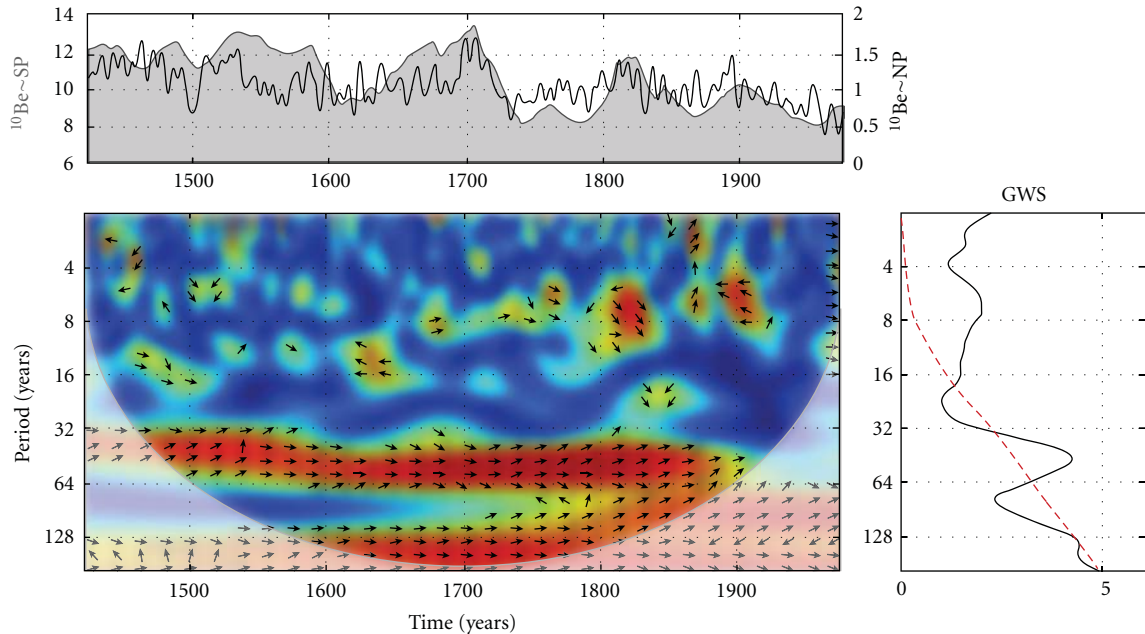


FIGURE 6: The upper panel shows the time series of  $^{10}\text{Be}$  at the South Pole versus the  $^{10}\text{Be}$  time series at the North Pole (black line). The middle panel shows a high coherence ( $>0.9$ ) between both series, according to the color bar for coherence level in Figure 1. The right panel shows the global wavelet spectrum where the dotted line represents the border of 95% of reliability.

of  $^{10}\text{Be}$  (Figure 11) for different measurement periods (see the data in the graphs). Calculations were made using the spectra of autoregressive spectral analysis with simultaneous ARMA (see Appendix B) and filtering the input data with the suppression of 11-year and 22-year variations.

All the above figures show the presence of stable 30-year fluctuations for almost all the processes. Although the coefficients of coherence are not always superior to a 95%

confidence interval probability the observed peaks are almost always above 90%.

#### 4. The Standard Lomb-Scargle Periodogram Method

The author in [28] using the Lomb-Scargle technique has built periodograms based on the long-time series data:

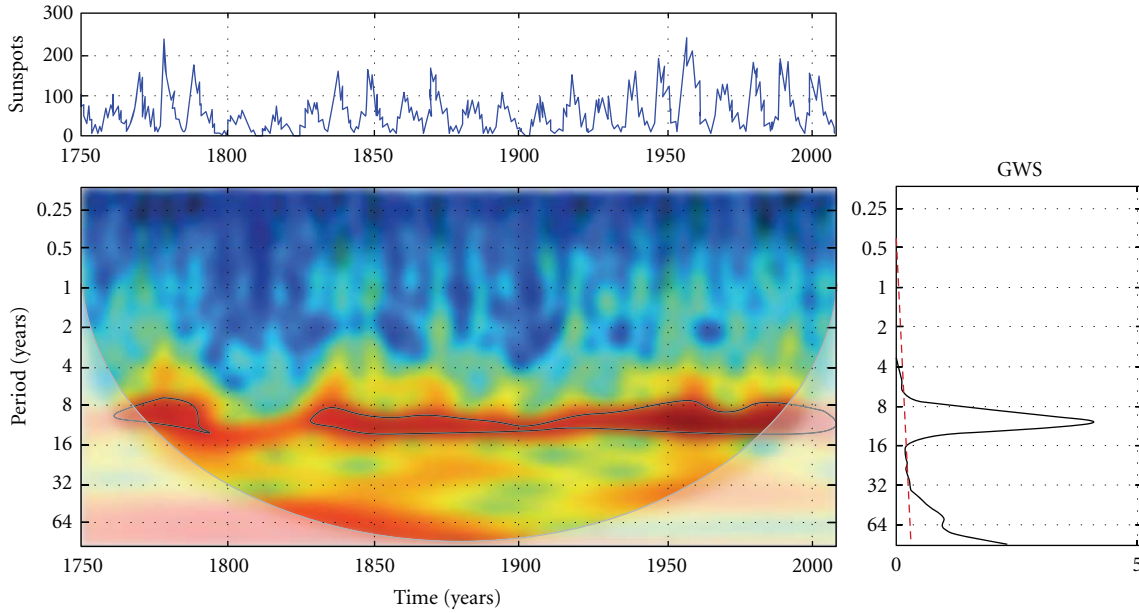


FIGURE 7: The upper panel shows the sunspot time series, the middle panel shows the wavelet spectrum, and the right panel shows the global spectrum, where the 30-year periodicity appears as a very small jump relative to the 11-year peak.

Figure 12 shows the periodogram, based on data from direct monthly stratospheric measurements of CR provided routinely over a long time period [29, 30]:

It can be seen that an approximately 34-year cycle is present in the data. A similar indication was obtained from the data of a modulation parameter of CR from [31], as shown in Figure 13.

## 5. Conclusions

We have shown the existence of a 30-year periodicity for cosmic rays. We can argue here that such a frequency is quite probably a modulator for terrestrial phenomena: it seems that in some way cosmic rays modulate climatic phenomena, such as the Atlantic Multidecadal Oscillation (AMO) and sea-surface temperature (SST), and these, in turn, modulate hurricane development [31, 32]. Furthermore, a wavelet analysis applied to paleoclimatic proxy data for large scale atmospheric phenomena (Atlantic Multidecadal Oscillation and Southern Oscillation Indexes) has revealed coherence between climatic oscillations and cosmic rays on a 30-yr cycle [14]. Since this periodicity is present throughout the entire interval under study, the origin of such a periodicity may be associated with the 120-year secular cycle of solar activity whose presence has been demonstrated in [17]. It corresponds to continuous periods of increasing and decreasing activity during maxima and minima of that secular cycle. The 60- and 240-year solar activity cycles may, then, also be associated with the 30-year cycle. This would confirm that *Solar Activity is the source of all cosmophysical modulators of Solar-Terrestrial relationships*, through a number of intermediaries at short, medium and long frequencies. One of them, in particular, is the 30-years periodicity found in this

work, which allows for the analysis of a reasonable long-term variability for Cosmic rays.

## Appendices

### A.

*Inverse Wavelet Transform.* We use the inverse wavelet transform to obtain the decomposition of a signal which can be obtained from a time-scale filter [27]. The inverse wavelet transform is defined [25] as

$$X_n = \frac{\delta_j \delta_t^{1/2}}{C_\delta \psi_0(0)} \sum_{j=0}^J \frac{\text{Re}\{W_n(s_j)\}}{s_j^{1/2}}, \quad (\text{A.1})$$

where  $\delta_j$  is the factor for scale averaging,  $C_\delta$  is a constant ( $\delta_j = 0.6$  and  $C_\delta = 0.776$ , for the Morlet wavelet), and  $\psi_0$  removes the energy scaling. We use the inverse wavelet transform to obtain the time series.

### B.

*Autoregressive Moving-Average Model.* The autoregressive moving-average model (ARMA) is one of the mathematical models used for the analysis and prediction of stationary time series in statistics. The ARMA model is a generalization of two simpler time series models—an autoregressive model (AR) and the moving average model (MA).

The ARMA ( $p, q$ ) model, where  $p$  and  $q$  are integers that specify the order of the model is called the next generation process time series  $\{X_t\}$ :

$$X_t = c + \varepsilon_t + \sum_{i=1}^p \alpha_i X_{t-i} + \sum_{i=1}^q \beta_i \varepsilon_{t-i}, \quad (\text{B.1})$$

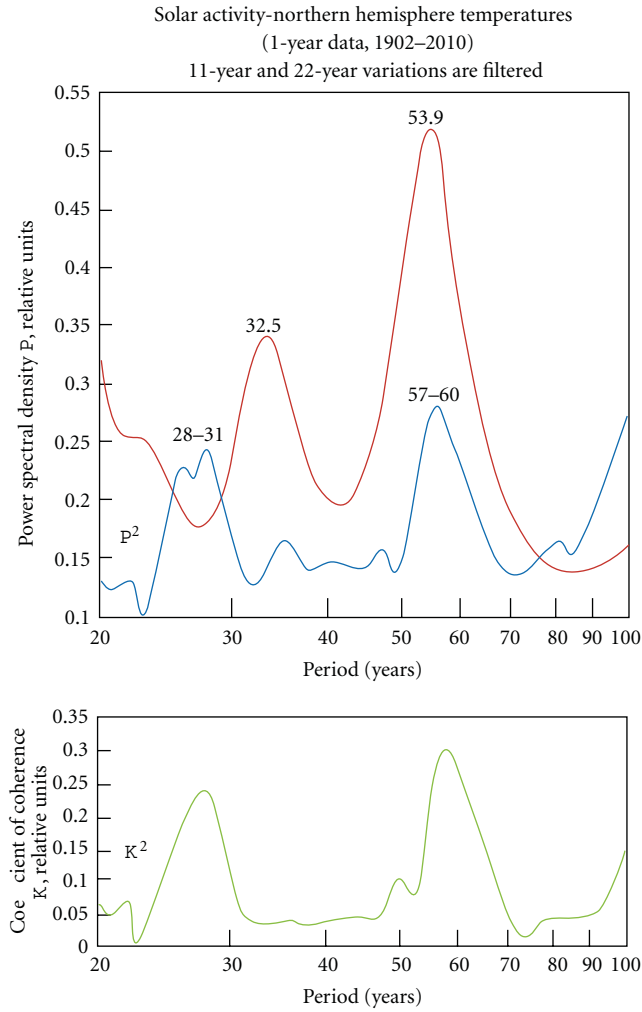


FIGURE 8: Power spectra density of solar activity and northern hemisphere temperature (1902–2010, blue) and power spectra density of greenland ice cores (red).  $K^2$  for solar activity and temperature.

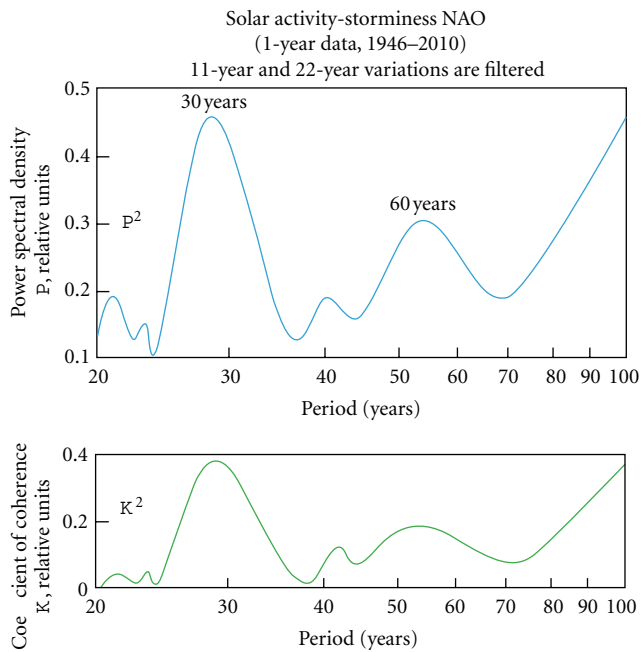


FIGURE 9: Power spectra density of solar activity and storminess (1946–2010)

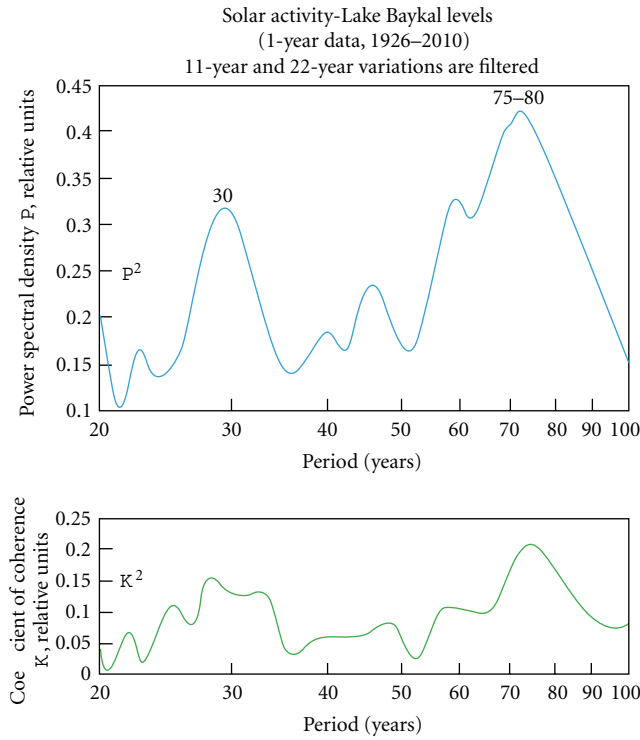


FIGURE 10: Power spectra density of solar activity and lake baykal levels l (1926–2010).

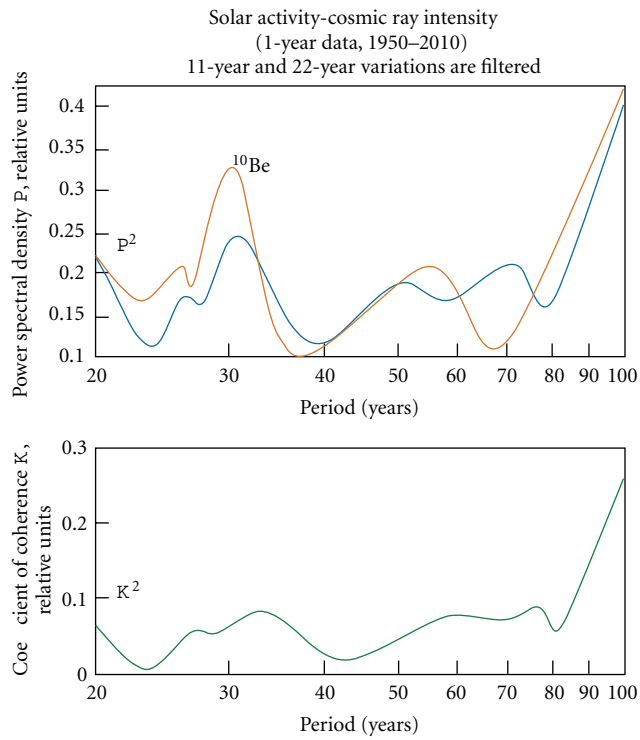


FIGURE 11: Power spectra density of solar activity and cosmic ray intensity (1950–2010, blue) and power spectra density of solar activity and  $^{10}\text{Be}$  (1482–2010, red).  $K^2$  for Solar Activity and Cosmic ray Intensity.

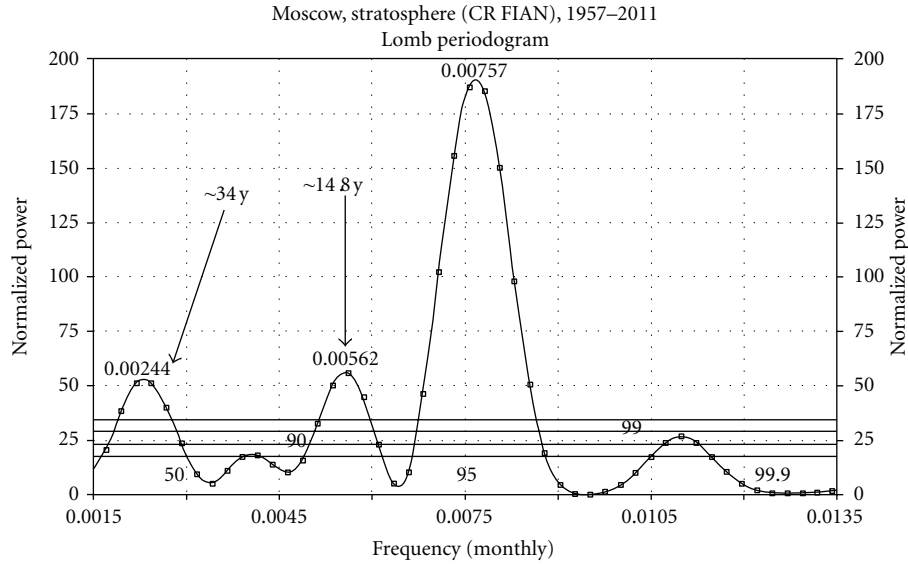


FIGURE 12: Periodogram of the monthly means of monthly stratospheric CR measurements near Moscow [29, 30]. Along with the highest peak at approximately 11 years, the approximately 34-year cycle peak and the approximately 14.8-year peak exceed a significance level of 0.99.

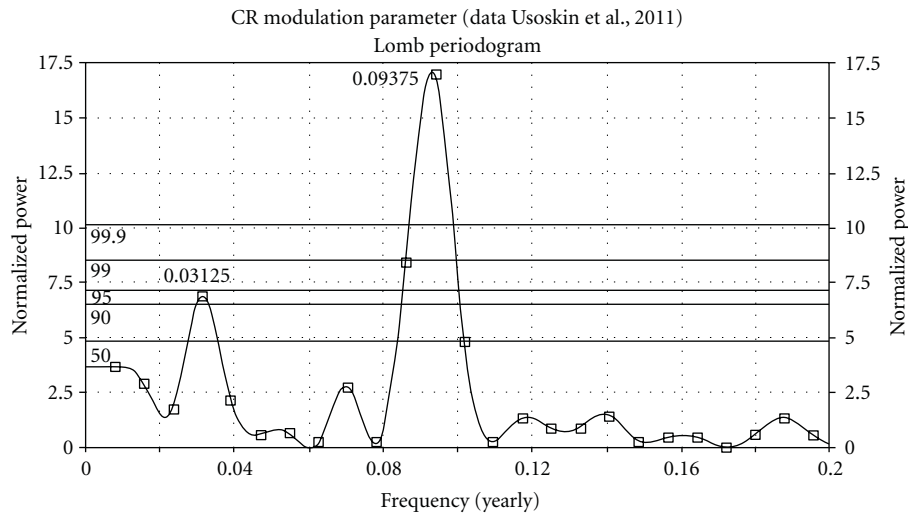


FIGURE 13: The highest maximum is at 11 years. The second most pronounced one is at approximately 0.031, corresponding to approximately 32 years. Here the levels of significance correspond to white noise.

where  $C$  is constant,  $\{\varepsilon_t\}$  represents white noise, and  $\alpha_1, \dots, \alpha_p$  and  $\beta_1, \dots, \beta_q$  are real numbers, the coefficients of the autoregressive, and moving average coefficients, respectively.

Such a model can be interpreted as a linear multiple regression model, in which the explanatory variables are the past values of the dependent variable itself, but as a regression balance—moving averages of the elements of white noise. ARMA-processes are more complex compared to similar processes in a pure form; however the ARMA processes are characterized by fewer parameters, which is one of their advantages.

If we introduce the lag operator  $L : Lx_t = x_{t-1}$ , then the ARMA model can be written as follows:

$$\left(1 - \sum_{i=1}^p \alpha_i L^i\right) X_t = c + \left(1 + \sum_{i=1}^q \beta_i L^i\right) \varepsilon_t. \quad (\text{B.2})$$

Introducing the shorthand notation for polynomials of the left and right sides, the previous equation can be written as

$$\alpha(L)X_t = c + \beta(L)\varepsilon_t. \quad (\text{B.3})$$

For the process to be stationary, it is necessary for the roots of the characteristic polynomial of the autoregressive part  $\alpha(z)$  to lie outside the unit circle in the complex plane (in modulus strictly greater than one). The stationary ARMA process can be represented as an infinite MA process:

$$X_t = \alpha^{-1}(L)c + \alpha^{-1}(L)\beta(L)\varepsilon_t = \frac{c}{a(1)} + \sum_{i=0}^{\infty} c_i \varepsilon_{t-i}. \quad (\text{B.4})$$

For example, the process ARMA (1,0) = AR (1) can be represented as an MA process of infinite order with coefficients in decreasing geometric progression:

$$X_t = \frac{c}{(1-a)} + \sum_{i=0}^{\infty} a^i \varepsilon_{t-i}. \quad (\text{B.5})$$

Thus, the ARMA processes can be considered to be MA processes of infinite order with certain restrictions on the structure coefficients. There is a small number of parameters to describe the processes they enable rather than a complex structure. All stationary processes can be arbitrarily approximated by an ARMA model of a certain order with considerably fewer parameters than MA models use.

*NonStationary (Integrated) ARMA.* In the presence of unit roots of the  $p$  autoregressive polynomial, the process is nonstationary. Roots of less than unity in practice are not considered, since they are processes which exhibit explosive behavior. Accordingly, to test the stationary nature of a time series of basic tests, tests must be run for unit roots. If the tests confirm the presence of unit roots, then we need to analyze the difference between the original time series and a stationary process of the differences of one or two orders (usually the first order is sufficient and sometimes the second) of the ARMA-based model.

Such models are called ARIMA models (integrated ARMA) or Box-Jenkins models. The ARIMA model  $(p, d, q)$ , where  $d$  is the order of integration (the order of differences in the original time series);  $p$  and  $q$ , the order of AR; MA the parts of the ARMA-process differences  $d$ , the order can be written in the operator form:

$$\alpha(L)\Delta^d X_t = c + \beta(L)\varepsilon_t, \quad \Delta = 1 - L. \quad (\text{B.6})$$

The ARIMA process  $(p, d, q)$  is equivalent to the ARMA process  $(p + d, q)$  with  $d$  unit roots.

To construct the ARMA model on a proxy data series of observations, it is necessary to determine the model order (numbers  $p$  and  $q$ ), and then the coefficients themselves.

To determine the order of the model an investigation of these characteristics of the time series can be done, seen as its autocorrelation function and partial autocorrelation function.

To determine the coefficients the method of least squares and maximum likelihood method can be used.

*ARMAX Models.* In the classic ARMA model, it can add exogenous factors  $x$ . In general, the model involves not only

the current values of these factors but also lagged values. Such models are usually denoted ARMAX  $(p, q, k)$ , where  $k$ -lags come from the exogenous factors. In an operator form, such models can be written as follows (an exogenous factor):

$$a(L)y_t = c + b(L)\varepsilon_t + d(L)x_t, \quad (\text{B.7})$$

where  $(L)$ ,  $b(L)$ ,  $d(L)$  are the order polynomial, respectively,  $p$ ,  $q$ ,  $k$  of the lag operator.

It should be noted that such models can be interpreted differently, for example, ADL  $(p, q)$  mode with random errors MA  $(q)$ .

## Acknowledgments

V. Velasco gives special thanks to the CONACyT (project 180148) for financial support to this work.

## References

- [1] L. I. Dorman, *Cosmic Ray Variations and Space Exploration*, North Holland, Amsterdam, 1974.
- [2] V. L. Gorshkov, in *Proceedings of the 8th Congress of Astronomical Community and International Symposium 'Astronomy 2005—Status and Prospects of Development'*, MSU-GAISH, Moscow, Russia, June 2005.
- [3] A. N. Pushkov and T. A. Chernova, *Features of Spatial and Temporal Structure of the Secular Variation of the Geomagnetic Field*, vol. 18, IZMIRAN, Moscow, Russia, 1972.
- [4] Papitashvili, N. E. Papitashvili, N. M. Rotanova, and A. N. Pushkov, *Geomagnetism and Aeronomy*, vol. 20, pp. 711–717, 1980.
- [5] N. V. Papitashvili and N. M. Rotanova, *Geomagnetism and Aeronomy*, vol. 22, no. 4, pp. 1010–1015, 1982.
- [6] V. P. Golovkov, S. V. Yakovleva, and T. I. Zvereva, "Detection of fast secular variations based on the data of satellite magnetic surveys," *Geomagnetism and Aeronomy*, vol. 50, no. 2, pp. 274–277, 2010.
- [7] H. S. Ahluwalia, "Three activity cycle periodicity in galactic cosmic rays," in *Proceedings of the 25th International Cosmic Ray Conference*, vol. 2, pp. 109–112, Durban, South Africa, 1997.
- [8] H. S. Ahluwalia, "Meandering path to solar activity forecast for cycle 23," in *Proceedings of the 10th International Solar Wind Conference*, M. Velli, R. Bruno, and F. Malra, Eds., vol. CP679, The American Institute of Physics, 2003.
- [9] H. S. Ahluwalia, "The predicted size of cycle 23 based on the inferred three-cycle quasi-periodicity of the planetary index  $A_p$ ," *Journal of Geophysical Research*, vol. 103, no. A6, pp. 12, 103–12, 112, 1998.
- [10] H. S. Ahluwalia, "Timelines of cosmic ray intensity,  $A_p$ , IMF, and sunspot numbers since 1937," *Journal of Geophysical Research*, vol. 116, Article ID A12106, 9 pages, 2011.
- [11] L. B. Klyashtorin and A. A. Lyubushin, *Cyclic Climate Changes and Fish Productivity*, VNIRO Publishing, 2005.
- [12] I. Libin and J. Perez-Peraza, *Helioclimatology*, MAOK, Moscow, Russia, 2009.
- [13] S. T. Gray, L. J. Graumlich, J. L. Betancourt, and G. T. Pederson, "A tree-ring based reconstruction of the Atlantic Multidecadal Oscillation since 1567 A.D.," *Geophysical Research Letters*, vol. 31, no. 12, Article ID L12205, 4 pages, 2004.
- [14] J. Pérez-Peraza, V. Velasco, and S. Kavlakov, "Solar, geomagnetic and cosmic ray intensity changes, preceding the cyclone

- appearances around Mexico,” *Advances in Space Research*, vol. 42, pp. 1601–1613, 2008.
- [15] K. Kudela, H. Mavromichalaki, A. Papaioannou, and M. Gerontidou, “On mid-term periodicities in cosmic rays,” *Solar Physics*, vol. 266, pp. 173–180, 2010.
- [16] V. M. Velasco and B. Mendoza, “Assessing the relationship between solar activity and some large scale climatic phenomena,” *Advances in Space Research*, vol. 42, no. 5, pp. 866–878, 2008.
- [17] V. Velasco, J. F. Valdés-Galicia, and B. Mendoza, “The 120-year solar cycle of the cosmogenic isotopes,” in *Proceedings of the 30th International Cosmic Ray Conference*, vol. 1, pp. 553–556, 2008.
- [18] J. Pérez-Peraza, V. Velasco, J. Zapotitla, L. I. Miroshnichenko, E. Vashenyuk, and I. Ya Libin, “Classification of GLE’s as a function of their spectral content for prognostic goals,” in *Proceedings of the 32nd International Cosmic Ray Conference*, pp. 149–152, Beijing, China, 2011.
- [19] M. Fligge, S. K. Solanki, and J. Beer, “Determination of solar cycle length variations using continuous wavelet transform,” *Astronomy & Astrophysics*, vol. 346, pp. 313–321, 1999.
- [20] M. Ossendrijver, “The solar dynamo,” *The Astronomy and Astrophysics Review*, vol. 11, pp. 287–367, 2003.
- [21] J. Beer, A. Blinov, G. Bonani et al., “Use of  $^{10}\text{Be}$  in polar ice to trace the 11-year cycle of solar activity,” *Nature*, vol. 347, pp. 164–166, 1990.
- [22] A. M. Berggren, J. Beer, G. Possnert et al., “A 600-year annual  $^{10}\text{Be}$  record from the NGRIP ice core, Greenland,” *Geophysical Research Letters*, vol. 36, no. 11, Article ID L11801, 5 pages, 2009.
- [23] E. Bard, G. Raisbeck, F. Yiou, and J. Jouzel, “Solar irradiance during the last 1200 years based on cosmogenic nuclides,” *Tellus B*, vol. 52, no. 3, pp. 985–992, 2000.
- [24] L. Hudgins, C. A. Friehe, and M. E. Mayer, “Wavelet transforms and atmospheric turbulence,” *Physical Review Letters*, vol. 71, pp. 3279–3282, 1993.
- [25] C. Torrence and G. Compo, “A practical guide to wavelet analysis,” *Bulletin of the American Meteorological Society*, vol. 79, pp. 61–78, 1998.
- [26] A. Grinsted, J. C. Moore, and S. Jevrejeva, “Application of the cross wavelet transform and wavelet coherence to geophysical time series,” *Nonlinear Process Geophysics*, vol. 11, pp. 561–566, 2004.
- [27] I. Daubechies, *Ten Lectures on Wavelet*, Society For Industrial and Applied Mathematics, 1992, Edited by: Rutgers University and AT&T Bell Laboratories.
- [28] K. Kudela, “Space weather near Earth and energetic particles: selected results,” *Journal of Physics*. In press.
- [29] Y. I. Stozhkov, N. S. Svirzhevsky, G. A. Bazilevskaya et al., “Fluxes of Cosmic rays in the maximum of absorption curve in the atmosphere and at the atmosphere boundary (1957–2007),” preprint FIAN, 14, 2007.
- [30] Y. I. Stozhkov, N. S. Svirzhevsky, G. A. Bazilevskaya et al., “Cosmic rays in the stratosphere in 2008–2010,” *Astrophysics and Space Sciences Transactions*, vol. 7, pp. 379–382, 2011.
- [31] I. G. Usoskin, G. A. Bazilevskaya, and G. A. Kovaltsov, “Solar modulation parameter for cosmic rays since 1936 reconstructed from ground-based neutron monitors and ionization chambers,” *Journal of Geophysical Research*, vol. 116, Article ID A02104, 9 pages, 2011.
- [32] J. Pérez-Peraza, V. Velasco, and S. Kavlakov, “Wavelet coherence analysis of Atlantic hurricanes and cosmic rays,” *Geofisica Internacional*, vol. 47, no. 3, pp. 231–244, 2008.

## Research Article

# Long-Term Cosmic Ray Variability and the CME-Index

**Helen Mavromichalaki and Evangelos Paouris**

*Faculty of Physics, National and Kapodistrian University of Athens, Zografos, 15784 Athens, Greece*

Correspondence should be addressed to Helen Mavromichalaki, emavromi@phys.uoa.gr

Received 25 September 2012; Accepted 28 November 2012

Academic Editor: Karel Kudela

Copyright © 2012 H. Mavromichalaki and E. Paouris. This is an open access article distributed under the Creative Commons Attribution License, which permits unrestricted use, distribution, and reproduction in any medium, provided the original work is properly cited.

The cosmic ray modulation in relation to solar activity indices and heliospheric parameters during the period January 1996–October 2011, covering the solar cycle 23 and the ascending phase of solar cycle 24, is studied. The new perspective of this contribution is that the CME-index, obtained from only the CMEs with angular width greater than 30 degrees, gives much better results than in previous works. The proposed model for the calculation of the modulated cosmic ray intensity obtained from the combination of solar indices and heliospheric parameters gives a very satisfactory value of the standard deviation. The best reproduction of the cosmic ray intensity is obtained by taking into account solar and interplanetary indices such as sunspot number, interplanetary magnetic field, CME-index, and heliospheric current sheet tilt. The standard deviation between the observed and calculated values is about 6.63% for the solar cycle 23 and 4.13% for the ascending part of solar cycle 24.

## 1. Introduction

The cosmic ray (*CR*) intensity, as it is observed from Earth and in Earth's orbit, exhibits an approximate 11-year variation anti correlated with solar activity, with perhaps some time lag, firstly studied by Forbush [1]. Many research groups have tried to express this long-term variation of the galactic *CR* intensity through means of appropriate solar indices and geophysical parameters. The modulation of galactic cosmic rays in the heliosphere using theoretical as well as empirical approaches is successful and advanced rapidly [2]. However, an adequate description of the effect of the heliosphere on cosmic rays still does not appear to be a simple task. To be adequate, theoretical models should consider the complex shape and dynamics of the heliospheric current sheet, the heliolatitudinal distribution of the solar wind velocity, boundaries between fast and slow solar wind streams, various sporadic and recurrent structures, and the role of the termination shock and the heliopause. Exarhos and Moussas [3] tried to estimate the magnetic field at the heliospheric termination shock and to study the effects of its temporal variation on the galactic cosmic ray long-term modulation starting from the Parker's model and using in-ecliptic measurements from

different Spacecrafts at 1 AU near the Earth. Morishita and Sakukibara [4] tried to estimate the size of the heliosphere derived from the long-term modulation of neutron monitor intensities. Using a construction of the open solar magnetic flux from sunspot data as an input to a spherically symmetric quasisteady state model of the heliosphere, the expected intensity of galactic cosmic rays at the Earth's orbit was calculated in [5]. This calculated cosmic ray intensity is in good agreement with the neutron monitor measurements during the last 50 years. Particular consideration of the cosmic ray modulation is given to the correlation of long-term cosmic ray variations with different solar-heliospheric parameters and to existing empirical models of cosmic ray intensity, as it is described in the review paper by [6]. A method to predict cosmic ray intensity and solar modulation parameters was proposed in [7]. This method gives satisfactory results when applied to prediction of the dose received on-board commercial aeroplane flights. He notes that prediction of the galactic cosmic ray intensity observed at a given station is preferable than prediction of the different potentials such as the modulation potential in terms of sunspot numbers [8]. The importance of this choice is that the cosmic ray intensity is the only variable directly observed. Records of cosmic ray intensity

are available and homogeneous over a long period, while that is not the case for the data obtained from space observations. Two models were proposed in [9], a quasilinear and a model assuming a power-law relation between the modulation potential and the magnetic flux during the neutron monitor area 1951–2005 useful for predictions, if the corresponding global heliospheric variables can be independently estimated.

Recently, an empirical relation based on solar and interplanetary parameters was presented by [10] in order to describe the long-term modulation of cosmic ray intensity during the last solar cycle. Emphasis was given to the different behaviour of the heliospheric parameters compared with the solar ones regarding interesting properties of the cosmic ray intensity modulation. These are the hysteresis phenomenon and the cross-correlation analysis of these parameters with the cosmic ray intensity in the three phases of the solar cycle and according to the solar magnetic field polarity as well. This model has so far been applied to four solar cycles (20, 21, 22, and 23) and can be considered as a useful tool for understanding cosmic ray modulation. The proposed model can be extended backward in time or used for predictions, as it has practical implications for planning solar observations and forecasting space weather phenomena.

Solar cycle 23 was a cycle of great interest firstly, as it was characterized by a lot of violent periods of extreme solar events mainly in the descending phase, such as October–November 2003, January 2005, July 2005, and December 2006 and secondly, it had an extraordinary and extended minimum with duration more than three years. In this solar minimum, the cosmic ray intensity was much higher than in the previous cycles [11]. This long, quiet period was characterized by limited magnetic flux emergence at the photosphere, mostly in the southern hemisphere, and low coronal mass ejections (CMEs) and flare activity in the corona.

In our last work [10], we have shown that the long-term modulation of the intensity of cosmic-rays has reproduced using sunspot number ( $R_z$ ), CME-index ( $P_i$ ), interplanetary magnetic field (IMF), and heliospheric current sheet (HCS) tilt. In this work, we are showing the strong connection between the cosmic ray intensity and the CMEs by the use of CME-index, and the main criterion for the form of this index is the angular width of CMEs. According to [12], slow and narrow CMEs are ineffective for modulation, and as a result, we are showing the modulation with the previous form of the index and the new one.

## 2. Data Collection

In order to study the long-term cosmic ray modulation through the years 1996–2011, monthly values of cosmic rays from Lomnický Stit neutron monitor (cut-off rigidity 3.84 GV) were used. For the purposes of this study, the time series of cosmic ray variations was normalized taking the cosmic ray intensity maximum (July 2009) equal to 1.00 and the cosmic ray intensity minimum (November 2003) equal to 0.00. We note that the cosmic ray intensity in the period of October–November 2003 during the declining phase of

the solar cycle has been used only for normalization reasons and does not coincide with the activity maximum of the solar cycle during the years 2000–2002 [13]. But it is also very important the fact that this minimum of cosmic ray intensity coinciding with the maximum of CME-index shows the strong connection of these two variables.

In this study, we have also used data of the mean monthly sunspot number ( $R_z$ ), taken from the National Geophysical Data Center (<ftp://ftp.ngdc.noaa.gov/index.html>), the intensity of the interplanetary magnetic field (IMF) is obtained from the OMNI database (<http://omniweb.gsfc.nasa.gov/>). The data on the tilt of the heliospheric current sheet using the classic PFSS model [14] (HCS) were obtained from the Wilcox Solar Observatory database (<http://wso.stanford.edu/Tilts.html>). The CMEs data, for the formation of the coronal mass ejection index ( $P_i$ ), are taken from the SOHO/LASCO CME catalog ([http://cdaw.gsfc.nasa.gov/CME\\_list/](http://cdaw.gsfc.nasa.gov/CME_list/)). Unfortunately, the SOHO database has no data for CMEs for the months of July, August, and September of 1998 and January of 1999. In order to fill these data gaps, a smoothing method has been used. In Figures 1(a) and 1(b), the time profiles of all the examined parameters are presented.

## 3. CME-Index

For many years, the sunspot number was the most characteristic index of solar activity. This means that we can determine the phase of the cycle through the sunspot number, and the maximum values mean that we are in the maximum of the solar activity and minimum values that we are in the minimum of the solar cycle, while intermediate values are showing the ascending or descending phase of the cycle. At the maximum phase, we have some periods with very violent activity connected to the CMEs such as July 2000 and April 2001. On the other hand, we had a lot of very violent periods when the sunspot number was at the descending phase of the solar cycle or close to solar minimum, and as a result, we could not take safe results from the sunspot number only for the solar activity. These periods such as October–November 2003, January 2005, November–December 2006, or even February 2010 and August–September 2010 have the characteristic of violent solar activity, and most of them are connected to violent CMEs, X-flares, and finally ground-level enhancements (GLEs). There are CMEs with results on the Earth's magnetosphere causing magnetic storms, SEPs, or even GLEs. These CMEs are the interplanetary coronal mass ejections—ICMEs [15]—and are responsible for temporary disturbances of the Earth's magnetosphere. Now, it is clear that we have two types of CMEs with different characteristics: geoeffective CMEs which can produce geomagnetic storms and the SEP-effective CMEs which can cause SEP events [16, 17]. It is known that SEP events are originating from CME-driven shocks [15, 18, 19]. Based on this issue, a CME-index was introduced in our previous works [20–22].

In this work, the most extensive number of data as they now covers the whole solar cycle 23 and a part of the ascending phase of the new solar cycle 24 has an advantage for the application of this index. This extraordinary solar

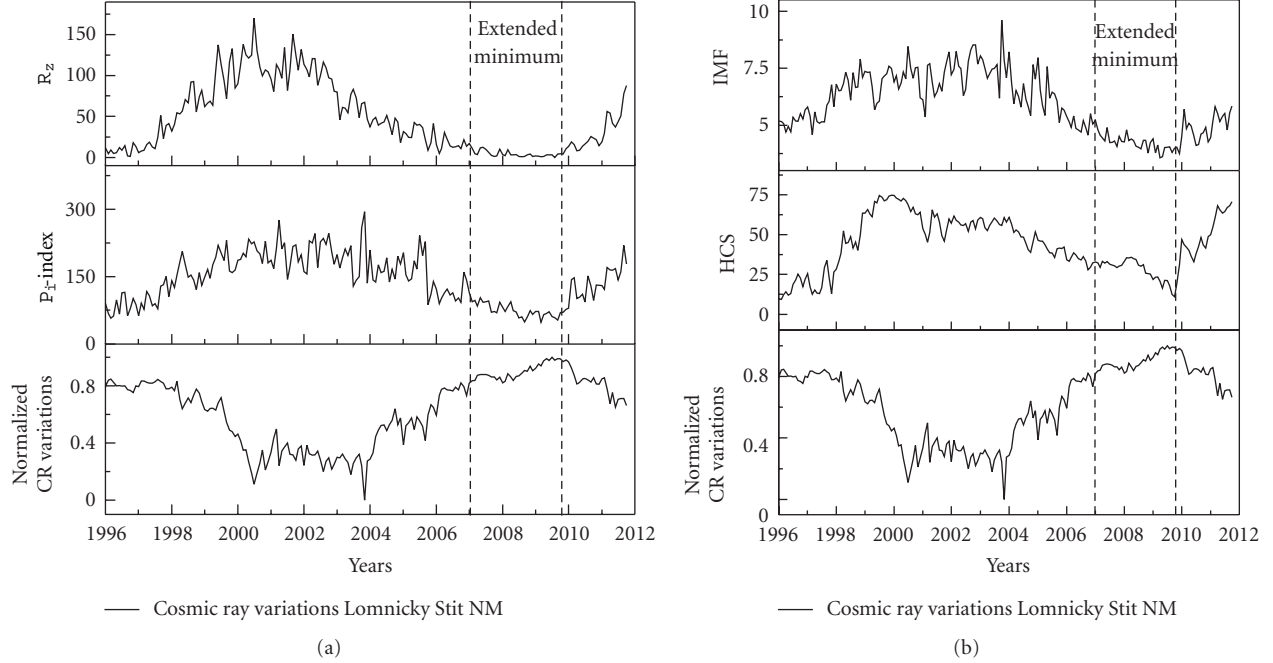


FIGURE 1: (a) Time profiles, starting from the top, of the sunspot number ( $R_z$ ), CME-index ( $P_i$ ), and the cosmic ray variations for the period of 1996–2011. The period of extended minimum is noted between the dashed lines for all the examined parameters. (b) Time profiles, starting from the top, of the interplanetary magnetic field (IMF), the heliospheric current sheet tilt (HCS), and the cosmic ray variations for the period of 1996–2011. The period of extended minimum is noted between the vertical dashed lines.

minimum between the solar cycles 23 and 24 is also very important. Now we have included data for previous periods as mentioned before, and it is clear the weakness of the sunspot number only to explain these periods.

One of the most characteristic parameters of a CME is the linear speed as a factor of the importance of the CME [16, 23], so we are using the mean monthly linear speed ( $V_p$ ) of the CMEs and their monthly number ( $N_c$ ) in a new dimensionless relation according to [12] with the form

$$P_i = \alpha \cdot \frac{N_c}{N_{c_{\max}}} + \beta \cdot \frac{V_p}{V_{p_{\max}}}, \quad (1)$$

where the factors  $\alpha$  and  $\beta$  are calculated with the best cross-correlation coefficient values, between the values of the index related to the cosmic ray intensity, for  $\alpha$  and  $\beta$  factors applies  $\alpha + \beta = 1$  and  $\alpha, \beta > 0$ . The maximum values  $N_{c_{\max}}$  and  $V_{p_{\max}}$  are the maximum values of the examined period. For the period January 1996–October 2011, we found the relation of the form:

$$P_i = 0.12 \cdot \frac{N_c}{N_{c_{\max}}} + 0.88 \cdot \frac{V_p}{V_{p_{\max}}}, \quad (2)$$

where  $N_{c_{\max}} = 178$  and  $V_{p_{\max}} = 834$  km/s. The factors 0.12 and 0.88 were the best values which maximize the correlation coefficient of  $P_i$ -index between cosmic ray intensity with  $r = -0.82$ . Between  $P_i$ -index and sunspot number, the correlation coefficient is  $r = 0.76$ .

We noticed also periods with a lot of CMEs even in minimum as a result of a lot of narrow and slow CMEs. In

this work, a new approach is presented using data for CMEs with width  $>30^\circ$  for  $P_i$ -index for the period January 1996–October 2011. The best relation is

$$P_i = 0.37 \cdot \frac{N_c}{N_{c_{\max}}} + 0.63 \cdot \frac{V_p}{V_{p_{\max}}}, \quad (3)$$

where  $N_{c_{\max}} = 152$  and  $V_{p_{\max}} = 915.6$  km/s. The correlation coefficient between  $P_i$ -index and cosmic rays is found to be  $r = -0.84$  and sunspot number  $r = 0.82$  respectively, and these are the best cross-correlation values in this work for the examined period (January 1996–October 2011). In Figure 2, it is obvious the increase of narrow CMEs especially after 2005. The number of CMEs using data from CMEs with width  $>30^\circ$  follows very well the sunspot number. For the entire examined period, the correlation coefficient between  $P_i$ -index from (3) and HCS tilt was  $r = 0.76$  and IMF was  $r = 0.83$  which is very important proving the strong connection between the index and the heliospheric parameters. We hope that for further studies in space weather and modulation of galactic cosmic rays, the  $P_i$ -index could be very helpful and must be a parameter in modulation formulas [10].

#### 4. Cosmic Ray Modulation

It is well known that the 11-year modulation of the cosmic ray intensity shows some time lag behind the solar activity which is a kind of hysteresis effect [1, 10, 21]. Keeping this in mind, we have carried out the analysis of correlation between the monthly values of the cosmic-ray variations and various

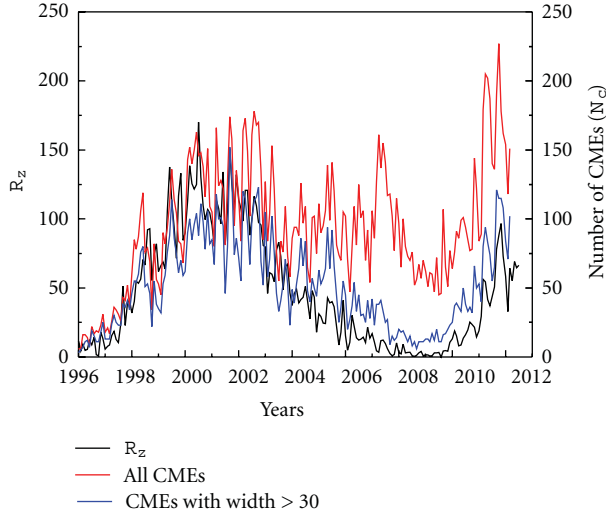


FIGURE 2: Time profiles of the mean monthly number of CMEs using the total number of CMEs (red line) and those with angular width greater than  $30^\circ$  (blue line). The sunspot numbers are also indicated with the black line.

solar and heliospheric activity parameters ( $R_z$ ,  $P_i$ , IMF, and HCS) for the examined period.

To calculate the time lag of each parameter in reference to the cosmic ray intensity [24, 25], we have calculated the cross-correlation coefficients between them with varying time lags from 0 to 30 months for the interval of the examined period. The maximum cross-correlation coefficients and the corresponding time lags are given in Table 1 for the examined period.

In this work, the same empirical relation of the cosmic ray modulation that was applied in the previous works to solar cycles 20, 21, 22, and 23 is adopted [21, 26]. This is derived by a generalization of Simpson's solar wind model using the diffusion-convection drift model [27], and it is expressed by the following relation:

$$I(t) = I - \int f(r)S(t-r)dr, \quad (4)$$

where  $I$  and  $I(t)$  are the galactic (unmodulated) and modulated cosmic ray intensities, respectively,  $S(t-r)$  is the source function representing some proper solar activity indices at a time  $t-r$  ( $r \geq 0$ ), and  $f(r)$  is the characteristic function that expresses the time dependence of solar disturbances represented by  $S(t-r)$  [28, 29]. According to the previous model, the modulated cosmic ray intensity  $I(t)$  is expressed by a constant  $C$  and the sum of a few source functions appropriately selected from the solar and interplanetary indices that affect cosmic ray modulation. This relation is given by the following expression:

$$I(t) = C - 10^{-3}(a_1X + a_2Y + a_3Z + a_4W), \quad (5)$$

where  $C$  is a constant,  $X$ ,  $Y$ ,  $Z$ , and  $W$  are the selected time-lagged solar-heliospheric parameters, and  $\alpha_i$  ( $i = 1$  to 4) are coefficients calculated by the RMS-minimization method.

TABLE 1: Cross-correlation coefficients and the corresponding time lags for the entire period (1996–2011).

Indices	Correlation coefficients ( $r$ ) (95% significance level)	Time lags (months)
Sunspot number $R_z$	$-0.91 \pm 0.01$	+14
Coronal mass ejections index $P_i$	$-0.84 \pm 0.01$	0
Interplanetary magnetic field IMF	$-0.86 \pm 0.01$	+1
Heliospheric current sheet HCS	$-0.82 \pm 0.01$	+8

Constant  $C$  is linearly correlated to the cut-off rigidity of each station according to the following relation:

$$C = 0.95 + 0.005P[\text{GV}], \quad (6)$$

where  $P$  is the cut-off rigidity for each neutron monitor station [30]. In this work, using data of the cosmic ray variations obtained from the Lomnický Stit neutron monitor with cut-off rigidity of 3.84 GV, constant  $C$  is found to be equal to 0.9692.

We will investigate the entire period of 1996–2011 and separately the period of 23rd solar cycle (May 1996–December 2008) and the ascending part of 24th solar cycle (January 2009–October 2011). The model parameters, the standard deviation for each case, and coefficients  $\alpha_i$  calculated by the RMS-minimization method are presented in Table 2. It is remarkable that the standard deviations for all cases are smaller than 7%. Comparing with the results of our last work [10], they have been improved for the entire period.

The best relation reproducing the cosmic ray variations is the combination of  $R_z$ ,  $P_i$ , IMF, and HCS [10]. This is expressed by the following relation:

$$I(t) = C - 10^{-3}(a_1R_z + a_2P_i + a_3\text{IMF} + a_4\text{HCS}), \quad (7)$$

where constant  $C$  was found equal to 0.9692, and  $R_z$ ,  $P_i$ , IMF, and HCS are the solar-interplanetary parameters incorporating the time lag. Coefficients  $\alpha_i$  were found equal to 2.42, 0.54, 54.08, and 2.02, respectively. The standard deviation for this relation is found to be 6.69% which is a very good approximation. It is noticed that the maximum phase of solar cycle 23 was very complicated including double peaks and the reversal of the solar magnetic field as well. It is interesting that there is a good agreement in the maximum and descending phases due to the use of  $P_i$  and IMF, mainly in the solar extreme period of October–November 2003, while the contributions of IMF and HCS complement each other and improve the agreement in the ascending and descending phases that are characterized by strong solar events.

As we mentioned earlier, the use of CMEs with angular width greater than  $30^\circ$  shows a very good behavior for the entire solar cycle, and as a result, we have the best cross-correlation values between the cosmic ray intensity and  $P_i$ -index [12]. If we use the  $P_i$ -index data which occurs from

TABLE 2: Standard deviation for different models during the solar cycles 23 and 24 and in total examined period. Coefficients  $\alpha_i$  factors are also given in the first column, respectively, for each variable.

Model parameters	Solar cycle 23 (May 1996–Dec 2008)	Solar cycle 24 (Jan 2009–Oct 2011)	Total (Jan 1996–Oct 2011)
$R_c, P_i, \text{IMF, HCS}$ (2.42, 0.54, 54.08, 2.02)	6.98%	4.79%	6.69%
$R_c, P_i$ (width $>30^\circ$ ), IMF, HCS (2.36, 0.91, 52.51, 2.12)	6.63%	4.13%	6.27%

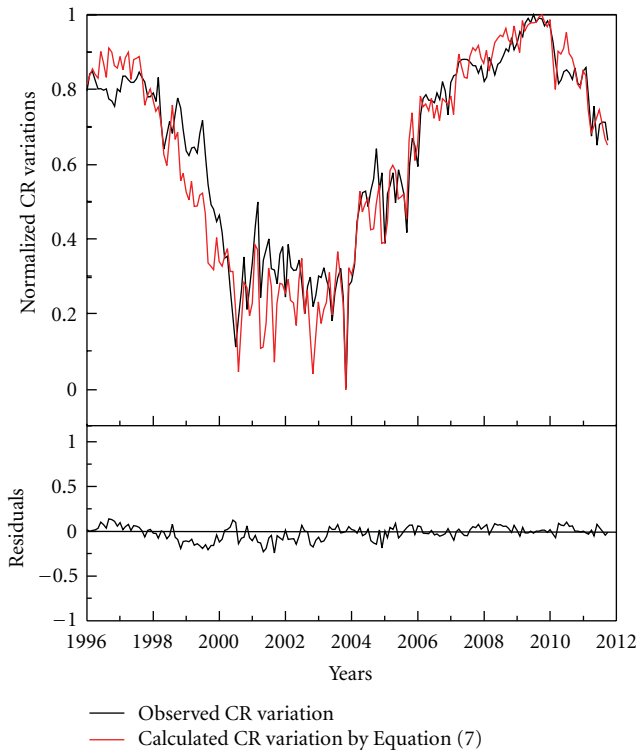


FIGURE 3: The observed values of cosmic ray intensity (black line) and those calculated by (7) (red line). The residuals are indicated in the lower panel. This modulation has a standard deviation of about 6.27%.

data of CMEs with width  $>30^\circ$  using the same modulation as in (7), the results are much better with a standard deviation of 6.27%. The coefficients  $\alpha_i$  were found equal to 2.36, 0.91, 52.51, and 2.12, respectively. These values of CME-index give much better results also between cosmic ray intensity and the number of CMEs ( $N_c$ ), with  $r = -0.72$ , and the mean linear speed ( $V_p$ ), with  $r = -0.79$ . In Figure 3, the observed and calculated cosmic ray variations by (7) using  $P_i$ -index from CMEs with width  $>30^\circ$  are presented.

The significant improvement of this empirical model is resulted from the use of the CME-index  $P_i$ , using only CMEs with angular width  $>30^\circ$ , which is highly correlated with the cosmic ray intensity variations ( $r = -0.84$ ). Between the monthly number of CMEs ( $N_c$ ), using CMEs with angular width  $>30^\circ$ , and CR intensity, we found  $r = -0.72$ , in opposition with the total number of CMEs per month and CR intensity with correlation coefficient  $r = -0.44$ . The

previous value of the correlation coefficient of the total number of CMEs was  $-0.78$  [22], which was obtained over a shorter time period, up to the beginning of 2006 (February 2006), without the period of the solar minimum which was examined here, where a lot of narrow and slow CMEs were recorded without any effect on the long-term modulation [12].

## 5. Ascending Part of Solar Cycle 24

As it was mentioned earlier, the slow decline of solar cycle 23 and the slow rise of cycle 24 resulted in a very long period of low solar activity which lasted from about 2006 to the end of 2009, with 2008 and 2009 being particularly quiet years. Therefore, the solar minimum between cycles 23 and 24 was very extended and deep in contrast to the previous solar minima with duration of tens of months instead of few months as in earlier cycles. In [21], the solar cycle dependence of the cosmic ray intensity time lag behind the sunspot number was studied extensively. For cycles 17–23, the mean value of this time lag is  $2.4 \pm 1.9$  months for even cycles and  $12.4 \pm 7.2$  for odd cycles [21, 27].

During the last solar cycle 23, the minimum of the monthly mean sunspot number occurred on August 2009. According to [31], the maximum of cosmic ray intensity was observed in October 2009, and the onset of the current solar cycle 24 of galactic cosmic rays was noted in January 2010. Kane [11] noticed that the cosmic ray intensity decreased only after March 2010.

In this section, the period of the ascending part of solar cycle 24 from January 2009 to October 2011 is studied separately from the whole time interval. The cross-correlation coefficients for this period between the cosmic ray intensity and the sunspot number were calculated, and a maximum coefficient  $r = -0.90$  with a corresponding time lag of 2 months was found. Kane [11] found a time lag for this minimum about 6–7 months. Ahluwalia and Ygbuhay [31] also calculated a time lag of about 3 months between a large, sharp increase of the HCS tilt angle and the onset of cosmic ray modulation, in agreement to our calculations where a time lag of about 2–3 months ( $2.3 \pm 0.3$  months), with respect to HCS, is found, with a very high correlation coefficient of  $r = -0.96$ . The time lag between the cosmic ray intensity and the sunspot number from the best nonlinear fitting is calculated to the value of  $1.9 \pm 0.3$  months. This value coincides—up to now—with the expected value for even cycles as mentioned in a previous work [10]. Between the cosmic ray intensity and the IMF, a time lag of about 1

TABLE 3: Cross-correlation coefficients and the corresponding time lags for the ascending part of 24th solar cycle.

Indices	Correlation coefficients ( $r$ ) (95% significance level)	Time lags (months)
Sunspot number $R_z$	$-0.90 \pm 0.02$	+2
Coronal mass ejections index $P_i$	$-0.85 \pm 0.02$	0
Interplanetary magnetic field IMF	$-0.84 \pm 0.02$	+1
Heliospheric current sheet HCS	$-0.96 \pm 0.02$	+2

month was found, with  $r = -0.84$ . The maximum cross-correlation coefficients and the corresponding time lags for this period are given in Table 3.

## 6. Discussion and Conclusions

The cosmic ray modulation is a complex phenomenon which occurs all over the heliosphere and depends on many factors. No single solar index, however sophisticated, can account for cosmic ray variations. Different scientists proposed empirical relations describing the long-term cosmic ray variations based on the joint use of solar and/or heliospheric indices. At first, the solar indices such as sunspot number and solar flares were used [26]. Later, Belov et al. [32] proposed a multiparametric description of long-term CR variations, based on a joint use of the HCS tilt and intensity variations of the IMF. The effect of IMF intensity variations on cosmic ray modulation is even easier to substantiate theoretically than the effect of the HCS tilt. The main determining parameter of particle transport—gyroradius—is inversely proportional to the IMF strength ( $H$ ). According to theory [32], an increase of  $H$  should lead to a decrease of transport path and the diffusion coefficient and, consequently, to an increase of the CR modulation. The relationship between the IMF strength and long-period variations of CR was corroborated experimentally [32, 33] when long data series of solar wind measurements were built up. Indeed, these parameters—the HCS tilt and the IMF intensity—successfully supplement each other. The point is that the HCS tilt manifests the structure of the heliosphere, while the IMF intensity characterizes quantitatively its effect on cosmic rays. In our previous work [21], the solar indices ( $R_z, N_c$ ) together with the heliospheric variables IMF, HCS, and Ap were found to explain better the cosmic ray modulation. In this approach, the use of the CME parameters represented by the CME-index  $P_i$  based on the number of CMEs and the mean plasma velocity taking account only CMEs with width  $>30^\circ$  improved significantly the relation between the observed and the calculated values of the cosmic ray intensity measured by a single neutron monitor station. By applying a similar correlative analysis and the same empirical relation of the previous work [10], the following conclusions were outlined.

- (i) As concerns the modulation effect, in the proposed model, the standard deviation is smaller than 7%.

The best one obtained from (7) using the parameters  $R_z, P_i$ , IMF, and HCS gives a standard deviation of 6.63% for the 23rd solar cycle, 4.13% for the 24th solar cycle, and 6.27% for the total time period. The total improvement between the previous [10] and current empirical models for the cosmic ray modulation is significant.

- (ii) This significant improvement of this empirical model is resulted from the use of the CME-index  $P_i$ , using CMEs with angular width  $>30^\circ$ , which is highly correlated with the cosmic ray intensity variations ( $r = -0.84$ ) which confirm our results according the correlation coefficient factors in our previous work [12].
- (iii) Between the monthly number of CMEs ( $N_c$ ), using CMEs with angular width  $>30^\circ$ , and CR intensity, we found  $r = -0.72$ , in opposition with the total number of CMEs per month, and CR with correlation coefficient  $r = -0.44$ . The previous value of the correlation coefficient between the total number of CMEs and CR was  $-0.78$  [22], which was obtained over a shorter time period, up to the beginning of 2006 (February 2006), without the period of the solar minimum which was examined here, where a lot of narrow and slow CMEs were recorded without any effect on the long-term modulation [12].
- (iv) Examining the period of solar minimum and the ascending part of the solar cycle 24, a small time lag between cosmic ray intensity and solar activity of about 2 months with  $r = -0.90$  was underlined, as it was expected for the even solar cycles [24, 27]. Cosmic ray intensity and heliospheric current sheet present a time lag of  $\sim 2$  months with a very significant correlation coefficient  $r = -0.96$ . Between CR intensity and IMF, a time lag of about 1 month was noticed with  $r = -0.84$ .

Examining the entire period, we can conclude that all the selected heliospheric parameters ( $P_i$ , IMF, and HCS) can give a very good approximation to the modulated cosmic ray intensity. Moreover, we note that some of the indices used, such as  $R_z, P_i$ , and HCS, are global indices, whereas others, such as IMF, are limited to the ecliptic plane. According to [34], the cosmic ray modulation is defined mainly by the global indices because of their complicated transport in the heliosphere, consistent with our results in this work.

Summarizing, we can say that the empirical model proposed in the previous works and also in this work with significant improvements has been studied finally for a lot of solar cycles 19, 20, 21, 22, and 23, and the obtained results are a confirmation of the reliability of this. In a future work, we hope that the consideration of another solar parameter such as the polar magnetic field of the Sun will be able to throw more light to the investigation of the long-term cosmic ray modulation. All these studies will be a useful tool for solar cycle prediction and space weather applications.

## Acknowledgments

The authors are grateful to the providers of the solar, interplanetary, neutron monitors, and geomagnetic data used in this work. Especially, they acknowledge Professor Karel Kudela and Igor Parnahaj for providing cosmic ray data from Lomnický Stit neutron monitor. Data of coronal mass ejections for the formation of the CME-index ( $P_i$ ) are taken from the SOHO/LASCO CME catalog ([http://cdaw.gsfc.nasa.gov/CME\\_list/](http://cdaw.gsfc.nasa.gov/CME_list/)). This CME catalog is generated and maintained at the CDAW Data Center by NASA and The Catholic University of America in cooperation with the Naval Research Laboratory. SOHO is a project of international cooperation between ESA and NASA.

## References

- [1] S. Forbush, "World-wide cosmic ray variations, 1937–1952," *Journal of Geophysical Research*, vol. 59, no. 4, p. 525, 1954.
- [2] M. S. Potgieter, "The modulation of galactic cosmic rays in the heliosphere: theory and models," *Space Science Reviews*, vol. 83, no. 1–2, pp. 147–158, 1998.
- [3] G. Exarhos and X. Moussas, "Time variations of the magnetic field at the heliospheric termination shock—galactic cosmic-ray modulation," *Solar Physics*, vol. 187, no. 1, pp. 157–175, 1999.
- [4] I. Morishita and S. Sakukibara, "Size of heliopause derived from long term modulation of neutron monitor intensities," in *Proceedings of the 26th International Cosmic Ray Conference (ICRC '99)*, p. 87, 1999.
- [5] I. Usoskin, K. Mursula, S. Solanki, M. Schüssler, and G. Kovaltsov, "A physical reconstruction of cosmic ray intensity since 1610," *Journal of Geophysical Research*, vol. 107, p. 1374, 2002.
- [6] A. Belov, "Large scale modulation: view from the earth," *Space Science Reviews*, vol. 93, pp. 79–105, 2000.
- [7] P. Lantos, "Predictions of galactic cosmic ray intensity deduced from that of sunspot number," *Solar Physics*, vol. 229, no. 2, pp. 373–386, 2005.
- [8] G. D. Badhwar and P. M. O'Neil, "Time lag of twenty two year solar modulation," in *Proceedings of the 23rd International Cosmic Ray Conference*, vol. 3, pp. 535–539, 1993.
- [9] K. Alanko-Huotari, K. Mursula, I. G. Usoskin, and G. A. Kovaltsov, "Global heliospheric parameters and cosmic-ray modulation: an empirical relation for the last decades," *Solar Physics*, vol. 238, no. 2, pp. 391–404, 2006.
- [10] E. Paouris, H. Mavromichalaki, A. Belov, R. Gushchina, and V. Yanke, "Galactic cosmic ray modulation and the last solar minimum," *Solar Physics*, vol. 280, pp. 255–271, 2012.
- [11] R. P. Kane, "Hysteresis of cosmic rays with respect to sunspot numbers during the recent sunspot minimum," *Solar Physics*, vol. 269, no. 2, pp. 451–454, 2011.
- [12] E. Paouris, "Ineffectiveness of narrow CMEs for cosmic ray modulation," in *Advances in European Solar Physics*, V. M. Nakariakov, M. K. Georgoulis, and S. Poedts, Eds., Solar Physics.
- [13] R. P. Kane, "Comparison of the variations of CMEs and ICMEs with those of other solar and interplanetary parameters during solar cycle 23," *Solar Physics*, vol. 233, pp. 107–115, 2006.
- [14] J. T. Hoeksema, "The large-scale structure of the heliospheric current sheet during the Ulysses epoch," *Space Science Reviews*, vol. 72, pp. 137–148, 1995.
- [15] I. G. Richardson and H. V. Cane, "Near-earth interplanetary coronal mass ejections during solar cycle 23 (1996–2009): catalog and summary of properties," *Solar Physics*, vol. 264, pp. 189–237, 2010.
- [16] N. Gopalswamy, "Coronal mass ejections of solar cycle 23," *Journal of Astrophysics and Astronomy*, vol. 27, pp. 243–254, 2006.
- [17] M. Gerontidou, H. Mavromichalaki, A. Belov, and V. Kurt, "Solar proton enhancements in different energy channels and coronal mass ejections during the last solar cycle," *Advances in Space Research*, vol. 43, no. 4, pp. 687–693, 2009.
- [18] N. Gopalswamy, S. Yashiro, A. Lara et al., "Large solar energetic particle events of cycle 23: a global view," *Geophysical Research Letters*, vol. 30, p. 8015, 2003.
- [19] S. W. Kahler, "The correlation between solar energetic particle peak intensities and speeds of coronal mass ejections: effects of ambient particle intensities and energy spectra," *Journal of Geophysical Research*, vol. 106, p. 20947, 2001.
- [20] H. Mavromichalaki, E. Paouris, and T. Karalidi, "Long-term cosmic-ray modulation during solar cycle 23," in *Proceedings of the AIP Conference Proceedings*, N. H. Solomos, Ed., vol. 848, pp. 184–193, September 2005.
- [21] H. Mavromichalaki, E. Paouris, and T. Karalidi, "Cosmic-ray modulation: an empirical relation with solar and heliospheric parameters," *Solar Physics*, vol. 245, no. 2, pp. 369–390, 2007.
- [22] E. Paouris, "A new statistical index ( $P_i$ ) for coronal mass ejections," in *Proceedings of the 3rd Solar Extreme Events International Symposium-COSPAR Colloquium*, H. Mavromichalaki and A. Papaioannou, Eds., pp. 284–287, 2007.
- [23] A. Kilcik, V. B. Yurchyshyn, V. Abramenko et al., "Maximum coronal mass ejection speed as an indicator of solar and geomagnetic activities," *Astrophysical Journal Letters*, vol. 727, no. 1, p. 44, 2011.
- [24] H. Mavromichalaki and B. Petropoulos, "An empirical model for the 11-year cosmic-ray modulation," *Earth, Moon and Planets*, vol. 37, no. 1, pp. 79–88, 1987.
- [25] C. J. Hatton, "Solar flares and the cosmic ray intensity," *Solar Physics*, vol. 66, no. 1, pp. 159–165, 1980.
- [26] H. Mavromichalaki, A. Belehaki, and X. Rafios, "Simulated effects at neutron monitor energies: evidence for a 22-year cosmic-ray variation," *Astronomy and Astrophysics*, vol. 330, no. 2, pp. 764–772, 1998.
- [27] K. Nagashima and I. Morishita, "Long term modulation of cosmic rays and inferable electromagnetic state in solar modulating region," *Planetary and Space Science*, vol. 28, no. 2, p. 117, 1980.
- [28] J. Xanthakis, H. Mavromichalaki, and B. Petropoulos, "Cosmic-ray intensity related to solar and terrestrial activity indices in solar cycle no. 20," *Astrophysics and Space Science*, vol. 74, no. 2, pp. 303–317, 1981.
- [29] S. E. S. Ferreira and M. S. Potgieter, "Long-term cosmic-ray modulation in the Heliosphere," *The Astrophysical Journal*, vol. 603, p. 744, 2004.
- [30] H. Mavromichalaki, E. Marmatsouri, and A. Vassilaki, "Simulation of long-term cosmic-ray intensity variation," *Solar Physics*, vol. 125, no. 2, pp. 409–414, 1990.
- [31] H. S. Ahluwalia and R. C. Ygbuhay, "The onset of sunspot cycle 24 and galactic cosmic ray modulation," *Advances in Space Research*, vol. 48, no. 1, pp. 61–64, 2011.
- [32] A. V. Belov, R. T. Gushchina, and V. G. Yanke, "The spectrum of cosmic rays variations during 19–22 solar cycles," in *Proceedings of the 26th International Cosmic Ray Conference*, vol. 7, pp. 175–178, 1999.

- [33] H. V. Cane, G. Wibberenz, I. G. Richardson, and T. T. von Roseninge, "Cosmic ray modulation and the solar magnetic field," *Geophysical Research Letters*, vol. 26, no. 5, pp. 565–568, 1999.
- [34] I. Usoskin, H. Kananen, K. Mursula, P. Tanskanen, and G. A. Kovaltsov, "Correlative study of solar activity and cosmic ray intensity," *Journal of Geophysical Research*, vol. 103, p. 9567, 1998.

## Research Article

# Measurement by FIB on the ISS: Two Emissions of Solar Neutrons Detected?

Y. Muraki,<sup>1</sup> K. Koga,<sup>2</sup> T. Goka,<sup>2,3</sup> H. Matsumoto,<sup>2</sup> T. Obara,<sup>2,4</sup> O. Okudaira,<sup>2</sup>  
S. Shibata,<sup>5</sup> and T. Yamamoto<sup>6</sup>

<sup>1</sup>Solar-Terrestrial Environment Laboratory, Nagoya University, Nagoya 464-8601, Japan

<sup>2</sup>Tsukuba Space Center, JAXA, Tsukuba 305-8505, Japan

<sup>3</sup>Department of Physics, Tokyo Metropolitan University, Tokyo 192-0397, Japan

<sup>4</sup>Planetary Plasma and Atmospheric Research Center, Tohoku University, Sendai 980-8578, Japan

<sup>5</sup>Department of Information Science, Chubu University, Kasugai 487-8501, Japan

<sup>6</sup>Department of Physics, Konan University, Kobe 658-8501, Japan

Correspondence should be addressed to Y. Muraki, muraki@stelab.nagoya-u.ac.jp

Received 15 August 2012; Revised 14 October 2012; Accepted 29 November 2012

Academic Editor: Karel Kudela

Copyright © 2012 Y. Muraki et al. This is an open access article distributed under the Creative Commons Attribution License, which permits unrestricted use, distribution, and reproduction in any medium, provided the original work is properly cited.

A new type of solar neutron detector (FIB) was launched on board the Space Shuttle Endeavour on July 16, 2009, and began collecting data at the International Space Station (ISS) on August 25, 2009. This paper summarizes the three years of observations obtained by the solar neutron detector FIB until the end of July 2012. The solar neutron detector FIB can determine both the energy and arrival direction of neutrons. We measured the energy spectra of background neutrons over the South Atlantic Anomaly (SAA) region and elsewhere and found the typical trigger rates to be 20 and 0.22 counts/sec, respectively. It is possible to identify solar neutrons to within a level of 0.028 counts/sec, provided that directional information is applied. Solar neutrons were possibly observed in association with the M-class solar flares that occurred on March 7 (M3.7) and June 7 (M2.5) of 2011. This marked the first time that neutrons had been observed in M-class solar flares. A possible interpretation of the production process is provided.

## 1. Introduction: A Brief History of Solar Neutron Detection

High-energy protons coming from the Sun on February 28 and March 3, 1942 were first discovered by Forbush and published in 1946 [1]. In 1951, Biermann et al. had predicted the potential discovery of solar neutrons on Earth [2]. Neutrons are produced when the accelerated ions strike the solar surface. However, solar neutrons were actually detected 29 years after this prediction. A clear signal of gamma rays and neutrons was detected in association with a large solar flare on June 21, 1980, with an X-ray intensity of X2.5, by the Gamma Ray Spectrometer composed of the NaI and CsI detectors on board the Solar Maximum Mission (SMM) satellite [3, 4]. Figure 1 shows the results. The first peak corresponds to the gamma-ray signal, while the second was induced by the neutron signal. Because neutrons cannot travel from the Sun to Earth at the speed of light, their arrival

time distribution is associated with a time delay from the speed of light, even when simultaneously released from the Sun. For the time distribution presented in Figure 1, if the same departure time for neutrons is set, a neutron energy spectrum is obtained, which assumed an impulsive production of neutrons on the Sun. The spectrum can be expressed by a power law:  $E_n^{-\gamma} dE_n$  with  $\gamma = 3.5 \pm 0.1$  [3, 4].

Two years later, on June 3, 1982, the SMM satellite again detected a neutron signal [5]. However, neutron monitors located on the ground have successively detected neutron signals in association with a large X8.2 solar flare [6, 7], which shed new light on the production time of neutrons in the solar atmosphere. One component involved in the data cannot be explained by an impulsive production mechanism alone. Only two solar neutron events had been accumulated until solar cycle 21, and it was too early to judge the production time of neutrons in the solar atmosphere, namely, whether high-energy neutrons are produced impulsively

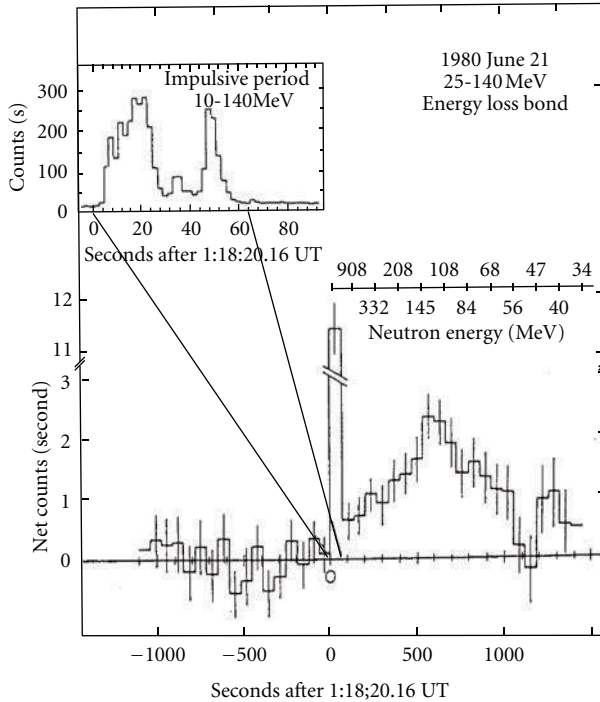


FIGURE 1: Solar neutrons detected on June 21, 1980. Gamma-rays accounted for the first peak; neutrons accounted for the second. The original picture was prepared by the authors of [3, 4].

or gradually. Both scenarios were possible for the same event and this would be a great challenge for solar physicists.

To identify the production time of neutrons at the solar surface in the solar cycle 22, new detectors capable of measuring the energy of neutrons were expected. Therefore a new type of solar neutron detector—the solar neutron telescope (SONTEL)—was designed, based on the plastic scintillator. SONTEL can measure the energy and direction of neutrons using the charge exchange process of neutrons into protons [8, 9]. Therefore SONTEL can determine the flight time from the Sun to Earth. Of course, conventional Simpson-type neutron monitors were also operated [10–13]. At the same time, the possibility of launching a new type of solar neutron detector into space was considered (the idea was proposed in a symposium at Nagoya University held on April 17 and July, 1989. Also presented in the symposiums organized by JSUP of NASDA). To resolve the mystery regarding the production time of neutrons, it is inevitable to have a new type of detector capable of measuring the energy of neutrons in space. We could then identify *when* those neutrons left the Sun.

An attempt to measure the energy of neutrons was found in a paper dated around 1985 [14]. Scintillator bars composed of two layers were equipped (in  $x$  and  $y$  directions) and the device was circulated over the Southern hemisphere by a Racoon balloon flight from Alice Springs, Australia to detect solar neutrons within the energy range of 20 to 150 MeV, but detected no signals. Almost the same year 1985, another new instrument was proposed, capable of unambiguously determining the energy and direction of

incident neutrons using a technique, the double Compton scattering method [15]. The detector was named SONTRAC. Independent from these activities, most of which were developed in the USA, in Japan, a detector comprising a mass of the scintillation fiber is proposed to detect antideuterium in space and neutron and anti-neutron oscillation in the space between the Sun and Earth. In 1991, we proposed a new type of detector for the Japanese Experimental Module (JEM) of the International Space Station (ISS) [16, 17].

In April 1991 and August 1991, a large gamma-ray satellite CGRO and a solar satellite Yohkoh were launched. An image of the Sun using neutron signals was successfully drawn, using the Compton scattering function of the COMPTEL detector [18, 19] and beautiful photographs of solar flares were taken by using the soft and hard X-ray telescope of Yohkoh satellite. They have left very important archives on the solar activities [20].

During the solar cycle 22, several new discoveries involving solar neutrons were made, based not only on many ground level detectors but also a few that were space-borne. Consequently, more solar neutron events were accumulated, including one highlight, the discovery of an extremely strong signal of neutrons in association with the large X9.3 solar flare on May 24, 1990 [21, 22]. The signal was the strongest ever observed by the neutron monitor. In association with this flare, two Soviet satellites, GRANAT/PHEBUS [23] and GAMMA-1 [24, 25] successfully captured very impulsive high-energy gamma rays starting at 20:48 UT. One minute later (20:49 UT), strong neutron signals were detected by many neutron monitors located throughout the North American continent [26, 27]. Subsequently, from around 21:00 UT, Ground Level Enhancement (GLE) was observed, induced by high-energy protons. The key knowledge obtained by the event on May 24, 1990, reviewing some 20 years after the discovery, may be the sudden increase in the ratio between 70 and 95 MeV gamma rays and 4–7 MeV nuclear gamma rays 3 minutes later. Chupp and Ryan summarized that the change in ratio may have been induced by accelerated protons to several hundred MeV [28, 29]. It is worth noting that to detect high-energy neutrons at ground level, conventional neutron monitors were not only used to detect solar neutrons in the large solar flare on May 24, 1990, but also in the X9.4 flare on March 22, 1991 [30].

The subsequent scope of remarkable events from solar cycle 22 may also include the detections of high-energy gamma rays and neutrons in association with the six extremely powerful solar flares with X12 observed during June 1 and 15, 1991. Solar neutrons were detected in association with two large solar flares on June 4 and 6, 1991, respectively, using two kinds of solar neutron detectors located on Mt. Norikura: the solar neutron telescope [31, 32] and the neutron monitor [33]. Via simultaneous observations with the neutron monitor and the neutron telescope, the capability of the new solar neutron telescope was demonstrated.

It should be mentioned that in the solar flare on June 4, 1991, the BATSE [34] and OSSE [35] detectors on board the CGRO satellite observed the long-standing emission of gamma rays with a decay time of 330 seconds after

a sharp impulse signal. OSSE observed a neutron capture line (2.223 MeV) and a carbon de-excitation line (4.44 MeV) that continued for three hours. High-energy gamma rays were detected by the EGRET detector with energies of 50 to 100 MeV and  $>150$  MeV for the flare events on June 4, 6, 9, and 11. Moreover, in the flare event on June 11, a particularly long-lasting emission of high-energy gamma rays was recorded, lasting 10 hours [36].

Many arguments concerning the long-lasting gamma rays emerged at the time, namely whether they were induced by the continuous acceleration process of protons (such as in the shock acceleration model [37]) or by protons trapped in the magnetic loop and precipitating on the solar surface [38, 39]. The impulsive production mechanism of neutrons on the solar surface was attributable to the reconnection process of magnetic loops [40–43] or the DC acceleration mechanism [44], while long-lasting emissions of gamma rays may be closely related to the shock acceleration process. The question of whether the long-lasting high-energy gamma-ray emission is attributable to the continuous acceleration of the protons above 300 MeV [29], or the injection of flare accelerated particles into a large coronal loop with release at the mirror points of the loop where the gamma rays are produced, is very interesting [38, 39], the final answer to which will hopefully be obtained in solar cycle 24.

During the solar flare event on September 7, 2005, solar neutron telescopes located on Mt. Sierra Negra in Mexico (at 4780 m) and Mt. Chacaltaya in Bolivia (at 5,250 m) both observed a clear solar neutron signal [45], which was also recorded by three different counters located in the Northern and Southern Hemispheres. This made it possible to compare the detection efficiency of a solar neutron telescope with that of a conventional neutron monitor. The detection efficiency ratios were found to be 1 and 0.7, for the neutron monitor and neutron telescope respectively, pertaining to the same area of both detectors. Since the solar neutron telescope cuts low-energy neutrons of less than 30 or 40 MeV, its detection efficiency is also lower than that of the neutron monitor [46]. The neutron monitor is highly sensitive to neutrons with energy exceeding about 10 MeV [12, 13]. It is worth noting here that the data suggests the involvement of neutrons produced by both the impulsive and gradual phases [45].

The FERMI-LAT satellite also recently observed two gamma-ray events in association with M-class solar flares on March 7 and June 7, 2011 [47]. Again a long duration component lasting more than 14 hours was observed and the continuous emission of GeV gamma rays from the Sun was detected. This mechanism may indicate a different mechanism in the gamma-ray production process in addition to that responsible for the impulsive production of gamma rays, which is discussed in the final part of this paper. An effective summary on solar neutron research has been recently published in a book, which also contains more detailed bibliography [48].

The aim of this paper is to present new results using the FIB detector on board the ISS. Actually Section 2 introduces details of the new solar neutron telescope FIB detector, followed by the neutron observation results on the ISS in

Section 3. Section 4 covers the solar neutron events observed using the new detector in association with the M-class solar flares on March 7, 2011 (M3.7), and on June 7, 2011 (M2.5). Section 5 discusses our results compared to other observations, and Section 6 summarizes the results.

## 2. New Solar Neutron Detector FIB on the ISS

*2.1. SEDA-AP-FIB Detector.* The new solar neutron telescope has been designed as a component of SEDA-AP. A detector for Space Environment Data Acquisition equipment—Attached Payload (SEDA-AP) was originally proposed to measure radiation levels at the International Space Station (ISS) in 1991 [16, 17]. In 2001, an actual Flight Module (FM) was ready to be deployed, but an accident involving the Space Shuttle resulted in the FM being stored in a special clean room for eight years until it could finally be launched.

SEDA-AP was designed as one of the detectors on board the Japan Exposure Module (JEM). This equipment not only comprises a neutron detector but also various other detectors, such as charged particle detectors, a plasma detector, an atomic oxygen monitor, and electronic device evaluation equipment. The system even includes a micro-particle capture detector.

The neutron detector consists of two parts: a conventional Bonner Ball Detector (BBD) and a FIBer detector (FIB). The name FIB is so-called because the main part of the sensor is comprised by the mass of the scintillation fiber. The BBD measures low-energy neutrons; the FIB measures high-energy neutrons. Technical details can be found on the JAXA website (<http://kibo.jaxa.jp/en/experiment/ef/seda-ap/>).

The neutron detector can be extended 1 m from the main frame via a mast to reduce the background neutrons coming from the vessel of the SEDA-AP. The system has a 220-watt power supply and a total weight of 450 kg. The FIB was launched by the Space Shuttle Endeavour on July 16, 2009, and began taking measurements at the ISS on August 25, 2009. Since then, the detectors have been working problem-free. Although the official mission lifetime was estimated as three years, given the importance of the measurements, it would be highly desirable to extend this period to cover at least one solar cycle of 11 years, provided that the system continues to operate.

*2.2. The Experimental Purposes.* This experiment has three main scientific goals as follows.

- (1) Accurate measurements of radiation levels in the ISS environment [49–51].
- (2) Rapid prediction of the imminent arrival of numerous charged particles from the Sun by monitoring GeV GLE particles for the flares of the western part of the solar surface (space weather forecast). However for the flares of the eastern part of the solar surface, the amount of emitted high energy particles may be estimated by observing neutrons.
- (3) Identification of the production time of neutrons induced by the accelerated protons above the solar

surface. We wish to know *when* and *how* high-energy particles are produced over the solar surface. When high-energy charged particles arrive at Earth and are detected, important information may be lost concerning the production time at the Sun. To understand the acceleration mechanism of charged particles at the Sun, it is necessary to compare the data of neutrons and gamma rays with images taken by a soft X-ray telescope [52], RHESSI, and/or the UV telescope launched on the Solar Dynamical Observatory [53, 54].

To determine the neutron production time at the Sun, it is necessary to employ a neutron detector capable of measuring the energy of neutrons. Currently, no such detector has been used in space other than an FIB detector, although the ground-based Solar Neutron Telescopes (SONTEL) have been operating for a number of years [55–58]. Accordingly, the FIB detector installed in SEDA-AP may provide a crucial data measuring neutron energy in space in the solar cycle 24.

**2.3. Sensor Design, Detection Efficiency, and Trigger.** To achieve the scientific goals listed earlier, a fine-grated neutron detector FIB has been designed, consisting of a plastic scintillator with 32 layers (sheets) and dimensions of 3 mm (height)  $\times$  96 mm (width)  $\times$  96 mm (length). Sixteen stacks of scintillation bars are used per layer, with each bar having dimensions of 3 mm (height)  $\times$  6 mm (width)  $\times$  96 mm (length). Each layer is located along the  $x$ -axis and  $y$ -axis alternatively, forming a stratified block and an optical fiber is coupled to the end of each bar to collect photons produced in the scintillator. These photons are then sent to a 256-channel multi-anode-photomultiplier (Hamamatsu H4140-20). Figure 2 shows a schematic image of the FIB detector, which measures the tracks of recoil protons produced by incident neutrons and determines neutron energy using the range method.

It can also identify the direction of neutron incidence. Neutrons and protons are discriminated by an anti-coincidence system consisting of six scintillator plates surrounding the FIB sensor in a cubic arrangement. To measure the total radiation dose at the ISS, we actually collect neutron data obtained over the South Atlantic Anomaly (SAA) region. The maximum count rate of the anti-coincidence system for the SAA region is 60,000 counts per second, and it works.

The cubic-shaped sensor used for neutron detection has sides measuring 10 cm and maximum kinetic energy of about 120 MeV. As shown in Figure 3, the sensor is monitored from two directions by two multi-anode photomultipliers (PMT1 and PMT2), meaning the arrival direction of the tracks can be identified. To determine the arrival direction of neutrons, protons must penetrate at least four sensor layers, each of which consists of plastic bars 3-mm thick. Consequently, the lowest neutron energy that can be measured is 35 MeV.

A trigger signal is produced by dynode signals from the PMTs (it is set at  $\gtrsim 30$  MeV proton equivalent). When the dynode signals from both PMTs exceed a certain threshold, a trigger signal is produced. When the trigger rate is less than

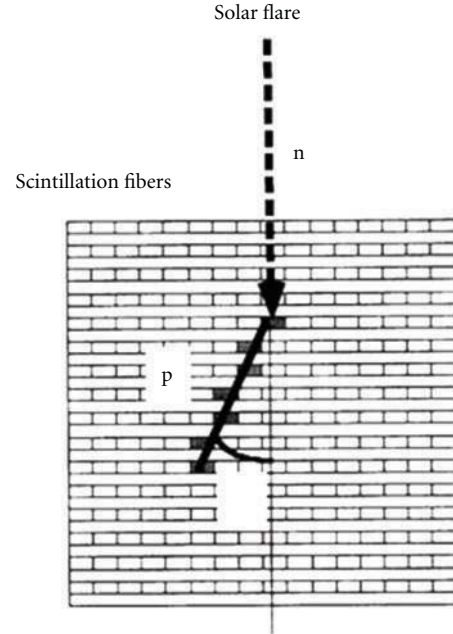


FIGURE 2: Schematic view of the FIB detector's sensor. One layer consists of 16 plastic scintillator bars with dimensions of 3 mm (height)  $\times$  6 mm (width)  $\times$  96 mm (length). The direction of the Sun is identified by tracking two layers of the scintillator in both  $x$  and  $y$  directions; the energy of neutrons is measured by the range of protons.

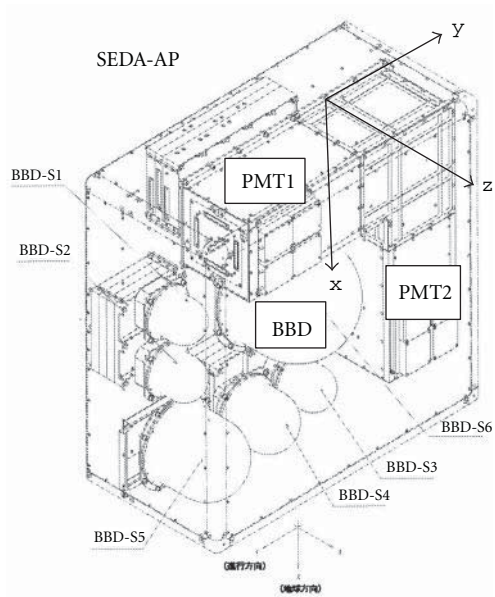
2 counts/sec, all ADC values for each channel are recorded in memory. The analog memory can handle all 512 channels of both PMTs. When the trigger rate exceeds 2 counts/sec, only the on-off signal (1 or 0) of each channel is recorded. When it exceeds 15 counts/sec, only the total output signal of the dynode is recorded. The technical details can be found elsewhere [59–62].

**2.4. Detection Efficiency.** We now discuss the neutron detection efficiency of the sensor. Because of the cubic-shaped detector has sides measuring 10 cm, if neutrons with kinetic energy not exceeding 120 MeV interact at the top of the detector, the track of protons will be fully contained in the apparatus. However, if n-p scattering occurs in the lower part of the detector, the recoil protons will escape by crossing one anticounter plane. This means the anticounter is triggered and the neutron event will not be recorded, resulting in a geometrical factor dependent on energy. Furthermore, the nuclear interaction cross-section also depends on the energy of neutrons, which imposes a greater energy dependence on detection efficiency.

We actually obtained detection efficiency ( $\epsilon$ ) using the Monte Carlo method and the Geant4 program, during which the collisions between neutrons and the carbon target were also taken into account. The detection efficiency of neutrons for vertical incidence without using any anti-coincidence panel can be approximated by  $\epsilon = 3.45 \times E [\text{MeV}]^{-0.7118}$ . For example, neutrons with incident kinetic energy of 100 MeV is expected to be detected by an efficiency of 0.13 or 13%.



(a)



(b)

FIGURE 3: (a) The photograph of Japan Exposure module onboard the International Space Station. The coordinate of the FIB sensor is drawn on by the blue arrows ( $x$  coordinate blue,  $y$  coordinate in red, and  $z$  coordinate by green), (b) An FIB sensor was mounted on SEDA-AP together with BBD. Proton tracks are measured by a photomultiplier (PMT2) that looks the scintillation fibers from the bottom side ( $z$ - $y$  plane), while for the  $x$ - $z$  plane the other photomultiplier (PMT1) is used looking from the preceding section of the ISS.

For the incidence with  $\theta = 10, 20,$  and  $30^\circ$ , the coefficient 3.45 is replaced by 3.1, 2.9, and 2.6, respectively. However, another condition has been applied to data analysis, whereby the minimum energy deposited in the sensor exceeds 35 MeV. According to the Monte Carlo calculation, the detection efficiency ( $\epsilon$ ) can be expressed as  $\epsilon = 1.15 \times (E - 25[\text{MeV}]) \times E [\text{MeV}]^{-1.8}$ . The results are given in Figure 4. In fact, the detection efficiency ( $\epsilon$ ) could be approximately expressed by a constant value of 0.021 (almost 2%) over a wide energy range of incident neutrons where  $E_n = 50\text{--}120$  MeV. We took account of these efficiencies when obtaining the energy spectrum of neutrons.

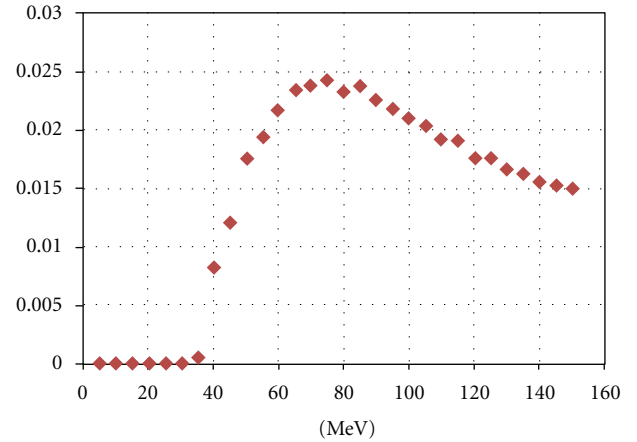


FIGURE 4: The detection efficiency of the FIB sensor for neutrons as a function of incident energy. The vertical value of 0.02 corresponds to the detection efficiency of 2%. The curve was obtained by the Geant 4 program, taking account of the collision processes of neutrons with the proton or carbon target inside the scintillation fibers. The anticounter trigger condition was also taken into consideration.

### 3. Measurement of Neutrons on the ISS

This section presents the actual neutron measurement results obtained on the ISS. Figure 5 shows a typical event detected by the NEM sensor. The image on the right was taken by the PMT located in the preceding section of the ISS ( $x$ - $z$  plane), while that on the left is a photo taken from underneath the sensor ( $z$ - $y$  plane) (i.e., looking up from Earth, see Figure 3(b)). The  $z$ - $y$  sensor points upward toward Earth and the  $z$ -direction points towards the opposite side of the pressurized ISS module. The color represents the amount of energy deposited in each scintillating bar of dimensions of  $6 \times 3 \times 96$  mm. Figure 6 presents the counting rate of the FIB on March 7, 2011. Each panel of Figure 6 shows from the top to the bottom, the position of ISS, the strength of the magnetic field, the counting rate per minute and the integral counting rate, respectively. The satellite observed the solar flare after 20:02 UT.

As evidence that the FIB detector has been working stably, the energy spectrum of neutron-converted-protons is given in Figure 7. The graph has been made by analyzing all data collected during January 1, 2010 and July 31, 2010. The observed proton spectrum can be expressed by a power law with a differential power index of  $-1.75$  within the proton energy range where  $E_p = 45\text{--}85$  MeV. The data taken over the SAA region were excluded.

The trigger rate for neutrons was 0.22 counts/sec on average (see Figure 6 the third panel) and 20 counts/sec over the South Atlantic Anomaly (SAA) region, which is about 90 times greater than anywhere else. The orbital average value 0.22counts/sec is obtained after excluding the counting over the SAA. We have also measured neutron energy spectra using the range method. This may be the first time the energy of neutrons in space has been measured using the range method. As the trigger system occasionally encounters

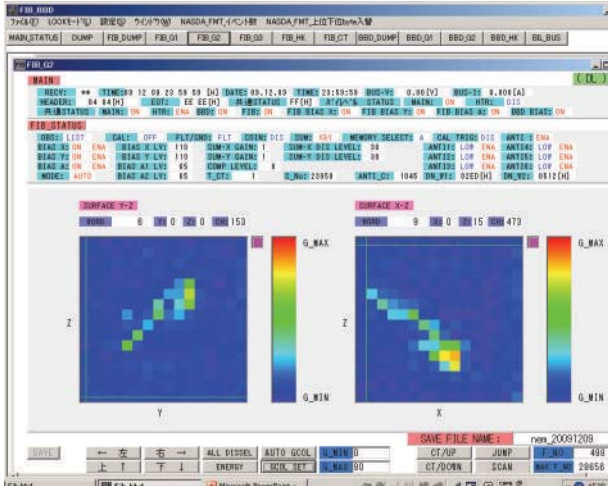


FIGURE 5: A typical background neutron event. The neutrons enter from the preceding section of the ISS (small to large in the horizontal scale  $y$  of the left side picture) and from the top to the bottom (small to large of the right side picture  $x$  in horizontal axis). The incident neutrons are converted into protons inside the scintillator. The energy deposit in each bar is color-coded. At the termination point of the track, the Bragg peak can be recognized. The  $G_{min}$  and  $G_{max}$  correspond to the ADC channel 0 and 90. The linear ADC has a range of 256 channels and the dip and peak correspond to 11 (dark blue) and 22 (light blue) respectively induced by the minimum ionizing particles. Orange spot corresponds to about channel 70.

problems with memory saturation over the SAA region, it began recording only on-off data for each channel. At the end of this section, we mention the possibility of electron detection by this sensor. Using information on ionization loss ( $-dE/dX$ ), each of the electrons is separated from the neutron-converted-protons. The internal sensor can detect electrons with energy of between 2.5 and 30 MeV, as a thin track. Figure 8 shows a candidate electron track.

#### 4. Solar Neutrons Associated with M-Class Solar Flares

**4.1. Search for Solar Neutrons by the FIB Detector.** According to the calculations of Imaida et al. [63] and Watanabe [64], the typical event rate induced by solar neutrons is expected to be within the range 10 to 1,000 counts/sec in FIB. As mentioned earlier, the background rate is as low as 0.22 counts/sec, making it possible to detect all solar neutrons exceeding this level. Between September 2009 and February 15, 2011, no solar flare occurred with intensities exceeding the X-class. However, during the period February 6 to 8, 2010, four large M-class solar flares were observed, hence we analyzed the NEM data recorded at the time. Fortunately, during all four peaks of X-ray intensity, the satellite was flying over the daylight side of Earth. The peaks in X-ray intensity were observed by the GOES satellite on February 6 at 18:59 UT (M2.9), February 7 at 02:34 UT (M6.4), February 8 at 07:53 UT (M4.3), and again on February 8 at

13:47 UT (M2.0). Although we carefully searched the NEM records, there was no evidence of neutrons arriving from the Sun during any of these periods.

**4.2. List of Flares and Search Conditions.** We searched solar neutrons for every solar flare of GOES X-ray intensity exceeding M2, the results of which are summarized in Table 1. The first to third columns correspond to the event date, peak X-ray intensity, and flare class, respectively. The fourth column indicates the ISS location, namely whether on the night (X) or day (O) side of Earth. The fifth column indicates whether solar neutrons are involved in the data. The  $\odot \rightarrow X$  and  $X \rightarrow \odot$  notations in the fourth column indicate that the ISS was moving from the sunny side to the occultation side or vice versa 30 minutes from the peak flare time. A ? mark in the fifth column indicates a possible neutron signal with statistical significance less than  $3\sigma$ .

Thanks to past observations, neutrons are known to be typically produced when the X-ray intensity peaks, and are observed within 30 minutes of this time via an X-ray detector [3–5, 31–33, 45]. Solar neutrons with energy of 35 MeV need 23 minutes more than light to travel from the Sun to Earth. Of course, the maximum time observed by the GOES X-ray detector does not always correspond to the neutron production time by the accelerated protons. Neutron energy of 35 MeV corresponds to the minimum energy for tracking protons in the FIB detector. By taking these conditions into account, we set a data analysis time of 30 minutes and then searched for neutrons coming from the Sun.

**4.3. Background.** Before introducing the actual neutron events, let us briefly describe the background. As shown in the third panel of Figure 6, when the ISS approaches the northern or southern polar regions from the Equator, the neutron counting rate of the FIB detector increases from 0.04 to 0.5 counts/sec. The ISS completes an orbit around Earth every 90 minutes. Therefore, should solar neutrons arrive when the ISS passes over the Equator, high quality data are obtained. However, it also passes over either side of the polar regions during each 45-minute period.

For this period, the FIB detector demonstrates new functions to discriminate background and squeeze signals. We assume that the direction of protons induced by solar neutrons was observed within a cone with an opening angle of about 45 degrees relative to the direction of the Sun. By applying a simple acceptance calculation ( $1/2 * \pi$  steradian /  $4\pi$  steradian = 1/8), the background may be reduced to 1/8. We can therefore identify neutron signals under a background level of 0.028 counts/sec (=0.22/8). In other words, when the intensity of solar neutrons is weaker than 0.028 counts/sec, solar neutrons will become far more difficult to detect.

**4.4. Actual Event Observed on March 7, 2011.** On March 7, 2011, in association with the M3.7 flare, a possible signal of solar neutrons was captured by the FIB detector and more than 54 proton events were identified as coming from the direction of the Sun. In Figure 9, we present a distribution of

TABLE 1: The list of solar flares with X-ray intensity exceeding  $X > 2.0$ . The first to third columns of Table 1 correspond to the event date, maximum time of X-ray intensity, and flare size, respectively. The fourth column indicates the ISS location regarding whether on the shadow or sunny side of Earth (X or  $\odot$ ). The fifth column indicates whether solar neutrons are involved in the data. The  $\odot \rightarrow X$  and  $X \rightarrow \odot$  notations in the fourth column indicate that the ISS was moving from the sunny side to the shadow side or vice versa 30 minutes from the peak flare time. The ? mark of the fifth column indicates a possible neutron event with statistical significance of less than  $3\sigma$ .

Date	Max. X-ray time	Class	Satellite position	Neutron existence
Feb. 6, 2010	18:59	M2.9	Sun side $\odot$	Neutron X
Feb. 7, 2010	02:34	M6.4	Sun side $\odot$	Neutron X
Feb. 8, 2010	07:43	M4.0	Sun side $\odot$	Neutron X
Feb. 8, 2010	13:47	M2.0	Sun side $\odot$	Neutron X
Feb. 12, 2010	13:47	M2.0	Sun side $\odot$	Neutron X
Feb. 13, 2011	17:38	M6.6	Eclipse X	Neutron X
Feb. 15, 2011	01:44	X2.2	Eclipse X	Neutron X
Feb. 18, 2011	10:11	M6.6	Sun side $\odot$	Neutron ?
Feb. 24, 2011	07:35	M3.5	Eclipse X	Neutron X
<b>Mar. 7, 2011</b>	<b>20:12</b>	<b>M3.7</b>	<b>Sun side <math>\odot</math></b>	<b>Neutron</b> $\odot$
Mar. 8, 2011	10:44	M5.3	Eclipse X	Neutron X
Mar. 8, 2011	18:28	M4.4	Eclipse X	Neutron X
Mar. 9, 2011	23:23	X1.5	Eclipse X	Neutron X
<b>Jun. 7, 2011</b>	<b>06:30</b>	<b>M2.5</b>	$\odot \rightarrow X$	<b>Neutron</b> $\odot$
Jul. 30, 2011	02:09	M9.3	Sun side $\odot$	Neutron ?
Aug. 3, 2011	13:48	M6.0	Sun side $\odot$	Neutron X
Aug. 4, 2011	03:57	M9.3	Sun side $\odot$	Neutron X ?
Aug. 8, 2011	18:10	M3.5	Sun side $\odot$	Neutron ?
Aug. 9, 2011	03:54	M2.5	Sun side $\odot$	Neutron ?
Aug. 9, 2011	08:05	X6.9	Sun side $\odot$	Neutron X
Sep. 6, 2011	01:50	M5.3	Sun side $\odot$	Neutron X
Sep. 6, 2011	22:20	X2.1	Sun side $\odot$	Neutron X
Sep. 7, 2011	22:38	X1.8	Sun side $\odot$	Neutron X?
Sep. 8, 2011	15:46	M6.7	Sun side $\odot$	Neutron $\odot$
Sep. 9, 2011	06:11	M2.7	$\odot \rightarrow X$	Neutron X
Sep. 22, 2011	11:01	X1.4	$\odot \rightarrow X$	Neutron ?
Sep. 24, 2011	09:40	X1.9	$X \rightarrow \odot$	Neutron X
Sep. 24, 2011	13:20	M7.1	Sun side $\odot$	Neutron X
<b>Sep. 24, 2011</b>	<b>19:18</b>	<b>M3.0</b>	<b>Sun side <math>\odot</math></b>	<b>Neutron</b> $\odot$
Sep. 24, 2011	20:36	M5.8	Sun side $\odot$	Neutron X
Sep. 25, 2011	02:33	M4.4	Eclipse ( $X \rightarrow \odot$ )	Neutron ?
Sep. 25, 2011	04:50	M7.4	Eclipse ( $X \rightarrow \odot$ )	Neutron ?
Sep. 25, 2011	15:33	M3.7	Sun side $\odot$	Neutron X
Sep. 26, 2011	05:08	M4.0	Sun side $\odot$	Neutron X
Sep. 26, 2011	14:45	M2.6	Sun side $\odot$	Neutron X
Oct. 2, 2011	00:50	M3.9	Sun side $\odot$	Neutron X

TABLE 1: Continued.

Date	Max. X-ray time	Class	Satellite position	Neutron existence
Nov. 2, 2011	22:01	M4.3	Sun side ○	Neutron X
<b>Nov. 3, 2011</b>	<b>20:27</b>	<b>X1.9</b>	<b>Sun side</b> ○	<b>Neutron</b> ○
Nov. 5, 2011	03:35	M3.7	Sun side ○	Neutron X
Dec. 25, 2011	18:16	M4.0	Eclipse X	Neutron X
Jan. 19, 2012	16:05	M3.2	Sun side X → ○	Neutron X
<b>Jan. 23, 2012</b>	<b>03:59</b>	<b>M8.7</b>	<b>Sun side</b> ○ → X	<b>Neutron</b> ○
Jan. 27, 2012	18:37	X1.7	Sun side ○	Neutron X
Mar. 2, 2012	17:46	M3.3	Sun side ○	Neutron ?
Mar. 4, 2012	10:45	M2.0	Eclipse X	Neutron X
Mar. 5, 2012	04:05	X1.1	X → ○	Neutron ?
Mar. 7, 2012	00:24	X5.4	○ → X	Neutron X
Mar. 9, 2012	03:45	M6.3	Sun side ○	Neutron ?
Mar. 10, 2012	17:50	M8.4	Eclipse X	Neutron X
Mar. 13, 2012	17:25	M7.8	Sun side ○	Neutron ?
May. 9, 2012	12:32	M4.7	Sun side ○	Neutron X
May. 9, 2012	21:05	M4.1	Sun side ○	Neutron X
May. 10, 2012	04:18	M5.7	Sun side ○	Neutron X
May. 17, 2012	01:47	M5.1	Sun side ○	Neutron X
Jul. 2, 2012	10:50	M5.6	Eclipse X	Neutron X
Jul. 2, 2012	20:05	M3.8	Eclipse X	Neutron X
Jul. 4, 2012	09:55	M5.3	Sun side ○	Neutron X
Jul. 4, 2012	22:05	M4.6	Sun side ○	Neutron X
Jul. 5, 2012	11:40	M6.1	Sun side ○	Neutron X
Jul. 6, 2012	23:05	X1.1	X → ○	Neutron X
Jul. 8, 2012	16:30	M6.9	Eclipse X	Neutron X
Jul. 17, 2012	17:15	M1.7	Sun side ○	Neutron X
Jul. 19, 2012	05:58	M7.7	Sun side ○	Neutron X

the arrival direction of those 54 events over the background at the same time.

The statistical significance of the event was  $6.8\sigma$  (based on the Li-Ma method). We regard those protons as being produced by solar neutrons inside the FIB sensor. Figure 10 shows an example of actual event involving “solar” neutrons. The direction of the Sun was to the lower-left side for pictures on the left ( $y$ - $z$  coordinate) in Figure 10, while the solar direction was to the lower-center side for pictures on the right ( $x$ - $z$  coordinate). The track in Figure 10 corresponds to proton energy of 44 MeV. The event was observed at 20:10:26 UT and departed time from the Sun is estimated as to be 19:50:38 UT.

Figure 11 presents the arrival time distribution of neutron-induced protons. The horizontal axis represents minutes after 20:00 UT. The red curve represents the result, with equivalent analytical conditions applied to the data obtained exactly 90 minutes later. As can be seen, contamination from the background to the possible signal involved time is relatively small. Figure 11 also involves important information. The final candidate of neutrons arrived near

Earth 11 minutes later than the first one. The energy of neutrons was 44 MeV, so we can estimate the latest departure time from the Sun to be after 19:52:36 UT.

The FIB sensor has a function of measuring the energy of neutron-induced protons. Therefore the flight time of neutrons can be estimated. The result is shown in Figure 12. In making Figure 12, the events are used that were emitted in the forward cone with an opening angle of less than 20 degrees. Figure 12 suggests that neutrons were emitted from the Sun during 19:41 and 19:54 UT. It is worthwhile to note that the highest channel (7–20 MeV) of the RESSHI satellite observed an enhancement during 19:42–20:05 UT. The time of peak intensity of the hard X-rays observed by the RHESSI satellite (50–100 keV) for this flare was 20:02 UT.

*4.5. An Interpretation on the Time of Flight Distribution of Neutrons.* The neutron-induced protons of Figure 12 do not necessarily reflect correct flight time of neutrons from the Sun. There is a possibility that the first bump around 19:48 UT was induced by the n-C scattering. Therefore we

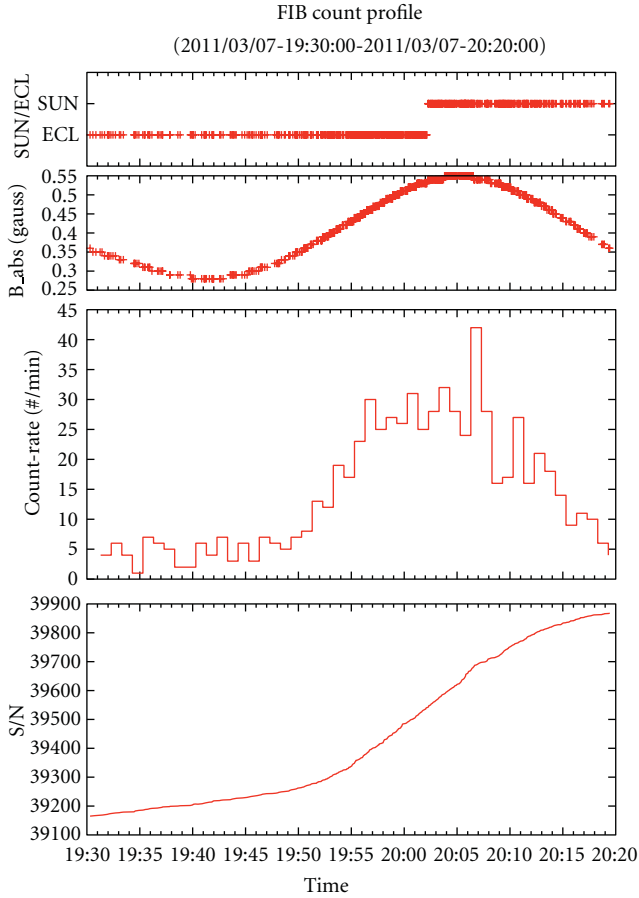


FIGURE 6: From the top to the bottom, each figure corresponds to (1) the location of the satellite, whether it was over the day side of the Earth or the night side, (2) the strength of the magnetic field measured by SEDA-AP, (3) the differential event rate per minute, and (4) the integral counting rate with Universal Time. The SUN or ECL of the top panel represents whether the satellite was on the day side (1) or the night side (0) of the Earth, respectively. The satellite observed the Sun after 20:02 UT. Every 45 minutes, the satellite passes over the Equator and approaches both Polar Regions. The FIB is an omnidirectional sensor and detects neutrons from all directions. The peak during 20:06–20:07 UT may be induced by solar neutrons.

present in the  $E_p/E_n$  distribution Figure 13. To make this figure an assumption is made that those neutrons were produced at the same time on the solar surface at 19:52 UT. We could then evaluate their energy  $E_n$  from the flight time to the top of the atmosphere.  $E_p$  can be obtained for each neutron-induced proton using the range method by the FIB sensor itself. Interestingly, about more than two-thirds of incoming neutron energy is converted into protons, which suggests that some of the break-up neutrons of the carbon target induced by neutrons may have escaped from the sensor to outside. This assumption has been supported by our Monte Carlo calculation based on the Geant-4 program. According to the MC calculation, the mean proton energy  $\langle E_p \rangle$  observed by the FIB sensor can be written by the inverse square root of the incident energy of neutrons  $E_n$ ;  $\langle E_p \rangle$

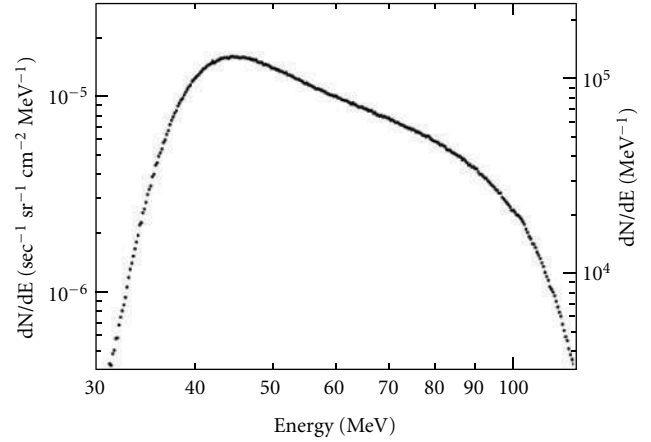


FIGURE 7: Energy spectrum of protons recorded in the FIB sensor during January 1–July 31, 2010. The data obtained over the SAA region is unrelated to this data. The left side axis represents the differential flux of neutron-induced protons denoted by the unit of  $(\text{sec}^{-1} \cdot \text{sr}^{-1} \cdot \text{cm}^{-2} \cdot \text{MeV}^{-1})$ .

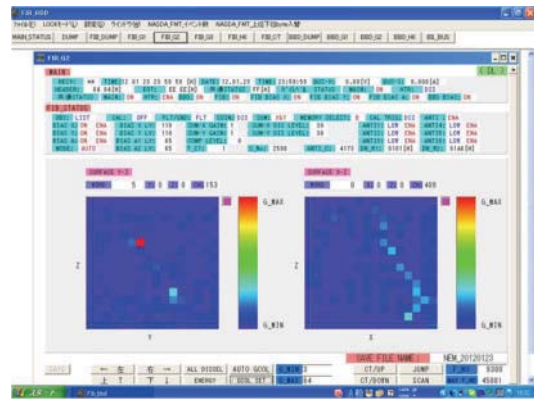
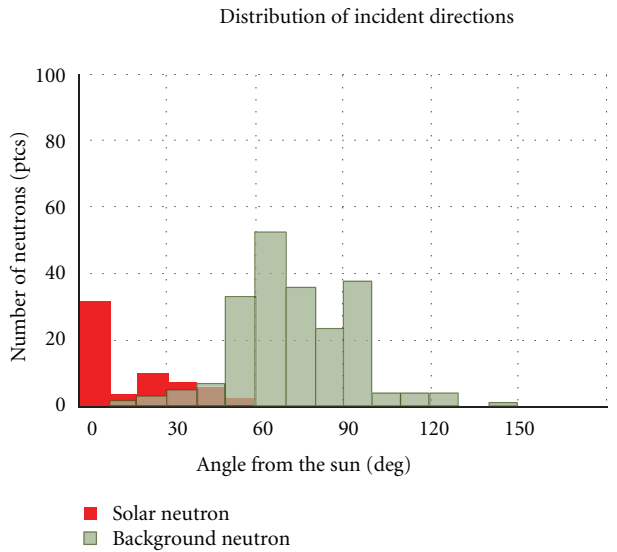


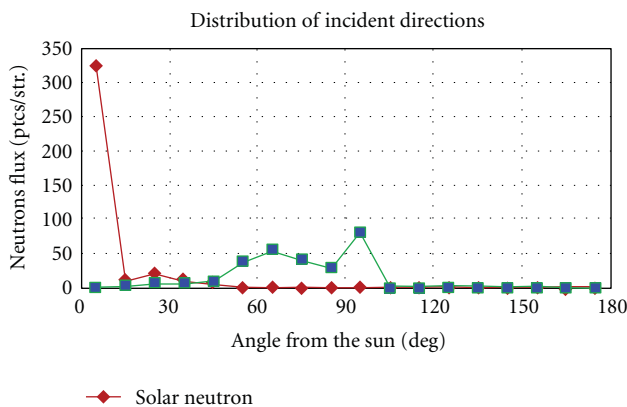
FIGURE 8: A candidate electron track. A photon enters from the top of the sensor ( $y$ - $z$  plane). An electron apparently deposited energy inside one vertical bar (where the red spot denotes a large deposit of energy) while running vertically, thus enabling the recording of a long thin track in the  $x$ - $z$  plane. Since the ionization loss of electrons is smaller than that of protons, thin tracks are expected.

$= 0.55 \cdot E_n / \text{sqrt}(E_n / 100 \text{ MeV})$ . For example neutrons with incident energy of 100 MeV will be observed as protons with an average energy of 55 MeV in the FIB sensor. However we must note here since the event number of the dip between 19:49–19:50 UT is not enough, so this dip has not been confirmed statistically.

Taking account of these facts (1) the angular distribution presented in Figure 9, (2) the production time distribution of neutrons (presented in Figure 12) coincides with the duration of the flare start time (19:43 UT) and the peak time (20:12 UT) (measured by the GOES X-ray detector), (3) the coincidence of the flight time of the last event with an assumption that they were produced around 19:52 UT, and (4) no such enhancement was observed in the data after 90 minutes later, it would be the most natural to think this



(a)



(b)

FIGURE 9: (a) The arrival directions of neutrons, as observed by the FIB sensor during the period 19:59:43–20:16:34 UT. Neutrons coming from the Sun (red) are shown separately from the background neutrons (dark green), but those neutrons are actually observed together by the FIB sensor. The number of events recorded during the above period was 364, and for 44, it was difficult to determine the arrival direction due to low energy. A clear peak of neutrons can be identified within the region 0–20 degrees from the solar direction. Meanwhile, the candidates between 20 and 40 degrees may be neutrons from the Sun, induced by n-C scattering and also distributed at a relatively wide angle due to the limited angular resolution of the FIB sensor for the lowest energy neutrons (about 35 MeV). The bump of the background within the region 40–100 degrees from the solar direction corresponds to the background neutrons produced in the material of JEM by galactic cosmic rays. (b) The same data as used in the plot of (a). However the data were normalized by the solid angle. A sharp peak can be recognized for neutrons from the solar direction (red), while the background neutrons distribute in different angles presented by the green curve. The vertical value represents  $dN/d\Omega$ . Total number of events during 20:02–20:16 UT was 273 and 54 for the background and for the signal respectively.

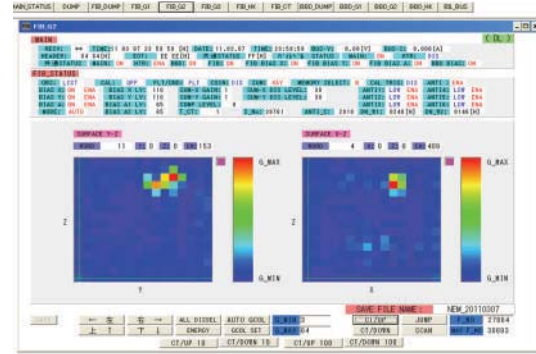


FIGURE 10: Solar neutron the event number 39,761 detected by the FIB sensor at 20:10:26 UT on March 11, 2011. The solar direction was located toward the lower left side in  $y$ - $z$  plane (the left side panel), while in the right side panel the solar direction was downward almost vertically. The energy of the track is estimated as  $(44 \pm 5)$  MeV and the neutron may be emitted around 19:50:38 UT at the Sun, if the track was induced by the n-p collision.

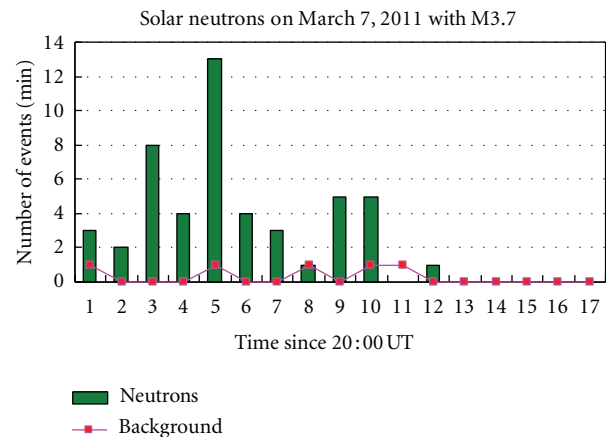


FIGURE 11: The arrival time distribution of neutron-induced protons. The horizontal axis represents minutes after 20:00 UT. The green histogram corresponds to neutrons from the solar direction. The red curve represents the result, with equivalent analytical conditions applied to the data obtained exactly 90 minutes later.

event as following: those neutrons were produced at the Sun in association with the M3.7 solar flare.

4.6. *Other Events.* Three months later, the FIB detector observed another neutron event. This time the flare’s intensity was only M2.5, hence far below the X-class scale. A total of 36 neutron events were identified. The statistical significance of the event was  $5.8\sigma$ . The enhancement was observed during 06:21 and 06:41 UT. Figure 14 shows the angular distribution of those events from the solar direction. On this event, the direction of the Sun was the opposite side of the pressurized module of ISS. So the identification from the background was easily made. The discrimination was also made by confirming the Bragg peak.

We observed three more candidate solar neutron events up to the end of July 2012: the flare events on Sep. 24, 2011

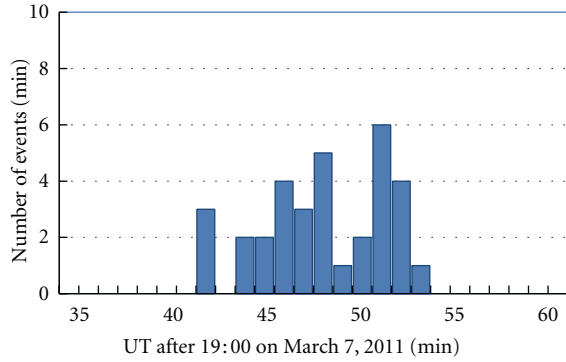


FIGURE 12: The departure time distribution of solar neutrons. The histogram has been made being based on neutrons detected within a cone angle of 20 degrees from the solar direction. From the energy, the time of flight was calculated and converted the value into the departure time of neutrons from the Sun. There were two bumps around 19:48 UT and 19:52 UT.

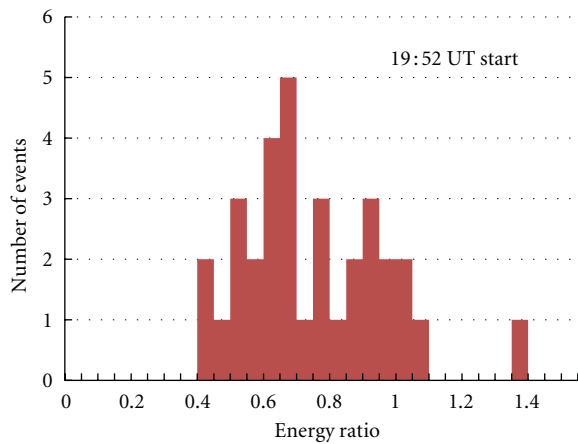


FIGURE 13: Energy ratio between converted protons ( $E_p$ ) versus incident neutrons ( $E_n$ ). Proton energy ( $E_p$ ) was measured using the range method by the FIB sensor, while neutron energy was estimated by flight time. We assumed that the solar neutrons departed at the same time (19:52 UT) from the Sun. There is an event beyond 1.0. However taking account of the energy resolution of the sensor, it sometimes happens.

(M3.0), Nov. 30, 2011 (X1.9), and Jan. 23, 2012 (M8.7). As few as 27 events were observed on September 24, compared to the 42 events on Nov. 30, 2011, while a total of 50 neutrons were observed in association with the flare event on Jan. 23, 2012. Those results are under preparation and will be published in elsewhere. Table 2 summarizes those observation results, along with other observations.

## 5. Discussions and Comparisons with Other Observations

A solar neutron event was observed on March 7, 2011, followed by another on June 7, 2011. Both provided a new perspective regarding the production process of solar neutrons. To date, neutrons have been observed on the occasion

TABLE 2: A score table between each satellite. The numbers of solar neutron events, from first to third, represent protons induced by neutrons, the incidents of which are consistent with those coming from the Sun, low-energy events difficult to identify as solar neutrons and ambiguous events due to low energy respectively. The marks  $\circ$ ,  $\Delta$ , and  $\times$  imply that each satellite was passing over the day side ( $\circ$ ), partial day side ( $\Delta$ ) or night side ( $\times$ ) of Earth, respectively. The event observed on September 8, 2011, was not involved in this table, because it was observed near the SAA.

ISS SEDA-FIB neutron event			Hinode	RHESSI	Fermi-LAT
Mar. 7, 2011	M3.7	54, 35, 28	$\times$	$\circ$	$\Delta$
Jun. 7, 2011	M2.5	86, 2, 20	$\circ$	$\circ$	$\circ$
Sep. 24, 2011	M3.0	27, 2, 20	$\circ$	$\circ$	$\Delta$
Nov. 3, 2011	X1.9	42, 15, 8	$\Delta$	$\times$	$\times$
Jan. 23, 2012	M8.7	50, 14, 20	$\circ$	$\times$	$\times$

of strong solar flares with X-ray intensity of  $\gtrsim X10$  [65]. However, the present results indicate that even solar neutrons are produced by M-class solar flares. The difference in X-ray intensity between X10 and M2.5 is about 40 times greater. The present results thus suggest that solar neutrons including M-class solar flares require a careful and complete search.

The SONG detector on board the Russian satellite CORONUS-F actually observed solar neutrons on three occasions in the solar cycle 23. However, the solar neutrons were only detected for X-class solar flares on August 25, 2001, October 28, 2003 and November 4, 2003 [66] respectively. Moreover, neutron monitors or solar neutron telescopes observed no solar neutrons from August 2009 to the end of July 2012, which may suggest that the soft X-ray flux measured by the GOES satellite does *not necessarily* correspond to the intensity of solar neutrons from the Sun. Although the link between this fact and the magnetic field structure [67] remains unclear, it remains a fascinating subject to be studied.

Another surprising fact is for such medium-class solar flares as those that occurred on March 7 (M3.7) and June 7, 2011 (M2.5), the LAT detector on board the Fermi satellite had observed long-lasting gamma-ray emissions. The emission of gamma rays with energies of 100 MeV to 1 GeV continued for more than 14 hours [47]. This marked a new discovery as the EGRET detector on board the CGRO satellite observed such long-lasting gamma-ray emissions with energy exceeding 150 MeV for the flare event on June 11, 1991 [29]. The RHESSI satellite observed the flare event on March 7 from its start time to the peak time, although the time profile of hard X-rays showed no unusual features and had a normal shape. The telescope of the Solar Dynamical Observatory (SDO) observed a very interesting feature; Coronal Mass Ejection (CME) started before the flare observed by the GOES/RHESSI satellites. A prominent injection of hot plasma into the base of the CME via loops was also observed by the SDO telescope. The signal of neutrons detected by the SEDA-FIB might be produced after that at the top of the inverse U-shaped loop around 19:58 UT [37], while the long-lasting high-energy gamma rays of FERMI-LAT may be produced by the precipitation

TABLE 3: A comparison of solar neutron events observed by the SEDA-FIB detector with SMM event. The average trigger rate is simply obtained by dividing the total number of events by the observation time, while the mean flux is obtained taking the detection efficiency of both detectors into account (0.021 and 0.3 for SEDA and SMM) and also the detector area (100 and 450 cm<sup>2</sup> for SEDA and SMM).

Date of events			Total number of events	Average trigger rate (Hz)	Mean flux (events/cm <sup>2</sup> sec)
Mar. 7, 2011	M3.7	SEDA	89	0.09	0.042
Jun. 7, 2011	M2.5	SEDA	88	0.06	0.029
Jun. 21, 1980	X2.5	SMM	2,000	2.0	0.13

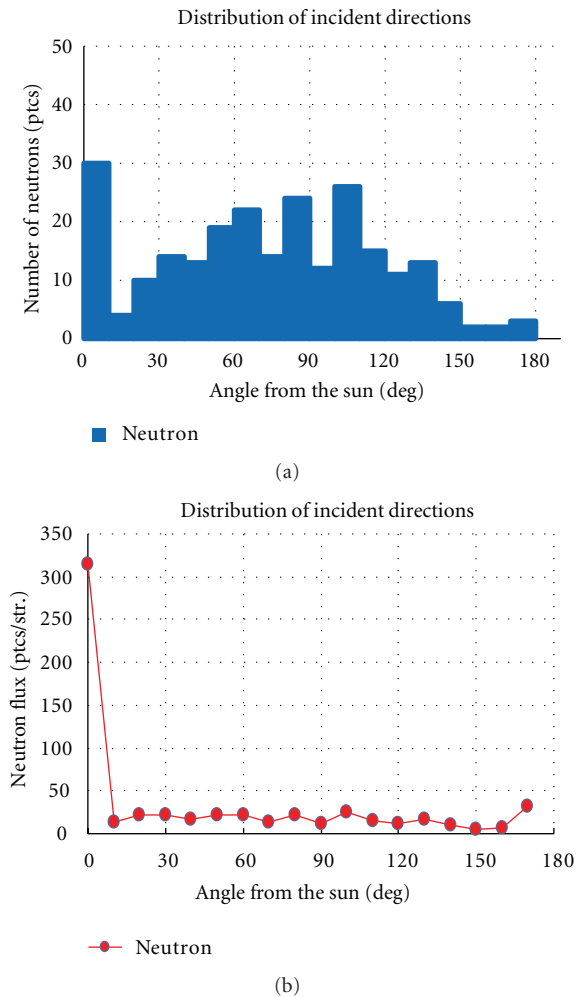


FIGURE 14: (a) The angular distribution of neutrons detected by the FIB sensor during 06:20 UT and 06:41 UT on June 7, 2011. Total number of neutrons detected above duration was 240. (b) The histogram of (a) is divided by the solid angle. The vertical axis represents  $dN/d\Omega$ . A sharp peak is recognized at the solar direction, while beyond 10 degrees, almost flat distribution is seen.

of the accelerated protons on the solar surface. The activity continued for more than 10 hours [47].

For the solar flare event on June 7, 2011, hard X-ray data are available from the Fermi-GBM and RHESSI detectors. Once again, the telescope of the Solar Dynamical Observatory took a very interesting picture of this flare. The UV detector (sensitive to 171 nm) observed the very large-scale precipitation of plasma onto the solar surface

[53, 54]. In coincidence with this precipitation, protons trapped inside the upper “plasma bag” may precipitate over the solar surface. What resembles a “blow brush” over the reconnection point emits the high-energy protons confined in the plasma bag onto the solar surface, at which time the long-lasting gamma rays may be produced. However, the neutrons observed by the FIB detector may be produced when the protons accelerate, when magnetic loops are reconnected on top of the solar surface rather impulsively.

The UV telescope of SDO, however, did not observe any precipitation of plasma for the flare event on March 7, 2011, but instead a clear picture of the beginning of Coronal Mass Ejection (CME). After the seed of CME had been ejected, all loops under the CME started shining brightly. The protons were probably accelerated and neutrons possibly produced in one such loop via loop-to-loop interactions [68] when those protons struck the solar surface.

## 6. Summary

A new solar neutron detector was launched on July 16, 2009, on board the Space Shuttle Endeavour, and began operation at the ISS on August 25, 2009. The sensor can determine both the energy and arrival direction of neutrons. We measured some signals of solar neutron events in association with M-class solar flares that occurred on March 7 and June 7, 2011. It is interesting to note that even for M-class solar flares, we had better search solar neutrons by using both the satellite and ground level detectors.

The precipitation of plasma bubbles, the long-lasting emission of gamma rays, and the starting of CME seeds were among the interesting features observed together with these flares. The new data obtained certainly provides us with a new perspective on the process behind the production of gamma rays and neutrons at the Sun.

The FIB detector on board the ISS observed three further solar neutron events on Sep. 24, 2011 (M3.0), Nov. 30, 2011 (X1.9), and Jan. 23, 2012 (M8.7). More in-depth analysis is now being conducted in connection with other data. In Table 3, we compared the March 7 and June 7, 2011 events with the solar neutron event on June 21, 1980.

## Acknowledgments

The authors acknowledge the crew of the Space Shuttle Endeavour who successfully mounted the SEDA-FIB detector on the ISS Kibo exposed facility. They also extend thanks to the members of the Tsukuba operation center of Kibo for taking the SEDA-FIB data every day. The authors also

acknowledge Dr. Satoshi Masuda of Solar-Terrestrial Environment laboratory of Nagoya University and Professor Masahiro Hoshino of the University of Tokyo for valuable discussions on the solar flares of March 7 and June 7, 2011 and the acceleration mechanism of protons over the solar surface, respectively.

## References

- [1] S. E. Forbush, "Three unusual cosmic-ray increases possibly due to charged particles from the sun," *Physical Review*, vol. 70, no. 9-10, pp. 771-772, 1946.
- [2] L. Biermann, O. Haxel, and A. Schlüter, "Neutral cosmic rays produced in the Sun," *Zeitschrift für Naturforschung*, vol. 6, no. 1, pp. 47-48, 1951.
- [3] E. L. Chupp, D. J. Forrest, J. M. Ryan et al., "A direct observation of solar neutrons following The 0118 UT flare on 1980 June 21," *The Astrophysical Journal*, vol. 263, pp. L95-L98, 1982.
- [4] D. J. Forrest, E. L. Chupp, and J. M. Ryan, "Model calculations on fast solar neutrons and the 2.2 MeV line emission from solar flares," in *Proceedings of the 17th International Cosmic Ray Conference (ICRC '81)*, vol. 10, p. 5, 1981.
- [5] E. L. Chupp, H. Debrunner, E. Flückiger et al., "Solar neutron emissivity during the large flare on 1982 June 3," *The Astrophysical Journal*, vol. 318, pp. 913-925, 1987.
- [6] H. Debrunner, E. O. Flückiger, J. A. Lockwood, and D. J. Forrest, "The solar cosmic ray neutron event on June 3, 1982," in *Proceedings of the 18th International Cosmic Ray Conference (ICRC '83)*, vol. 4, pp. 75-78, Bangalore, India, 1983.
- [7] Y. E. Efimov, G. E. Kocharov, and K. Kudela, "On the solar neutrons observation on high mountain neutron monitor," in *Proceedings of the 18th International Cosmic Ray Conference (ICRC '83)*, vol. 10, pp. 276-278, Bangalore, India, 1983.
- [8] S. Shibata, K. Murakami, Y. Muraki et al., in *Proceedings of the 22nd International Cosmic Ray Conference (ICRC '91)*, vol. 3, pp. 788-791, Dublin, Ireland, 1991.
- [9] R. Bütiköfer, E. O. Flückiger, L. Desorgher et al., "SONTEL-measurements at Gornergrat and environmental radioactivity," in *Proceedings of the 28th International Cosmic Ray Conference (ICRC '03)*, vol. 7, pp. 4189-4192, Tsukuba, Japan, 2003.
- [10] J. A. Simpson, "The cosmic ray nucleonic component: the invention and scientific uses of the neutron monitor," *Space Science Reviews*, vol. 93, no. 1-2, pp. 11-32, 2000.
- [11] K. R. Pyle and J. A. Simpson, in *Proceedings of the 22nd International Cosmic Ray Conference (ICRC '00)*, vol. 3, pp. 53-56, Dublin, Ireland, 2000.
- [12] M. A. Shea and D. F. Smart, "Fifty years of cosmic radiation data," *Space Science Reviews*, vol. 93, pp. 229-262, 2000.
- [13] J. M. Clem and L. I. Dorman, "Neutron monitor response functions," *Space Science Reviews*, vol. 93, no. 1-2, pp. 335-359, 2000.
- [14] R. Koga, G. M. Frye Jr., A. Owens, B. V. Deneby, O. Mace, and T. Jenkins, "A search for solar neutrons on a long duration balloon flight," in *Proceedings of the 19th International Cosmic Ray Conference (ICRC '85)*, vol. 4, pp. 142-145, La Jolla, Calif, USA, 1985.
- [15] R. S. Miller, J. R. Macri, M. L. McConnell, J. M. Ryan, E. Flueckiger, and L. Desorgher, "Nuclear instruments and methods in physics research section A: accelerators, spectrometers, detectors and associated equipment," in *Proceedings of the 10th Symposium on Radiation Measurements and Applications*, vol. 505, pp. 36-40, 2003.
- [16] J. Shimizu, in *Proceedings of the 19th Workshop on Space Station Utilization*, pp. 8.32-8.55, 1997.
- [17] R. Chikaoka, "Minutes of the 12th Space development, Committee of the Ministry of Education, Science and Culture," Reports 13-1 and 12-3, 1997.
- [18] M. McConnell, K. Bennett, D. Forrest et al., "Comptel observations of solar flare gamma-rays," *Advances in Space Research*, vol. 13, no. 9, pp. 245-248, 1993.
- [19] M. McConnell, "High-energy solar phenomena—a new era of spacecraft measurements," in *Proceedings of the AIP Conference*, vol. 294, pp. 21-25, American Institute of Physics, New York, NY, USA, 1993.
- [20] *The Yohkoh HXT/SXT Flare Catalogue*, Edited by J. Sato, M. Sawa, K. Yoshimura, S. Masuda and T. Kosugi, Montana State University and the Institute of Space and Astronautical Science, 2003.
- [21] M. A. Shea, D. F. Smart, and K. R. Pyle, "Direct solar neutrons detected by neutron monitors on 24 May 1990," *Geophysical Research Letters*, vol. 18, no. 9, pp. 1655-1658, 1991.
- [22] M. A. Shea, D. F. Smart, and K. R. Pyle, in *Proceedings of the 22nd International Cosmic Ray Conference (ICRC '91)*, vol. 3, pp. 57-60, Dublin, Ireland, 1991.
- [23] G. E. Kocharov, L. G. Kocharov, G. A. Kovaltsov et al., in *Proceedings of the 23rd International Cosmic Ray Conference (ICRC '93)*, vol. 3, pp. 107-110, Calgary, Canada, 1993.
- [24] V. V. Akimov, N. G. Leikov, A. V. Belov et al., "Some evidences of prolonged particle acceleration in the high-energy gamma-ray flare of June 15, 1991," in *Proceedings of the AIP Conference*, J. Ryan and W. Vestrand, Eds., vol. 29 of *High-Energy Solar Phenomena—A New Era of Spacecraft Measurements*, pp. 106-111, 1993.
- [25] A. V. Belov and M.A. Livshits, "Neutron burst on may 24, 1990," *Astronomy Letters*, vol. 21, no. 1, pp. 37-40, 1995.
- [26] D. F. Smart, M. A. Shea, and K. O'Brien, in *Proceedings of the 24th International Cosmic Ray Conference (ICRC '95)*, vol. 4, pp. 171-174, Rome, Italy, 1995.
- [27] H. Debrunner, J. A. Lockwood, C. Barat et al., "Energetic neutrons, protons, and gamma rays during the 1990 May 24 solar cosmic-ray event," *The Astrophysical Journal*, vol. 479, no. 2, pp. 997-1011, 1997.
- [28] E. L. Chupp and J. M. Ryan, *Research in Astronomy and Astrophysics*, vol. 9, pp. 11-40, 2009.
- [29] G. Rank, J. Ryan, H. Debrunner, M. McConnell, and V. Schonfelder, "Extended gamma-ray emission of the solar flares in June 1991," *Astronomy & Astrophysics*, vol. 378, no. 3, pp. 1046-1066, 2001.
- [30] K. R. Pyle and J. A. Simpson, in *Proceedings of the 22nd International Cosmic Ray Conference (ICRC '91)*, vol. 3, pp. 53-56, Dublin, Ireland, 1991.
- [31] Y. Muraki, K. Murakami, M. Miyazaki et al., "Observation of solar neutrons associated with the large flare on 1991 June 4," *Astrophysical Journal Letters*, vol. 400, no. 2, pp. L75-L78, 1992.
- [32] Y. Muraki, "New solar neutron detector and large solar-flare events of June 4th and 6th, 1991," *Journal of Geomagnetism and Geoelectricity*, vol. 47, no. 11, pp. 1073-1078, 1995.
- [33] A. Struminsky, M. Matsuoka, and K. Takahashi, "Evidence of additional production of high-energy neutrons during the solar flare on 1991 June 4," *Astrophysical Journal Letters*, vol. 429, no. 1, pp. 400-405, 1994.
- [34] R. A. Schwartz, B. R. Dennis, G. J. Fishman, C. A. Meegan, R. B. Wilson, and W. S. Paciesas, "BATSE flare observations in

- Solar Cycle 22,” in *Proceedings of the Compton Observatory Science Workshop*, vol. 3137, pp. 457–468, NASA, 1992.
- [35] R. J. Murphy, G. H. Share, and J. E. Grove, “OSSE observations of the 4 June 1991 solar flare,” in *Proceedings of the AIP Conference*, J. Ryan and W. Vestrand, Eds., vol. 294, pp. 15–20, 1993.
- [36] E. J. Scheneid, K. T. S. Brazier, and G. Kanbach, “EGRET observations of extended high-energy emissions from the nuclear line flares of June,” in *Proceedings of the AIP Conference*, J. Ryan and W. Vestrand, Eds., vol. 294, pp. 94–99, 1993.
- [37] S. Tsuneta and T. Naito, “Fermi acceleration at the fast shock in a solar flare and the impulsive loop-top hard x-ray source,” *Astrophysical Journal Letters*, vol. 495, no. 1, pp. L67–L70, 1998.
- [38] R. Ramaty and N. Mandzhavidze, “Theoretical models for high-energy solar flare emissions,” in *Proceedings of the AIP Conference*, J. Ryan and W. Vestrand, Eds., vol. 294, pp. 26–44, 1993.
- [39] N. Mandzhavidze and R. Ramaty, “High-energy gamma-ray emission from pion decay in a solar flare magnetic loop,” *Astrophysical Journal Letters*, vol. 389, no. 2, pp. 739–755, 1992.
- [40] H. E. Petschek, “Magnetic field annihilation,” in *Proceedings of the AAS-NASA Symposium*, p. 425, Goddard Space Flight Center, 1964.
- [41] S. Masuda, T. Kosugi, H. Hara, S. Tsuneta, and Y. Ogawara, “A loop-top hard X-ray source in a compact solar flare as evidence for magnetic reconnection,” *Nature*, vol. 371, no. 6497, pp. 495–497, 1994.
- [42] K. Shibata, “Evidence of magnetic reconnection in solar flares and a unified model of flares,” *Astrophysics and Space Science*, vol. 264, pp. 129–144, 1999.
- [43] T. Yokoyama and K. Shibata, “A two-dimensional magneto-hydrodynamic simulation of chromospheric evaporation in a solar flare based on a magnetic reconnection model,” *The Astrophysical Journal*, vol. 494, pp. L113–L116, 1998.
- [44] G. D. Holman, “Particle acceleration in large-scale DC electric fields,” in *Proceedings of the AIP Conference*, R. Ramaty and N. Mandzhavidze, Eds., vol. 206, pp. 135–144, 2000.
- [45] T. Sako, K. Watanabe, Y. Muraki et al., “Long-lived solar neutron emission in comparison with electron-produced radiation in the 2005 September 7 solar flare,” *Astrophysical Journal Letters*, vol. 651, no. 1, pp. L69–L72, 2006.
- [46] Y. Muraki, in *Proceedings of the 30th International Cosmic Ray Conference (ICRC '09)*, R. Caballero, J. C. D’Olivo, G. Medina-Tanco, and J. F. Valdés-Galicia, Eds., vol. 6, pp. 181–194, Merida, Mexico, 2009.
- [47] Y. T. Tanaka, IAU telegram #3417 (for the flare of June 7, 2011) and #3886 (for the flare of January 23, 2012). Paper presented at ICRC, Beijing, China, paper no. #683, 2011.
- [48] L. Dorman, *Solar Neutrons and Related Phenomena, Astrophysics and Space Science Library Series 365*, Springer, 2010.
- [49] H. Matsumoto, T. Goka, K. Koga et al., “Real-time measurement of low-energy-range neutron spectra on board the space shuttle STS-89 (S/MM-8),” *Radiation Measurements*, vol. 33, pp. 321–333, 2001.
- [50] T. Doke, “Radiation hazard for the astronauts who stay for long time in the space,” *Science Asahi*, vol. 9, pp. 38–43, 1997.
- [51] H. Koshiishi, H. Matsumoto, A. Chishiki, T. Goka, and T. Omodaka, “Evaluation of the neutron radiation environment inside the International Space Station based on the Bonner Ball Neutron Detector experiment,” *Radiation Measurements*, vol. 42, no. 9, pp. 1510–1520, 2007.
- [52] Hinode, [http://solar-b.nao.ac.jp/index\\_e.shtml](http://solar-b.nao.ac.jp/index_e.shtml).
- [53] Solar Dynamical Observatory, [http://sdo.gsfc.nasa.gov/assets/img/browse/2011/06/07/20110607\\_062513\\_1024\\_0171.jpg](http://sdo.gsfc.nasa.gov/assets/img/browse/2011/06/07/20110607_062513_1024_0171.jpg).
- [54] N. Vilmer, A. L. MacKinnon, and G. J. Hurford, “Properties of energetic ions in the solar atmosphere from gamma-ray and neutron observations,” *Space Science Reviews*, vol. 159, pp. 167–224, 2011.
- [55] E. O. Flückiger, R. Büttikofer, A. Chlingalian et al., “Search for solar neutrons in association with large solar flares in July 2000 and March–April 2001,” in *Proceedings of the 27th International Cosmic Ray Conference (ICRC '01)*, pp. 3044–3047, 2001.
- [56] Y. Muraki, H. Tsuchiya, K. Fujiki et al., “A solar neutron telescope in Tibet and its capability examined by the 1998 November 28th event,” *Astroparticle Physics*, vol. 28, no. 1, pp. 119–131, 2007.
- [57] J. F. Valdés-Galicia, Y. Muraki, H. Tsujihara et al., “An improved solar neutron telescope installed at a very high altitude in Mexico,” *Nuclear Instruments and Methods in Physics Research A*, vol. 535, pp. 656–664, 2004.
- [58] L. X. González, F. Sánchez, and J. F. Valdés-Galicia, “Geant4 simulation of the solar neutron telescope at Sierra Negra, Mexico,” *Nuclear Instruments and Methods in Physics Research A*, vol. 613, pp. 263–271, 2010.
- [59] K. Koga, T. Goka, H. Matsumoto, Y. Muraki, K. Masuda, and Y. Matsubara, “Development of the fiber neutron monitor for the energy range 15–100 MeV on the International Space Station (ISS),” *Radiation Measurements*, vol. 33, no. 3, pp. 287–291, 2001.
- [60] K. Koga, T. Goka, H. Matsumoto, and Y. Muraki, in *Proceedings of the 31st International Cosmic Ray Conference (ICRC '09)*, vol. 831, Lodz, Poland, 2009.
- [61] K. Koga, T. Goka, H. Matsumoto, T. Obara, Y. Muraki, and T. Yamamoto, in *Proceedings of the 21st ECRS*, K. Kudela, P. Kiraly, and A. Wolfendale, Eds., pp. 199–200, Kosice, Slovakia, 2008.
- [62] K. Koga, T. Goka, H. Matsumoto, T. Obara, Y. Muraki, and T. Yamamoto, “Measurement of high-energy neutrons at ISS by SEDA-AP,” *Astrophysics and Space Sciences Transactions*, vol. 7, pp. 411–416, 2011.
- [63] I. Imaida, Y. Muraki, Y. Matsubara et al., “A new tracking satellite-borne solar neutron detector,” *Nuclear Instruments and Methods in Physics Research A*, vol. 421, no. 1-2, pp. 99–112, 1999.
- [64] K. Watanabe, in *Proceedings of the Cosmic-Ray Research of Nagoya University*, vol. 46, pp. 1–249, 2005.
- [65] Y. Muraki, Y. Matsubara, S. Masuda et al., “Detection of high-energy solar neutrons and protons by ground level detectors on April 15, 2001,” *Astroparticle Physics*, vol. 29, no. 4, pp. 229–242, 2008.
- [66] S. N. Kuznetsov, V. G. Kurt, I. N. Myagkova, B. Y. Yushkov, and K. Kudela, “Gamma-ray emission and neutrons from solar flares recorded by the SONG instrument in 2001–2004,” *Solar System Research*, vol. 40, no. 2, pp. 104–110, 2006.
- [67] D. Shiota, S. Tsuneta, M. Shimojo, N. Sakao, D. Orozco Suárez, and R. Ishikawa, “Polar field reversal observations with Hinode,” *The Astrophysical Journal*, vol. 753, p. 157, 2012.
- [68] Y. Hanaoka, “Double-loop configuration of solar flares,” *Solar Physics*, vol. 173, no. 2, pp. 319–346, 1997.

## Research Article

# New Insights on Cosmic Ray Modulation through a Joint Use of Nonstationary Data-Processing Methods

A. Vecchio,<sup>1</sup> M. Laurenza,<sup>2</sup> M. Storini,<sup>2</sup> and V. Carbone<sup>1,3</sup>

<sup>1</sup>Dipartimento di Fisica, Università della Calabria, 87036 Rende (CS), Italy

<sup>2</sup>IAPS, INAF, Via del Fosso del Cavaliere 100, 00133 Roma, Italy

<sup>3</sup>Liquid Crystal Laboratory, INFN, Ponte P. Bucci Cubo 33B, 87036 Rende (CS), Italy

Correspondence should be addressed to A. Vecchio, antonio.vecchio@fis.unical.it

Received 3 August 2012; Accepted 31 October 2012

Academic Editor: Badruddin

Copyright © 2012 A. Vecchio et al. This is an open access article distributed under the Creative Commons Attribution License, which permits unrestricted use, distribution, and reproduction in any medium, provided the original work is properly cited.

The time variability of the cosmic ray (CR) intensity, recorded by the Climax neutron monitor and covering the period 1953–2004, has been analyzed by the joint application of the wavelet and the empirical mode decomposition (EMD) analyses. Dominant time scales of variability are found at  $\sim 11$  yr,  $\sim 22$  yr,  $\sim 6$  yr and in the range of the quasi-biennial oscillations (QBOs). The combination of the 11 yr cycle and QBOs explains the Gnevychev Gap (GG) phenomenon and many step-like decreases characterizing the CR modulation. The additional scales of variability at  $\sim 22$  yr and  $\sim 6$  yr are responsible for other features of the long-term CR trend, such as the intensity flat-topped profile, following the maxima of even-numbered cycles during positive polarity state of the heliosphere ( $A > 0$ ). Comparison with basic time scales of variability derived from the sunspot area (SA) allows the association of the 11 yr cycle and QBOs with solar activity variations, whereas the other two modes with the drift effects govern the CR entrance in the heliosphere.

## 1. Introduction

It has been known for a long time that galactic CRs are modulated by solar activity (see the pioneering works performed by Forbush [1, 2]). In hundred years of research from the CR discovery [3] the topic of cosmic ray modulation has been widely investigated. During the sixties and seventies, the different forms of modulation (short-, medium-, and long-) were identified by a deep analysis of the available experimental data. Solar and interplanetary structures were recognized as the sources of the 3D variability of the incoming charged particles in the heliosphere and several mathematical techniques were applied on the different datasets during the eighties and nineties to improve the knowledge of the solar-heliospheric domain (see, e.g., [4]). Among them, the Wavelet Transform (WT) was widely recognized as a good tool to investigate the time evolution of periodic or quasi-periodic trends in the experimental data sets [5, 6]. The WT, by decomposing a time series into the time-frequency space, allows to analyze processes containing multiscale features and it is able to determine

both the dominant variability modes and how those modes vary in time. The possibility to evaluate a local spectrum distinguishes the use of the wavelet analysis from, for example, Fourier approaches or other mathematical filtering techniques used in the past. Since this technique provides information both in frequency and time domains it allowed to characterize the evolution of CR variability at different scales [7, 8], to identify and characterize the contribution of the different periodicities in the cosmic ray intensity profile for distinct solar cycles and/or different phases of each cycle [9, 10], and to correlate variations, detected in solar cycle indices, with the corresponding fluctuations in CR intensity [11, 12]. Finally the wavelet represented a very useful tool to investigate transitions between different periodicities and to identify a clear difference in the solar activity evolution during odd and even solar activity cycles [9, 10, 13, 14].

More recently, the Empirical Mode Decomposition (EMD) analysis, developed as a signal processing for non-linear and nonstationary data [15, 16], was also introduced in the study of the solar-heliospheric domain (e.g., [17–21]). The method allows to decompose any complicated dataset

into a finite number of components (called Intrinsic Mode Functions: IMF), representing simple oscillatory modes in the time domain with the signal described by a time-dependent amplitude and phase functions.

In this paper we analyze the cosmic ray variations together with sunspot areas recorded for the period from 1953 to 2004. In Section 2 we present results obtained by applying the WT and the EMD to the data set, showing that the EMD modes add more information with respect to the WT only. Section 3 describes two reconstructions of the CR signal, by using different selected EMD modes and discuss the possible association with the different sources of the CR variability, namely solar activity and drift effects. In Section 4 conclusions are drawn.

## 2. Data Used and Method of Investigation

In order to study the behavior of the CR intensity, monthly mean values derived from records of the Climax neutron monitor (Geographic latitude-longitude: N39.37°-E253.82°; cutoff rigidity:  $\sim 3$  GV; height: 3400 m a.s.l.; <http://ulysses.sr.unh.edu/NeutronMonitor/>) have been analyzed for the period 1953–2004. Moreover, monthly averages of sunspot area (SA; <http://solarscience.msfc.nasa.gov/greenwch.shtml>) have also been considered as a parameter of solar activity responsible for the CR modulation. Search for periodicities in the above data sets is performed by using the WT and the EMD techniques.

As stated in the introduction, the WT analysis offers a significant advantage with respect to the classical Fourier transformation because it allows to localize in time possible periodicities, even those not always present through the whole considered time interval. As mother function we assume the Morlet one, which supplies a better resolution in frequency compared to other available functions. The scales have been chosen as fractional power of 2:

$$s_j = s_0 2^{j\delta_j}, \quad \text{for } j = 0, 1, \dots, J, \quad (1)$$

$$J = \delta_j^{-1} \log_2 \left( \frac{N\delta_t}{s_0} \right). \quad (2)$$

The following parameters have been used:  $\delta_j = 0.125$ , is the frequency resolution,  $s_0 = 2$  months, is the smallest resolvable scale, and  $J = 8/\delta_j$  determines the largest scale. Since the set of scales is nonlinear, the associate error is asymmetric. The left and right uncertainties on each wavelet period  $T_j$  can be derived as  $\Delta T_j^+ = (T_{j+1} - T_j)/2$ ,  $\Delta T_j^- = (T_j - T_{j-1})/2$  by using (1) and the relation  $T_j = 1.03s_j$ , valid for the Morlet wavelet.

The Wavelet Power Spectrum (WPS), as a function of time and frequency, has been computed in order to characterize the frequencies of the main periodicities. The significance of the power peaks is evaluated against a white noise background [22]. We remark that the wavelet analysis is based on a priori definition of the mother functions, which could not be representative of the eigenfunctions of the investigated phenomenon. For this reason, the EMD, which is an adaptive technique, is more appropriate to deal with nonstationary data [15]. In the EMD framework, a signal  $S(t)$

can be decomposed into a finite number  $m$  of intrinsic mode functions (IMFs) as

$$S(t) = \sum_{j=1}^m s_j(t) + r_m(t). \quad (3)$$

The mode  $s_j(t)$  is a zero-mean oscillation, variable in both amplitude and frequency, which can be expressed as  $s_j(t) = A_j(t) \cos \omega_j(t)$ , where  $A_j(t)$  and  $\omega_j(t)$  represent the instantaneous amplitude and phase of the  $j$ th EMD mode, respectively. Each IMF has its own characteristic period  $\tau_j$ , defined as the average time difference between  $s_j(t)$  local extrema (local maxima and minima). The standard deviation of the differences between local extrema quantifies the uncertainty associated with each period. This kind of decomposition is local, complete, and orthogonal [15, 23] and the residue  $r_m(t)$  in (3) describes the mean trend. The statistical significance of each IMF, with respect to white noise, can be checked by applying a specific test based on the following argument [24]. When EMD is applied to a white noise series, the constancy of the product between the energy density of each IMF and its corresponding averaged period can be deduced. This relation can be used to derive the analytical energy-density spread function of each IMF as a function of different confidence levels. This approach represents the analogy of the statistical significance test used to evaluate the significance levels in the Wavelet power spectrum [22]. Thus, by comparing the energy density of the IMFs extracted from the actual data with the theoretical spread function, IMFs containing information at the selected confidence level can be distinguished from purely noisy modes. Finally, the orthogonality of EMD modes allows to reconstruct the signal at a chosen time scale through partial sums in (3) (see also [17–19]).

We take advantage of both WT and EMD for a detailed study of the CR variability. First, we determine the characteristic periodicities of the signal through the wavelet analysis, which provide frequencies equivalent to the Fourier's ones. Then, we investigate the time variability of all the basic modes, obtained through the EMD, that contribute to the periodicities identified in the WPS. Figure 1 shows the WPS derived from CLI data. The highest values of power are found, as expected, at  $T = 11.01_{-0.40}^{+0.5}$  yr and  $T = 22.04_{-0.90}^{+1.00}$  yr (where the right and left errors are reported as superscript and subscript, resp.). These periodicities are related to the Schwabe cycle and to the polarity inversion of the Sun's magnetic field (Hale cycle), respectively. Nevertheless, the former cannot be well isolated, because high power is detected in a broad range of periods from 5 to 15 yr; the latter is not reliable, being under the cone of influence, determined by the short length of the data set. Enhanced power is also visible between 1 and 4 yr, but it is significant only during the maximum phases of cycles 21 and 22, being above the confidence level of 80% with respect to white noise.

In order to better characterize the oscillations in the frequency ranges identified through the wavelet analysis, we decomposed the CLI data into a set of IMFs. Ten  $s_j$  modes were obtained and displayed in Figure 2 along with their characteristic periods. The energy density  $E_j$  of each

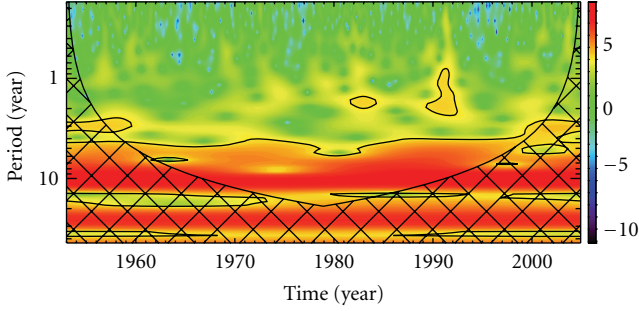


FIGURE 1: WPS of CLI data by using the Morlet mother wavelets. Black contours correspond to the 80% confidence level. The WPS is meaningless inside the cone of influence (cross-hatched region). The following parameters have been used: frequency resolution  $\delta_j = 0.125$ , Morlet wavelet nondimensional frequency,  $w_0 = 6$ ;  $s_0 = 2$  months is the smallest resolvable scale and  $J = 8/\delta_j$  determines the largest scale.

IMF ( $E_j = \langle s_j(t)^2 \rangle$ , where  $\langle \cdot \rangle$  denotes time averages) is shown in Figure 3 as a function of its corresponding characteristic period, to understand which modes dominate the CR variability. The highest amplitude mode  $j = 8$ , having  $\tau_8 = 10.6 \pm 0.3$  yr, can be associated with the Schwabe cycle, whereas  $j = 9$ , having  $\tau_9 = 29 \pm 7$  yr, possibly to the Hale cycle, because its period is comparable with  $\sim 22$  yr within the error.

The IMF  $j = 7$  ( $\tau_7 = 6.5 \pm 0.5$  yr) is found to be the third important mode, although it was not separated from the  $\sim 11$  yr periodicity when using the wavelet analysis. Other modes with comparable amplitude are  $j = 4$ ,  $j = 5$ ,  $j = 6$ , having periods  $\tau_4 = 1.3 \pm 0.1$  yr,  $\tau_5 = 2.2 \pm 0.1$  yr,  $\tau_6 = 3.5 \pm 0.3$ , respectively, that is, time scales of the so-called quasi-biennial oscillations (QBOs [25–27]). Mode  $j = 10$ , with  $\tau_{10} \sim 41$  yr, presents only one oscillation which cannot be considered as reliable, given the limited time extent of the data set. Finally, modes  $j = 1$ ,  $j = 2$ ,  $j = 3$  with  $\tau < 1$  yr have the lowest amplitudes. Moreover, Figure 3 shows that all the computed IMFs are significant, their amplitude being located above the spread lines (dashed, dot-dashed, and dotted lines at 90th, 95th, and 99th confidence level, resp.), obtained by performing the significance test described above.

In order to better understand the links between the identified periodicities and the solar activity, we also performed the EMD analysis on the SA data. The derived modes are shown in Figure 4. Four IMFs ( $j = 1$ ,  $j = 2$ ,  $j = 3$ ,  $j = 4$ , having characteristic periods  $\tau_j < 1$  yr) were found to be not significant at least at 90th confidence level (see Figure 5). Two significant modes ( $j = 5$ ,  $j = 6$ ) have characteristic periods in the QBO range ( $\tau_5 = 1.9 \pm 0.1$  yr and  $\tau_6 = 3.5 \pm 0.2$  yr, resp.), whereas the IMF  $j = 7$  with  $\tau_7 = 10.8 \pm 0.4$  yr has the highest energy (as shown in Figure 5) and it is representative of the Schwabe cycle. Finally, the IMFs  $j = 8$ ,  $j = 9$  (having periods  $\tau_8 = 17.3 \pm 0.6$  yr and  $\tau_9 = 28.3 \pm 10$  yr, resp.) could be both related to the shape of 11 yr cycle, possibly related to the Gnevyshev-Ohl rule. We underline that no mode at  $\sim 6$  yr is detected in SA. This indicates that the IMF  $j = 7$ , detected

in CLI data, could not have a solar origin, as will be discussed in Section 3.2.

### 3. Reconstruction of the CR Signal

**3.1. CR Modulation Driven by Solar Activity.** An important source of CR modulation is represented by solar activity, which is variable on a wide range of temporal scales. The main modulation is at 11 yr time scale and it is related to the well known Schwabe cycle. As a consequence, the CR intensity shows a pronounced 11 yr variation, with the intensity maximum corresponding almost with the solar minimum and vice versa. In addition, many manifestations of solar magnetism as well as some interplanetary phenomena show quasi-biennial variations. The QBOs have been found in photospheric magnetic field and in many solar activity indices such as the sunspot number and area, the number of  $H\alpha$  flares [26], the 10.7 cm radio emission [12], and the coronal emission ([28], and references therein). In the interplanetary medium, QBOs have been observed in the solar wind speed and the interplanetary magnetic field intensity (e.g., [29]), in the number and flux of interplanetary energetic protons at Earth's orbit [8, 27], in the density of galactic CRs at 1 AU [9, 14], and in the outer heliosphere [10].

It has been shown that the effect of solar activity on CR flux can be essentially described by superposing QBOs to the  $\sim 11$  yr mode (e.g., [18, 21]). Thus, in order to investigate the CR modulation driven by the solar activity we perform the reconstruction of both the CR and SA signals, by considering QBOs and the  $\sim 11$  yr mode. As the wavelet analysis indicates that QBOs are located in the Fourier equivalent period 1–4 yr, we reconstructed the signal at QBOs scales through partial sums of IMFs as in (3) considering only the significant modes ( $s_4$ ,  $s_5$ ,  $s_6$ ) having characteristic periods in this range ( $\tau_4 = 1.3$ ,  $\tau_5 = 2.2$ ,  $\tau_6 = 3.5$ , resp.). This is also consistent with the criterion used by Laurenza et al., [21] for the selection of clear and unambiguous EMD components contributing to the QBOs. Note in Figure 2 that  $s_5$  is generally the dominant mode for the CLI QBOs, having the highest amplitude during most of the time. Nevertheless, mode  $s_5$  has a smaller amplitude than  $s_4$  during 1988–1992, although they are almost in phase with each other. In addition, the  $s_6$  amplitude is higher only during the period 1953–1967 and comparable with  $s_5$  during the period 1970–1973. The full QBO signal is depicted in Figure 6 and has a high amplitude during the maximum phase of each solar cycle as expected from results of Bazilevskaya et al. [26], whereas they almost vanish during the sunspot minima.

The importance of QBOs with respect to the  $\sim 11$  yr, around a solar maximum has been evaluated by computing the ratio between the mean square amplitude of the QBOs and that of the  $\sim 11$  yr mode. Being  $s_{\text{QBO}}$  the superposition of the modes  $s_4$ ,  $s_5$ ,  $s_6$ , representing the contribution of the QBO, the ratio  $\langle |s_{\text{QBO}}(t)|^2 \rangle / \langle |s_8(t)|^2 \rangle$  quantifies the importance of QBOs with respect to the  $\sim 11$  yr mode (being the average computed over a time interval of 5 yr around

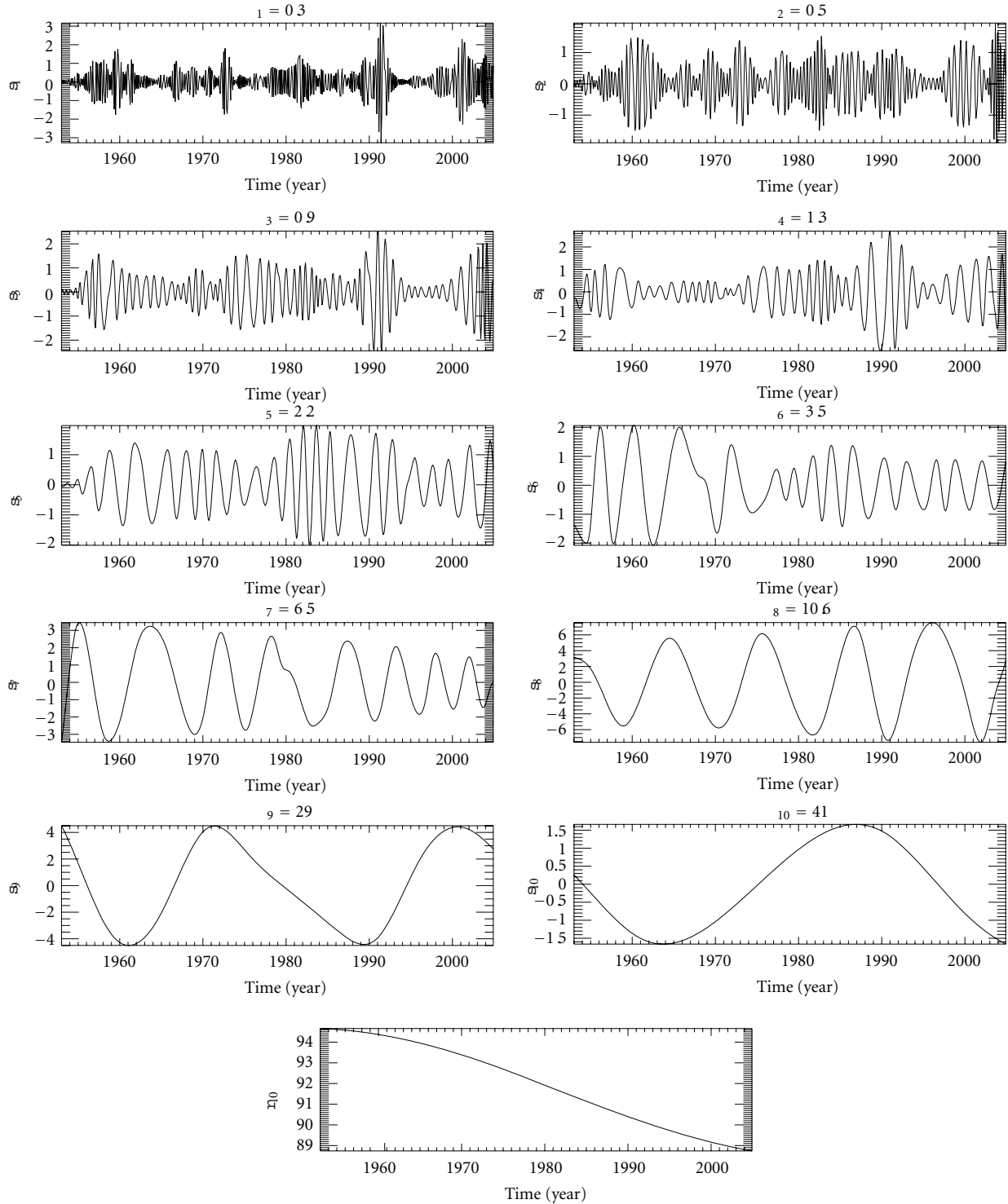


FIGURE 2: IMFs ( $j$  values from 1 to 10) obtained by performing the EMD on CLI data, along with their characteristic periods  $\tau_j$  in years.

each maximum of the 11 yr cycle). The QBO contribution is estimated to be higher than 30% with respect to the amplitude of the  $\sim 11$  yr mode for all the considered cycles (34%, 32%, 38%, 54%, and 31% for cycles 19, 20, 21, 22, and 23, resp., in agreement with the findings of Laurenza et al. [21]).

Then, we compare the superposition of the QBOs and the  $\sim 11$  yr mode with actual CR data. It is apparent in the upper panel of Figure 7 that the superposition of the  $\sim 11$  yr and QBOs well reproduces the general trend of CR data, mainly during the maximum and descending phase of sunspot cycles; that is when QBOs reach their highest

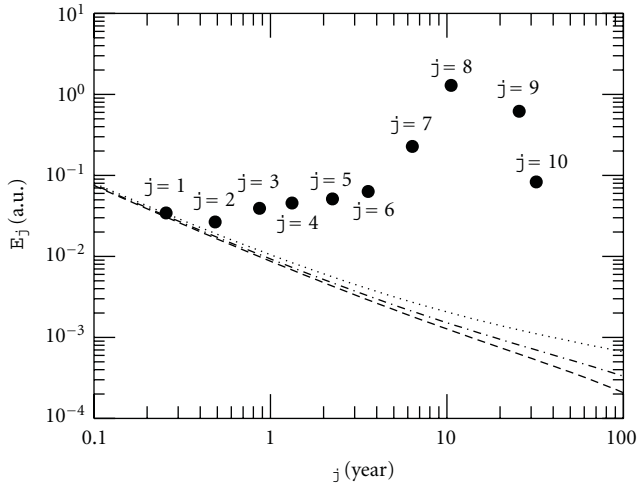


FIGURE 3: Average amplitude ( $E_j$ ) versus typical period ( $\tau_j$ ) of the  $j$  IMFs ( $j$  values from 1 to 10) identified in the CLI data through the EMD. Dashed, dot-dashed, and dotted lines indicate the 90th, 95th, and 99th percentile, respectively.

amplitude. In particular, this superposition accounts for the majority of the step-like decreases, which characterize the CR modulation. Notice that the so-called mini-cycle during 1974 is reproduced. The cosmic ray depression during the mini-cycle was related [30] to a decrease in the radial diffusion coefficient  $K$  (leading to a reduced efficiency of cosmic ray particles to enter the inner solar system). Under the assumption that  $K$  scales inversely with  $B$  as  $K \sim B^{-2}$ , the depression was attributed to increases in the field magnitude through a diffusion dominated process [31], also consistently with findings of Laurenza et al. [21].

The GG phenomenon, namely the peculiar decrease in the temporal trend of various solar-terrestrial indices ([32] and references therein) during the maximum phase of the Schwabe cycles (for early works see [33, 34]), is also observed to be generated by adding QBOs and the  $\sim 11$  yr mode.

The short term variations of the CR intensity, not explained by the QBOs, could be due to the so called merged interaction regions [35], acting as a barrier to cosmic rays [36]. In fact, solar wind transient flows may interact with one another and with corotating streams to form a large-scale interaction region with a shell-like geometry (global merged interaction region—GMIR) that persists over several solar rotations. These time scales are comparable with the high frequency modes ( $\tau < 1$  yr) we detected in CR data, although their possible connection with GMIR has to be further investigated.

We remark that, around sunspot minima, other low frequency modes would be necessary to explain the variability of the CR flux more related to drift effects in the large scale field of the heliosphere that will be treated in the following subsection.

Finally, we study the relationship between medium and long term CR variations and sunspot area. We describe the temporal variability of SA by superposing the  $\sim 11$  yr mode and QBOs ( $s_5$  and  $s_6$  are the contributing IMFs),

which are of the order of 50% with respect to the  $\sim 11$  yr component during the maximum phase. Figure 8 shows the reconstruction for both CLI and SA, which present almost the same profile and are shifted between each other. In particular, the GG is well detected in CR for all solar cycles and delayed, with respect to SA, of an average value of about 6 months. Similar results were obtained in the past (e.g., [37, 38]) in correlative studies between CR data and solar activity indicators. As SA are a proxy for solar activity causing interplanetary disturbances, which act on CR as propagating diffusion barriers, the found delay can be explained in terms of the propagation time of magnetic perturbations from the Sun towards the edge of CR modulation region. Simple estimations of the propagation time can be obtained for distances of 80 AU ( $T_1$ ) and 100 AU ( $T_2$ ), where the cosmic ray modulation should be still important [39, 40]. In fact, by assuming the average solar wind speed  $V^{\text{SW}} = 450$  km/s, the CME mean speed during solar maximum  $V^{\text{CME}} = 550$  km/s [41] and the velocity of the high speed streams  $V^{\text{HSS}} = 750$  km/s as characteristic velocities of three different solar wind regimes, the corresponding propagation time are  $T_1^{\text{SW}} = 10$  months/ $T_2^{\text{SW}} = 13$  months,  $T_1^{\text{CME}} = 8$  months/ $T_2^{\text{CME}} = 10$  months,  $T_1^{\text{HSS}} = 6$  months/ $T_2^{\text{HSS}} = 7$  months. Indeed, such values are also consistent with the delay time between transient CR decreases measured at different heliocentric distances, following intense solar-interplanetary events. For instance, a large propagating transient CR decrease was detected at neutron monitor energies at the Earth in October 2003 (the Halloween event; Plainaki et al. [42]) and about 6–8 months later by CR detectors aboard Voyager 2 and Voyager 1 at 73 AU and 92 AU, respectively [43, 44].

**3.2. CR Modulation and Drift Effects.** It is widely known that the CR intensity curve follows a 22 yr cycle with alternate maxima being flat-topped and peaked (e.g., [45]). This peculiar behavior is described by models of CR modulation [46–52], based on the observed reversal of the Sun’s magnetic field polarity, curvature and gradient drifts in the interplanetary magnetic field. In the drift formalism, during epochs when  $A > 0$  (i.e., when the Sun’s dipole magnetic field is positive in the northern hemisphere) the approach in the inner heliosphere of positively charged CRs is from over the poles, while during epochs when  $A < 0$  the preferred direction is from along the heliospheric current sheet (HCS). The average excursion, during a solar rotation, of the HCS from the heliographic equator is referred to as tilt angle (e.g., [53]), which characterize the drift effects on CRs (e.g., [50, 54, 55]). In periods of minimum solar activity, that is, when the CR modulation by solar activity is reduced, the effects related to the polarity state of the heliosphere and to the HCS tilt are supposed to be more important. In order to account for the CR behavior described above, modes  $s_7$ ,  $s_9$  have to be considered. As clearly seen in the lower panel of Figure 7, the superposition of these IMFs to the  $\sim 11$  yr one is necessary to reproduce the long term variation of the actual CR data during the minimum solar activity periods and the maxima of odd numbered cycles. Hence, the combination

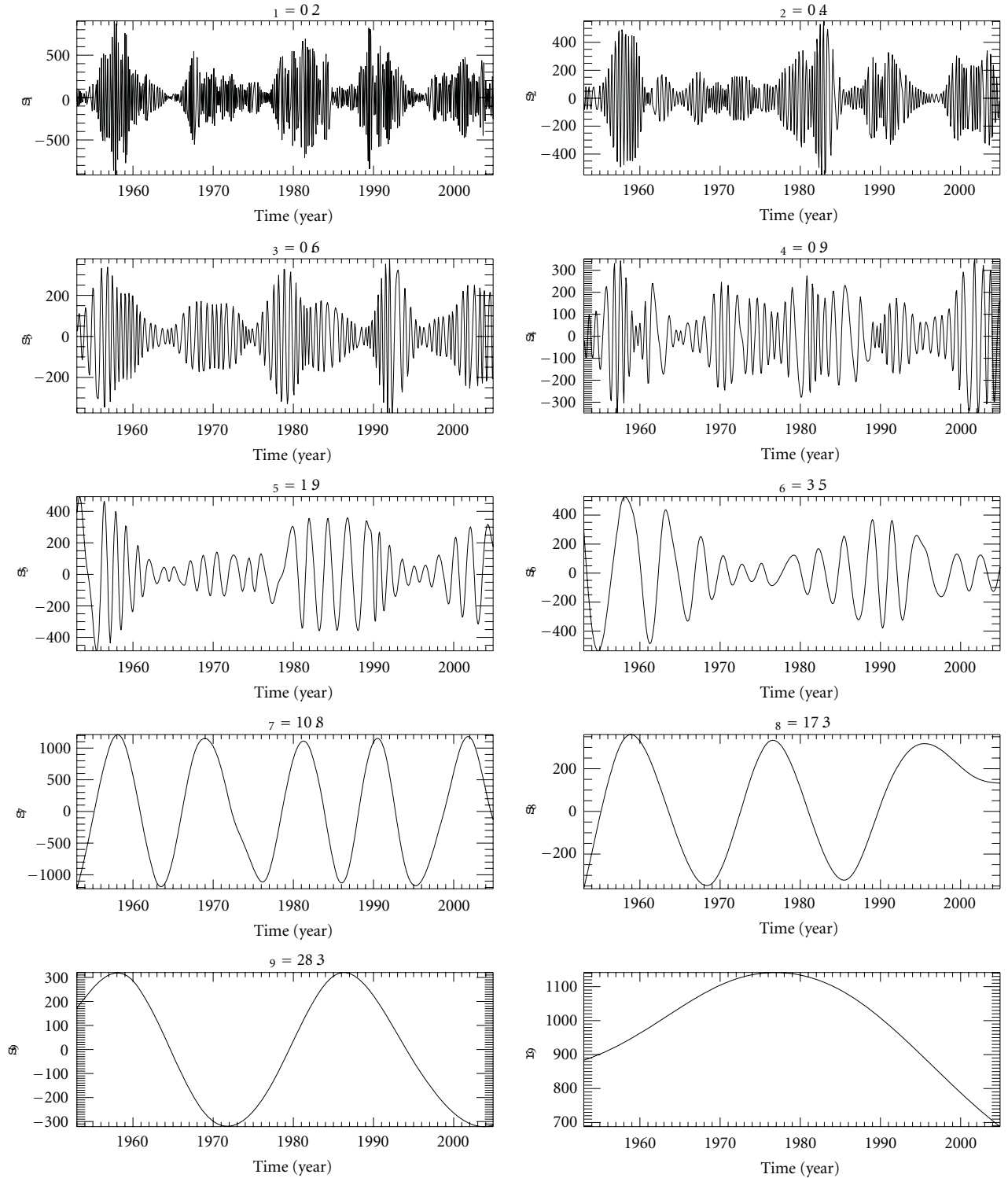


FIGURE 4: IMFs ( $j$  values from 1 to 9) obtained by performing the EMD on SA data, along with their characteristic periods  $\tau_j$  in years.

of both  $j = 7, 9$  IMFs is fundamental to take into account the full contribution of the drifts to the CR modulation. In fact,  $s_9$  should be representative of the heliosphere polarity changes, its characteristic average period  $\tau_9$  being  $\sim 22$  yr. In addition, the mode  $s_7$  seems to be unrelated to solar activity

perturbations, because no comparable periodicity was found in the sunspot area, as outlined in Section 2. We suggest that a possible reason for the CR variability at this time scale can be the particle drift related to the variation during the solar cycle of the latitude extent of the HCS. As a matter of fact,

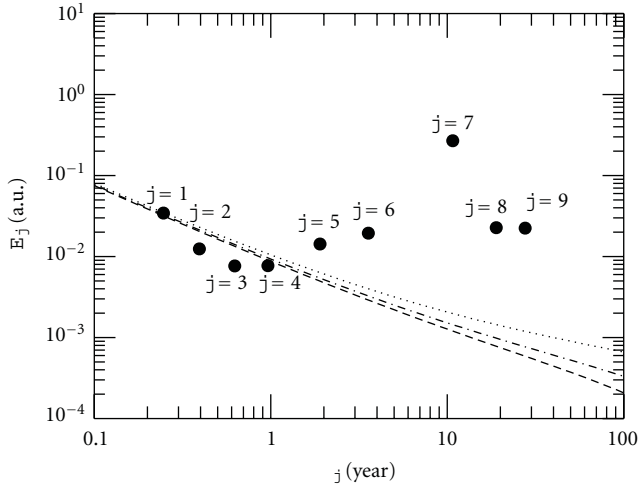


FIGURE 5: Average amplitude ( $E_j$ ) versus typical period ( $\tau_j$ ) of the  $j$  IMFs ( $j$  values from 1 to 9) identified in the SA data through the EMD. Dashed, dot-dashed, and dotted lines indicate the 90th, 95th, and 99th percentile, respectively.

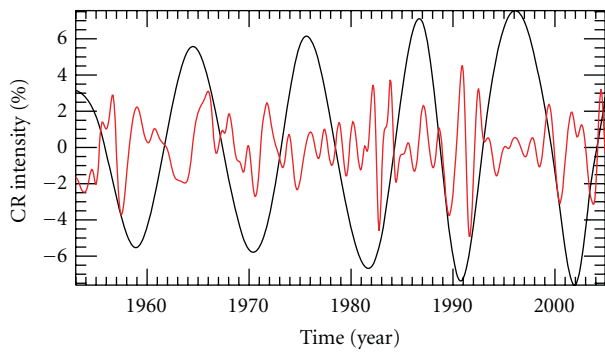
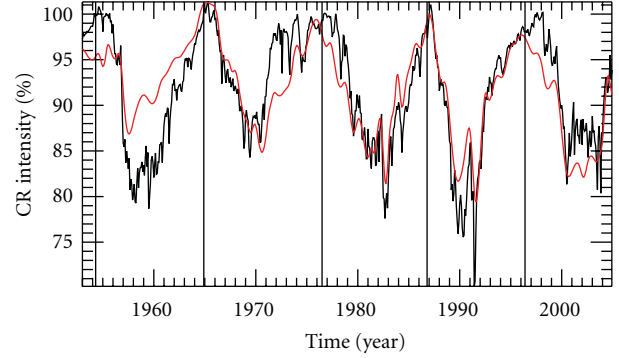


FIGURE 6: Time history of the QBOs (red line) and the  $\sim 11$  yr mode (black line) obtained through the EMD for CLI data.

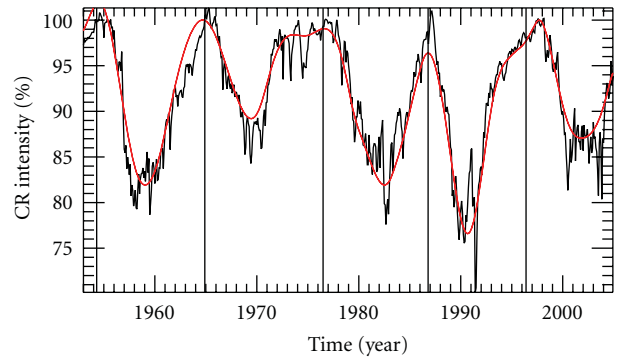
the characteristic period  $\tau_7 \sim 6.5$  yr is a reasonable average time for the latitudinal excursion of the HCS (although the HCS decrease time during the descending phase of the sunspot cycle is usually higher than the rise time, especially for odd numbered cycles, e.g., [56]). Moreover, the mode  $s_7$  plays a crucial role in determining the flat-topped maximum of CRs during even sunspot cycles, in agreement with the expectations of drift models that include the changing of HCS inclination during the 11 yr solar cycle (e.g., [50, 55]). Nevertheless, a better understanding of the nature of the mode  $s_7$  is needed and will be faced in a future paper.

#### 4. Conclusions

A new approach, through the combined application of two powerful techniques, such as the wavelet and EMD, was performed on CR data from the Climax neutron monitor to investigate the time variability and the relationship with the variations of the solar activity, as parametrized by the sunspot area. Our results provide the first evidence for the



(a)



(b)

FIGURE 7: (a) CR intensity (black line), superposition (red line) of the  $\sim 11$  yr mode, and the QBOs computed from CLI data. (b) CR intensity (black line), superposition (red line) of the  $\sim 11$  yr and modes  $s_7$  and  $s_9$  computed from CLI data. Dashed vertical lines indicate the time of the solar minima as provided by [ftp://ftp.ngdc.noaa.gov/STP/SOLAR\\_DATA/SUNSPOT\\_NUMBERS/docs/maxmin.new](ftp://ftp.ngdc.noaa.gov/STP/SOLAR_DATA/SUNSPOT_NUMBERS/docs/maxmin.new).

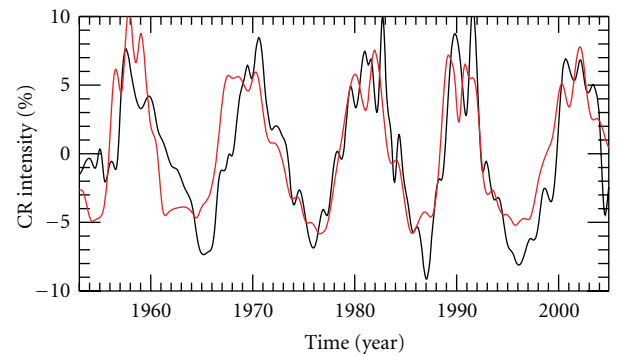


FIGURE 8: Superposition of the  $\sim 11$  yr mode and the QBOs computed from CLI (inverted, black line) and SA (red line) data.

different causes producing the CR modulation, identified according to the temporal scales characterizing the CR variability. In particular, we were able to discern the CR variations directly induced by the solar activity and those possibly related to the particle drift in the large scale magnetic field in the heliosphere. Solar activity is found to be responsible for the GG phenomenon and for most of the

step-like CR modulation, through the combined effect of the 11 yr cycle and QBOs.

The effect of the drifts has been clearly identified and associated with the CR variations at  $\sim 22$  yr and  $\sim 6$  yr. In particular, time variations at  $\sim 22$  yr are due to the polarity state of the heliosphere, whereas those at  $\sim 6$  yr could reflect the latitudinal excursion of the HCS. Both contributions explain the CR time profile, as expected from the drift theory and models, during the descending and minimum phase of solar activity of even numbered solar cycles (compare top and bottom panel of Figure 7), that is when  $A > 0$  and the CRs enter the heliosphere from the poles, while the HCS tilt decays rapidly to low angles, leading to a fast recovery of the CR intensity soon after the solar maximum. In addition, the shape of the CR intensity during the ascending and maximum phase of the odd numbered cycles (again in periods when  $A > 0$ ) is determined by these variations as well.

## Acknowledgments

This work was partially supported by the ASI/INAF Contract no. I/022/10/0, by the European Social Fund, European Commission, and by Regione Calabria. Thanks are due also to the Italian PNRA for the use of the RAC-ANT database, prepared at the former IFSI-Roma (now IAPS) under Contract PROGDEF09\_37 (code 2009/A3.07).

## References

- [1] S. E. Forbush, "World-wide cosmic ray variations, 1937–1952," *Journal of Geophysical Research*, vol. 59, p. 525, 1954.
- [2] S. E. Forbush, "Time variations of cosmic rays," in *Handbuch der Physik*, S. Flugge, Ed., vol. 49, p. 159, Springer, New York, NY, USA, 1966.
- [3] V. F. Hess, *Zeitschrift Für Physik*, vol. 13, p. 1084, 1912.
- [4] M. Storini, "Cosmic rays for solar-terrestrial physics," *Nuovo Cimento della Societa Italiana di Fisica C*, vol. 20, no. 6, pp. 871–880, 1997.
- [5] I. Dauberschies, "The wavelet transform, time-frequency localization and signal analysis," *IEEE Transactions on Information Theory*, vol. 36, pp. 961–1005, 1990.
- [6] P. Kumar and E. Fofoula-Georgiou, "Wavelet analysis for geophysical applications," *Reviews of Geophysics*, vol. 35, no. 4, pp. 385–412, 1997.
- [7] K. Kudela, S. Yasue, K. Munakata, and P. Bobik, "cosmicray variability at different scales: a wavelet approach," in *Proceedings of the 26th International Cosmicray Conference*, vol. 7, pp. 163–166, Salt Lake City, Utah, USA, August 1999.
- [8] M. Laurenza, S. Giangravé, M. Storini et al., in *Proceedings of the 30th International Cosmicray Conference. July 3–11, 2007, Mrida, Yucatn, Mexico*, R. Caballero, J. C. D'Olivo, G. Medina-Tanco, L. Nellen, F. A. Snchez, and J. F. Valds-Galicia, Eds., vol. 1, pp. 513–516, Universidad Nacional Autónoma de México, Mexico City, Mexico, 2008.
- [9] K. Kudela, J. Rybak, A. Antalovà, and M. Storini, "Time evolution of low-frequency periodicities in cosmic ray intensity," *Solar Physics*, vol. 205, pp. 165–175, 2002.
- [10] C. Kato, K. Munakata, S. Yasue, K. Inoue, and F. B. McDonald, "A  $\sim 1.7$ -year quasi-periodicity in cosmic ray intensity variation observed in the outer heliosphere," *Journal of Geophysical Research A*, vol. 108, no. 10, Article ID 1367, 7 pages, 2003.
- [11] J. Rybak, A. Antalovà, and M. Storini, "The wavelet analysis of the solar and cosmic-ray data," *Space Science Reviews*, vol. 97, no. 1–4, pp. 359–362, 2001.
- [12] J. F. Valdés-Galicia and V. M. Velasco, "Variations of mid-term periodicities in solar activity physical phenomena," *Advances in Space Research*, vol. 41, pp. 297–305, 2008.
- [13] M. Laurenza and M. Storini, *Memorie Della Societa Astronomica Italiana*, vol. 9, p. 109, 2006.
- [14] M. Laurenza and M. Storini, in *Proceedings of the 31st International Cosmicray Conference*, 2009, paper ID: 00475, <http://icrc2009.uni.lodz.pl>.
- [15] N. E. Huang, Z. Shen, S. R. Long et al., "The empirical mode decomposition and the Hilbert spectrum for nonlinear and non-stationary time series analysis," *Royal Society of London Proceedings A*, vol. 454, p. 903, 1998.
- [16] P. Flandrin, G. Rilling, and P. Gonçalves, "Empirical mode decomposition as a filter bank," *IEEE Signal Processing Letters*, vol. 11, no. 2, pp. 112–114, 2004.
- [17] J. Terradas, R. Oliver, and J. L. Ballester, "Application of statistical techniques to the analysis of solar coronal oscillations," *Astrophysical Journal*, vol. 614, no. 1, pp. 435–447, 2004.
- [18] A. Vecchio, M. Laurenza, V. Carbone, and M. Storini, "Quasi-biennial modulation of solar neutrino flux and solar and galactic cosmic rays by solar cyclic activity," *Astrophysical Journal Letters*, vol. 709, no. 1, pp. L1–L5, 2010.
- [19] A. Vecchio, M. Laurenza, D. Meduri, V. Carbone, and M. Storini, "The dynamics of the solar magnetic field: polarity reversals, butterfly diagram, and quasi-biennial oscillations," *Astrophysical Journal*, vol. 749, no. 1, Article ID 27, 2012.
- [20] B. L. Barnhart and W. E. Eichinger, "Analysis of sunspot variability using the hilbert—huang transform," *Solar Physics*, vol. 269, no. 2, pp. 439–449, 2011.
- [21] M. Laurenza, A. Vecchio, V. Carbone, and M. Storini, "Quasi-biennial modulation of galactic cosmic rays," *The Astrophysical Journal*, vol. 749, p. 167, 2012.
- [22] C. Torrence and G. P. Compo, "A practical guide to wavelet analysis," *Bulletin of the American Meteorological Society*, vol. 79, no. 1, pp. 61–78, 1998.
- [23] D. A. T. Cummings, R. A. Irizarry, N. E. Huang et al., "Travelling waves in the occurrence of dengue haemorrhagic fever in Thailand," *Nature*, vol. 427, no. 6972, pp. 344–347, 2004.
- [24] Z. Wu and N. E. Huang, "A study of the characteristics of white noise using the empirical mode decomposition method," *Proceedings of the Royal Society A*, vol. 460, no. 2046, pp. 1597–1611, 2004.
- [25] E. E. Benevolenskaya, "A model of the double magnetic cycle of the sun," *Astrophysical Journal Letters*, vol. 509, no. 1, pp. L49–L52, 1998.
- [26] G. A. Bazilevskaya, M. B. Krainev, V. S. Makhmutov, E. O. Flückiger, A. I. Sladkova, and M. Storini, "Structure of the maximum phase of solar cycles 21 and 22," *Solar Physics*, vol. 197, no. 1, pp. 157–174, 2000.
- [27] G. A. Bazilevskaya, V. S. Makhmutov, and A. I. Sladkova, "Gnevyshev gap effects in solar energetic particle activity," *Advances in Space Research*, vol. 38, no. 3, pp. 484–488, 2006.
- [28] A. Vecchio and V. Carbone, "Spatio-temporal analysis of solar activity: main periodicities and period length variations," *Astronomy and Astrophysics*, vol. 502, no. 3, pp. 981–987, 2009.
- [29] E. Forgàcs-Dajka and T. Borkovits, "Searching for mid-term variations in different aspects of solar activity—looking for probable common origins and studying temporal variations of

- magnetic polarities," *Monthly Notices of the Royal Astronomical Society*, vol. 374, pp. 282–291, 2007.
- [30] G. Wibberenz and H. V. Cane, "Simple analytical solutions for propagating diffusive barriers and application to the 1974 minicycle," *Journal of Geophysical Research*, vol. 105, no. 8, p. 18315, 2000.
- [31] G. Wibberenz, H. V. Cane, I. G. Richardson, and T. T. von Rosevinge, "The influence of tilt angle and magnetic field variations on cosmic ray modulation," *Space Science Reviews*, vol. 97, pp. 343–347, 2001.
- [32] M. Storini, G. A. Bazilevskaya, E. O. Flückiger, M. B. Krainev, V. S. Makhmutov, and A. I. Sladkova, "The Gnevyshev gap: a review for space weather," *Advances in Space Research*, vol. 31, no. 4, pp. 895–900, 2003.
- [33] M. Storini, "Testing solar activity features during the descending phase of sunspot cycle 22," *Advances in Space Research*, vol. 16, no. 9, pp. 51–55, 1995.
- [34] F. Feminella and M. Storini, "Large-scale dynamical phenomena during solar activity cycles," *Astronomy and Astrophysics*, vol. 322, no. 1, pp. 311–319, 1997.
- [35] L. F. Burlaga, F. B. McDonald, and N. F. Ness, "Cosmic ray modulation and the distant heliospheric magnetic field: voyager 1 and 2 observations from 1986 to 1989," *Journal of Geophysical Research*, vol. 98, no. 1, p. 1, 1993.
- [36] M. S. Potgieter and J. A. le Roux, "The long-term heliospheric modulation of galactic cosmic rays according to a time-dependent drift model with merged interaction regions," *The Astrophysical Journal*, vol. 423, p. 817, 1994.
- [37] I. Sabbah and M. Rybanský, "Galactic cosmic ray modulation during the last five solar cycles," *Journal of Geophysical Research A*, vol. 111, Article ID A01105, 2006.
- [38] M. Singh, Y. P. Singh, and Badruddin, "Solar modulation of galactic cosmic rays during the last five solar cycles," *Journal of Atmospheric and Solar-Terrestrial Physics*, vol. 70, pp. 169–183, 2008.
- [39] W. R. Webber, "Voyager measurements of galactic cosmic rays and implications for modulation in the heliosheath and beyond," in *Proceedings of the 5th Annual International Astrophysics Conference*, vol. 858, pp. 135–140, March 2006.
- [40] M. S. Potgieter, "Challenges to cosmic ray modeling: from beyond the solar wind termination shock," *Advances in Space Research*, vol. 41, pp. 245–458, 2008.
- [41] N. Gopalswamy, S. Nunes, S. Yashiro, and R. A. Howard, "Variability of solar eruptions during cycle 23," *Advances in Space Research*, vol. 34, no. 2, pp. 391–396, 2004.
- [42] C. Plainaki, A. Belov, E. Eroshenko, V. Kurt, H. Mavromichalaki, and V. Yanke, "Unexpected burst of solar activity recorded by neutron monitors during October–November 2003," *Advances in Space Research*, vol. 35, no. 4, pp. 691–696, 2005.
- [43] J. D. Richardson, C. Wang, J. C. Kasper, and Y. Liu, "Propagation of the October/November 2003 CMEs through the heliosphere," *Geophysical Research Letters*, vol. 32, Article ID L03S03, 4 pages, 2005.
- [44] D. S. Intriligator, W. Sun, M. Dryer, C. D. Fry, C. Deehr, and J. Intriligator, "From the Sun to the outer heliosphere: Modeling and analyses of the interplanetary propagation of the October/November (Halloween) 2003 solar events," *Journal of Geophysical Research A*, vol. 110, no. 9, Article ID A09S10, 2005.
- [45] E. J. Smith, *Journal of Geophysical Research*, vol. 95, p. 731, 1990.
- [46] J. R. Jokipii, E. H. Levy, and W. B. Hubbard, "Effects of particle drift on cosmic-ray transport. I—general properties, application to solar modulation," *Astrophysical Journal Letters*, vol. 213, pp. 861–868, 1977.
- [47] M. S. Potgieter and J. A. le Roux, "The simulated features of heliospheric cosmic-ray modulation with a time-dependent drift model. I—general effects of the changing neutral sheet over the period 1985–1990," *The Astrophysical Journal*, vol. 386, pp. 336–346, 1992.
- [48] J. A. le Roux and M. S. Potgieter, "The simulated features of heliospheric cosmic-ray modulation with a time-dependent drift model. II—on the energy dependence of the onset of new modulation in 1987," *The Astrophysical Journal*, vol. 390, pp. 661–667, 1992.
- [49] J. A. le Roux and M. S. Potgieter, "The simulated features of heliospheric cosmic-ray modulation with a time-dependent drift model. IV—the role of heliospheric neutral sheet deformation," *The Astrophysical Journal*, vol. 397, pp. 686–693, 1992.
- [50] S. E. S. Ferreira and M. S. Potgieter, *Advances in Space Research*, vol. 32, p. 2003, 2004.
- [51] S. E. S. Ferreira and M. S. Potgieter, "Long-term cosmic-ray modulation in the heliosphere," *The Astrophysical Journal*, vol. 603, p. 744, 2004.
- [52] R. Manuel, S. E. S. Ferreira, and M. S. Potgieter, "Cosmic ray modulation in the outer heliosphere: predictions for cosmic ray intensities up to the heliopause along Voyager 1 and 2 trajectories," *Advances in Space Research*, vol. 48, pp. 874–883, 2011.
- [53] J. T. Hoeksema, J. M. Wilcox, and P. H. Scherrer, "Structure of the heliospheric current sheet in the early portion of Sunspot Cycle 21," *Journal of Geophysical Research*, vol. 87, p. 10331, 1982.
- [54] J. R. Jokipii and B. Thomas, "Effects of drift on the transport of cosmic rays. IV—modulation by a wavy interplanetary current sheet," *Astrophysical Journal Letters*, vol. 243, pp. 1115–1122, 1981.
- [55] K. Kota and J. R. Jokipii, "Effects of drift on the transport of cosmic rays. VI—a three-dimensional model including diffusion," *The Astrophysical Journal*, vol. 265, pp. 573–581, 1983.
- [56] E. W. Cliver and A. G. Ling, "22 Year patterns in the relationship of sunspot number and tilt angle to cosmic-ray intensity," *Astrophysical Journal Letters*, vol. 551, no. 2, pp. L189–L192, 2001.